2017

Development of a multifunctional photovoltaic integrated insulated concrete sandwich panel

Mostafa Yossef
Iowa State University

Development of a multifunctional photovoltaic integrated insulated concrete sandwich panel

by

Mostafa Yossef

A dissertation submitted to the graduate faculty

in partial fulfillment of the requirements for the degree of

DOCTOR OF PHILOSOPHY

Major: Civil Engineering (Structural Engineering)

Program of Study Committee:
An Chen, Major Professor
Simon Laflamme
Behrouz Shafei
Ashely Buss
Wei Hong

Iowa State University

Ames, Iowa

2017

DEDICATION

To my parents, Youssef and Tahia, for their help and unconditional love.

To my brothers, Mohamed and Ahmed, and my sister, Aisha.

To my wife, Dina and my parents in-law.

TABLE OF CONTENTS

Page

LIST OF FIGURES vii
LIST OF TABLES xi
ACKNOWLEDGMENTS xii
ABSTRACT xiv
CHAPTER 1. INTRODUCTION 1
1.1 Background 1
1.2 Problem Statement 11
1.3 Contributions and Objectives 12
1.4 Thesis Organization 13
1.5 References 13
CHAPTER 2. A COMPARATIVE STUDY OF DIFFERENT METHODS TO CALCULATE DEGREES OF COMPOSITE ACTION FOR PRECAST, PRESTRESSED INSULATED CONCRETE SANDWICH PANELS 18
Abstract 18
2.1. Introduction 19
2.1.1. Degree of composite action 21
2.2. Experimental Investigation 22
2.2.1. Test setup 22
2.3. Finite Element Analysis 26
2.3.1. Geometry 27
2.3.2. Material properties 28
2.3.3. Loading and analysis procedure 38
2.4. Correlations between FE and Test Results 38
2.5. Results and Parametric Study 39
2.5.1. Displacement method 41
2.5.2. Load method 42
2.5.3. Strain method 43
2.6. Summary and Conclusions 45
2.7. References 46

CHAPTER 3. DEVELOPMENT OF A MULTIFUNCTIONAL PHOTOVOLTAIC INTEGRATED INSULATED CONCRETE SANDWICH PANEL 51
Abstract 51
3.1. Introduction 52
3.2. Experimental Program 54
3.2.1. Material properties 54
3.2.2. Evaluating solar cell performance 55
3.2.3. Specimen fabrication 56
3.3. Validation and Results 67
3.3.1. Linear stage 67
3.3.1. Nonlinear stage 75
3.4. Conclusions 80
3.5. References 81
CHAPTER 4. STRAIN EFFECT ON THE PERFORMANCE OF AMORPHOUS SILICON AND PEROVSKITE SOLAR CELLS 83
Abstract 83
4.1. Introduction 84
4.2. Experimental Program 87
4.2.1. Testing plan 87
4.2.2. Materials 87
4.2.3. Sample fabrication 88
4.2.4. Sample details 91
4.2.5. Testing setup 92
4.3. Testing Results 97
4.3.1. Temperature effect 98
4.3.2. Loading effect 99
4.4. Discussions And Conclusions 105
4.5. References 106
CHAPTER 5. A SOLUTION CONSIDERING PARTIAL DEGREE OF COMPOSITE ACTION FOR INSULATED SANDWICH PANELS WITH GENERAL CONFIGURATION FLEXIBLE SHEAR CONNECTORS 108
Abstract 108
5.1. Introduction 109

5.1.1. Insulated sandwich panels 109
5.1.2. Shear lag effect 109
5.1.3. Degree of Composite action (DCA) 112
5.2. Analytical Model 115
5.2.1. Boundary conditions 118
5.2.2. Single box-section 119
5.2.3. Multiple shear connectors (Multi-cell box section) 124
5.2.4. Cantilever cross-section 127
5.2.5. WF section 129
5.3. Degree of Composite Action 130
5.4. Verification 132
5.5. Applications 141
5.6. Simplified Method to Calculate the Deflection and Strain Distribution 144
5.7. Conclusions 149
5.8. References 149
CHAPTER 6. ANALYTICAL MODEL FOR DECK-ON-GIRDER COMPOSITE BEAM SYSTEM WITH PARTIAL COMPOSITE ACTION 154
Abstract 154
6.1. Introduction 154
6.2. Research Significance 158
6.3. Analytical Model 159
6.4. Degree of Composite Action 167
6.5. Verification 168
6.6. Application 176
6.7. Simplified Method to Calculate the Deflection and Strain Distribution 179
6.8. Discussions 181
6.9. Conclusions 183
6.10. References 184
CHAPTER 7. CONCLUSIONS AND FUTURE WORK 187
7.1. Study on a Full-Scale Insulated Concrete Sandwich Panel 187
7.2. Integrated Insulated Concrete Sandwich (PVICS) Panel 188
7.3. Performance of Solar Cells under Strain 188
7.4. Shear-Lag Analytical Model for Sandwich Panels 189

7.5. Shear-Lag Analytical Model for Deck-On-Girder Composite Beam System 189
7.6. Future Work and Recommendations 190

LIST OF FIGURES

Page
Figure 1.1 PV modules mounted to the wall of a multistory parking at NREL, CO 3
Figure 1.2 Prestressed precast sandwich panel components 5
Figure 1.3 Partial DCA for deck slab on beam (Lorenz and Stockwell, 1984) 9
Figure 1.4 Effective width resulting from shear-lag effect 10
Figure 2.1 Concrete sandwich panel 19
Figure 2.2 Typical sandwich panel production prior to placing top concrete wythe 23
Figure 2.3 Cross section of test panel 23
Figure 2.4 Test setup 24
Figure 2.5 Final load placement 24
Figure 2.6 Load deflection curve for the tested panel 25
Figure 2.7 Top layer of longitudinal prestressing strand splitting failure 26
Figure 2.8 Uniform and symmetrical bottom transverse cracks 26
Figure 2.9 FE model of the test panel 27
Figure 2.10 CFRP shear grid in the FE model 28
Figure 2.11 Typical compressive stress-strain curve 30
Figure 2.12 Tensile stress-strain response (ABAQUS, 2013) 33
Figure 2.13 Tensile stress-strain curve (Wahalathantri et al., 2011) 34
Figure 2.14 Constitution model for WWM 4x4-W2.1xW2.1 36
Figure 2.15 Load vs. deflection of experimental and FE model with different mesh sizes 38
Figure 2.16 Bottom view of tension damage 39
Figure 2.17 Sandwich panel with connectors 40
Figure 2.18 Load-deflection curve for 100%, 72%, 50%, 25%, and 0% DCA 42
Figure 2.19 Partial DCA for deck slab on beam (Lorenz and Stockwell, 1984) 43
Figure 2.20 Partial DCA for sandwich panels 44
Figure 2.21 Strain profile at different DCAs at load 17876.3 lbf 45
Figure 3.1 MPP vs. strain 56
Figure 3.2 Typical sandwich panel 56
Figure 3.3 Shifted rubber bolted to the formwork to achieve 90^{o} angle 57
Figure 3.4 Formwork with four rubber connection at each side 58
Figure 3.5 Attaching solar cells and laying down the glass fiber CSM 58
Figure 3.6 Different processes to fold FRP with aggregates (a) Applying epoxy and aggregates on the sides and base at the same time, (b) Applying epoxy and aggregates at the sides and base and leaving a 2'' gap at the corner, (c) Folding the sides and applying epoxy and aggregates at the corner. 59
Figure 3.7 FRP-aggregate shell 60
Figure 3.8 Installing strain gages 60
Figure 3.9 Assembling rebars 60
Figure 3.10 PVICS test setup 61
Figure 3.11 PVICS panel manufacturing process (a) placing first reinforcement set and pouring concrete, (b) placing insulation layer and second reinforcement set, (c) smoothing concrete surface 61
Figure 3.12 Side strain gages location 63
Figure 3.13 PVICS panel under three-point loading 63

Figure 3.14 Nonlinear loading setup with installed lamps, fans and thermocouple 64
Figure 3.15 Multiple solar cell and temperature data acquisition setup 65
Figure 3.16 Strain, deflection and load data acquisition setup along with manual hydraulic jack 66
Figure 3.17 FE model (insulation foam is removed for clarification purpose) 68
Figure 3.18 Correlation of strain across the width of the panel 69
Figure 3.19 Correlation of mid-span deflection 70
Figure 3.20 Strain across the thickness 71
Figure 3.21 Validation of analytical results with experimental and FE results 73
Figure 3.22 J-V curve before applying the load 74
Figure 3.23 MPP and FF versus strain 74
Figure 3.24 Load-displacement curve for experimental test and FE model 76
Figure 3.25 FRP shear connector failure; (a) Southwest side buckling, (b) debonding of shear connector at the southwest side, (c) Failure of shear connector at mid-span 76
Figure 3.26 Progress of Cracks on the lower wythe 77
Figure 3.27 (a) Slip at the end of the south side, (b) No slip is detected at the north side 77
Figure 3.28 Wrinkling of the top FRP, (a) view for east side and from the (b) west side 78
Figure 3.29 Strain distribution at 6 in away north mid-span at different loads 78
Figure 3.30 Strain distribution at 8 in away south the mid-span at different loads 79
Figure 3.31 Strain at mid-width vs. load 79
Figure 4.1 Sample preparation process (a) solar modules attached to peel ply, (b) sealed bag during curing process, (c) solar module attached to FRP plate, (d) Cutting compression samples, (e) Soldering wires to tension samples, (f) installing strain gages 90
Figure 4.2 Taped CSM 91
Figure 4.3 A-Si solar module SP3-12 91
Figure 4.4 Perovskite solar connected to wires using fast drying silver paste 91
Figure 4.5 Compression sample dimensions 92
Figure 4.6 Tension sample dimensions 92
Figure 4.7 Keithley SourceMeter 2400 (a) connecting 4 test lead at the front, (b) GPIB-USB cable connected at the back, (c) connecting test lead to the sample wires 92
Figure 4.8 LabVIEW program screenshot 93
Figure 4.9 Compression test setup under Kodak carsoul projector illumination 94
Figure 4.10 Close shots of the compression fixture 95
Figure 4.11 Tension setup for perovskite solar cell samples 96
Figure 4.12 J-V curve of monotonic compression tests for different strain values 97
Figure 4.13 J-V curve of monotonic tension tests for different strain values 97
Figure 4.14 Normalized MPP through time 99
Figure 4.15 MPP vs. strain for a-Si solar cells subjected to tension monotonic loading 101
Figure 4.16 MPP vs. strain for amorphous silicon solar-FRP subjected to monotonic compression loading 101
Figure 4.17 Different modes of buckling of amorphous silicon solar subjected to compression loading 102
Figure 4.18 MPP vs. strain for perovskite solar on glass substrate 102
Figure 4.19 Compression stress-strain curve 103
Figure 4.20 Normalized MPP vs. strain for compression loading and unloading 103

Figure 4.21 Normalized MPP vs. strain for tension loading and unloading 104
Figure 4.22 A-Si compression samples failure modes 104
Figure 4.23 Failure modes for a-Si tension samples subjected to tension loading and unloading 104
Figure 4.24 Failure modes for a-Si tension samples subjected to tension monotonic loading 105
Figure 4.25 Perovskite tension sample failure modes 105
Figure 5.1 Sandwich panels with FRP connectors (a)Tested panel with FRP shear grid (Frankl et al., 2011) (b) Cross section of test panel (Hopkins et al., 2014) 110
Figure 5.2 Effective width 110
Figure 5.3 FE model 110
Figure 5.4 Partial composite action defined by AISC (Lorenz and Stockwell, 1984) 110
Figure 5.5 Forces in a wythe 117
Figure 5.6 box cross-section with two shear connectors 119
Figure 5.7 Shear Force Transformation 121
Figure 5.8 Axial and bending moment on sandwich panels 121
Figure 5.9 Partial Composite Action for Sandwich Panels 121
Figure 5.10 Distribution factors multiple shear connectors 125
Figure 5.11 Cantilever cross-section 127
Figure 5.12 Stress distribution at mid-span for wide flange (WF) section 134
Figure 5.13 Stress distribution at mid-span for single box section 134
Figure 5.14 Stress distribution at mid-span for double box section 135
Figure 5.15 Stress distribution at mid-span for 3-cell box section 135
Figure 5.16 Stress distribution at mid-span for 4-cell box section 136
Figure 5.17 Stress distribution at mid-span for single box with double cantilever section 136
Figure 5.18 Deflection at mid-span for wide flange (WF) section 137
Figure 5.19 Deflection at mid-span for single box section 137
Figure 5.20 Deflection at mid-span for double box section 138
Figure 5.21 Deflection at mid-span for 3-cell box section 138
Figure 5.22 Deflection at mid-span for 4-cell box section 139
Figure 5.23 Deflection at mid-span for box section with double cantilever section 139
Figure 5.24 FE model for single box with double cantilever 140
Figure 5.25 Effective width ratio (b_{eff}/b) vs. DCAs for different configuration 141
Figure 5.26 EWR vs. core/wythe thickness ratio for different DCAs 142
Figure 5.27 EWR vs. aspect ratio for different DCAs 143
Figure 5.28 EWR vs. DCA for different panel stiffness 143
Figure 5.29 EWR vs. DCA for panel thickness ratio (t_1/t_2) 144
Figure 5.30 Mid-span deflection vs. DCA 148
Figure 5.31 Mid-span stress vs. DCA 148
Figure 6.1 Effective Flange Width (Zou et al. 2011), (a) Stress Distribution under out-of-plane Moment, (b) Shear Lag Effect 159
Figure 6.2 Bridge deck supported by two beams (Zou et al., 2011) 160
Figure 6.3 Forces in the deck 161
Figure 6.4 Partial Composite Action defined by AISC (Lorentz and Stockwell, 1984) 166
Figure 6.5 Composite beam with partial degree of composite action, (a) cross Section, (b) internal forces with partial DCA, (c) strain distribution with partial DCA,

(d) internal forces with 0% DCA, (e) strain distribution with 0% DCA,
(f) internal forces with 100% DCA, (g) strain distribution with 100% DCA 168
Figure 6.6 T-beam test (1 inch=25.4 mm; 1 ft=304.8 mm) (Newmark et al. 1951) 169
Figure 6.7 FE model 170
Figure 6.8 Load-deflection curves at mid-span 171
Figure 6.9 Load vs. strain at 457 mm away from mid-span 171
Figure 6.10 Stress distribution at mid-depth and mid-span of the deck 172
Figure 6.11 Bridge configuration (Chen and Davalos 2014) 173
Figure 6.12 FRP deck configurations (reprinted from Chen and Davalos 2014),
(a) 3D image of FRP deck, (b) facesheet configurations 174
Figure 6.13 Strain at the bottom flange of the girder vs. DCA at mid-span 175
Figure 6.14 Mid-span deflection vs. DCA 175
Figure 6.15 Effective width ratio (b_{eff}/b) vs. DCA 175
Figure 6.16 Stress distribution at mid-depth and mid-span of the deck 176
Figure 6.17 Effective width ratios (b_{eff}/b) for different deck stiffness 177
Figure 6.18 Effective width ratio (beff/b) vs. aspect ratio for different DCAs,
(a) 100% deck stiffness, (b) 25% deck stiffness 178
Figure 6.19 Mid-span deflection vs. DCA 182
Figure 6.20 Mid-span stress vs. DCA 183

LIST OF TABLES

Page

Table 2.1 Test panel load and deflection data 25
Table 2.2 Material properties 28
Table 2.3 Concrete compressive behavior 32
Table 2.4 Concrete tension behavior 34
Table 2.5 Material properties of shear connectors 36
Table 2.6 Material properties for prestressing strand grade 270 37
Table 2.7 Variation of area with the strand elements for the development length 37
Table 2.8 DCA displacement method calculations 41
Table 2.9 Yield and ultimate point values 43
Table 2.10 DCA strain method calculations 45
Table 3.1 Material properties 55
Table 3.2 Electrical properties 55
Table 3.3 Aggregates optimum size and distribution 59
Table 3.4 Material properties 68
Table 3.5 DCA calculation based on deflection method 70
Table 3.6 DCA calculation based on strain method 70
Table 4.1 Material properties 87
Table 4.2 Mechanical properties of solar module 87
Table 4.3 Electrical properties of solar module 87
Table 5.1 Shear connector stiffness (K) for different configurations 140
Table 6.1 Beam dimensions 169
Table 6.2 Material properties (Newmark et al. 1951) 169
Table 6.3 Equivalent properties of FRP panel (Chen and Davalos 2014) 173

ACKNOWLEDGMENTS

All praise is due to Allah (God) for what I have achieved, which would not be possible without his guidance.

I would like to thank Dr. An Chen for his support along my PhD study, encouraging me for high standards all the way. I would like to express my appreciation for his advice, support and motivation throughout the course of this research and other aspects of life.

Special thanks go to Austin Downey, Ahmed Alateeq and Moneim Elshobaki. Without their support, I would not be able to complete the solar cell testing.

I would also like to thank Dr. Simon Laflamme for providing equipment and allowing me to use his laboratory, in addition to his continuous support through my study.

I am also grateful for Dr. Wei Hong for his fruitful discussions regarding my analytical models, Dr. Ashely Buss for her support and friendly advice, and Dr. Behrouz Shafei for serving on my POS committee.

I would like to extend my gratitude to Douglas Wood, Owen Steffens, Connor Schaeffer, David Morandeira, Hao Wu, and Joseph Podolsky for their help with manufacturing the panel.

I would like to thank Drs. Kai Zhu, Chao Zhang, Joe Berry, and Mengjin Yang at National Renewable Energy Laboratory for providing the perovskite solar cells and the opportunity of testing them using their facility.

I would also like to thank my friends and colleagues from University of Idaho, to whom I owe a huge debt, especially Nicolas Pena, Drs. Paul Hopkins, Kris Brown and Fouad Bayomy.

Furthermore, I would like to thank all my friends and colleagues: Hussam, Liang, M. Youssef, M. Alaa, A. Fathi, Abdullah Alshehri, Irvin, Sharif, Parnian, Zahra and many more.

In addition, I am grateful for the financial support from the Arab Academy for Science and Technology and Maritime Transport (AASTMT), especially Dr. Abdel Moneim Sanad, Dr. Adel Belal and Dr. Ismail AbdelGhafar for facilitating the scholarship towards my PhD, as well as my friends Mohammed Ashraf and Hassan Ahmed who kept track of my status and helped me while I am abroad.

I want to thank my family, especially my aunts, Nagwa and Amina, for being as my second mom to me during my residence in the United States; my wife, Dina, for keeping encouraging me to be a better person; my parents, Youssef and Tahia, and my siblings, Mohamed, Ahmed and Aisha for supporting me, believing in me, and their endless love.

ABSTRACT

Insulated concrete sandwich panels are designed to provide an energy-efficient and fast construction solution. They typically consist of two concrete wythes separated by an inner layer of insulation. Recently, Fiber-Reinforced Polymer (FRP) has been used as shear connectors to connect the two concrete wythes, which is expected to reduce thermal bridging and increase strength-to-weight ratio. To study the effectiveness of FRP shear connectors, a nonlinear Finite Element (FE) model was constructed, and its accuracy was proven through good correlations between the FE and existing test results. The FE model was further used to conduct a parametric study by varying the stiffnesses of the shear connectors. Different methods to calculate DCA were evaluated. It was concluded that FRP connectors can provide enough strength, although they have lower stiffness compared to steel, resulting in partial Degree of Composite Action (DCA).

Motivated by the promising results from the FE study on the sandwich panel, this dissertation aims to develop a multifunctional photovoltaic (PV) integrated insulated concrete sandwich (PVICS) panel, through integrating photovoltaic (PV) cells on the top of the panel. The PVICS panel can act both as an active energy system by harvesting solar energy using the solar cells; and a passive energy system, where the energy saving is provided by the insulation layer, similar to a traditional insulated concrete sandwich panel. The combined active and passive energy system can achieve a zero-carbonate building system.

A combined experimental and FE study on a prototype PVICS panel was conducted to prove the concept. An FRP shell was manufactured as the stay-in-place formwork for the sandwich panel. Solar cells were attached to the exterior surface of the FRP shell using an innovative co-curing scheme. Polymer concrete was applied to the inner surface of the FRP

shell to enhance the bond between the FRP and concrete. In addition to acting as an interface to bond solar cells and concrete, the FRP shell can provide a confining effect, and act as shear connectors and reinforcement to improve the structural performance of the PVICS panel. It was found that FRP shear connectors can provide nearly 85% DCA and solar cells worked properly, which proves the concept of PVICS. Furthermore, two issues were identified which need further investigation to properly design the PVICS panel: (1) the performance of the solar cells under different strain states; and (2) the non-uniform strain distribution across the width of the panel, known as shear-lag effect.

To address those two issues, the performance of thin-film amorphous silicon (a-Si) and perovskite solar cells were investigated under different strain states. Compression and tension tests were conducted on a-Si solar cells bonded to FRP plates and tension tests were conducted on perovskite solar cells attached to glass substrates. J-V characteristic curves were measured at different strains until the samples failed. It can be concluded that there are strain thresholds for both compression and tension for a-Si solar cells, which worked properly below the thresholds but degraded rapidly once the thresholds were passed. Perovskite solar cells are more ductile, which can withstand a strain of 3%. No degradation of the performance was observed before the substrate failed.

To study the shear-lag effect, an analytical solution is developed where the partial DCA and boundary conditions from various configurations of the flexible shear connectors are considered. The effective width, an important parameter to describe the shear lag effect, is defined. The analytical model is then verified through close correlations between FE and analytical results for an insulated concrete sandwich panel with FRP shear connectors. A parametric study is finally conducted using the analytical model to study the effects of deck

stiffness and aspect ratio on the effective width. The results from this study can be used for the design of insulated sandwich panels. Similarly, the analytical solution could also be used to study the partial DCAs for FRP deck-on-steel girder system, as illustrated by a combined analytical and FE studies on the system.

CHAPTER 1. INTRODUCTION

1.1 Background

Insulated concrete sandwich panels consist of two outer layers of concrete separated by an inner layer of insulation, as shown in Figure 1.2, which can be used as wall and roof/floor panels. They can protect the inside of the building from thermal gradients by eliminating the thermal bridging between the concrete wythes. In addition, they are considered as structurally efficient elements that can provide fast construction, reduced labor cost, quality control, different shape design, and lower material cost through mass production at the precast concrete plant. The following literature review is focused on the energy and structural performances of the panels.

1.1.1. Energy performance

Steel shear connectors have been commonly used since 1990's, including small bent bars, steel wire trusses, continuous bent bar (Bush and Stine, 1994; Bush and Wu, 1998; Einea et al., 1991). However, steel has a high thermal conductivity, which can cause thermal bridging. In addition, it is easy to corrode. Recently, Fiber-Reinforced Polymer (FRP) shear connectors have been proposed to replace steel shear connectors due to several advantages, such as low thermal conductivity, high resistant to corrosion, and high strength-to-weight ratio.

Although FRP shear connectors can increase the energy efficiency of the sandwich panel, it is still considered as a passive energy system since it reduces energy consumption by decreasing the thermal conductivity and heat losses. Active energy systems are systems that can provide energy to the structure through energy harvesting. The most common energy to harvest for buildings is solar energy, which can be achieved by integrating photovoltaic modules to buildings, known as Building Integrated Photovoltaic (BIPV).

1.1.2. Building Integrated Photovoltaic (BIPV)

The solar Investment Tax Credit (ITC) has successfully pushed hardware prices down and installer experience up. For example, the cost of solar electricity has decreased from $5.06/W in 2010 to $3.29/W in 2016, mostly due to the cost reduction of the photovoltaic (PV) module, which was 2.15/W in 2010 and is $0.7/W today. Although the price of the module will continue to decrease, there is little room for substantial reduction. Therefore, more effective ways are required to optimize the cost, such as BIPV system that can simplify the mounting system.

In a BIPV system, PV modules can be either fully integrated with the buildings or mounted on the roofs or walls, as shown in Figure 1.1, thereby reducing the cost of the mounting system, BIPV can also enhance the aesthetic appeal of the building and provide more space which is usually occupied by the stand-alone PV modules. The concept of BIPV started in the early 1990's. Later in the 2000's, the interest in designing net-zero energy buildings and the development of thin-film solar cells enabled the expansion of BIPV system, since the thin-film solar cells can be easily integrated with concrete tiles or just spread over the roof slab. The thin-film solar cells include amorphous silicon (a-Si), cadmium telluride (CdTe), copper indium diselenide (CIS) and copper indium gallium selenide (CIGS). The efficiency of a-Si solar cells varies from 4% to 14% while the efficiency of the CIGS and CdTe can reach up to 22.6% and 22.1%, respectively (Jelle et al., 2012). When subjected to high temperature, the efficiency of a-Si solar cells drops about 0.25%/ ^{o}C, compared to 0.4 to 0.5%/^{o}C for crystalline silicon-based cells (Zhao et al., 2011). Until now, a-Si solar cells are the most widely commercially available solar cells.

Figure 1.1 PV modules mounted to the wall of a multistory parking at NREL, CO

Combining the advantages of BIPV and insulated concrete sandwich paper, this dissertation aims to develop a multifunctional photovoltaic (PV) integrated insulated concrete sandwich (PVICS) panel, through integrating photovoltaic (PV) cells on the top of the panel, which can act as both an active and passive energy system. Furthermore, the proposed PVICS panel completely eliminates the mounting system, thereby achieving additional cost savings. However, the performance of the solar cells under strain needs to be investigated since solar cells become a part of the structure. Until now, the research on BIPV was mainly focused on the performance of the solar cell considering the effects of the inclination, temperature and other factors related to the weather. Only limited studies were available on the loading effect on the performance of solar cell, as described below.

1.1.3. Performance of solar cells under strain

Sugar et al. (2007) conducted tension tests on solar cells, measured their performances, and plotted the relationships between the Maximum Power Point (MPP), Fill Factor (FF) and the strain.

Additional cyclic loading tests were performed on the same type of solar cells. It was concluded that the MPP and FF decreased with the increase of the applied load (Sugar 2007). Maung et al. (2010) attached solar cells to Carbon FRP (CFRP) and tested them under cyclic loading. They found that a slight degradation of solar cells was recorded after 0.3% strain and a significant degradation was observed at 1% strain when subjected to a cyclic loading up to 100 cycles. However, the performance of the solar cells under compression loading need to be investigated. Moreover, the behavior of the solar cells when attached to Glass FRP (GFRP) is still unknown which is considered as non-conductive material and more common in structural applications due to its cheaper cost in comparison to CFRP. These issues will be addressed in this dissertation.

1.1.4. Structural performance of sandwich panels

FRP has begun to replace steel main reinforcement for structural members or shear connectors in sandwich panels. Different types of FRP shear connectors have been studied in the past. Einea et al. (1994) introduced hybrid steel/FRP connectors, where FRP connectors were used as the diagonal members of the truss web, and the top and bottom chords were prestressing strands. Full-scale tests and 2-D FE analysis were conducted. Salmon et al. (1998) tested four full-scale sandwich panels, two with FRP bent bars and the other two with steel connectors. They found that the FRP connectors could improve the thermal insulation of the sandwich. The strength of each panel is equal to a fully composite panel. Whitehead and Ibell (2005) investigated the performance of the aramid FRP as a transverse reinforcement for concrete beams using unbonded rectangular and circular helixes. They concluded that the unbonded rectangular helixes were 50% less effective than fully bonded helixes. Frankl et al. (2011) tested six full-scale precast prestressed sandwich panels with carbon FRP (CFRP) shear connectors. They concluded that the CFRP shear connectors could achieve full-composite action. Three different configurations of glass FRP (GFRP) were

used as shear connectors for sandwich panels and tested by Chen et al. (2015). They used continuous, segmental and discrete FRP shear plates, where the continuous and segmental had better performance than the discrete connector. Tomlinson and Fam (2015) investigated the performance of the sandwich panels using Basalt FRP (BFRP).

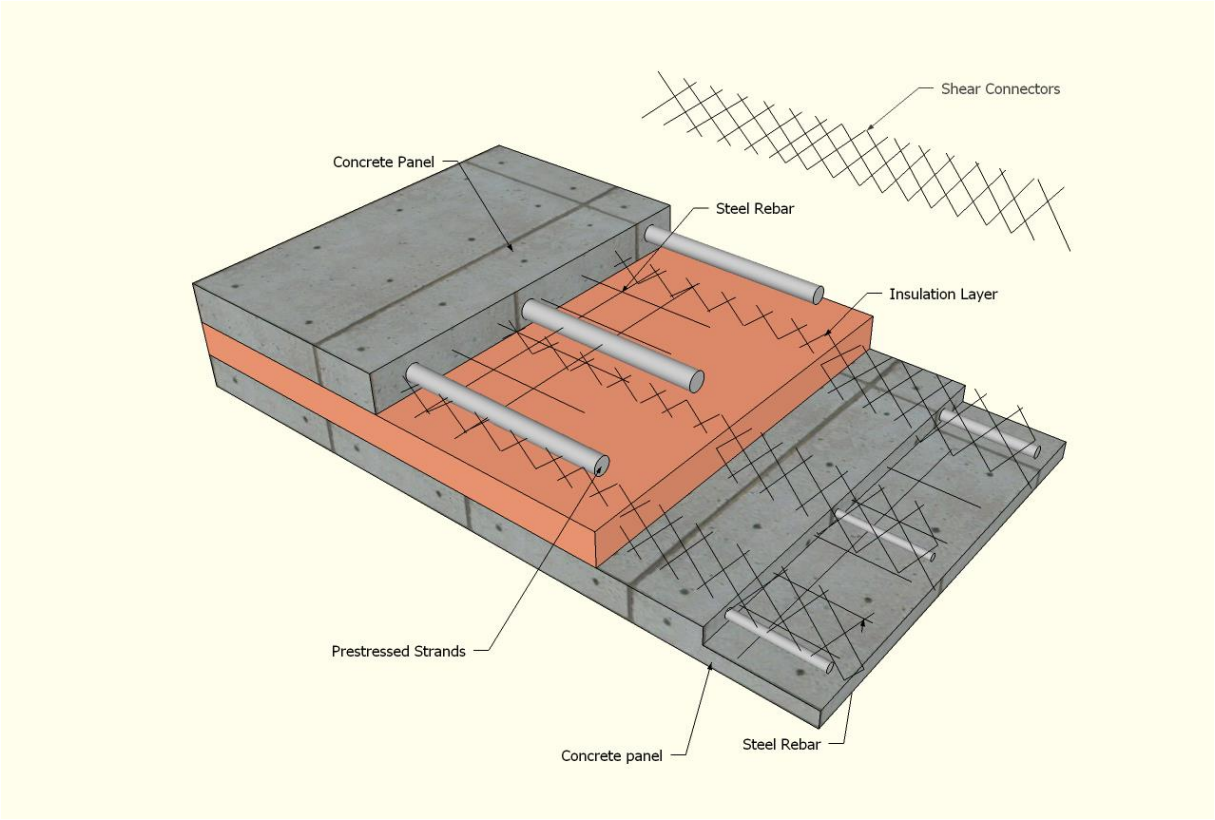

Figure 1.2 Prestressed precast sandwich panel components

FRP application on sandwich panels is not only limited to shear connectors. Norris and Chen (2016) bonded prefabricated plates to the top and sides of the sandwich panel to investigate the confining effect of the FRP on the sandwich panels. They found that the confining effect could increase the strength of the sandwich panel. To ensure a better bonding between the FRP and concrete, the authors used a dry-bond scheme where polymer aggregate was first bonded with the FRP, then the concrete was poured to the FRP/polymer aggregate sheet to provide a secure bond.

However, it was recommended to manufacture the whole FRP/polymer aggregate shell as one piece to achieve ultimate confining effect.

Dry bond scheme was initially studied by Cho et al. (2010), where they examined the effect of quartzite aggregate size and density on the shear and tensile bond characteristics. They concluded that the best configuration was 0.157-0.276 in for aggregate size and 0.82 lb/ft^2 for aggregate distribution density. Application of dry bond was later expanded to include Ultra High Portland Concrete (UHPC) (Chen and El-Hacha, 2013; El-Hacha and Chen, 2012), precast composite deck fatigue performance (Cho et al., 2011), and the effect of freeze and thaw on the bond interface (Cho et al., 2013). The aforementioned studies show that the dry bond can be used to achieve higher bond strength than wet bond method. Therefore, FRP shear connectors and dry bond will be adopted in this study.

1.1.5. Degree of composite action

Shear connectors can be classified into stiff and flexible shear connectors. Unlike steel, most FRP shear connectors can be classified as flexible shear connectors, where limited slip is permitted between the upper and lower wythes. Therefore, it is essential to study the slip between the concrete wythes for sandwich panels with FRP connectors.

The slip occurs in the sandwich panels can be defined using the concept "degrees of composite action (DCAs)." The percentage of composite action that a sandwich panel can exhibit is an important engineering design parameter. In some cases, the panel can be conservatively considered non-composite and only one of the outer wythes is used for the axial or flexural load carrying capacity. In many cases, the sandwich panel, which contains a concrete wythe on each side connected with some form of shear tie, will exhibit a percentage of composite. Successful sandwich panel design and construction depend on the correlation between the structural behavior

of the panel and the intended design (Losch et al., 2011). There have been several variations in the calculation of the degree or percent of composite action, composite moment and/or composite flexural stiffness.

Until now, there is no uniform method to determine DCA. Wade et al. (1988) and Bush and Stine (1994) used the calculated moments from the panel based on the section modulus and the average strain difference to calculate DCA as follows:

$$M_{com} = \frac{[M_{ext} - (M_{tw} + M_{bw})]}{M_{ext}} \times 100 \quad (1)$$

where,

M_{com} is the percent of composite moment,

M_{ext} is the external moment at mid-span of panel, $wl^2/8$,

$M_{tw,bw}$ is the internal non-composite moment on top or bottom wythe $= SE_c\varepsilon$,

where

S is the section modulus of a single uncracked wythe,

E_c is the modulus of elasticity of concrete,

ε is the average strain difference at outer faces of wythe, determined from test data.

Pessiki and Mlynarczyk (2003) defined DCA based on the theoretical values of moment of inertia as follows:

$$DCA = \frac{I_{exp} - I_{nc}}{I_c - I_{nc}} \times 100 \quad (2)$$

where

I_c and I_{nc} are the theatrical values of the full composite and non-composite moment of inertia of the panel, I_{exp} is the experimental moment of inertia which can be determined as:

$$I_{\exp} = \frac{5wL^4}{384\Delta E_c} \tag{3}$$

where

w is the uniform distributed load per panel length,

Δ is the corresponding deflection for the load applied for uncracked section,

L is the span of the panel.

Frankl et al. (2011) calculated DCA based on the deflections at selected load as follows:

$$DCA(100\%) = \frac{\Delta_{noncomposite} - \Delta_{partial}}{\Delta_{noncomposite} - \Delta_{composite}} \times 100 \tag{4}$$

where $\Delta_{noncomposite}$, $\Delta_{composite}$, and $\Delta_{partial}$ represent displacements at a given load corresponding to 0%, 100%, and partial DCA, respectively. This method can be termed as displacement method and is only applicable for the uncracked region.

Chen et al. (2015) calculated DCA of the test panels based on the panel stiffness as:

$$DCA = \frac{\left(\frac{1}{EI}\right)_{0\%} - \left(\frac{1}{EI}\right)_{Actual}}{\left(\frac{1}{EI}\right)_{0\%} - \left(\frac{1}{EI}\right)_{100\%}} (100\%) \tag{5}$$

where $\left(\frac{1}{EI}\right)_{0\%}$, $\left(\frac{1}{EI}\right)_{Actual}$, and $\left(\frac{1}{EI}\right)_{100\%}$ represent the values for panels with non-composite; partial DCA; and full-composite actions, respectively.

Tomlinson and Fam (2015) compared DCA based on load vs. DCA based on deflection, where they concluded that the load method should be used for the ultimate load while the deflection method can be used for serviceability limit state. This method can be termed as load method and is defined as:

$$DCA(100\%) = (1 - \frac{P_{composite} - P_{partial}}{P_{composite} - P_{noncomposite}}) \times 100 \quad (6)$$

where $P_{noncomposite}$, $P_{composite}$, and $P_{partial}$ represent the ultimate loads corresponding to 0%, 100%, and partial DCA, respectively.

Lorenz and Stockwell (1984) defined DCA based on strain for concrete deck on steel beams, as shown in Figure 1.3, where full composite or 100% DCA assumes no slip between the beam and concrete slab, while the non-composite or 0% DCA assumes full slip between the beam and concrete slab. This method can be termed as strain method and can be calculated as:

$$DCA = 1 - \frac{X}{X_{MAX}} \quad (7)$$

where X indicates the amount of the horizontal slip as shown in Figure 1.3. Equation (7) can be re-written as:

$$DCA = 1 - \frac{\varepsilon_2 - \varepsilon_1}{\varepsilon_{max}} \quad (8)$$

where ε_1 and ε_2 are the strains for the lower and upper parts.

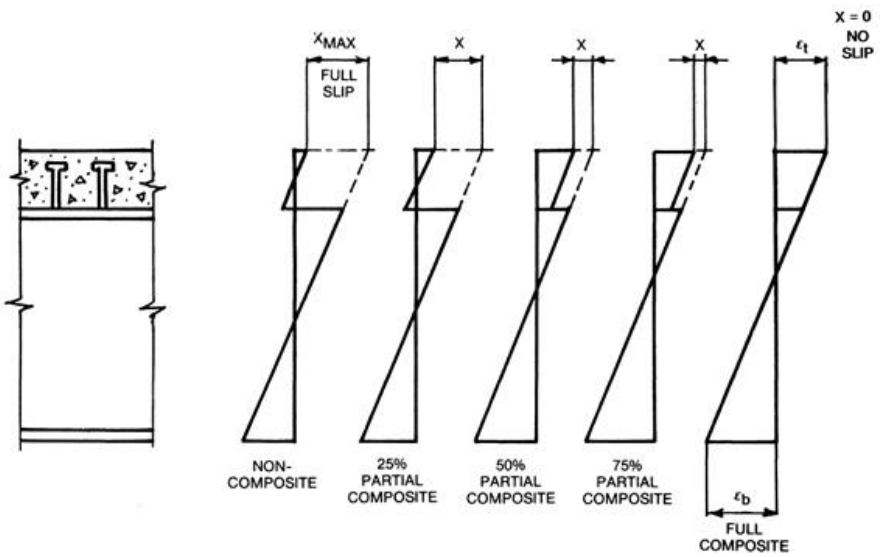

Figure 1.3 Partial DCA for deck slab on beam (Lorenz and Stockwell, 1984)

The effectiveness of different methods to evaluate DCA will be evaluated in this dissertation.

1.1.6. Shear-Lag effect

Although the concept of DCA has been used for a while, the effect of DCA on the stress/strain distribution over the width of the panel has not been tackled yet. Until now, the design of sandwich panel is based on the uniform distribution of stress over the width of the panel. However, the stress is high at the shear connectors and low in between, which indicates that the design is unreasonable based on the full width. Figure 1.4 shows that a uniform stress can be assumed along the reduced width b_{eff}. The area of this stress block is equivalent to the area of the actual stress distributed along the width b. This reduced width b_{eff} is called effective width.

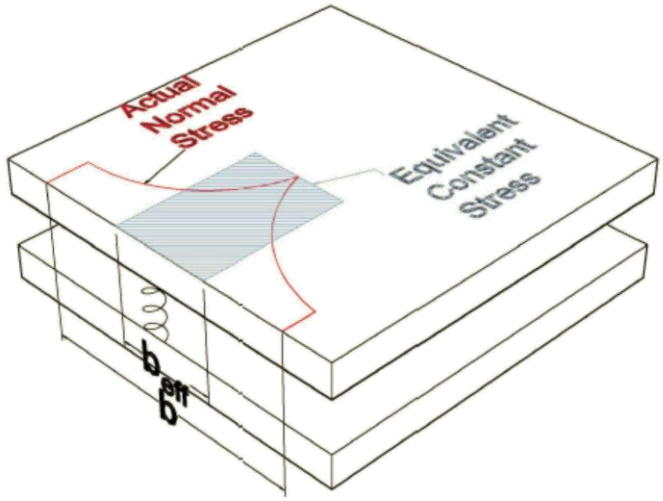

Figure 1.4 Effective width resulting from shear-lag effect

The concept of the shear-lag effect was introduced by Reissner (1941) for isotropic sections. Later, Reissner developed a shear lag model using the minimum potential energy for box beams (Reissner, 1946). Kemmochi et al. (1980) followed Reissner's concept to obtain the shear lag for FRP sandwich panels with aluminum channel shear connectors. However, the shear connectors were assumed to be rigid.

Kristek et al. (1990) proposed a shear lag model based on harmonic analysis. The method was applied to steel and steel-concrete composite box girders. This paper represents the keystone for the shear lag analysis due to its simplicity and fairly accurate results. Then, Evans et al. (1993) generalized the shear lag model to include multi-cellular structures. Kristek (2004) expanded the harmonic analysis model to account for the partial interaction between the concrete slab and steel box girder. However, the interaction was based on the friction between the overlapping area of concrete slab and steel flange and not the location of shear connectors, which limits this model to structures with one shear connector only.

Salim and Davalos (2005a) extended the harmonic method to model the shear lag for thin-walled composite beams. The model was based on the mechanics of laminated beams model proposed by Barbero et al. (1993). Explicit formulas were derived for single box, multi-box and wide-flange sections. Later, Zou et al. (2011) applied Salim's model for orthotropic FRP bridge decks, where good correlation was achieved between the analytical and experimental results.

In all these studies, effective flange width was used to describe the shear lag effect, reducing the three-dimensional behavior of the structural system to the analysis of a two-dimensional section with a reduced width of flange. However, they were based on the full composite action and did not consider partial DCA. Therefore, further research is needed to develop an analytical model for stress and deflection based on partial DCA taking into consideration the shear-lag effect, which will be included in this dissertation.

1.2 Problem Statement

Energy-efficient sandwich panel is considered as a passive energy system. This dissertation aims to develop a PVICS panel, which can act as both an active and passive energy system. To

this end, a method needs to be developed to integrate solar cells with the insulated concrete sandwich panel. The performance of the solar cells under different strain states needs to be investigated since solar cells become a part of the structure. Stress distribution across the width of the panel needs to be studied because of the shear-lag effect from discrete shear connectors. Design equations need to be provided to simplify the design of the sandwich panels.

1.3 Contributions and Objectives

The objective of this study is to develop a multifunctional PVICS panel, which can harvest solar energy through attached thin-film solar cells and preserve energy through insulation layer. This combined active and passive energy system can achieve a zero-carbonate building system. Specifically, the contributions are to:

- Develop an innovative co-curing scheme to attach solar cells to the sandwich panel. An FRP shell is manufactured as a stay-in-place formwork for the sandwich panel. The solar cells are bonded to the FRP during its curing. Polymer concrete, i.e., aggregate mixed with epoxy, is applied to the inner surface of the FRP shell to enhance the bond between the FRP and concrete. The FRP shell can provide the confining effect, act as shear connectors and reinforcement to improve the structural performance of the sandwich panel.
- Study the performance of solar cells under strain.
- Derive a closed-form solution considering shear-lag effect for sandwich panels with single, multiple and edge shear connectors.
- Develop simplified equations to calculate stress/strain and deflection for sandwich panels based on partial DCA, which can be used for the design of PVICS.

- Extend the shear-lag model with partial DCA to other configurations such as FRP deck-on-girder system.

1.4 Thesis Organization

The dissertation is organized as follows. Chapter 2 reports a nonlinear FE model for a full-scale precast prestressed sandwich panel, where the DCA was evaluated using different methods. Chapter 3 presents the testing of a prototype PVICS panel and correlations of the test results with those from FE and analytical models. Chapter 4 studies the performance of solar cells under different strain states. Chapter 5 derives a closed-form solution considering shear-lag effect to predict stress/strain and deflection for sandwich panels with partial DCA. Chapter 6 applies the shear-lag theory to FRP deck-on-girder system. Chapter 7 presents the conclusions and future work.

1.5 References

Barbero, E. J., Lopez-Anido, R., and Davalos, J. F. (1993). "On the mechanics of thin-walled laminated composite beams." *Journal of Composite Materials*, Sage Publications, 27(8), 806–829.

Bush, T. D., and Stine, G. L. (1994). "Flexural behavior of composite precast concrete sandwich panels with continuous truss connectors." *PCI journal*, 39(2), 112–121.

Bush, T. D., and Wu, Z. (1998). "Flexural analysis of prestressed concrete sandwich panels with truss connectors." *PCI journal*, Precast/Prestressed Concrete Institute, 43(5), 76–86.

Chen, A., Norris, T. G., Hopkins, P. M., and Yossef, M. (2015a). "Experimental investigation and finite element analysis of flexural behavior of insulated concrete sandwich panels with FRP plate shear connectors." *Engineering Structures*, 98.

Chen, A., Norris, T. G., Hopkins, P. M., and Yossef, M. (2015b). "Experimental investigation and finite element analysis of flexural behavior of insulated concrete sandwich panels with FRP plate shear connectors." *Engineering Structures*, 98, 95–108.

Chen, D., and El-Hacha, R. (2013). "Damage tolerance and residual strength of hybrid FRP–UHPC beam." *Engineering Structures*, 49, 275–283.

Cho, J.-R., Cho, K., Park, S. Y., Kim, S. T., and Kim, B.-S. (2010). "Bond characteristics of coarse sand coated interface between stay-in-place fibre-reinforced polymer formwork and concrete based on shear and tension tests." *Canadian Journal of Civil Engineering*, 37, 706–718.

Cho, K., Cho, J.-R., Kim, S. T., Kim, B.-S., and Park, S. Y. (2011). "Fatigue Performance of Precast FRP-Concrete Composite Deck with Long Span." *Engineering*, 3(11), 1115–1123.

Cho, K., Park, S. Y., Kim, S. T., Cho, J.-R. C., and Kim, B.-S. (2013). "Freeze-Thaw Effect on Coarse Sand Coated Interface between FRP and Concrete." *Engineering*, 5(10), 807–815.

Einea, A., Salmon, D. C., Fogarasi, G. J., Culp, T. D., and Tadros, M. K. (1991). "State-of-the-Art of Precast Concrete Sandwich Panels." *PCI Journal*, 36(6), 78–98.

Einea, A., Salmon, D. C., Tadros, M. K., and Culp, T. (1994). "A New Structurally and Thermally Efficient Precast Sandwich Panel System." *PCI Journal (Precast/Prestressed Concrete Institute)*, 39(4), 90–101.

El-Hacha, R., and Chen, D. (2012). "Behaviour of hybrid FRP-UHPC beams subjected to static flexural loading." *Composites Part B: Engineering*, Elsevier Ltd, 43(2), 582–593.

Evans, H. R., Ahmad, M. K. H., and Kristek, V. (1993). "Shear lag in composite box girders of complex cross-sections." *Journal of Constructional Steel Research*, 24(3), 183–204.

Frankl, B. A., Lucier, G. W., Hassan, T. K., and Rizkalla, S. H. (2011). "Behavior of precast, prestressed concrete sandwich wall panels reinforced with CFRP shear grid." *PCI journal*, Precast/Prestressed Concrete Institute, 56(2), 42–54.

Jason Maung, K., Hahn, H. T., and Ju, Y. S. (2010). "Multifunctional integration of thin-film silicon solar cells on carbon-fiber-reinforced epoxy composites." *Solar Energy*, 84(3), 450–458.

Jelle, B. P., Breivik, C., and Drolsum Røkenes, H. (2012). "Building integrated photovoltaic products: A state-of-the-art review and future research opportunities." *Solar Energy Materials and Solar Cells*, Elsevier, 100(7465), 69–96.

Kemmochi, K., Akasaka, T., Hayashi, R., and Ishiwata, K. (1980). "Shear-Lag Effect in Sandwich Panels With Stiffeners Under Three-Point Bending." *Journal of Applied Mechanics*, 47(2), 383.

Kristek, V. (2004). "A Shear Lag Analysis for Composite Box Girders with Deformable Connectors." *Acta Polytechnica - Journal of Advanced Engineering*, 44(5–6), 1–21.

Kristek, V., Evans, H. R., and Ahmad, M. K. M. (1990). "A shear lag analysis for composite box girders." *Journal of Constructional Steel Research*, 16(1), 1–21.

Lorenz, R. F., and Stockwell, F. W. (1984). "Concrete Slab Stresses in Partial Composite Beams and Girders." *Engineering Journal-American institute of steel construction*, 21(3), 185–188.

Losch, E. D., Hynes, P. W., Andrews Jr., R., Browning, R., Cardone, P., Devalapura, R., Donahey, R., Freedman, S., Gleich, H. A., Goettsche, G., Kourajian, P., Krohn, J., Leaton, C., Li, Z., Long, R., Meinheit, D., Milkovitz, M., Miller, B., Nadeau, F., Nesset, B., Pessiki, S., Peterson, D. N., Peterson, S. H., Quiroga, R., Reay, S., Richardson, W., Seeber, K., Seshappa, V., Smith, D., Trimbath, B., Truderung, K., Wagner, M., Wynings, C., and Yan, L. (2011). "State of the art of precast/prestressed concrete sandwich wall panels." *PCI Journal*, 56(2), 131–176.

Norris, T. G., and Chen, A. (2016). "Development of insulated FRP-confined Precast Concrete Sandwich panel with side and top confining plates and dry bond." *Composite Structures*, Elsevier Ltd, 152, 444–454.

Pessiki, S., and Mlynarczyk, A. (2003). "Experimental Evaluation of the Composite Behavior of Precast Concrete Sandwich Wall Panels." *PCI Journal*, 48(2), 54–71.

Reissner, E. (1941). "Least Work Solutions of Shear Lag Problems." *Journal of the Aeronautical Sciences (Institute of the Aeronautical Sciences)*, American Institute of Aeronautics and Astronautics.

Reissner, E. (1946). "Analysis of shear lag in box beams by the principle of minimum potential energy." *Quarterly of applied mathematics*, 5(3), 268.

Salim, H. A., and Davalos, J. F. (2005). "Shear Lag of Open and Closed Thin-walled Laminated Composite Beams." *Journal of Reinforced Plastics and Composites* , 24(7), 673–690.

Salmon, D. C., Einea, A., Tadros, M. K., and Culp, T. D. (1998). "Full-Scale Testing of Precast Concrete Sandwich Panels." *ACI Structural journal*, 94(4), 354–362.

Sugar, J. G. (2007). "Photovoltaic Performance of Amorphous Silicon Flexible Solar Modules Under Mechanical Loading." UCLA.

Sugar, J. G. J. G. J. G., Scaffaro, R., Guo, Z., Maung, J. K. J. K., Ju, Y. S. Y. "Sungtaek," Hahn, H. T. T., Maung, J. K. J. K., and Ju, Y. S. Y. "Sungtaek." (2007). "Photovoltaic Performance of Amorphous Silicon Flexible Solar Modules Under Mechanical Loading." *6th International Workshop on Structural Health Monitoring*, Stanford, CA, September 11–13., 61.

Tomlinson, D., and Fam, A. (2015). "Flexural behavior of precast concrete sandwich wall panels with basalt FRP and steel reinforcement." *PCI Journal*.

Wade, T. G., Porter, M. L., and Jacobs, D. R. (1988). "Glass-fiber composite connectors for insulated concrete sandwich walls." *Engineering Research Institute, Iowa State University, Ames, Iowa*.

Whitehead, P. A., and Ibell, T. J. (2005). "Novel Shear Reinforcement for Fiber-Reinforced Polymer-Reinforced and Prestressed Concrete." *ACI Structural Journal*, American Concrete Institute, 102(2), 286.

Zhao, X., Zhang, X., Riffat, S. B., and Su, Y. (2011). "Theoretical study of the performance of a novel PV/e roof module for heat pump operation." *Energy Conversion and Management*, Elsevier Ltd, 52(1), 603–614.

Zou, B., Chen, A., Davalos, J. F., and Salim, H. A. (2011). "Evaluation of effective flange width by shear lag model for orthotropic FRP bridge decks." *Composite Structures*, 93(2), 474–482.

CHAPTER 2. A COMPARATIVE STUDY OF DIFFERENT METHODS TO CALCULATE DEGREES OF COMPOSITE ACTION FOR PRECAST, PRESTRESSED INSULATED CONCRETE SANDWICH PANELS[1]

A paper to be submitted to PCI Journal

Mostafa Yossef, Paul Hopkins and An Chen

Abstract

Precast concrete sandwich wall panels consist of two outer wythes of precast concrete separated by a middle layer of insulation. Various types of shear connectors, including steel shear connectors, have been used to connect the two concrete layers. In recent years, Fiber-Reinforced Polymer (FRP) shear connectors have been increasingly used since they have lower thermal conductivity compared to steel shear connectors, which can significantly reduce thermal bridging. However, FRP shear connectors have lower stiffness, resulting in partial Degree of Composite Action (DCA). DCA has a significant effect on the structural behavior of the panels. Different methods have been proposed to calculate DCAs, including displacement method, strain method, and load method. This paper will compare and evaluate the effectiveness of these methods. A bending test was conducted on a 277.5 in. x 119.375 in. precast, prestressed insulated concrete sandwich panel with FRP shear connectors. A non-linear Finite Element (FE) model is created, where good correlations can be achieved between the test and FE results. The FE model is further employed to conduct a parametric study by varying the stiffness of the shear connectors. DCAs for different stiffnesses are calculated using the aforementioned three methods. The applicability and limitations of each method are investigated.

[1] This chapter/paper is co-authored with the second author who carried out and contributed in writing the experimental test part. They also provided the first author with information needed to develop the FE model.

2.1. Introduction

Precast prestressed insulated concrete sandwich panels consist of two outer layers of precast concrete separated by a middle layer of insulation, usually using expanded polystyrene (EPS) or extruded polystyrene (XPS), as shown in Figure 2.1. These panels can provide strength and protect the interior of the building from thermal gradients by separating the thermal bridge in the concrete panel with the insulation layer. They can be used as wall (vertical) and roof/floor (horizontal) panels .

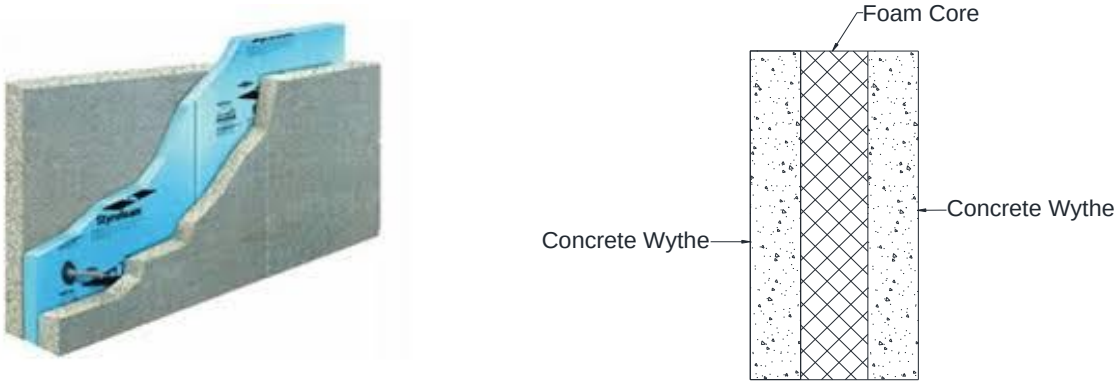

(a) 3-D view (b) Section View

Figure 2.1 Concrete sandwich panel

Since the two outer layers of the panels are separated, they need to be connected by shear connectors in order for the panels to provide full composite action. Steel shear connectors were commonly used from 1990's until 2005's, including small bent bars, steel wire trusses, continuous bent bar Bush and Stine (1994); Bush and Wu (1998); Einea et al. (1991). However, steel has a high thermal conductivity which can cause thermal bridging. In addition, it is susceptible to corrosion. To address these limitations, Fiber-Reinforced Polymer (FRP) shear connectors have been used, since they have a much lower thermal conductivity compared to steel and do not corrode, which can increase the lifetime of the structure.

Different types of FRP shear connectors have been studied in the past. Einea et al. (1994) introduced hybrid steel/FRP connectors where FRP connectors were used as the diagonal members of the truss web and the top and bottom chords were prestressing strands. Full-scale tests and 2-D FE analysis were conducted. Salmon et al. (1998) tested four full-scale sandwich panels, two with FRP bent bars and the other two panels with steel connectors. They found that the FRP connectors could improve the thermal insulation of the sandwich. The strength of each panel is equal to a fully composite panel.

Whitehead and Ibell (2005) investigated the performance of the aramid FRP as a transverse reinforcement for concrete beams using unbonded rectangular and circular helixes. They concluded that the unbonded rectangular helixes were 50% less effective than fully bonded helixes. Frankl et al. (2011) tested six full-scale precast prestressed sandwich panels with carbon FRP (CFRP) shear connectors. They concluded that the CFRP shear connectors could achieve full-composite action. Three different configurations of glass FRP (GFRP) were used as shear connectors for sandwich panels and tested by Chen et al. (2015). They used continuous, segmental and discrete FRP shear plates, where the continuous and segmental connectors had better performance than the discrete connectors. Tomlinson and Fam (2015) investigated the performance of the sandwich panels using basalt FRP (BFRP).

Shear connectors can be classified into stiff and flexible shear connectors. In contrast to steel, most types of FRP shear connectors can be classified under flexible shear connectors where limited slip is permitted between the outer wythes. Therefore, it is essential to study the slip between the concrete wythes for sandwich panels with FRP connectors.

2.1.1. Degree of composite action

The slip occurring in the sandwich panels can be defined using the concept “degree of composite action (DCA)”. The percentage of composite action that a sandwich panel can exhibit is an important engineering design parameter. In some cases, the panel can be conservatively considered non-composite and only one of the outer wythes is used to take axial or flexural load. However, in many cases, the sandwich panel, which contains concrete wythes at each side connected with some form of shear tie, will exhibit a percentage of composite action.

Until now, there is no uniform method to determine DCA. Bush and Stine (1994) used the moment of the panel to calculate DCA, which were calculated from the section modulus and the average strain difference. Pessiki and Mlynarczyk (2003) defined DCA based on the theoretical value of moment of inertia. Frankl et al. (2011) and Chen et al. (2015) calculated DCA based on the deflection at selected loads. This method can be termed as “deflection method”.

Tomlinson and Fam (2015) calculated DCA based on the ultimate load. They compared DCA based on load vs. DCA based on deflection and concluded that the load method can be used for the ultimate load while deflection method can be used during serviceability limit state. This method can be termed as “load method”.

Lorenz and Stockwell (1984) defined DCA based on strain for concrete deck on steel beams as shown in Figure 1.3. Full composite (100% DCA) assumes no slip between the beam and concrete slab, while the non-composite (0% DCA) assumes full slip between the beam and concrete slab. Similarly, partial DCA can occur at partial slip between the beam and concrete slab. The same concept can be adopted for sandwich panels as shown in Figure 2.20. This method can be termed as “strain method”. Details of the three methods are given in section 2.5

Since DCA can significantly affect the structural performance of the panel, there is a need to describe the DCA accurately. The objective of this paper is to compare the three methods as described previously and evaluate their applicability and limitations. A bending test on a full-scale sandwich panel was conducted and a nonlinear Finite Element (FE) model was constructed, as will be described in clause 2.3.

2.2. Experimental Investigation

The sandwich panel was manufactured by Central Pre-Mix Prestress Co. in Spokane, WA in accordance with ACI and PCI specifications and tested by Hopkins (2015). The panel was approximately 10’ x 23’ x 10” (width x length x thickness). The panel was constructed on a flat horizontal bed, as shown in Figure 2.2. The materials were assembled and the pre-stressing strands were stressed prior to the concrete pour. Truss grid connectors were installed to connect the two concrete wythes. They were placed in the form and the concrete, when poured, interlocked between openings in the connector truss elements. The spacing of the connectors and other details can be found from Figure 2.3.

2.2.1. Test setup

The test panel was laid flatwise and supported on two 6’’x6’’ wood blocks as shown in Figure 2.4. The loading applied consisted of precast concrete ecology blocks. The blocks were placed on the panel as shown in Figure 2.4 and Figure 2.5, in sequential manner with an approximate 10-minute gap between the block placement. Deflections were recorded between each block added. Both survey equipment measurement and a dial gauge were used for deflection recordings. The blocks were later weighed individually to obtain their exact weight.

Figure 2.2 Typical sandwich panel production prior to placing top concrete wythe

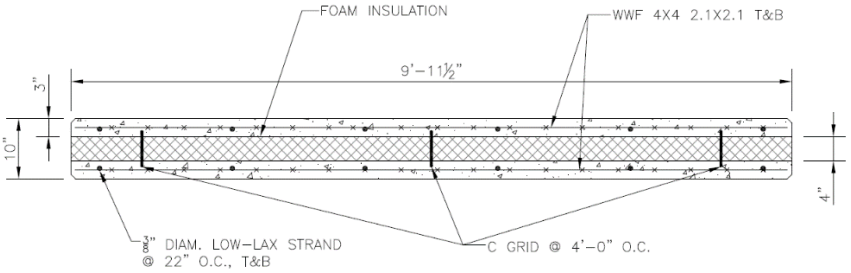

Figure 2.3 Cross section of test panel

The summary of the loading, deflections and an equivalent pressure load are shown in Table 2.1 and Figure 2.6. The service moment is derived by back calculating the flexural moment from corresponding load including the self-weight of the panel. The service pressure is the applied load divided by the entire area of the panel.

As the concrete wythes began to crack, the concrete in the top wythe experienced tensile splitting failures due to the overloading of the concrete by the radial tensile forces developed outward from the press-stress strand. This phenomenon is shown in Figure 2.7. The tensile stresses radiating outward from the pre-stress strand cause the splitting tensile crack to develop in the concrete. These types of cracks are difficult to predict and to simulate in an FE program. The

engineer should be mindful of this type of possible failure when designing a precast panel and during placing post-installed anchors.

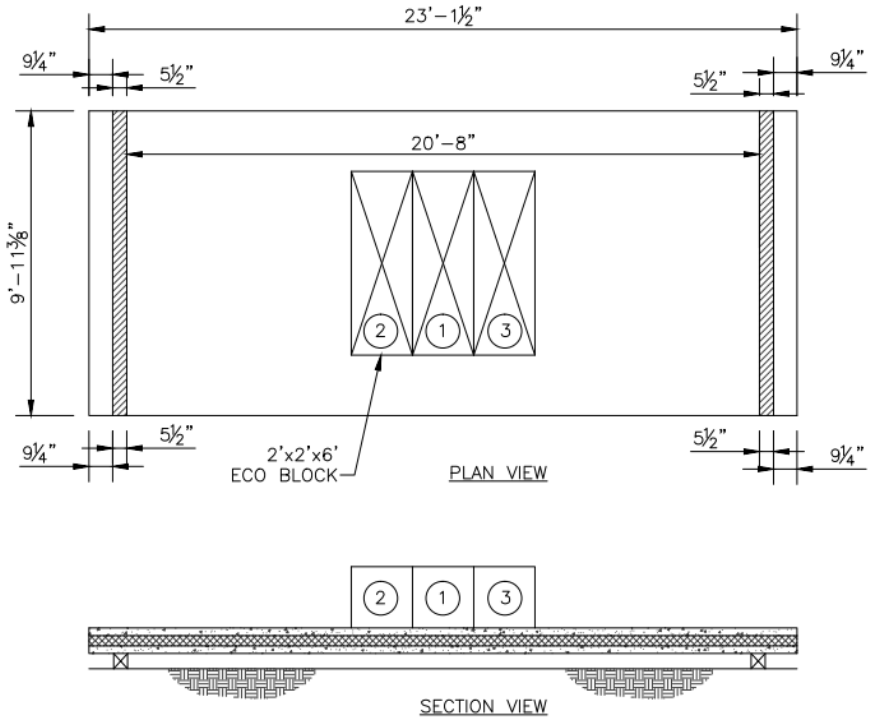

Figure 2.4 Test setup

Figure 2.5 Final load placement

Table 2.1 Test panel load and deflection data

Date	Blocks	Block Weight (lbs)	delta (in)	Difference (in)	Deflection (in)	Load (lbs)	Service Moment M (kip-ft)	Service Pressure Load (psf)
9/2/2011	none	0	0		0.0000	0	39.4	0.0
	1	3400	1/16	1/16	0.0625	3400	56.8	14.8
	2	3400	2/16	1/16	0.1250	6800	74.2	29.6
	3	3450	4/16	2/16	0.2500	10250	91.9	44.6
	4	3400	7/16	3/16	0.4375	13650	109.4	59.3
	5	2440	10/16	3/16	0.6250	16090	121.9	70.0
	6	2570	1 2/16	8/16	1.1250	18660	135.0	81.1
	7	2440	1 9/16	7/16	1.5625	21100	147.5	91.7
9/6/2011			2 12/16	1 3/16	2.7500	21100	147.5	91.7
9/9/2011			1 6/16	1 6/16	1.3750	0	39.4	0.0

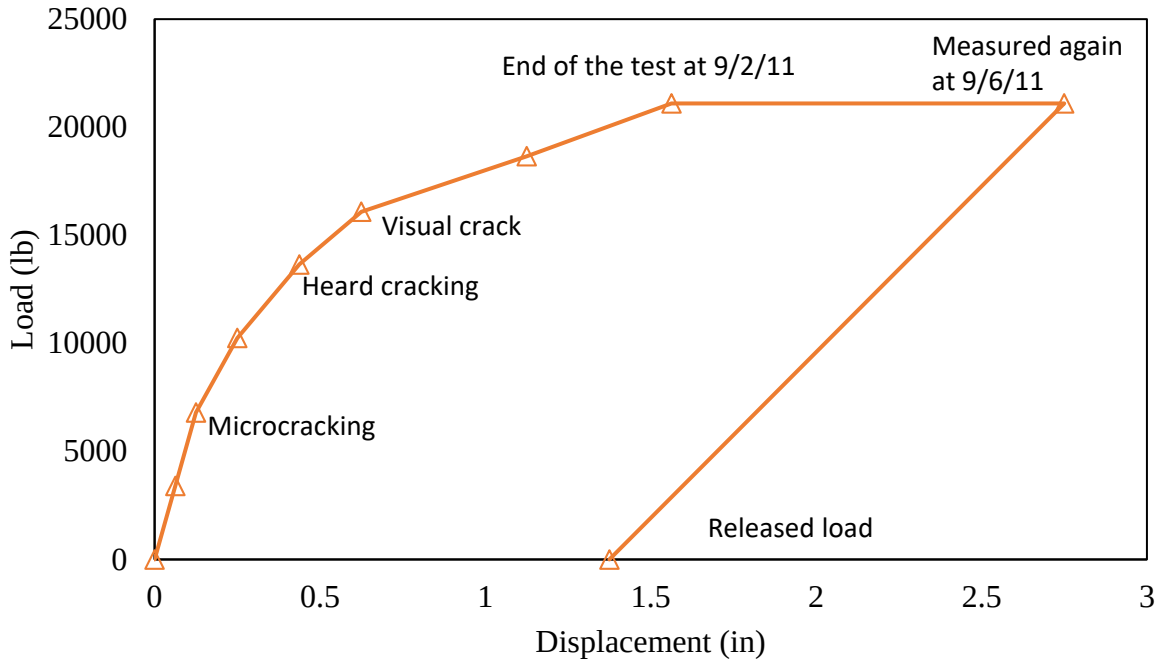

Figure 2.6 Load deflection curve for the tested panel

The bottom concrete wythe had near-uniform and symmetrical transverse cracks as shown in Figure 2.8. These cracks were most likely the ones that were heard during the test. We never heard popping of the anchorage of the shear connector. Although a strain gage was not placed on the panel and recordings were not taken to determine composite action, it is believed that the shear connector was acting compositely with the concrete wythes. Complete failure never occurred and

the concrete was cracked; therefore the continuous transfer of tension to compression forces in the bending section of the panel was maintained by the shear connector. Lee and Pessiki (2007) showed that the polystyrene insulation would also have provided additional shear resistance in transferring those compression and tension coupling forces

Figure 2.7 Top layer of longitudinal prestressing strand splitting failure

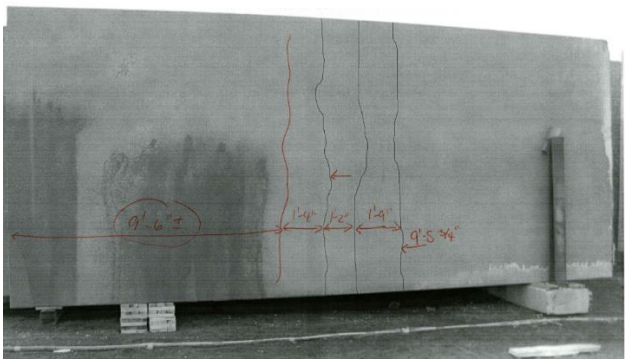

Figure 2.8 Uniform and symmetrical bottom transverse cracks

2.3. Finite Element Analysis

An FE model is developed and validated with the tested panel using commercial FE analysis software package ABAQUS (2013). This FE model takes into account nonlinear material properties, concrete damage model and induced stresses from prestressed strands. The use of concrete damage plasticity model in ABAQUS can detect the actual strain in the cracked sections, which can be used to study DCA for nonlinear stage. ABAQUS CAE module is used as a graphical user interface to facilitate the creation of the model and extraction of post-processing data.

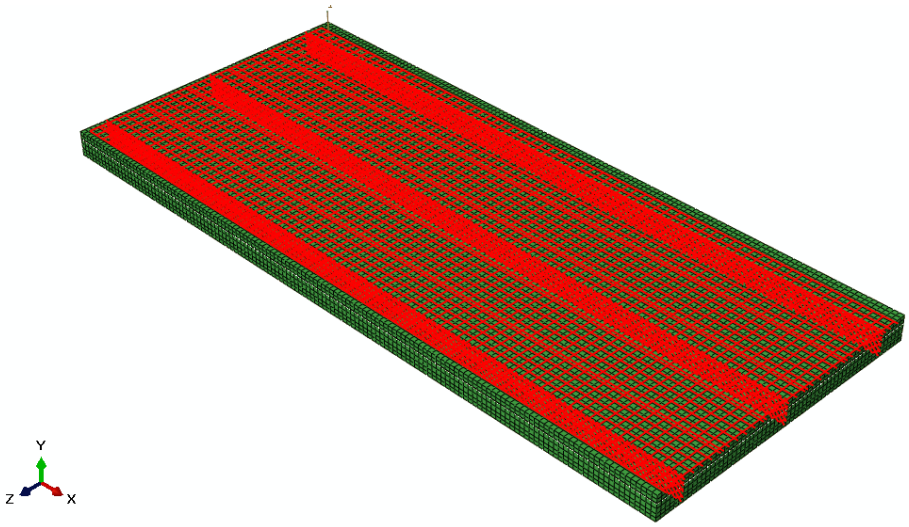

Figure 2.9 FE model of the test panel

2.3.1. Geometry

The model consists of five parts: concrete wythes, insulation layer, prestressing strands, steel wire mesh, and CFRP shear connector as shown in Figure 2.9. The linear hexahedral element with enhanced stiffness hourglass control and reduced integration C3D8R is used to model the concrete and the insulation. Three-dimensional linear truss element with two nodes T3D2 is used to model pre-stressing strands, steel wire mesh and shear connector. The pre-stressed strands are 3/8 in. diameter grade 270. The wire mesh is a smooth wire 4x4 –W2.1xW2.1. CFRP shear connector consists of grids with a spacing of 1.8 in. in the longitudinal direction and 1.6 in. in the transverse direction. The shear mesh is rotated 45 degrees to obtain the maximum benefit of the grid to carry shear load as shown in Figure 2.10. The insulation layer is connected to the concrete wythes using surface tie connection while the pre-stressing strands, steel wire mesh and shear connectors are embedded in the concrete. Based on a convergence study that will be discussed in details in the results section, 2 in. mesh size is used in the FE model for concrete, insulation, prestressing strands and steel wire mesh. As for the shear connector, the mesh size is based on the intersection between the strands as shown in Figure 2.10.

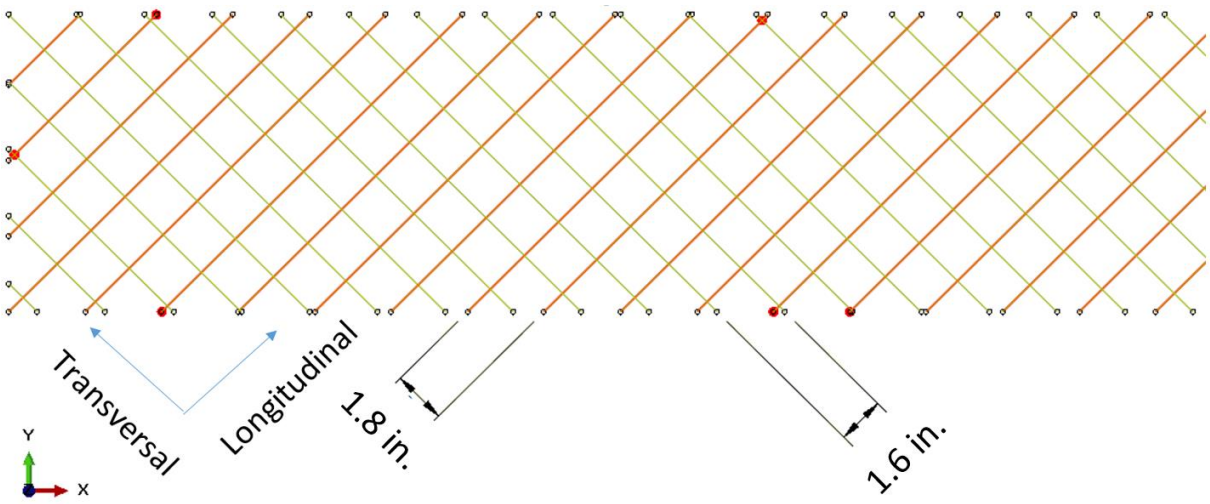

Figure 2.10 CFRP shear grid in the FE model

2.3.2. Material properties

In order to accurately simulate a concrete insulated sandwich test panel in the FE model, elastic and inelastic engineering properties are needed for the concrete and steel components of the structure. Elastic material properties are shown in Table 2.2. while inelastic material properties can be obtained through existing mathematical models as will be discussed in the following sections.

Table 2.2 Material properties

Material	Concrete	Insulation	Steel Wire	Pre-stressing Strand	CFRP Grid (Long.)	CFRP Grid (Trans.)
Strength (ksi)	7.8	-	68(yield) 87(ult.)	202.2(yield) 270(ult.)	290	255
Young's Modulus (ksi)	4253	479	19257	190	38	27
Poisson's Ratio (ν)	0.15	0.35	0.3	0.3	0.3	0.3
Density (pcf)	150	1.8	490	490	62.4	62.4

2.3.2.1. Concrete

ABAQUS offers three modeling techniques for nonlinear concrete finite element analysis. The concrete damaged plasticity model developed by Lubliner et al. (1989) and Lee and Fenves

(1998) was used for the FE modeling in this study as it incorporated both the compressive and tensile properties of the concrete material. The corresponding stiffness degradation values, or damage parameters, and tension stiffening were also considered in the damaged plasticity model. This damage model is recommended by ABAQUS to utilize this FE model for concrete flexural member analyses, which suits the study well.

2.3.2.1.1. Concrete compressive behavior

The behavior of concrete depends on many parameters such as the material properties; its interaction with other materials such as steel and fiber; the type of loading: static or dynamic; and boundary conditions such as confined or unconfined. Many mathematical models were developed to account for aforementioned parameters based on linear and nonlinear elasticity, fracture mechanics, and hardening plasticity. However, these models are formulated in terms of tensorial relation between the stress and strain. Consequently, closed-form expressions are required to obtain a stress-strain response based on parameters such as compressive strength and elastic modulus. Several researchers have developed empirical equations such as Collins et al. (1993), Hognestad et al. (1955), Hsu and Hsu (1994), Kent and Park (1971), Popovics (1973), Roy and Sozen (1965), Saatcioglu and Razvi (1992). In this study, Hsu and Hsu's model is used as it can generate the stress-strain relationship using only the concrete compressive strength after 28 days, and compatible with both normal and high strength concrete. As shown in Figure 2.11, the concrete compressive behavior under uniaxial compression follows a linear stress-strain curve according to Hooke's law, then Hsu and Hsu's model is used for nonlinear stage starting from yielding point at $0.5\sigma_c$ until the end of the softening part at $0.3\sigma_c$, which can be calculated as follows:

$$\sigma_c = \left(\frac{\beta(\varepsilon_c / \varepsilon_0)}{\beta - 1 + (\varepsilon_c / \varepsilon_0)^{\beta}}\right)\sigma_{cu} \quad (9)$$

where σ_c is the concrete compressive stress corresponding to the concrete compressive strain (ε_c). β is a shape parameter and ε_0 is strain at the peak stress, which can be calculated as follows:

$$\beta = \frac{1}{1-[\sigma_c/(\varepsilon_0 E_0)]} \tag{10}$$

$$\varepsilon_0 = 8.9\times10^{-5}\sigma_c + 2.114\times10^{-3} \tag{11}$$

where σ_{cu} is the concrete compressive strength. The initial tangential modulus, E_0 depends on the compressive strength as follows:

$$E_0 = 1.2431\times10^{2}\sigma_c + 3.28312\times10^{3}\ \text{(psi)} \tag{12}$$

For the tested panel, the concrete compressive strength was reported to be 7800 psi, which is within the model upper limit. Table 2.3 shows the calculation for the compressive stress-strain data when substituting the 7800 psi compressive strength into Equations (9) to (12).

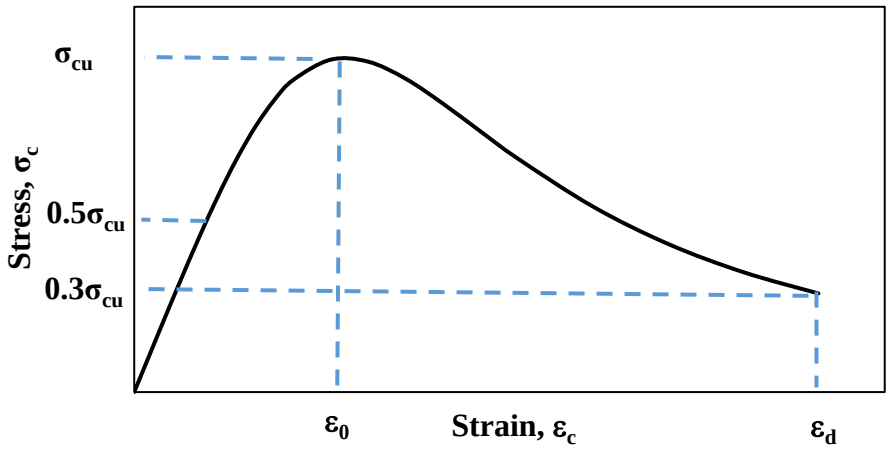

Figure 2.11 Typical compressive stress-strain curve

Inelastic strain (ε_c^{in}) is defined as the total strain (ε_c) minus the elastic strain corresponding to the undamaged material as follows:

$$\varepsilon_c^{in} = \varepsilon_c - \frac{\sigma_c}{E_0} \tag{13}$$

Concrete damage is defined by Lubliner et al. (1989) where the damage factor (d) was proposed as follows:

$$d = 1 - \frac{\sigma}{\sigma_{max}} \tag{14}$$

where σ_{max} is the strength of concrete. The damage factor (d) is assumed to be used only at the softening stage where the concrete stress is less than the concrete strength, as shown in Figure 2.12. The damage factor represents the degradation of the elastic stiffness, which is defined as:

$$E = (1-d)E_0 \tag{15}$$

where E_0 is the initial elastic stiffness.

The damage factor is evaluated according to Equation (14) as shown in Table 2.3. It should be noted that ABAQUS requires the user to input the stress-strain values from the beginning of the concrete crushing area, which are highlighted in Table 2.3. The increment of stress values are calculated so that the stress increment would not be less than 1% of the maximum strength to avoid numerical instability.

2.3.2.1.2. Concrete tensile behavior

Modeling of the reinforced concrete under tension loading is often known as tension stiffening model, which it was first introduced by Hegemier et al. (1985) to develop an analytical model to simulate the cracking of the concrete and the nonlinear responses of the steel and concrete. Since then, tension stiffening model has been developed by numerous studies including

Choi and Cheung (1996), Lee and Fenves (1998), Sato and Vecchio (2003), Fields and Bischoff (2004), Nayal and Rasheed (2006), Stramandinoli and La Rovere (2008), and many others.

Table 2.3 Concrete compressive behavior

Maximum Compression Strength, σ_{cu}			7800	**psi**
Initial Tangential Modulus, E_0			4,252,738	**psi**
Strain at Peak Stress, ε_0			0.002808	**in/in**
β-Parameter			2.88290	**unitless**
Linear Stage	**Strain (in/in) x10^{-3}**	**Stress (psi)**	**Inelastic strain (in/in) x10^{-3}**	**Damage factor (d)**
	0	0	0	0
	0.92	3900	0	0
Nonlinear stage	0.97	4039.45	0.02	0
	1.09	4468.28	0.04	0
	1.14	4676.44	0.04	0
	1.20	4879.96	0.05	0
	1.37	5459.38	0.09	0
	1.48	5816.49	0.12	0
	1.60	6147.54	0.15	0
	1.99	7075.82	0.33	0
	2.16	7356.31	0.43	0
	2.33	7565.61	0.55	0
	2.81	7800.00	0.97	0
	3.37	7545.72	1.60	0.03
	3.66	7276.87	1.95	0.07
	3.94	6953.13	2.31	0.13
	4.51	6229.93	3.04	0.29
	4.79	5861.82	3.41	0.38
	5.07	5502.83	3.78	0.46
	5.92	4527.58	4.86	0.66
	6.49	3978.08	5.55	0.74
	7.05	3506.74	6.23	0.81
	7.62	3104.82	6.89	0.85
	8.47	2610.45	7.85	0.89
	9.32	2219.40	8.79	0.92
	10.17	1907.08	9.72	0.94
	11.86	1448.79	11.52	0.95

Nayal and Rasheed (2006) stiffening model, which was modified by Wahalathantri et al. (2011), is used in this study to avoid convergence problems while implementing the stiffening model in ABAQUS. Similar to compression behavior, implementation of tension behavior on ABAQUS requires the user to define two stages: tension stiffening and tension damage. The tension stiffening can be defined as shown in Figure 2.13, where the concrete follows a linear elastic stage until its ultimate tensile strength (σ_{t0}). Then it experiences a steep degradation of stress until 0.77(σ_{t0}), which corresponds to 1.25(ε_{cr}). The stress then continues to decrease to 0.45(σ_{t0}) at 4(ε_{cr}), until it reaches 0.1 (σ_{t0}) at 8.7 (ε_{cr}). Cracking strain can be calculated according to Hooke's law as (σ_{t0}/E), where σ_{t0} corresponds to the concrete tensile strength.

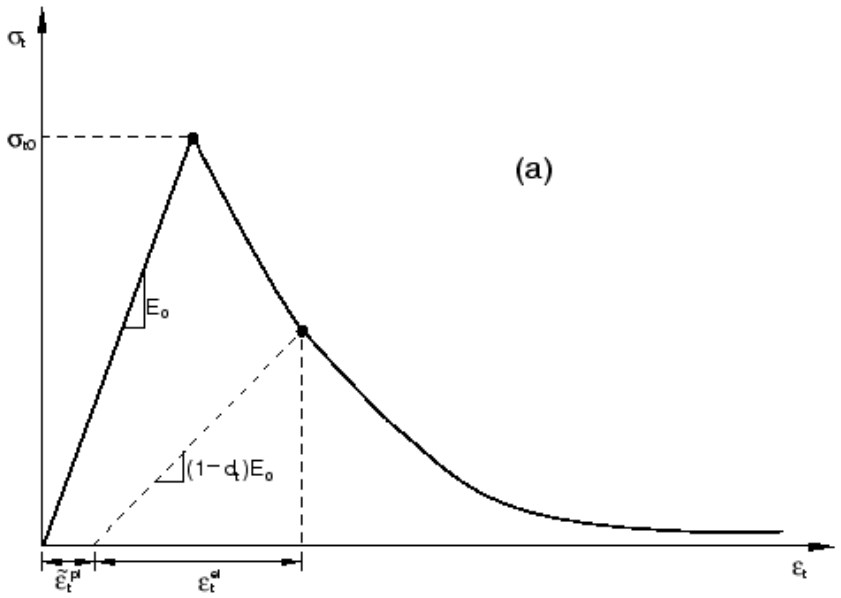

Figure 2.12 Tensile stress-strain response (ABAQUS, 2013)

The concrete tensile strength (σ_{t0}) can be determined based on CIB-FIP (1991) as follows:

$$\sigma_{t0} = 203.05\left(\frac{\sigma_{cu} - 8}{10}\right)^{2/3} \text{ (psi)} \tag{16}$$

where σ_{cu} is the concrete compressive strength.

Table 2.4 Concrete tension behavior

Maximum Tensile Stress, σ_{t0}		559.83			**psi**
Critical Tensile Strain, ε_{cr}		0.000131639			**in/in**
Tensile Uniaxial Data		**Concrete Damaged Plasticity**			
		Tensile Behavior		**Tension Damage**	
Nominal Stress (psi)	Eng. Strain (in/in)	Yield Stress (psi)	Cracking Strain (in/in)	Damage Parameter (d)	Cracking Strain (in/in)
0	0	559.82	0.00	0.000	0.00
559.82	0.000131639	431.06	6.32E-05	0.230	6.32E-05
431.06	0.000164549	251.92	4.67E-04	0.550	4.67E-04
251.92	0.000526557	55.98	1.13E-03	0.900	1.13E-03
55.98	0.001145261				

Damage model developed by Lubliner et al. (1989) as discussed in the compression damage shown in Equation (14) is used to obtain the tensile damage. The stiffening model and damage parameters are evaluated in Table 2.4.

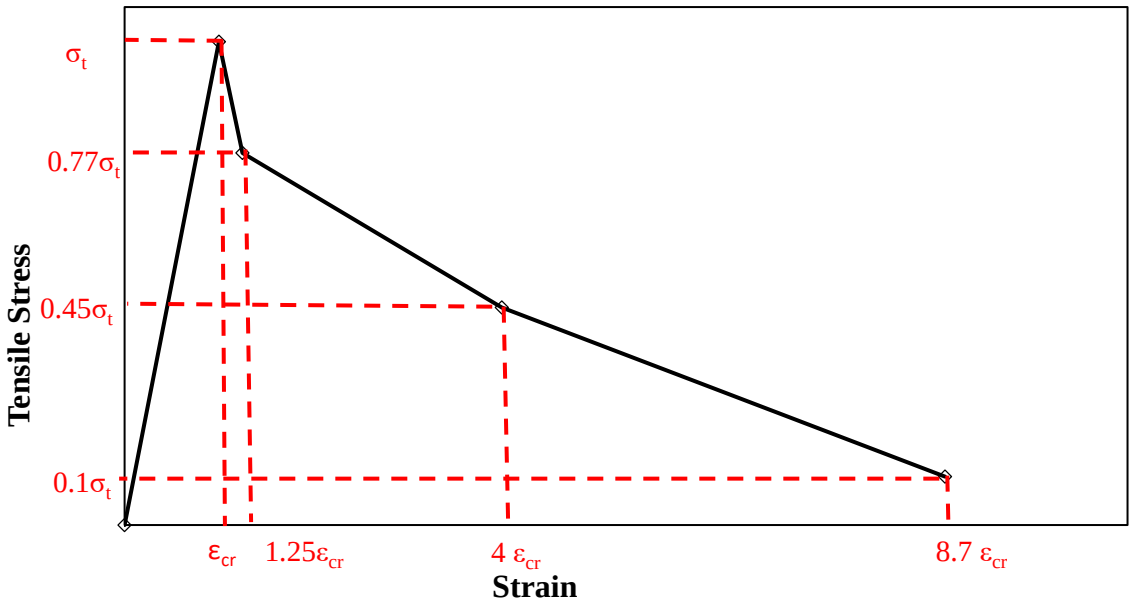

Figure 2.13 Tensile stress-strain curve (Wahalathantri et al., 2011)

2.3.2.1.3. Other concrete parameters

ABAQUS requires the user to input other concrete parameters that are related to the general behavior of the concrete. These parameters include dilation angle, flow potential eccentricity, the ratio of the initial equibiaxial compressive yield stress to initial uniaxial compressive yield stress, Kc, which is the ratio of the second stress on the tensile meridian to that on the compressive meridian, and viscosity parameter which is used for visco-plastic regularization of concrete. Some of the parameters could be obtained from the literature, and others are assumed as the default values in ABAQUS. In this study, the dilation angle is considered as 40°, K_c = 0.667, the stress ratio σ_{b0}/σ_{c0}=1.16 as suggested by Genikomsou and Polak (2015). The flow potential eccentricity is assumed to be equal to zero, a default value from ABAQUS. The viscosity parameter is determined through a convergence study, which yields to 0.001.

2.3.2.2. Shear Grid Connectors

Shear connectors are used to transfer the shear between the concrete wythes. Material and section properties are calculated for both longitudinal and transversal grids based on Table 2.5 and Figure 2.10. Equations (17) and (18) calculate areas for longitudinal and transversal strands. Equations (19) and (20) calculate the strength of a single strand in longitudinal and transversal directions, respectively.

$$A_{long.} = \frac{0.019390 \times 1.8}{12} = 0.00291 \text{ (in.}^2\text{/ft.)} \quad (17)$$

$$A_{trans.} = \frac{0.02145 \times 1.6}{12} = 0.0286 \text{ (in.}^2\text{/ft.)} \quad (18)$$

$$f_{c-long} = \frac{290000 \times 1.8}{12} = 43500 \text{ (psi)} \quad (19)$$

$$f_{c-transverse} = \frac{255000 \times 1.6}{12} = 34000 \text{ (psi)} \quad (20)$$

Table 2.5 Material properties of shear connectors

Shear grid type	Longitudinal Properties				Transverse Properties			
Proprietary shear connector	A (in^2/ft)	f_u (ksi/ft)	E(ksi)	ε_u (%)	A (in^2/ft)	f_u (ksi/ft)	E(ksi)	ε_u (%)
	0.019390	290	38000	0.76	0.021450	255	27000	0.76

2.3.2.3. Welded Wire Mesh (WWM)

Figure 2.14 shows the stress-strain curve for WWM adopted from Ayyub et al. (1994) for ASTM A185. The area per wire is calculated as follows:

$$\text{number of wires/unit ft} = \frac{12(in/\ ft)}{4(wire\ spacing)} = 3(wires/12in)$$

$$A_{wire} = \frac{0.062}{3} = 0.02067\ (\text{in}^2\ /\ wire) \qquad (21)$$

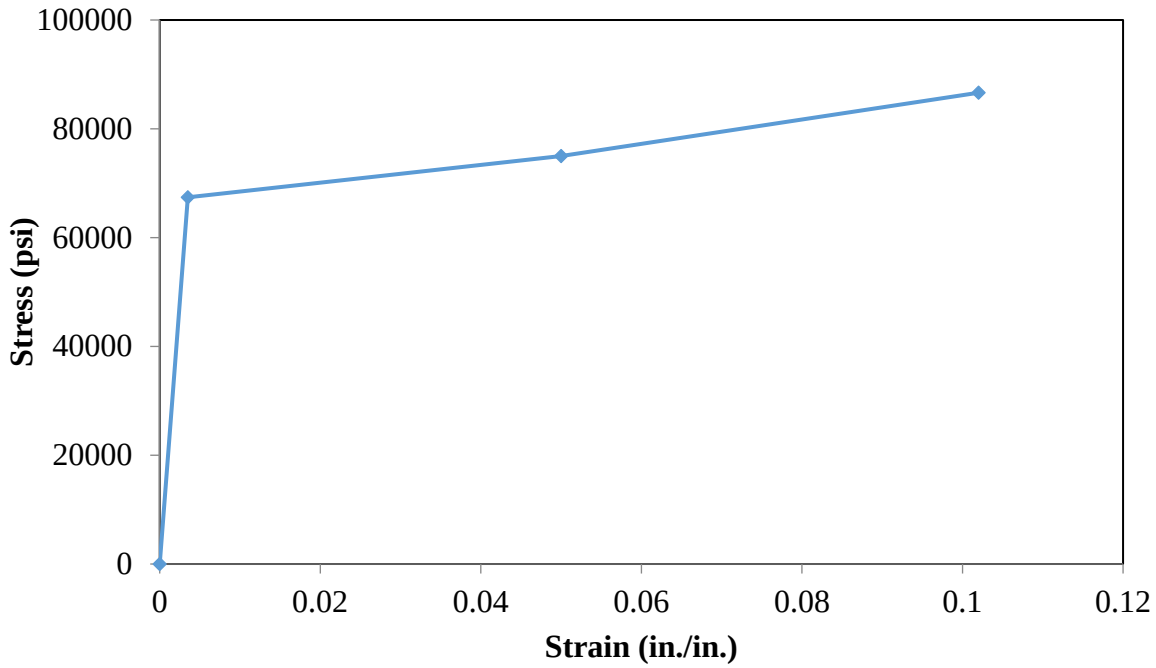

Figure 2.14 Constitution model for WWM 4x4-W2.1xW2.1

2.3.2.4. Prestressing Strands

Six prestressing strands are arranged over the width of the panel, where each strand is 3/8 in. diameter. Grade 270 is used, where the material properties are summarized in Table 2.6.

Table 2.6 Material properties for prestressing strand grade 270

Stress Equation	Stress (ksi)	Strain (in/in)
f_{pi}=0.75 f_{pu}	202.5	$\varepsilon = f_{pi} / E_{ps} = 0.00727$
f_{py}=0.85 f_{pu}	229.5	0.01
f_{pu}	270	0.05

Initial stress is provided to the strand elements equal to the initial prestressing stress (f_{pi}) shown in Table 2.6. The development length was calculated according to ACI 318 (2011) as shown in Equation (22):

$$l_d = (\frac{f_{se}}{3000})d_b + (\frac{f_{ps} - f_{se}}{1000})d_b \quad (22)$$

where, f_{se} is the effective stress in prestressing steel (psi) (after allowance for all prestressed losses), f_{ps} is the stress in the prestressing steel at nominal flexural strength (psi). In most cases $f_{ps} \cong f_{pi}$, d_b is the nominal diameter of the prestressing strand (in). f_{se} can be assumed to be 150,000 psi for grade 270 (Nawy, 2010). The strand is divided into multiple sections where each section was assigned a different area as shown in Table 2.7.

Table 2.7 Variation of area with the strand elements for the development length

element #	1	2	3	4	5	6	7	8	9
area (in^2)	0.003	0.0112	0.0188	0.0263	0.0338	0.0414	0.0489	0.0564	0.06398
element #	10	11	12	13	14	15	16	17	18
area (in^2)	0.068	0.0714	0.0739	0.0763	0.0788	0.0813	0.0837	0.085	0.085

2.3.3. Loading and analysis procedure

The loads are applied through multiple steps where each step had a different load as shown in Table 2.1. The panel is simply supported where one support was hinged and other was roller. Static analysis is used, however due to convergence problems, “STABILIZE” command was used to provide full convergence.

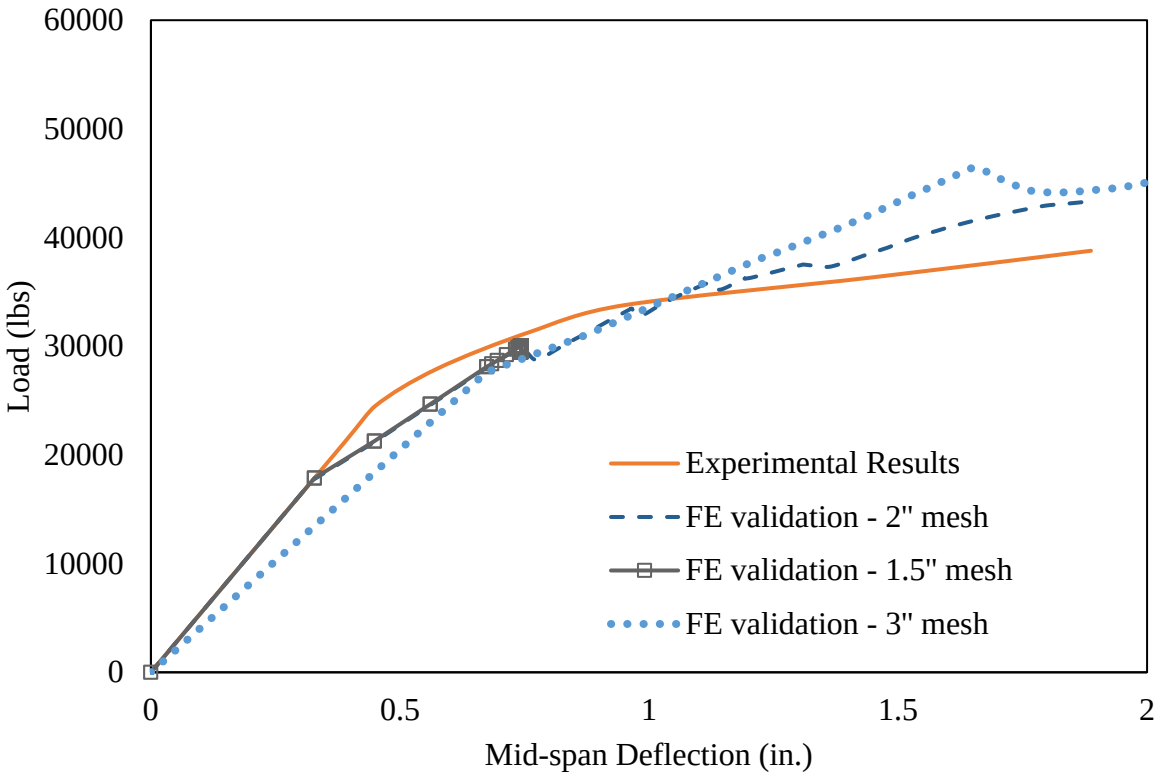

Figure 2.15 Load vs. deflection of experimental and FE model with different mesh sizes

2.4. Correlations between FE and Test Results

Convergence study is first conducted by varying the mesh size through 3 in., 2 in. and 1.5 in. Figure 2.15 shows the load-displacement for experimental and FE model results with different mesh sizes. As shown in the figure, the 2 in. mesh provides the best correlation between FE and experimental results. 3 in. mesh size, could not provide a good match with experimental while the 1.5 in. mesh size gives the same results as 2 in. mesh but requires more than triple the simulation

time and faces some convergence problems. Therefore, 2 in. mesh is chosen for this study. It is worth pointing out that the displacement from the test, as shown in Figure 2.6, was zeroed after the panel had been set up, i.e., deflection from the self-weight of the panel was not measured in the test. The tension damage plot shown in Figure 2.16 matches the cracks in Figure 2.8, which indicates that a good correlation is achieved.

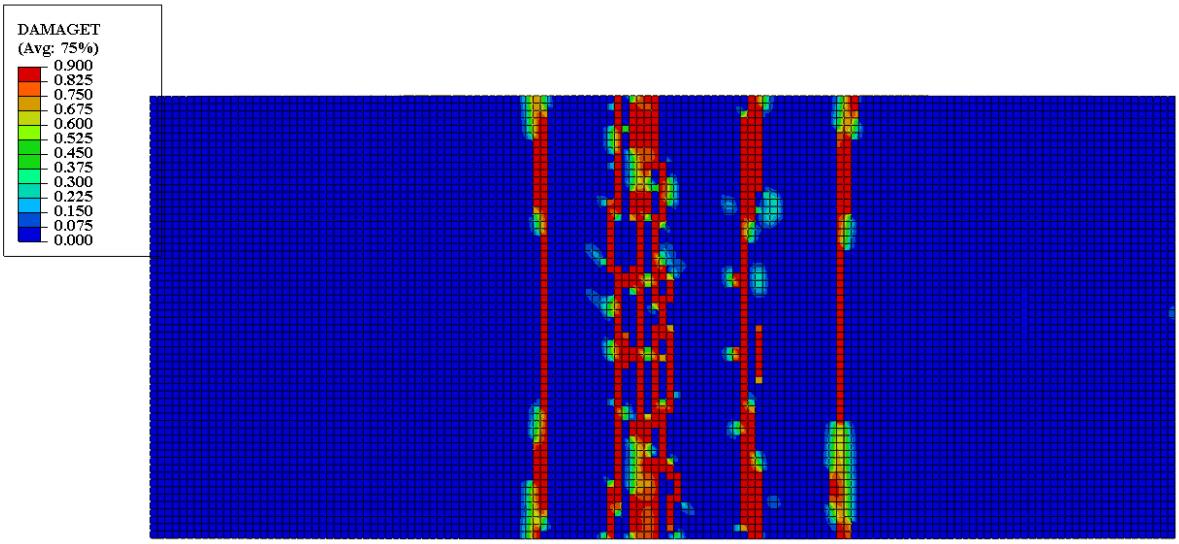

Figure 2.16 Bottom view of tension damage

2.5. Results and Parametric Study

A parametric study was performed to obtain 100% and 0% DCA. A solid panel with concrete replacing the insulation is modeled to provide the 100% DCA, where the shear force is fully transferred between the two layers. The 0% DCA is achieved by removing the shear grid, that will limit the longitudinal shear transfer where each layer is bending on its own. Another three models with different DCAs - 25%, 50% and 72% - are chosen to expand the evaluation range where the 72% DCA is chosen since it corresponds to the experimented panel.

In order to model different DCAs, the shear-grid is replaced by connector element "CONN3D2" with connector behavior set to Cartesian and Cardan. This element has the capability

of transferring forces and rotational moments based on the stiffness provided for each Degree of Freedom (DOF). Since the main function of the shear-grid is to transfer the longitudinal shear, therefore the stiffness of the longitudinal shear can be assigned different values based on the stiffness of the shear-grid, while other DOFs are assigned as rigid. The connector element can be used directly to transfer both transitional and rotational DOF when used with shell elements. However, in case of solid elements, “Coupling” command is needed to transfer rotation DOFs. Coupling is configured with uniform distributing of 1 in. influence radius. The function of the coupling command is to control the transmission of forces through weight factors over the surrounded nodes which can be equivalent of transferring rotation DOF. The connector elements are placed between the nodes along the locations of the shear-grid as shown in Figure 2.18.

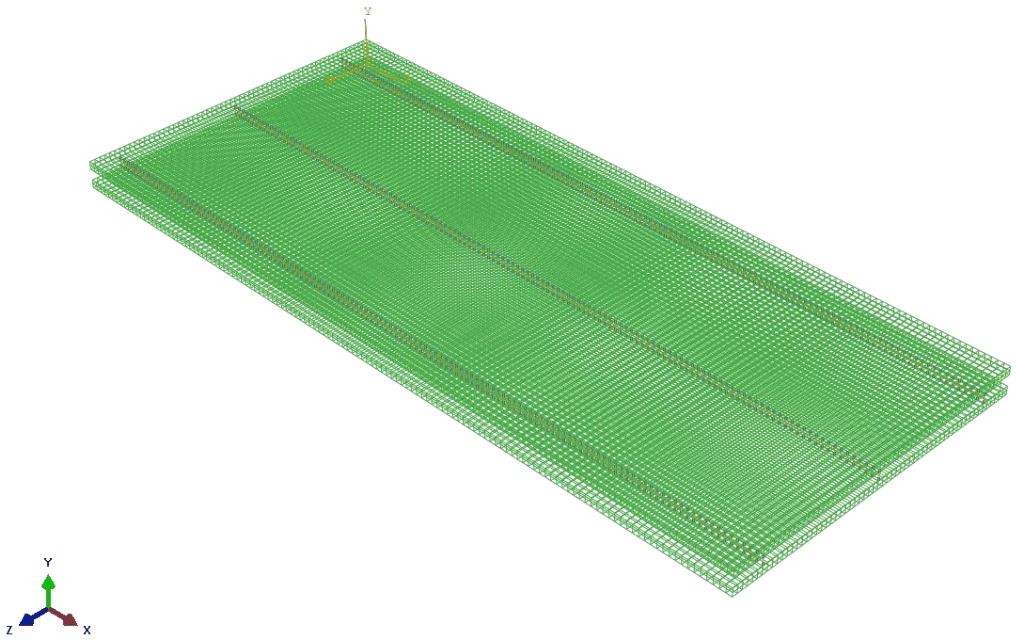

Figure 2.17 Sandwich panel with connectors

2.5.1. Displacement method

Figure 2.18 shows the load-displacement curve for 100% DCA, 0% DCA, and partial DCA. Partial DCA represents the FE model, which is correlated with the experimental results. DCA can be calculated using displacement method developed by Frankl et al. (2011) as follows:

$$DCA(100\%) = \frac{\Delta_{noncomposite} - \Delta_{partial}}{\Delta_{noncomposite} - \Delta_{composite}} \times 100 \quad (23)$$

where $\Delta_{noncomposite}$, $\Delta_{composite}$, and $\Delta_{partial}$ represent displacement at a given load corresponding to 0%, 100%, and partial DCA, respectively. This method can only be applied to the region before yielding. As shown in Figure 2.18, yield points are marked with a black hollow rounded mark, and ultimate points are marked with a black hollow triangle mark. Values of the yield and ultimate are shown in Table 2.9. Since the 0% DCA has the lowest yielding value (21317 lb) and this method can only be used before yielding, DCA is evaluated at a selected load before the lowest yielding point (21317 lb) as shown in Table 2.8. Other DCAs; 25%, 50% and 72% are modeled by varying the stiffness of the connector elements, and they are used as reference to evaluate other methods. Different stiffness values are shown in Table 2.8. It can be noted that the test panel achieved a 72% DCA based on the displacement method.

Table 2.8 DCA displacement method calculations

Selected load (P) (lbf.)	Mid-span deflection (Δ) (in.)	DCA	Stiffness (K)
16000	0.87	0	1E-04
	0.67	25	2400
	0.47	50	7300
	0.29	72	20000
	0.07	100	1E+07

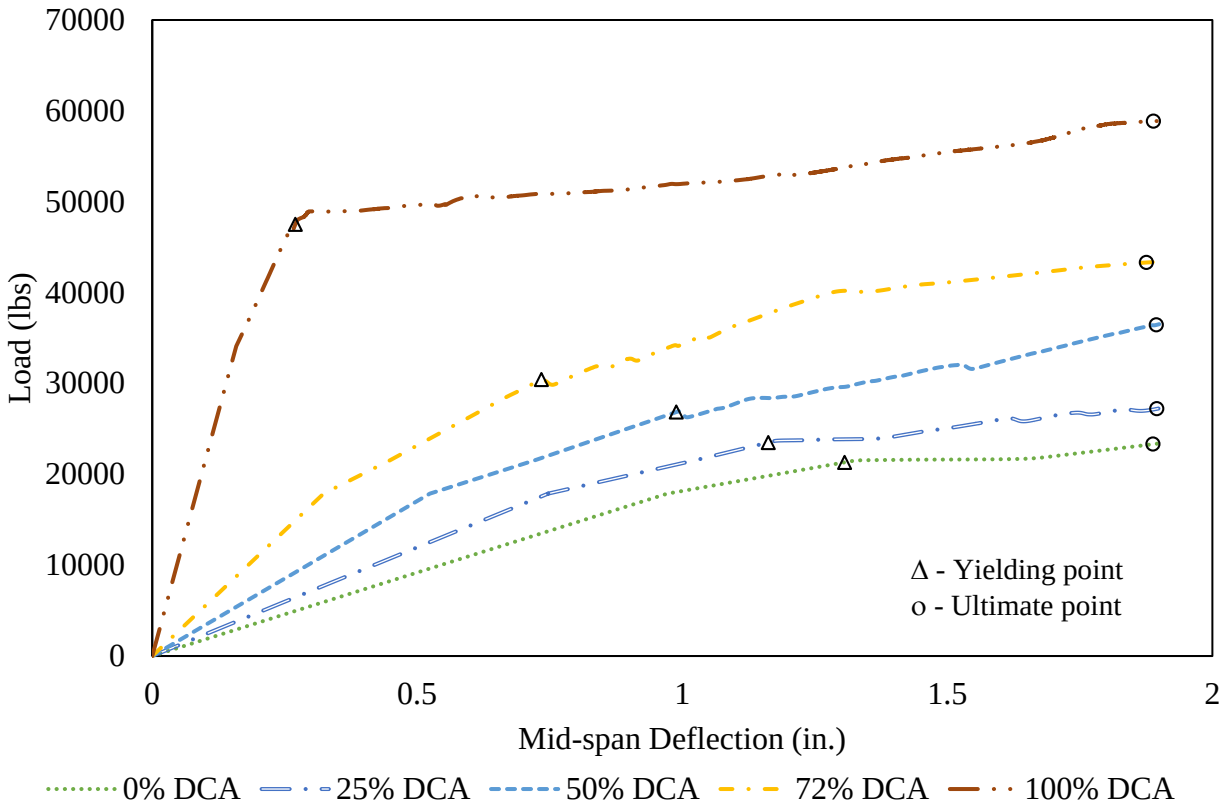

Figure 2.18 Load-deflection curve for 100%, 72%, 50%, 25%, and 0% DCA

2.5.2. Load method

As shown in Figure 2.18, for 100%, 0% and partial DCAs, the load increases linearly with respect to displacement until the yielding point. Afterward, the load increases with respect to displacement gradually until it reaches a constant value. The DCA can be calculated based on the ultimate load for each case as:

$$DCA(100\%) = (1 - \frac{P_{composite} - P_{partial}}{P_{composite} - P_{noncomposite}}) \times 100 \quad (24)$$

where $P_{noncomposite}$, $P_{composite}$, and $P_{partial}$ represent a selected load corresponding to 0%, 100%, and partial DCAs, respectively. Table 2.9 shows DCA calculated at the yield and ultimate load values

for the same stiffness values used for displacement method. However, load method led to different DCA values than the displacement method.

Table 2.9 Yield and ultimate point values

K	Yield displacement (in.)	Yield load (lbf)	DCA (Yield load)	Ultimate displacement (in.)	Ultimate load (lbf)	DCA (Ultimate load)
1E+07	0.270	47506	100%	1.89	58847	100%
20000	0.734	30427	35%	1.88	43310	56%
7300	0.989	26856	21%	1.90	36446	37%
2400	1.162	23500	8%	1.90	27206	11%
1E-04	1.306	21318	0%	1.89	23316	0%

2.5.3. Strain method

Strain method was proposed by Lorenz and Stockwell (1984) as shown in Figure 1.3 for deck slab on beam; this method can be generalized for sandwich panels as follows:

$$DCA = 1 - \frac{x}{x_{MAX}} \tag{25}$$

where x indicates the amount of the horizontal slip as shown in Figure 2.20.

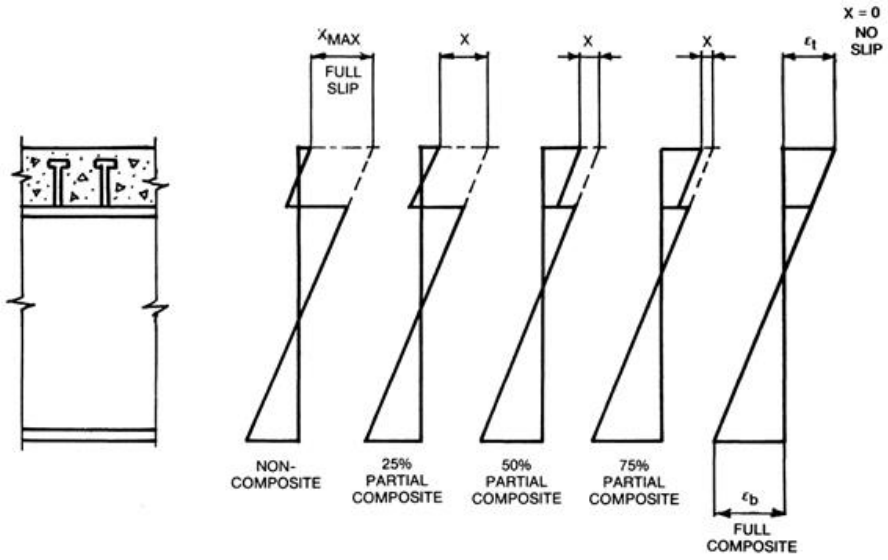

Figure 2.19 Partial DCA for deck slab on beam (Lorenz and Stockwell, 1984)

Equation (25) can be re-written as:

$$DCA = 1 - \frac{\varepsilon_2 - \varepsilon_1}{\varepsilon_{max}} \tag{26}$$

where ε_1 and ε_2 are the strains for lower and upper wythes, respectively. However, in order for this equation to be applied to sandwich panels, the strain need to be extrapolated to the neutral axis of the sandwich panel as shown in Figure 2.20.

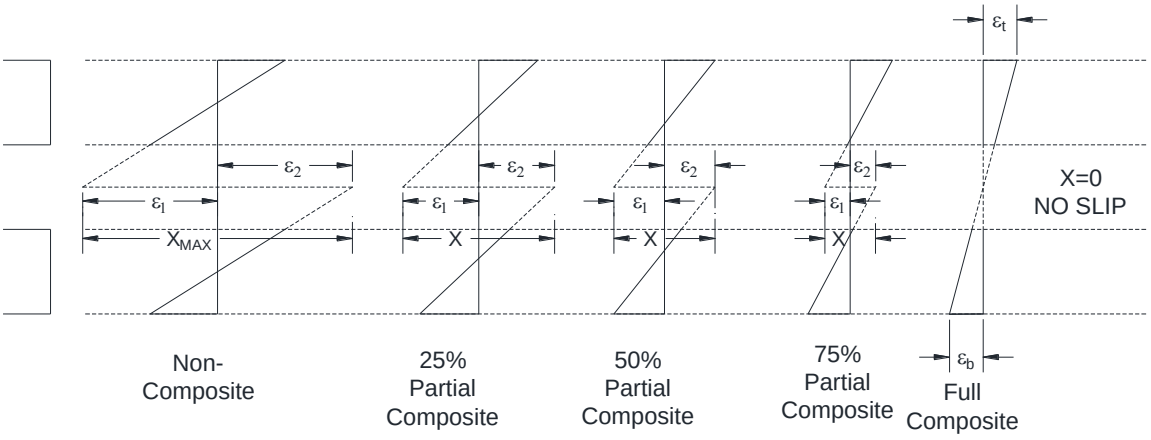

Figure 2.20 Partial DCA for sandwich panels

The strain in the concrete varies as the concrete properties changes from elastic to plastic stage. The strain method can be used in the linear stage as the strain profile follows a linear form and can be linearly extrapolated as shown in Figure 2.20. The strain values at the upper and lower wythes are exported from post-processed data at the intersection of the mid-span and the location of the edge shear connector to avoid any localized effect due to the applied loads. Two strain values are exported from each wythe since there are two elements per layer as shown in Figure 2.21. Once the strain profile versus the thickness is constructed, the strain values are then extrapolated to the neutral axis (5 in) for the upper and lower layers, where the difference between the extrapolated

values is calculated using Equation (26). The tested panel achieved 74% DCA as shown in Table 2.10, which provides similar results to the displacement method.

Table 2.10 DCA strain method calculations

Stiffness	Distance across the thickness						Difference	DCA
	0.75	2.25	5	5	7.75	9.25		
1E+07	67.24	-147.13	-540.14	412.76	19.36	-195.22	**953**	**0%**
20000	48.39	-116.41	-418.54	290.93	-11.44	-176.37	**709**	**26%**
7300	29.60	-85.76	-297.26	169.48	-42.14	-157.56	**467**	**51%**
2400	12.52	-57.93	-187.08	59.21	-69.99	-140.46	**246**	**74%**
1E-04	-7.65	-27.53	-63.97	-63.91	-100.36	-120.25	**0**	**100%**

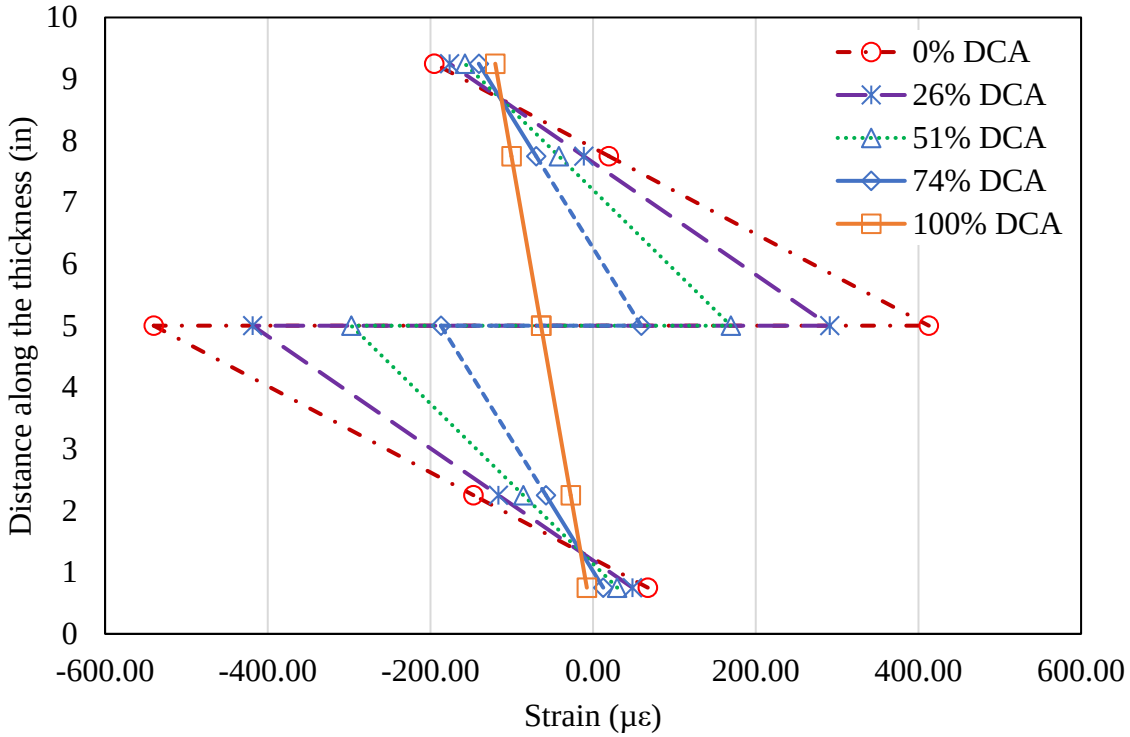

Figure 2.21 Strain profile at different DCAs at load 17876.3 lbf

2.6. Summary and Conclusions

A full-size panel was tested to study the behavior of the precast, prestressed concrete sandwich panel using CFRP shear connectors. The test results are used to validate a non-linear

3-D finite element model that can calculate partial degree of composite action (DCA). The FE model accounts for material nonlinear behavior, concrete damage plasticity and prestressing force. Next, the FE model is used to conduct a parametric study by varying the stiffness of the shear connectors. DCAs are then calculated and compared using displacement, load and strain methods. Based on this study, the following conclusions can be drawn:

1. CFRP shear connectors can transfer shear between concrete wythes.
2. The FE results agree well with the test results based on the load-deflection curve and crack patterns. Therefore, the FE model can be used to model insulated concrete sandwich panels.
3. Connector elements can provide similar behavior as the shear connectors and provide a stiffness value that can be used to design the precast sandwich panel.
4. The test panel achieved 72%, 35%, 56% and 74% DCA based on displacement, yielding load, ultimate load and strain method, respectively.
5. Displacement and strain method can be used for the linear region, while the load method can be used for the non-linear region.
6. Strain and displacement values provide close results, however, the load method can provide lower DCA results which can be used as a conservative method for design.

2.7. References

ABAQUS. (2013). “ABAQUS Documentation.” Dassault Systèmes, Providence, RI, USA.

ACI Committee 318. (2011). *Building Code Requirements for Structural Concrete (ACI 318-08). American Concrete Institute (ACI)*, Farmington Hills, MI.

Ayyub, B. M., Chang, P. C., and Al-Mutairi, N. A. (1994). “Welded Wire Fabric for Bridges. I: Ultimate Strength and Ductility.” *Journal of Structural Engineering*, American Society of Civil Engineers, 120(6), 1866–1881.

Bush, T. D., and Stine, G. L. (1994). "Flexural behavior of composite precast concrete sandwich panels with continuous truss connectors." *PCI journal*, 39(2), 112–121.

Bush, T. D., and Wu, Z. (1998). "Flexural analysis of prestressed concrete sandwich panels with truss connectors." *PCI journal*, Precast/Prestressed Concrete Institute, 43(5), 76–86.

Chen, A., Norris, T. G., Hopkins, P. M., and Yossef, M. (2015). "Experimental investigation and finite element analysis of flexural behavior of insulated concrete sandwich panels with FRP plate shear connectors." *Engineering Structures*, 98, 95–108.

Choi, C. K., and Cheung, S. H. (1996). "Tension stiffening model for planar reinforced concrete members." *Computers and Structures*, 59(1), 179–190.

Collins, M. P., Mitchell, D., and MacGregor, J. G. (1993). "Structural design considerations for high-strength concrete." *Concrete International*, 15(5), 27–34.

Comite Euro-International Du Beton. (1993). *CEB-FIP MODEL CODE 1990*. Thomas Telford Publishing.

Einea, A., Salmon, D. C., Fogarasi, G. J., Culp, T. D., and Tadros, M. K. (1991). "State-of-the-Art of Precast Concrete Sandwich Panels." *PCI Journal*, 36(6), 78–98.

Einea, A., Salmon, D. C., Tadros, M. K., and Culp, T. (1994). "A New Structurally and Thermally Efficient Precast Sandwich Panel System." *PCI Journal (Precast/Prestressed Concrete Institute)*, 39(4), 90–101.

Fields, K., and Bischoff, P. H. (2004). "Tension stiffening and cracking of high-strength reinforced concrete tension members." *ACI Structural Journal*, 101(4), 447–456.

Frankl, B. A., Lucier, G. W., Hassan, T. K., and Rizkalla, S. H. (2011). "Behavior of precast, prestressed concrete sandwich wall panels reinforced with CFRP shear grid." *PCI journal*, Precast/Prestressed Concrete Institute, 56(2), 42–54.

Genikomsou, A. S., and Polak, M. A. (2015). “Finite element analysis of punching shear of concrete slabs using damaged plasticity model in ABAQUS.” *Engineering Structures*, 98, 38–48.

Hegemier, G. A., Murakami, H., and Hageman, L. J. (1985). “On tension stiffening in reinforced concrete.” *Mechanics of Materials*, 4(2), 161–179.

Hognestad, E., Hanson, N. W., and McHenry, D. (1955). “Concrete stress distribution in ultimate strength design.” *Journal of the American Concrete Institute*, 52, 455–479.

Hopkins, P. (2015). " Non-linear finite element analysis of FRP-precast concrete sandwich panels." PhD. Dissertation, University of Idaho.

Hsu, L. S., and Hsu, C.-T. T. (1994). “Complete stress — strain behaviour of high-strength concrete under compression.” *Magazine of Concrete Research*, Thomas Telford Ltd , 46(169), 301–312.

Kent, D. C., and Park, R. (1971). “Flexural Members with Confined Concrete.” *Journal of the Structural Division*, 97(7), 1969–1990.

Lee, B.-J., and Pessiki, S. (2007). “Design and analysis of precast, prestressed concrete, three-wythe sandwich wall panels.” *PCI journal*, Precast/Prestressed Concrete Institute, 52(4), 70–83.

Lee, J., and Fenves, G. L. (1998). “Plastic-Damage Model for Cyclic Loading of Concrete Structures.” *Journal of Engineering Mechanics*, 124(8), 892–900.

Lorenz, R. F., and Stockwell, F. W. (1984). “Concrete Slab Stresses in Partial Composite Beams and Girders.” *Engineering Journal-American institute of steel construction*, 21(3), 185–188.

Lubliner, J., Oliver, J., Oller, S., and Oñate, E. (1989). “A plastic-damage model for concrete.” *International Journal of Solids and Structures*, Pergamon, 25(3), 299–326.

Nawy, E. G. (2010). *Prestressed concrete : A fundamental approach*. Prentice Hall, Upper Saddle River, NJ.

Nayal, R., and Rasheed, H. A. (2006). "Tension Stiffening Model for Concrete Beams Reinforced with Steel and FRP Bars." *Journal of Materials in Civil Engineering*, 18(6), 831.

Pessiki, S., and Mlynarczyk, A. (2003). "Experimental Evaluation of the Composite Behavior of Precast Concrete Sandwich Wall Panels." *PCI Journal*, 48(2), 54–71.

Popovics, S. (1973). "A numerical approach to the complete stress-strain curve of concrete." *Cement and Concrete Research*, Pergamon, 3(5), 583–599.

Roy, H. E. H., and Sozen, M. A. (1965). "Ductility of Concrete." *Proceedings of International Symposium on the Flexural Mechanics of Reinforced Concrete, ASCE-American Concrete Institute*, 12, 213–235.

Saatcioglu, M., and Razvi, S. R. (1992). "Strength and Ductility of Confined Concrete." *Journal of Structural Engineering*, 118(6), 1590–1607.

Salmon, D. C., Einea, A., Tadros, M. K., and Culp, T. D. (1998). "Full-Scale Testing of Precast Concrete Sandwich Panels." *ACI Structural journal*, 94(4), 354–362.

Sato, Y., and Vecchio, F. J. (2003). "Tension Stiffening and Crack Formation in Reinforced Concrete Members with Fiber-Reinforced Polymer Sheets." *Journal of Structural Engineering*, 129(June), 717–724.

Stramandinoli, R. S. B., and La Rovere, H. L. (2008). "An efficient tension-stiffening model for nonlinear analysis of reinforced concrete members." *Engineering Structures*, 30(7), 2069–2080.

Tomlinson, D., and Fam, A. (2015). "Flexural behavior of precast concrete sandwich wall panels with basalt FRP and steel reinforcement." *PCI Journal*.

Wahalathantri, B. L., Thambiratnam, D. P., Chan, T. H. T., and Fawzia, S. (2011). "A material model for flexural crack simulation in reinforced concrete elements using ABAQUS." *First International Conference on Engineering, Design and Developing the Built Environment for Sustainable Wellbeing*, 260–264.

Whitehead, P. A., and Ibell, T. J. (2005). "Novel Shear Reinforcement for Fiber-Reinforced Polymer-Reinforced and Prestressed Concrete." *ACI Structural Journal*, American Concrete Institute, 102(2), 286.

CHAPTER 3. DEVELOPMENT OF A MULTIFUNCTIONAL PHOTOVOLTAIC INTEGRATED INSULATED CONCRETE SANDWICH PANEL

A paper prepared to be submitted to ACI Special Publication (SP)

Mostafa Yossef, An Chen and Austin Doweny[1]

Abstract

Insulated concrete sandwich panels are composed of two concrete wythes separated by a layer of foam insulation, where the wythes are connected by different types of shear connectors. The foam insulation layer can provide energy savings, which is a typical passive energy system. This paper will develop a multifunctional photovoltaic (PV) integrated insulated concrete sandwich (PVICS) panel with the following features: passive energy savings and the ability to harvest its own solar energy using attached thin-film solar cells. The combined active and passive energy system assist in achieving a zero-carbonate building system. Attaching the solar cells to the sandwich panel is based on an innovative co-curing scheme, where a Fiber-Reinforced Polymer (FRP) shell is manufactured as the formwork for the sandwich panel. The solar cells are bonded to the FRP during its curing. Polymer concrete is applied to the inner surface of the FRP shell to enhance the bond between the FRP and concrete. In addition to acting as an interface to bond solar cells and concrete, the non-corrosive, lightweight, and high-strength FRP shell provides a confining effect acts as shear connectors, and provides reinforcement to improve the structural performance of the sandwich panel. FRP shear connectors can also significantly reduce the thermal bridging compared to steel shear connectors, thus improving the energy efficiency.

In the last few years, cost of solar electricity has decreased about 25%, mainly due to the cost reduction of photovoltaic (PV) modules. No additional mounting system for the solar cells is

[1] Helped in writing LabVIEW code, test setup and provided us with testing equipment.

required for PVICS. Eliminating the mounting system can reduce the PV cost up to 30%. The objectives of this paper are to (1) prove the concept of PVICS through a bending test. Unlike steel connectors, FRP shear connectors are flexible, which will affect both the strength and stiffness of the panel; (2) Correlate the test results with those from the Finite Element (FE) model and analytical model; and (3) Study the strain effect on the solar energy generation performance of the sandwich panel. It can be concluded that the developed sandwich panel can act as both an active and passive energy system. Bonding aggregates to the FRP can increase the bond strength between the FRP and concrete. The FRP shell can provide a confining effect to the concrete and act as shear connectors and reinforcement. The derived analytical model results can be correlated with the test and FE results, which can be used for design purposes.

3.1. Introduction

Insulated concrete sandwich panels are composed of two concrete wythes separated by a layer of foam insulation which can be used for both walls (Einea et al., 1991, Einea et al., 1994; Frankl et al., 2011) and roofs (Benayoune et al., 2008; Bush and Wu, 1998; Chen et al., 2015). The insulated sandwich panels are often used in low-rise buildings and warehouses where the two concrete wythes are connected with shear connectors that can provide composite action between the two wythes. These shear connectors can be steel wires, steel ties, solid concrete zones. Recently, steel shear connectors are being replaced by Fiber-Reinforced Polymers (FRP) as FRP provides a higher weight-to-strength ratio, non-corrosive property and more importantly, it reduces the thermal bridging of heat between the two wythes.

Insulated sandwich panels are an excellent precast solution providing a fast construction solution in addition to the reduction of concrete material which results in reduced cost, weight,

CO_2 emission and structural footprint. Additionally, it can be used as passive energy system to reduce heating and cooling costs.

The Solar Investment Tax Credit (ITC) has successfully pushed hardware prices down and installer experience up. For example, the cost of solar electricity has decreased from $5.06/W in 2010 to $3.29/W in 2016, mostly due to the cost reduction of the photovoltaic (PV) module, which was 2.15/W in 2010 and is $0.7/W today. Although the price of the module will continue to decrease, there is little room for substantial reduction. Therefore, more efficient ways are required to optimize the cost such as eliminating the mounting system and develop multifunctional PV system, which is the motivation of this study.

In this study, multifunctional photovoltaic (PV) cells were integrated with insulated sandwich panels to develop an active energy system through harvesting solar energy. The combined active and passive energy system can help achieve a zero-carbon building system. The solar cells are attached to concrete through FRP material by a co-curing process where the solar cells are bonded to the FRP during its curing. Polymer concrete is applied to the inner surface of the FRP shell to enhance the bond between the FRP and concrete. The co-curing effect can secure the bond between solar cells and concrete and eliminate the need of the mounting system for the solar cells. Moreover, the FRP can be used as formwork for concrete which will speed the construction process and provide confining effect to enhance the overall shear transfer mechanism (Norris and Chen, 2016).

The developed PV integrated concrete sandwich panel (PVICS) can provide multifunctionality by offering structural health monitoring, energy harvesting, structural function (load-bearing component), and reducing thermal bridging through insulation effect.

In this study, a PVICS panel was manufactured and subjected to a three-point bending test, where the solar cell performance was captured through J-V curves and correlated with strain recorded by installed strain gages. The data are further used to verify both Finite Element (FE) and analytical models.

3.2. Experimental Program

The purpose of this section is to investigate the performance of a full-scale PVICS panel under three-point flexural loading, and prove that solar cell can work under acting loads. The panel is consisted of two concrete wythes connected via insulation foam and confined from the top and side with FRP shell. The solar cells were integrated on the top of the panel.

3.2.1. Material properties

The materials used to manufacture this panel were solar cells, FRP, concrete, steel rebars and expanded polystyrene (EPS) foam. The mean compressive strength of concrete was 3213 psi (22.15 MPa) with a standard deviation of 938 psi (6.46 MPa) and 5988 psi (41.29 MPa) with a standard deviation of 248 psi (1.7 MPa) at 7 and 28 days, respectively. The steel rebars used were ASTM A615 Grade 60 steel, with a yield strength of 60 ksi (414 MPa). Glass FRP was manufactured using chopped strand mat (CSM) and isophthalic resin (US composites). Properties of the fiberglass and resin are shown in Table 3.1. Amorphous silicon thin-film solar cells (SP3-12) that were 0.6 in. (1.52 cm) wide and 2.5 in. (6.35 cm) long were manufactured by PowerFilm Solar. The electrical properties of the solar cells are listed in Table 3.2. Type I EPS foam with a typical yield compressive strength of 10 psi (69 kPa) was provided by Iowa EPS products.

Table 3.1 Material properties

	Type	Tensile Strength (MPa)	Tensile Modulus (GPa)	Compressive Strength (MPa)	Density (gm/cm^3)
Resin	404 Isophthalic Resin	503.3	36.5	82.73	1.1
E-Glass Fiber	Chopped Strand Mat	2000	72.4	--	2.56

Table 3.2 Electrical properties

Solar Module Type	Wattage (W)	Voltage (V)	Open-Circuit Voltage (V)	Current (mA)	Short-Circuit Current (mA)
SP3-12	0.0255	3.0	4.5	8.5	10.7

3.2.2. Evaluating solar cell performance

The performance of the solar cell attached to FRP under strain were investigated using material testing. Five samples were manufactured and tested under tension and compression loading. The strain was recorded by strain gages and validated by load and displacement data imported from a material testing machine (MTS machine). The attached solar cell was illuminated by a carousel projector (Kodak 750H) with 500W incandescent light bulb. Tension test setup is shown in Figure 4.9. Sugar (2007) justified that the quantum efficiency of the solar cells falls within the projector spectrum. Two wires were soldered to each end of the solar cell and connected to a Keithley 2400 SourceMeter where a LabVIEW program was used to import the J-V curve for the solar at each strain. Maximum Power Point (MPP) was calculated and correlated against strain for tension and compression as shown in Figure 3.1. More details will be discussed further in Chapter 4.

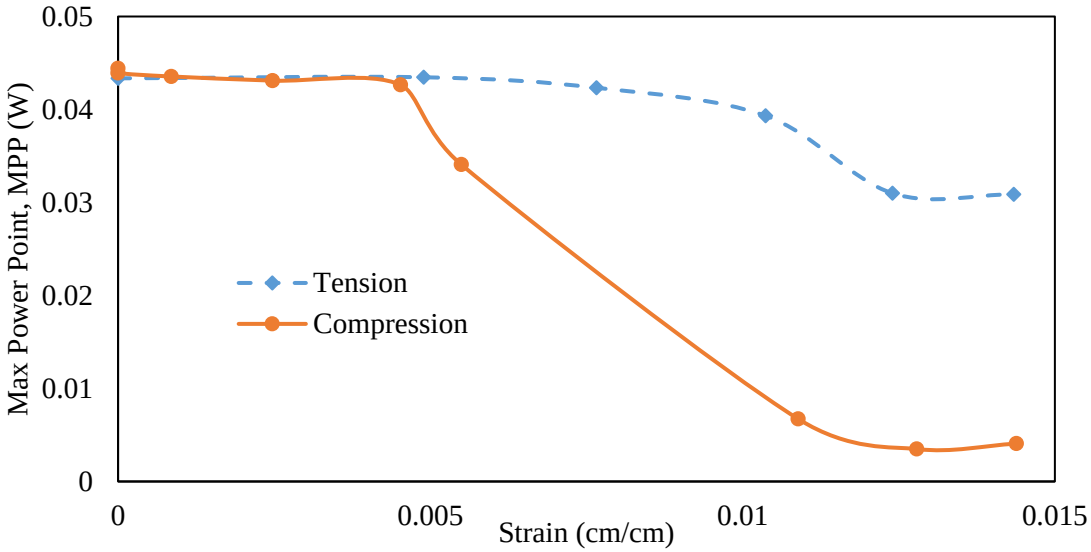

Figure 3.1 MPP vs. strain

3.2.3. Specimen fabrication

3.2.3.1. Specimen details

A 10 ft. (304.8 cm) long, 2.5 ft. (76.2 cm) wide and 10 in. (25.4 cm) thick PVICS panel with two 3 in. (7.62 cm) thick concrete wythes separated by a 4 in. (10.16 cm) EPS insulation foam was constructed, as shown in Figure 3.2.

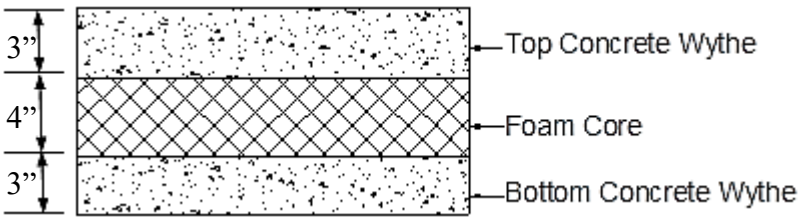

Figure 3.2 Typical sandwich panel

3.2.3.2. Solar and FRP preparation

In order to manufacture the FRP with solar cells, initial trials took place to determine the best practice regarding several factors. First, a steel formwork with 2.5 ft (76.2 cm) wide bed was assembled and connected to the 10’’ (25.4 cm) wide sides using rubber connection, as shown in

Figure 3.3, in order to obtain a 90-degree angle during folding of FRP. Four rubber connections were spaced evenly to prevent sliding of the sides while folding, as shown in Figure 3.4.

Figure 3.3 Shifted rubber bolted to the formwork to achieve 90^{o} angle

A nylon ply was laid down on the formwork to facilitate the removal of the FRP after manufacturing. They were stretched and tied to the end of each side to avoid any wrinkling of the FRP. Then, eight SP3-12 thin film solar cells were attached to the nylon peel ply using 0.5 in. (1.27 cm) double sided polyimide tape to protect the solar cell area. The solar cells were placed 6 in. (15.24 cm) away from the mid-span to measure the strain, as shown in Figure 3.5. The polyimide tape was placed in the center of the solar cell, leaving 0.05 in. (0.127 cm) on both sides to be embedded in the FRP. Next, glass fiber sheet was laid down on the formwork above the solar cell, as shown in Figure 3.5. It is worth mentioning that the width of the panel was chosen to be 2.5 ft. (76.2 cm), as the fiberglass CSM was manufactured with 50 in. (127 cm) width, which left the rest 20 in. (50.8 cm) to fit both sides.

Before applying resin to fiberglass, several trials took place to develop the best practice of folding the FRP. There were two major practices: the first was applying the resin on the bottom and sides, spreading the aggregates over the bottom and sides, and waiting for 45 min so the aggregates would attach to the sides. However, FRP buckled at the corner due to the attachment of the folding side with the formwork, as shown in Figure 3.6 (a). The second practice was covering

the corner and applying epoxy and aggregates at the sides, as shown in Figure 3.6 (b). Then, the FRP was left for at least 1 hour until it was solidified to ensure the aggregates was well bonded. Next, the epoxy was applied to the corner and more aggregates were spread over the corner, as shown in Figure 3.6(c).

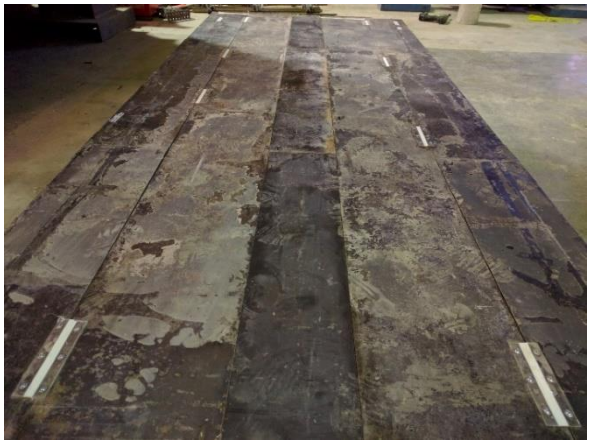

Figure 3.4 Formwork with four rubber connection at each side

Figure 3.5 Attaching solar cells and laying down the glass fiber CSM

The second method was chosen to manufacture the panel as the buckling effect was limited. The same epoxy used to manufacture FRP was used to bond the aggregates. The optimum size and distribution of aggregates were chosen according to Cho et al. (2010), as shown in Table 3.3. Cho et al. (2010) stated that the best aggregates should be a course silica sand, known as quartzite. Due to the lack of the quartzite in Iowa, it was brought from Minnesota (OMG Midwest) with 95% retained by 3/8'' and #4-sieve analysis. Since the concrete was only on the top and lower 3'' (7.62 cm), the aggregates were only applied to these areas, as shown in Figure 3.7. After the FRP had hardened, it was removed from the formwork. Oil was applied to the formwork to facilitate the removal of the FRP and panel after pouring. Before placing the steel, FRP sides were trimmed as low as 0.25 in. (0.635 cm) to provide space where the FRP can be embedded within the concrete.

(a) (b) (c)

Figure 3.6 Different processes to fold FRP with aggregates (a) Applying epoxy and aggregates on the sides and base at the same time, (b) Applying epoxy and aggregates at the sides and base and leaving a 2'' gap at the corner, (c) Folding the sides and applying epoxy and aggregates at the corner.

Table 3.3 Aggregates optimum size and distribution

Optimum Size	0.157 – 0.276 in
Optimum Distribution	0.82 lb/ft^2

3.2.3.3. Steel Reinforcement

Two sets of three steel rebars were cut and placed in each wythe. Two different sizes were chosen. No. 4 rebars with a nominal diameter of 0.5 in (1.27 cm) were placed in the top wythe, which was close to the FRP side as it will be subjected to compression. No. 5 rebars with a nominal diameter of 5/8 in. (1.59 cm) were placed in the bottom wythe. The steel rebars were cut into 117 in (297.18 cm) pieces, allowing 1.5 in. (3.81 cm) concrete cover from each side. Each rebar was sanded at the mid-span where strain gages were installed, as shown in Figure 3.8.

Figure 3.7 FRP-aggregate shell

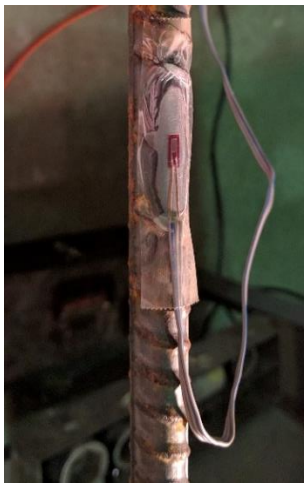

Figure 3.8 Installing strain gages

Figure 3.9 Assembling rebars

Temperature and shrinkage No. 4 steel rebars were cut into 27 in (68.6 cm) long and placed at a spacing required by ACI 318-14 ACI (2014). Figure 3.9 shows the assembling of the longitudinal and temperature rebars using steel ties, where 1.5 in (3.81 cm) plastic chairs were tied to the bottom of the longitudinal rebars to provide enough clearance so that the steel would be placed on the tension side of the wythe. Steel detailing and test setup are shown in Figure 3.10.

3.2.3.4. Concrete Pour

The two far ends of the formwork were closed using wood formwork. The FRP cage was placed in the formwork after it was coated with oil. The top steel mesh was then placed. Four anchor bolts were installed on the two far ends near FRP to facilitate handling and transporting of the concrete panel without subjecting it to cracking load due to its own weight.

Six concrete cylinders were poured and compacted according to ACI 318-14, where three cylinders were tested at 7 days and another three cylinders were tested at 28 days. Concrete was poured after the first set of the steel mesh was placed, where additional steel covers were installed on the top of the steel to mark the top of the concrete layer. After the pouring of the first layer,

EPS insulation foam was placed and fitted within the 2.5 ft. (76.2 cm) wide panel. The second steel mesh was then placed on the top of the insulation layer. Next, concrete was again poured and leveled to provide a smooth surface for testing purpose. Figure 3.11 (a-c) shows the manufacturing process of the PVICS.

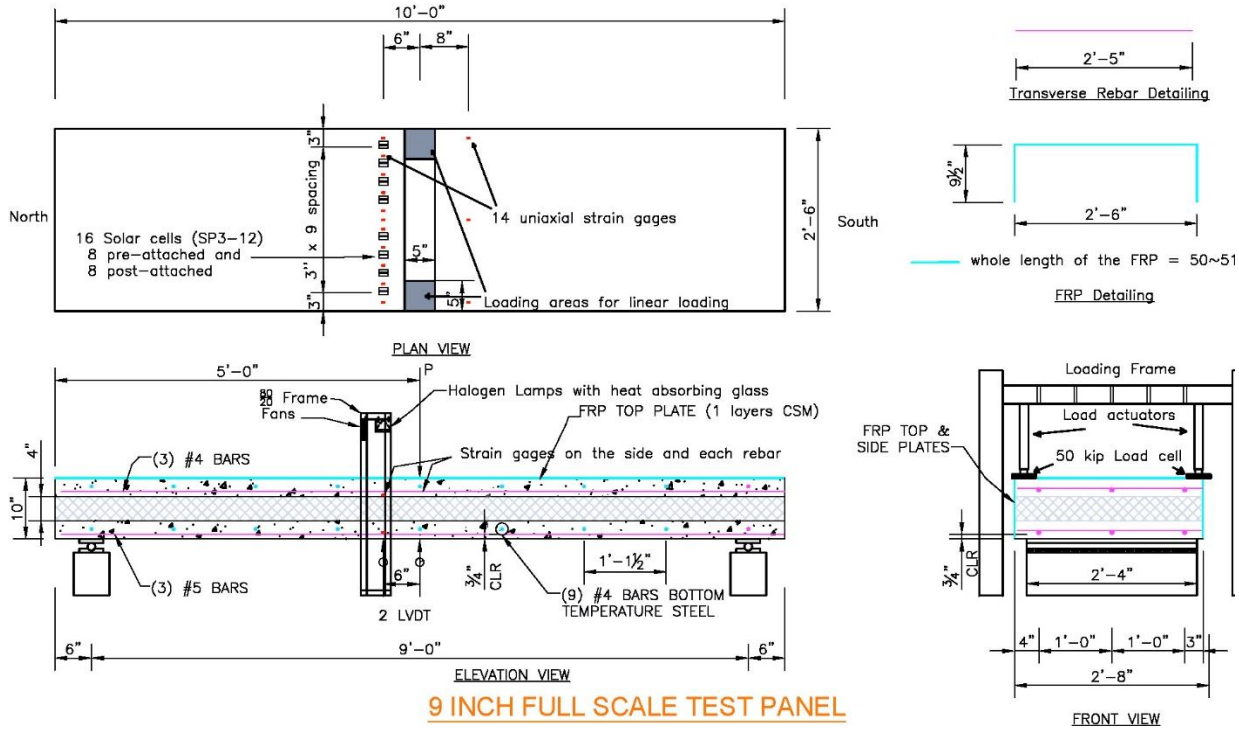

Figure 3.10 PVICS test setup

(a) **(b)** **(c)**

Figure 3.11 PVICS panel manufacturing process (a) placing first reinforcement set and pouring concrete, (b) placing insulation layer and second reinforcement set, (c) smoothing concrete surface

1.1.7. Test Setup

1.1.7.1. Linear stage

Concrete was cured and covered to limit the shrinkage effect. The formwork was removed after 28 days to ensure full strength recovery and limit any cracks that might happen due to the handling and transporting the panel. Visual inspection results showed that the FRP side plates were well attached to the concrete. It was also noted that FRP was embedded inside the concrete for the most of the panel, which could improve the performance of the FRP shear connector to resist shear loads.

Test setup for the PVICS panel is shown in Figure 3.10 and Figure 3.13. Two actuators were fixed on an outer frame to subject the panel to three-point loading. The load was measured by two 50 kips (222.4 kN) load cells resting on 9in x 9in. (22.86 cm x 22.86 cm) plates. These plates were resting on smaller plates of 5 in x 5in (12.7 cm x 12.7 cm) to simulate point loads. Two deflection transducers were installed to measure the slab at the mid-span and 6 in. (15.24 cm) away from the mid-span, respectively. Eleven Strain gages were installed along the width of the panel in between the solar cells. Another three strain gages were installed 8 in. (20.32 cm) away from the mid-span on the other side, where one strain gage was installed at the mid-width and the other at each edge. To measure the slip, two strain gages were installed at the side as shown in Figure 3.12. The 120 ohm. strain gages, load cells and deflection transducers were all connected to a data acquisition system (HP 38552A) where the data was synchronized and exported for analysis.

Figure 3.12 Side strain gages location

Figure 3.13 PVICS panel under three-point loading

In order to validate the linear elastic analytical model, the PVICS panel was first modeled using FE model, where the cracking load was obtained. It was found that the cracking load is about 2500 lbf (11.12 kN). Therefore, the PVICS panel was loaded first under a load of 2000 lbf (8.89 kN) using a manual hydraulic jack which was connected to the two actuators as shown in Figure 3.13.

To investigate the performance of the solar cells, an additional frame was assembled using protruded aluminum sections (80/20 Inc.) to hold lamps and fans connections. 4 projection halogen lamps (Philips 13117) with 150 W were installed to provide enough illumination for the 16 solar cells, where 8 solar cells were installed during the manufacturing of the slab, while another 8 solar cells were attached afterwards with different bonding configuration as a part of another study. Only the 8 pre-attached solar cells will be discussed in this study to avoid duplication of results. Two 20 Amp Variac transformers were used to provide power for the 4 lamps due to the high amperage drawn by these lamps, 8 A per lamp. Solar irradiance was measured using digital solar

power meter (D. Meter SM206) which fell within the accepted range. To avoid any increase of the temperature, 6 fans were installed close to the lamps and held together using a aluminum plate as shown in Figure 3.14.

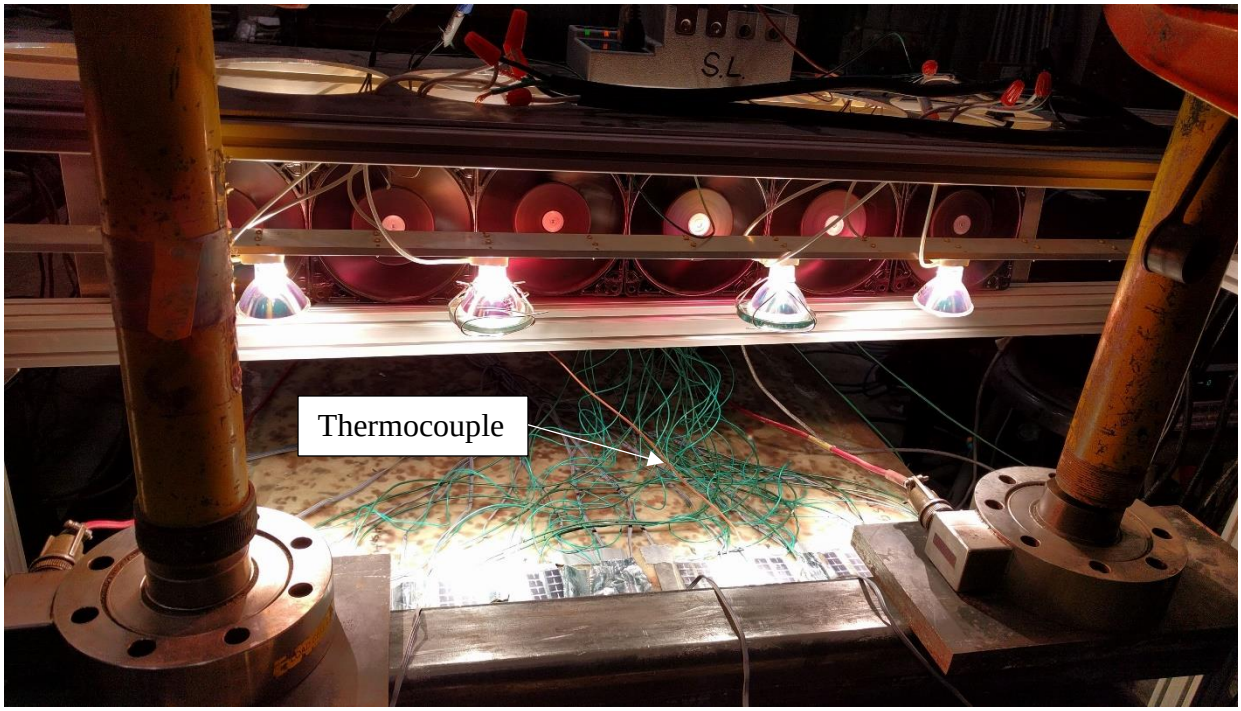

Figure 3.14 Nonlinear loading setup with installed lamps, fans and thermocouple

Each solar cell was connected to a terminal that was connected to an analog multiplexer (Texas Instruments CD74HC4067). The multiplexer chip was connected to National Instruments I/O module (NI-9403) installed in a chassis (NI cDAQ-9174). The multiplexer was used to switch between different solar cells which can be controlled by I/O module connected to LabVIEW code through the chassis. Each time the multiplexer received a signal from a solar cell, it directed it to Keithley 2400 SourceMeter, where J-V curves were measured and exported using the same LabVIEW code.

To avoid the temperature generated from the lamps, a 0.25 in. thick temperature glass was imported from the Kodak carsoul projectors and placed directly under the lamp. The temperature

was measured using a thermocouple (orange wire in Figure 15) placed under the second lamp. The thermocouple probe is connected to an NI-9214 module (0.25° C accuracy) which is installed in the chassis (NI cDAQ-9174) and controlled via LabVIEW code as well. Figure 3.15 shows a flow chart for the connection details for measuring multiple solar cell readings.

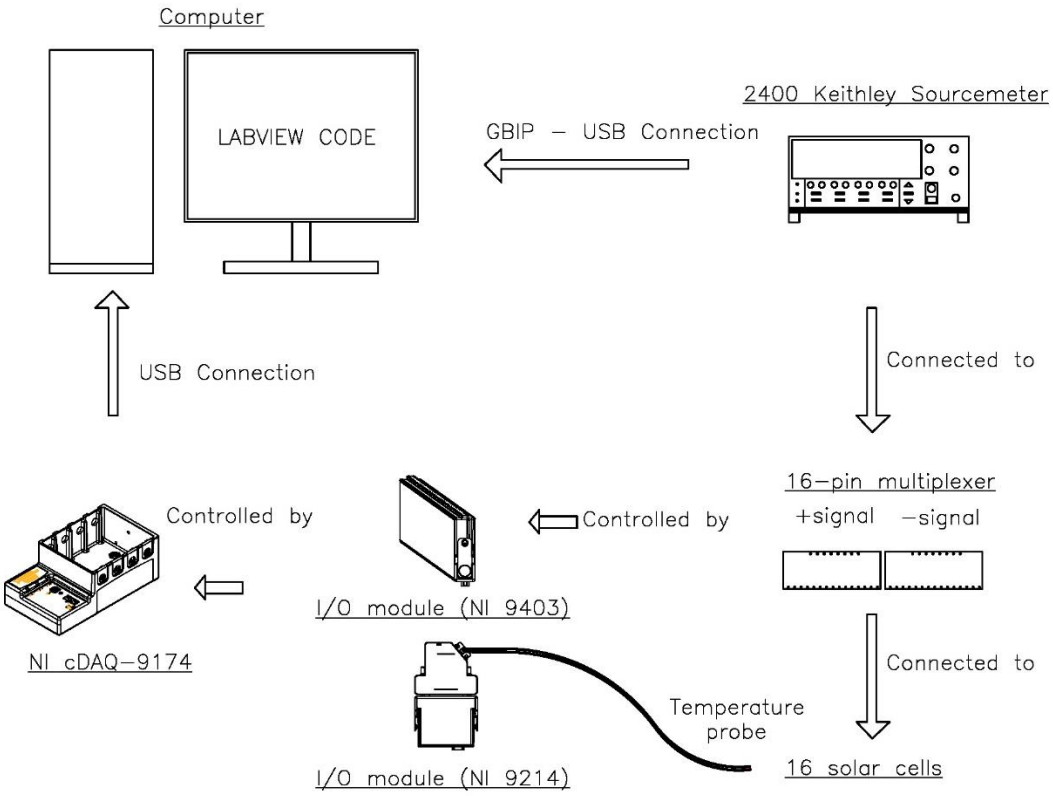

Figure 3.15 Multiple solar cell and temperature data acquisition setup

Recording of the results went through several steps; first, strain, deflection and load data acquisition was turned on to start recording results. Then, initial readings were recorded for the solar cells and temperature without turning on the lights. After that, the lights were turned on and multiple readings of the temperature and solar cell readings were captured to obtain the behaviour of the solar cells and strain gages under temperature. After around 15 min. the strain gages readings were almost steady which indicates that the effect of the temperature has become saturated. The

strain gages, deflection transducers and load cells readings were then zeroed to compensate for the temperature effect. Incremental loading was manually applied to the panel using hydraulic jack shown in Figure 3.16, where the solar cell and temperature were recorded at each increment. After the loading, the data was synchronized and analyzed as shown in the section 3.3.

Figure 3.16 Strain, deflection and load data acquisition setup along with manual hydraulic jack

1.1.7.2. Nonlinear stage

The panel was loaded again until failure to investigate the behaviour of the panel under nonlinear stage. The nonlinear setup is similar to the linear setup except for the loading part, where the two actuators were placed on the two plates where a 3 x 3 in beam with box section was placed underneath the plates. In order to avoid localized effect from the steel beam, a rubber mat was cut and placed in between the FRP and steel beam as shown Figure 3.14. The new setup will act as a distributed load to avoid any localized effect that can occur due to point loading.

3.3. Validation and Results

3.3.1. Linear stage

3.3.1.1. FE validation

To validate this panel, a 3D FE model shown in Figure 3.17 was modeled using ABAQUS (2013). Concrete wythes and insulation foam were modeled using solid elements (C3D8R), while longitudinal and transverse rebars were modeled as truss elements (T3D2) which were embedded inside the concrete wythes. FRP plates were created as shell elements (S4R) which were connected to each other and other parts using tie constraint. Loads were modeled as pressure loads on two surfaces at the edge where each surface is 5 in x 5 in (12.7 cm x 12.7 cm) to simulate the same loading conditions of the experimental test. The boundary conditions were set to pin and roller. Same material properties were used as previously listed in section 2.3.2. and Table 3.4. Figure 3.18 and Figure 3.19 show close correlation between the FE results and experimental results for strain and deflection results for linear region, respectively.

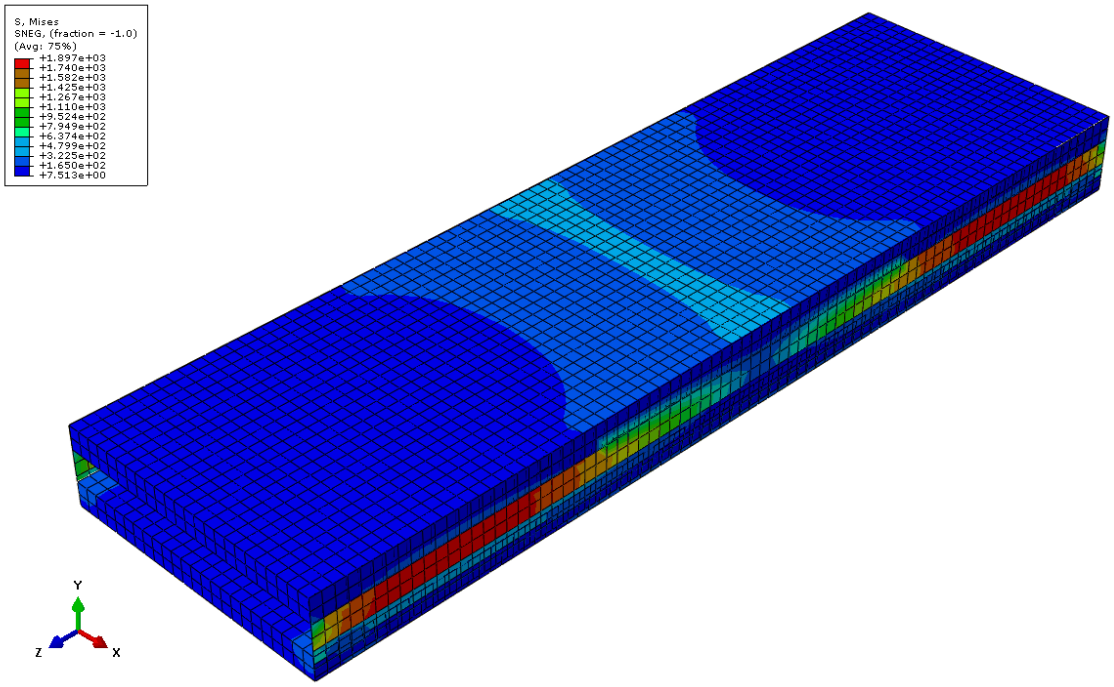

Figure 3.17 FE model (insulation foam is removed for clarification purpose)

Table 3.4 Material properties

Material	Concrete	Foam	Rebar	GFRP w Polymer aggregate
Young's Modulus (ksi)	4029	478.6	29000	5000
Poisson's Ratio (ν)	0.15	0.35	0.3	0.2
Density (pcf)	150	65	490	62.4

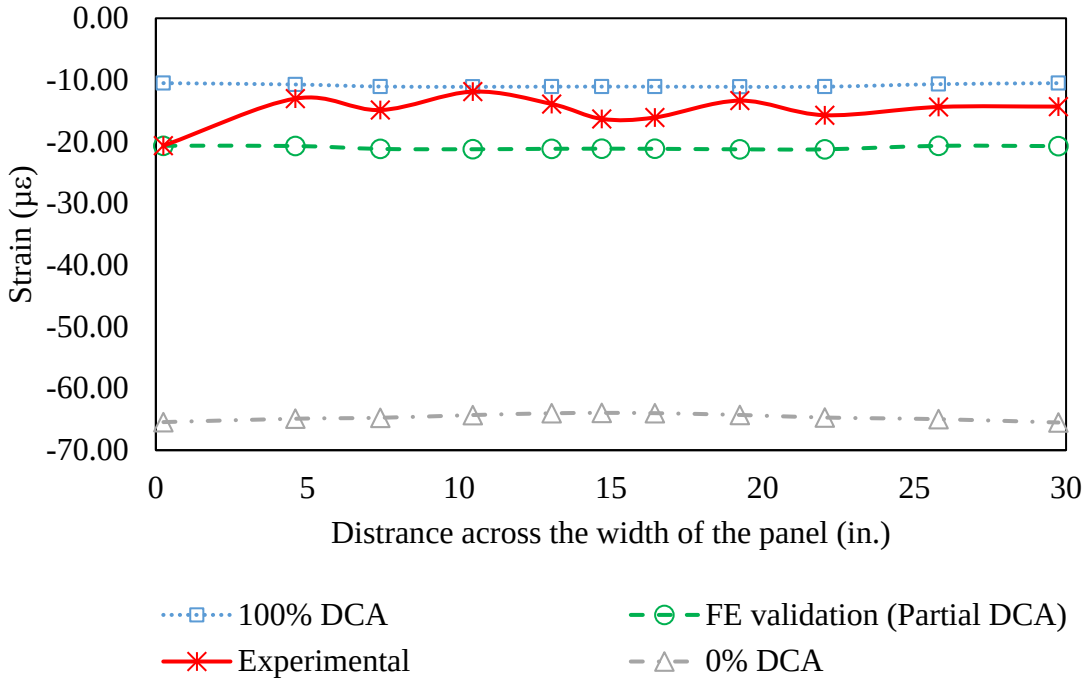

Figure 3.18 Correlation of strain across the width of the panel

To calculate the DCA for the panel, other FE models were modeled using connector elements (CONN3D2) with moment coupling to simulate different stiffness. The connector properties were set to rigid to simulate the panel with 100% DCA while the shear stiffness was assigned equal to zero to simulate the 0% DCA. The two results were compared with validated FE and experimental results as shown in Figure 3.19. To calculate the DCA was calculated as:

$$DCA(100\%) = \frac{\Delta_{noncomposite} - \Delta_{partial}}{\Delta_{noncomposite} - \Delta_{composite}} \times 100 \quad (27)$$

where $\Delta_{noncomposite}$, $\Delta_{composite}$, and $\Delta_{partial}$ represent displacement at a given load corresponding to 0%, 100%, and partial DCA, respectively. Deflection was interpolated at 1000 lb. (4448.22 N) load. It can be concluded that panel achieved a 82% DCA as shown in Table 3.5.

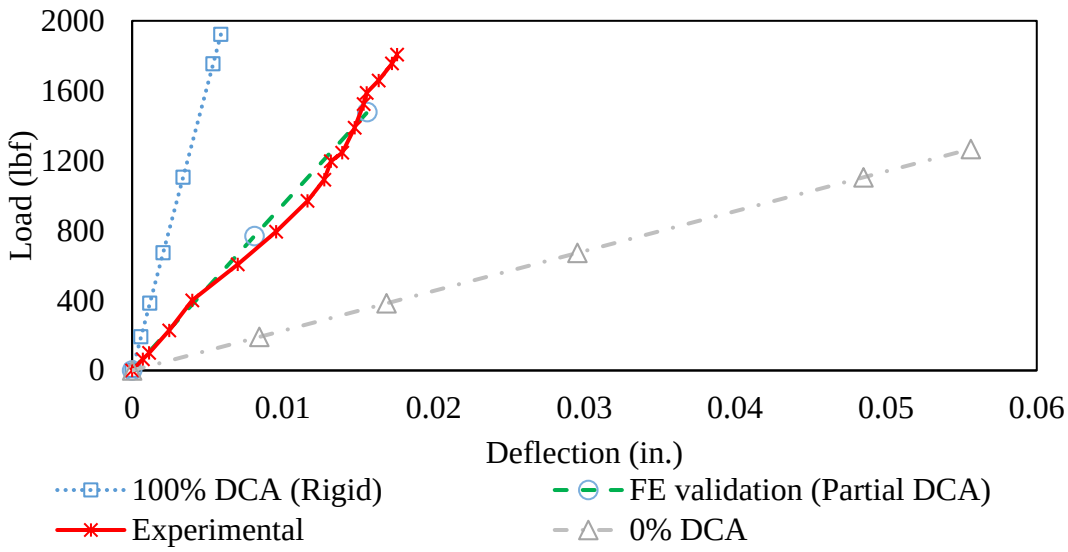

Figure 3.19 Correlation of mid-span deflection

Table 3.5 DCA calculation based on deflection method

Deflection (in.)				
Load	100% DCA	Partial	0% DCA	DCA
1000	0.00306333	0.01050388	0.043904	82%

Table 3.6 DCA calculation based on strain method

		0	1	2	3	5	5	7	8	9	10	x (Diff)
Strain (με)	100% DCA	10.1	9.00	6.68	5.53	2.17	-2.96	-5.83	-6.86	-8.86	-9.82	-5.14
	Partial DCA	17.2	12.4	3.07	-1.55	-15.2	13.55	0.77	-3.52	-12.3	-16.7	28.75
	0% DCA	37.0	18.4	-18.6	-37.2	-91.1	108.3	43.8	21.6	-22.7	-45.0	199.4
	DCA											86%

The DCA of the panel was evaluated using strain method as:

$$DCA = 1 - \frac{x}{x_{MAX}} \tag{28}$$

where x indicates the amount of the horizontal slip which can be calculated as shown in Table 3.6 and Figure 3.20. It can be concluded that good correlation was achieved between the FE and experimental results where DCA based on strain reached 86%.

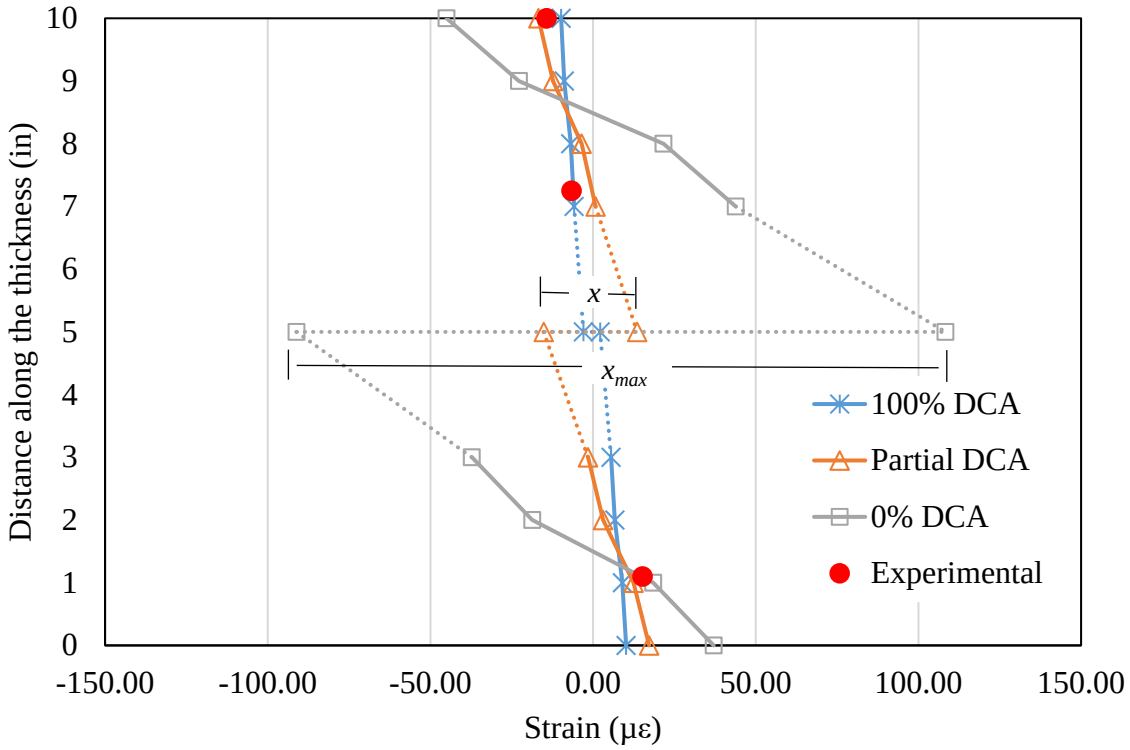

Figure 3.20 Strain across the thickness

3.3.1.2. Analytical model validation

An analytical model was developed to take into consideration the effective width based on partial degree of composite action. Based on the stiffness of the panel and other geometrical and mechanical properties, DCA can be calculated as

$$DCA = \frac{(\alpha_{11}^{(1)} + \alpha_{11}^{(2)})N_x(x,0) - 2\dfrac{F(x)(C')^2}{b[D_{11}^{(1)} + D_{11}^{(2)}]}}{\dfrac{[M(x)](C')}{b[D_{11}^{(1)} + D_{11}^{(2)}]}} \quad (29)$$

where α_{11}, b, D_{11} and C' are geometrical properties, while Nx is the stress across the wythe, $F(x)$ is the shear flow, $M(x)$ is the moment applied to the panel and subscripts 1 and 2 donate the upper and lower wythes, respectively. More details about the calculation of these parameters are presented in section 5.2.

Effective width b_{eff} can then be calculated for panel with two shear connectors as

$$b_{eff} = \frac{2 \cdot F'(x)}{N_x(x,b)} \tag{30}$$

where *F'(x)* can be expressed as:

$$F'(x) = \sum_{j=1}^{\infty} \frac{1}{\xi_j} (C_{1j} \sinh(\xi_j b) + C_{2j} \cosh(\xi_j b)) \sin(\frac{j\pi x}{a}) \tag{31}$$

The deflection $\Delta(x)$ can be calculated for a simply supported sandwich panel as:

$$\Delta(x) = (1 - DCA)\Delta_0(x) + DCA \times \Delta_{100}(x) \tag{32}$$

where Δ_0 and Δ_{100} are deflection of non-composite and full composite panels, respectively, and can be calculated as:

$$\Delta_0 = \frac{P \cdot a^3}{48 \cdot E \cdot I_{x0}}, \Delta_{100} = \frac{P \cdot a^3}{48 \cdot E \cdot I_{x100}} \tag{33}$$

where *P* is the applied load, *a* is the span, *E* is the equivalent Young's modulus and I_{x0} and I_{x100} are the second moment of inertia and can be calculated as:

$$I_{x0} = 2 \cdot b\left(\frac{t^3}{12}\right), I_{x100} = 2 \cdot \left[b_{eff}\left(\frac{t^3}{12}\right) + b_{eff} \cdot t \cdot \left(\frac{C'}{2}\right)\right] \tag{34}$$

where *t* is the wythe thickness, *b* is the panel width, *C'* is the distance between the centerline of the upper and lower wythes. Deflection was evaluated and compared with the experimental and FE model as shown in Figure 3.21.

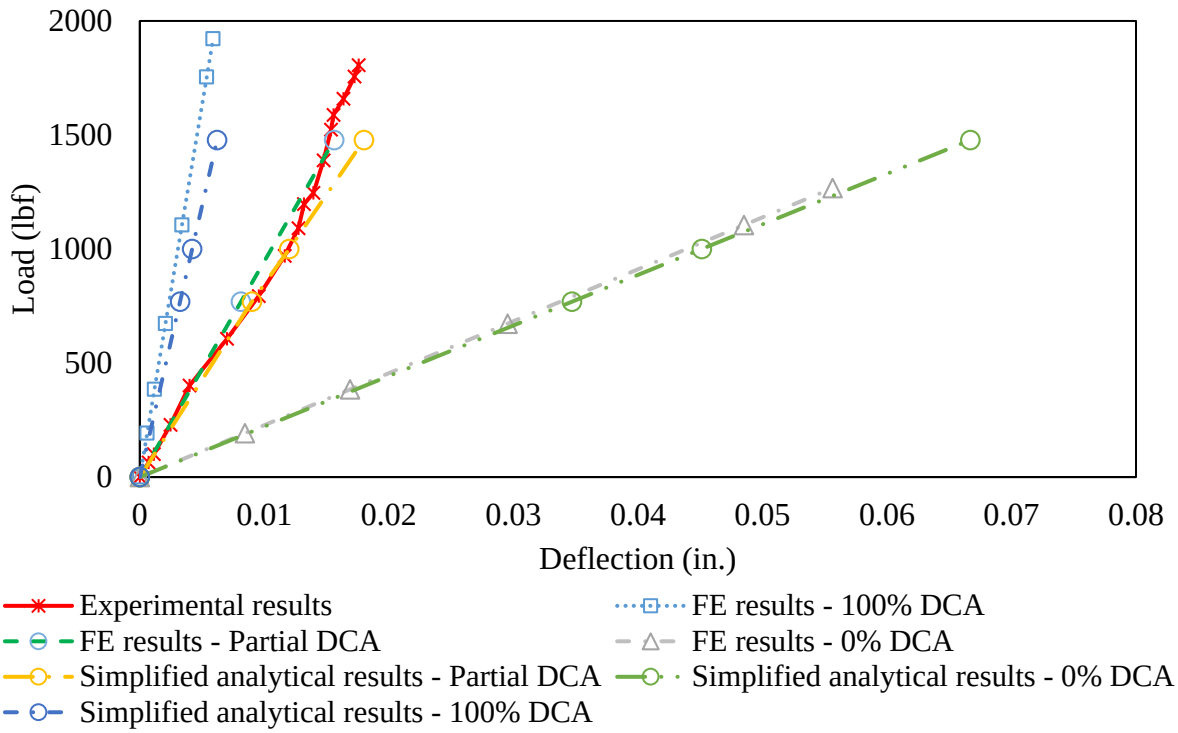

Figure 3.21 Validation of analytical results with experimental and FE results

3.3.1.3. Solar cell performance

The performance of the solar cells was evaluated under flexural loading while subjected to compression. Figure 3.22 shows the initial J-V curve for the to assess their performance before applying the load. It can be noted that the fifth solar cell is shunted or not operating which can occur due to manufacturing malfunction. Figure 3.23 shows a typical MPP and FF versus strain, where the performance of the strain remained constant. Therefore, it can be concluded that solar cells work properly under the service load.

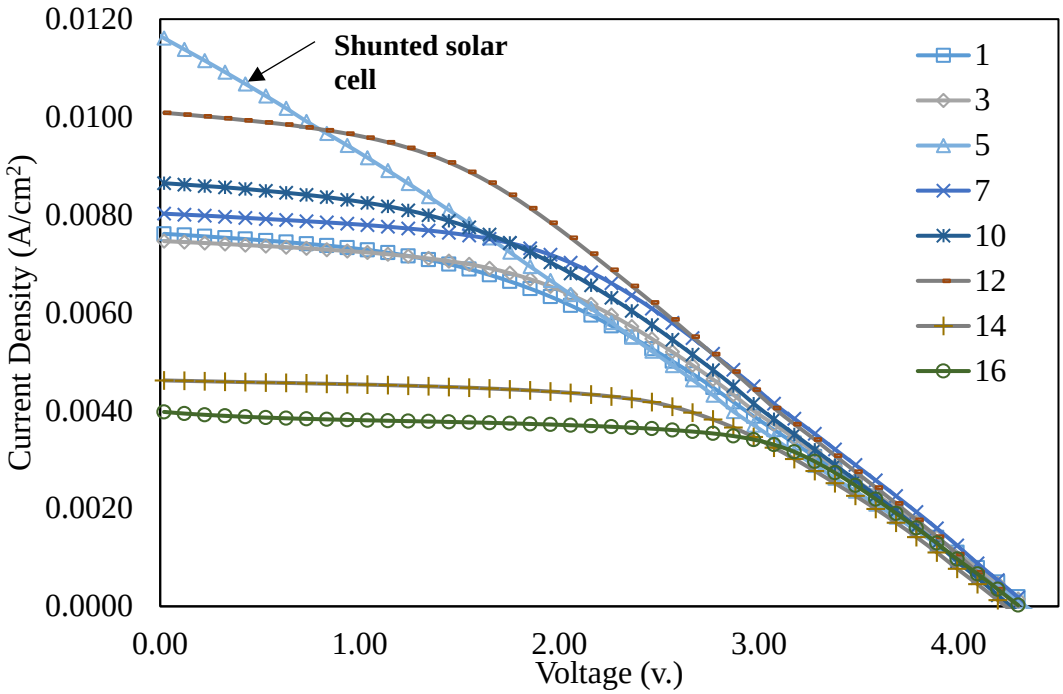

Figure 3.22 J-V curve before applying the load

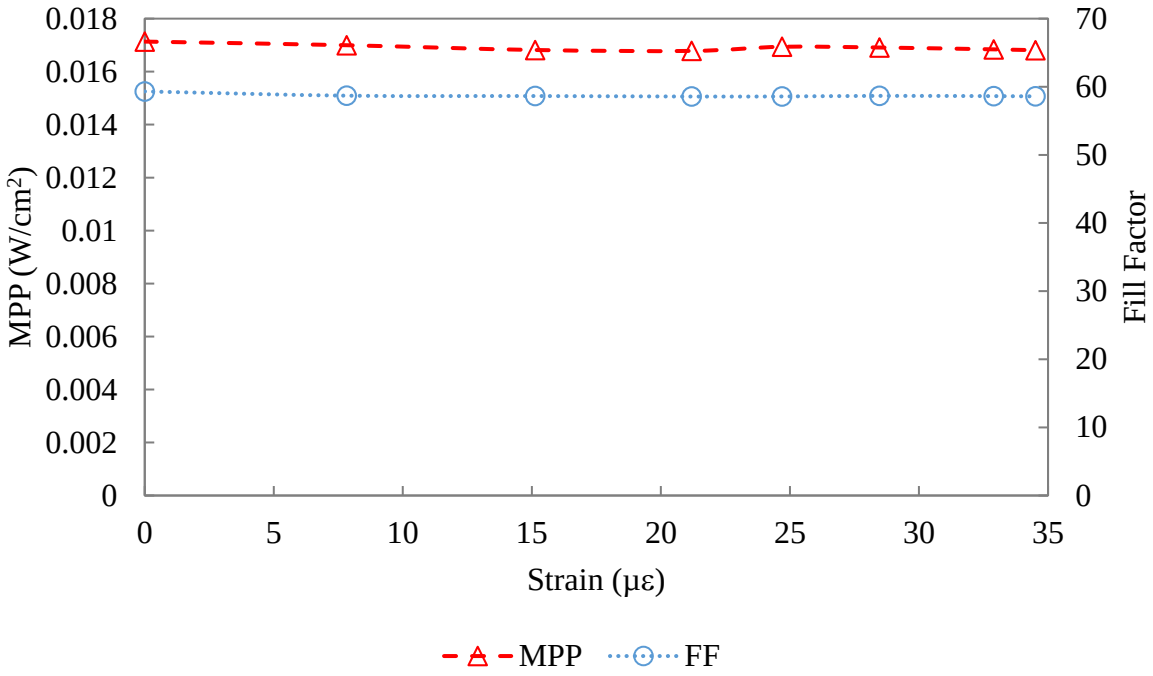

Figure 3.23 MPP and FF versus strain

3.3.1. Nonlinear stage

3.3.1.1. Structural performance

The main purpose of the nonlinear loading is first to identify the full capacity of the panel. The second purpose is to investigate the behaviour of the solar cells under high strain range. Figure 3.25 shows the load-deflection for the tested panel and FE results, where good correlation was achieved until FRP-concrete bond failure. The panel was first loaded through linear range up to 4 kips where cracking sound was heard at the interface between the shear connectors and concrete. The FRP shear connectors started to buckle at the southwest side first, right above the support where maximum shear occurs as shown in Figure 3.26 (a). Followed by buckling of the southeast side and then both sides started to debond until they reached near mid-span from the south side as shown in Figure 3.26 (b). Ultimate load was then achieved at 14.8 kips where sudden fracture of the FRP on the sides occurred as shown in Figure 3.26 (c) and transverse crack appeared at the bottom of the panel. As the loading continues, the deflection increased rapidly and the crack width shown in Figure 3.27 increased. The slip between the upper and lower wythes was clearly noticed at the south side of the panel, as the north side was not affected by the loading as shown in Figure 3.27, which indicates that panel acts as 0% after the FRP shear connector failure. It should be noted that FE results are based on perfect bonding due to the lack of traction-separation curve for FRP-concrete bond. Additional consideration, such as removing upper steel mesh, is needed for the design the panel as the panel failed before the concrete reached 3000 με.

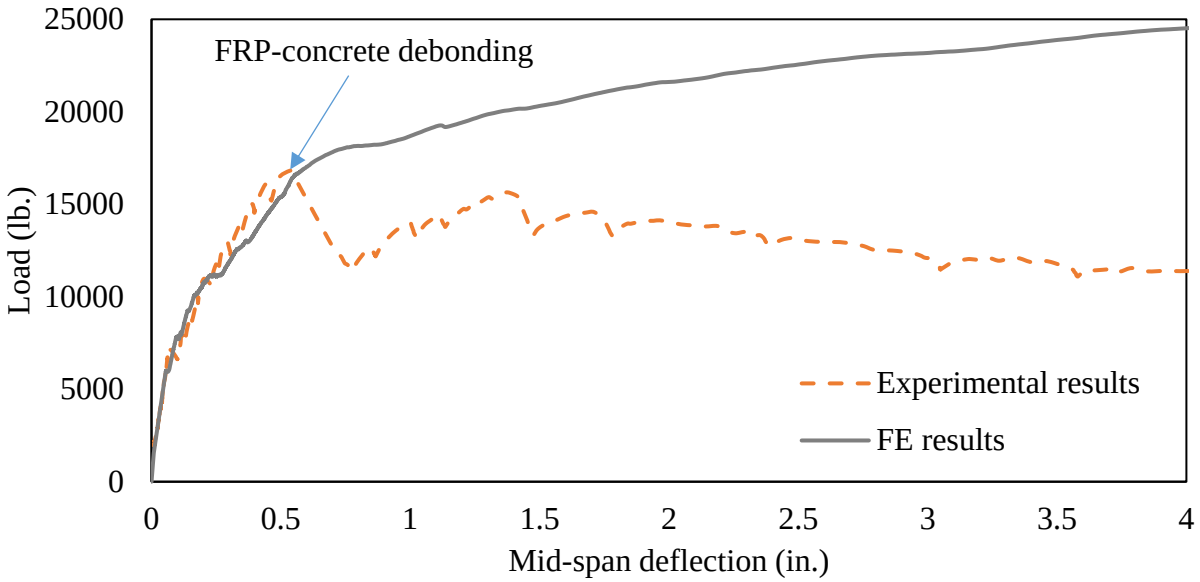

Figure 3.24 Load-displacement curve for experimental test and FE model

(a) (b) (c)

Figure 3.25 FRP shear connector failure; (a) Southwest side buckling, (b) debonding of shear connector at the southwest side, (c) Failure of shear connector at mid-span

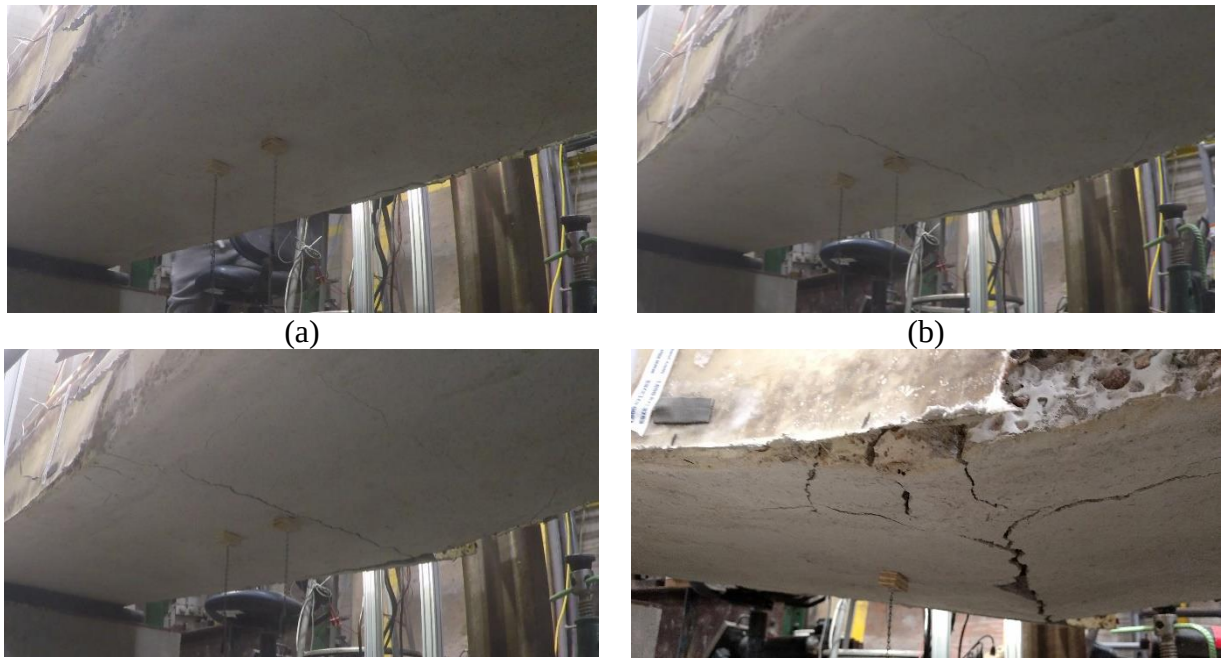

(a) (b)

(c) (d)

Figure 3.26 Progress of Cracks on the lower wythe

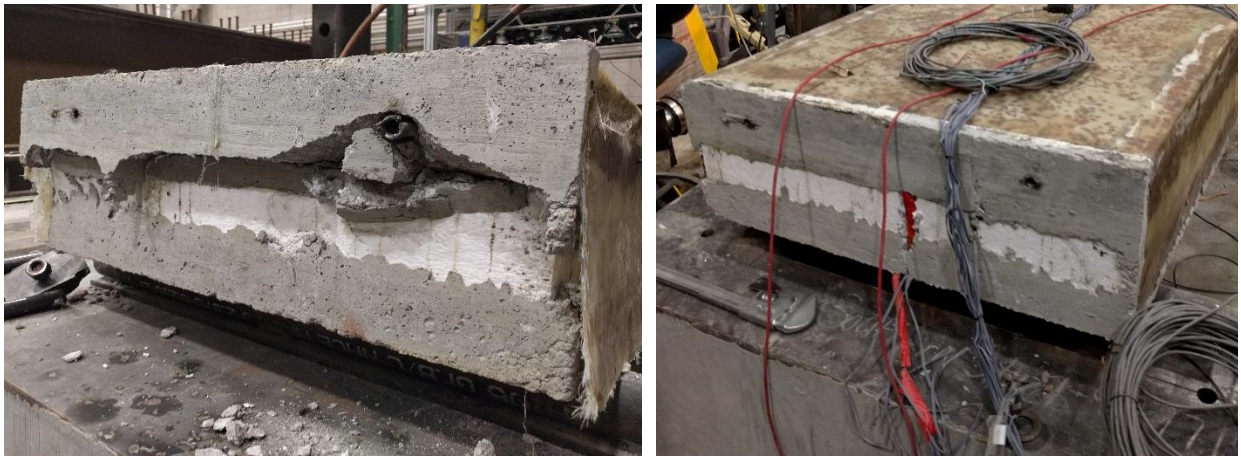

(a) (b)

Figure 3.27 (a) Slip at the end of the south side, (b) No slip is detected at the north side

The recorded strain at 6 in north the mid-span is plotted at different loading until failure as shown in Figure 3.29. The strain results illustrate the shear lag effect induced due to the shear connectors. Another strain values were recorded at 8 in south the mid-span as presented in Figure 3.30. Strain values were not symmetric due to localized manufacturing defect at the east side where

the FRP top plate was stiff enough at the east side to be subjected to wrinkling effect as the rest of the panel as shown in Figure 3.28, which mainly happened after the FRP shear connector broke at the mid-span.

(a) (b)

Figure 3.28 Wrinkling of the top FRP, (a) view for east side and from the (b) west side

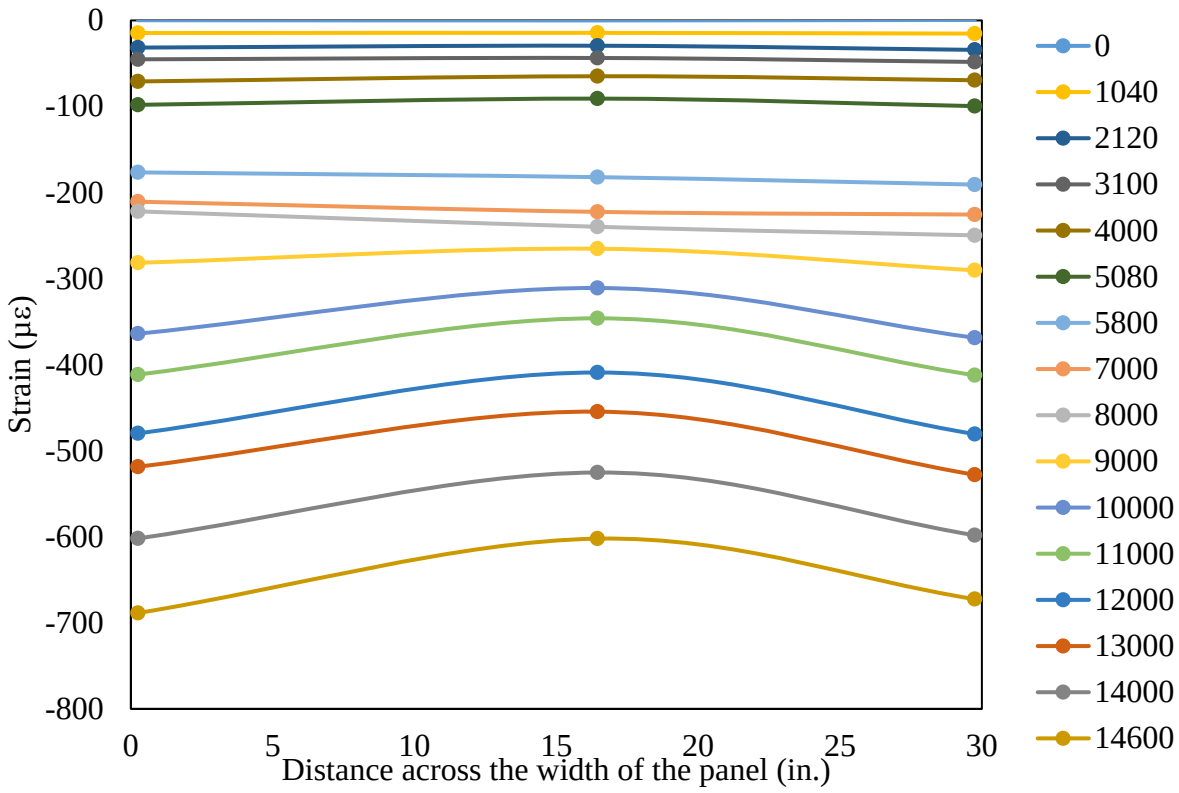

Figure 3.29 Strain distribution at 6 in away north mid-span at different loads

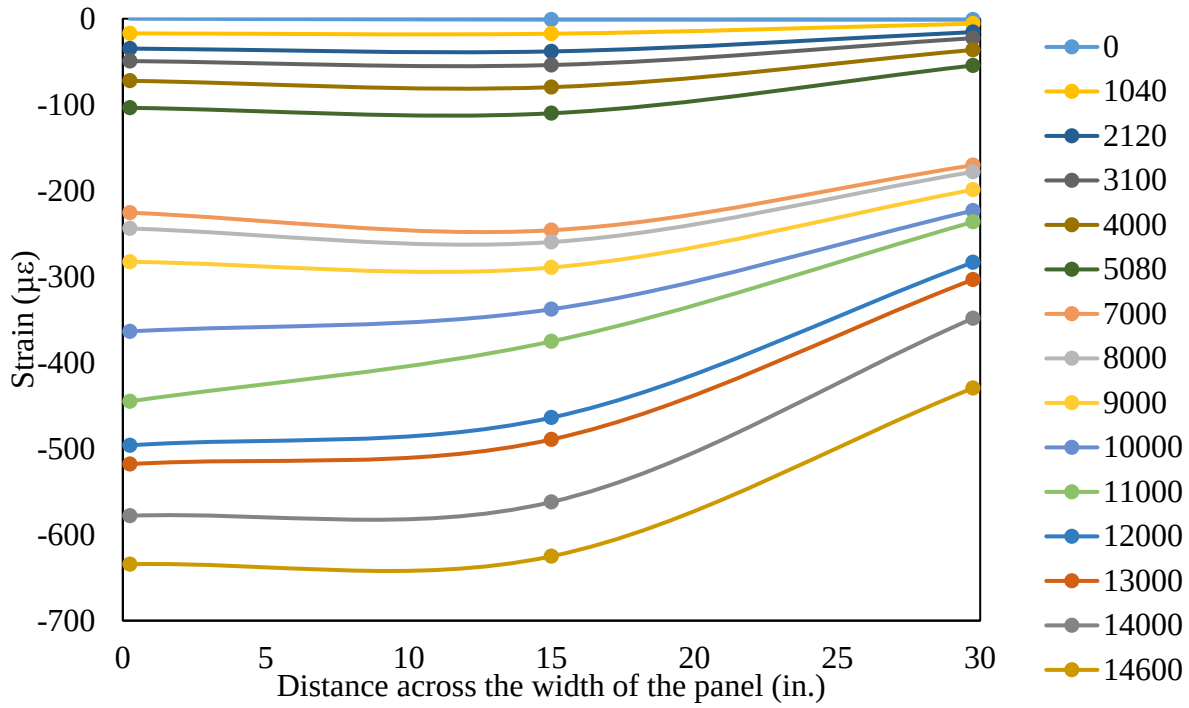

Figure 3.30 Strain distribution at 8 in away south the mid-span at different loads

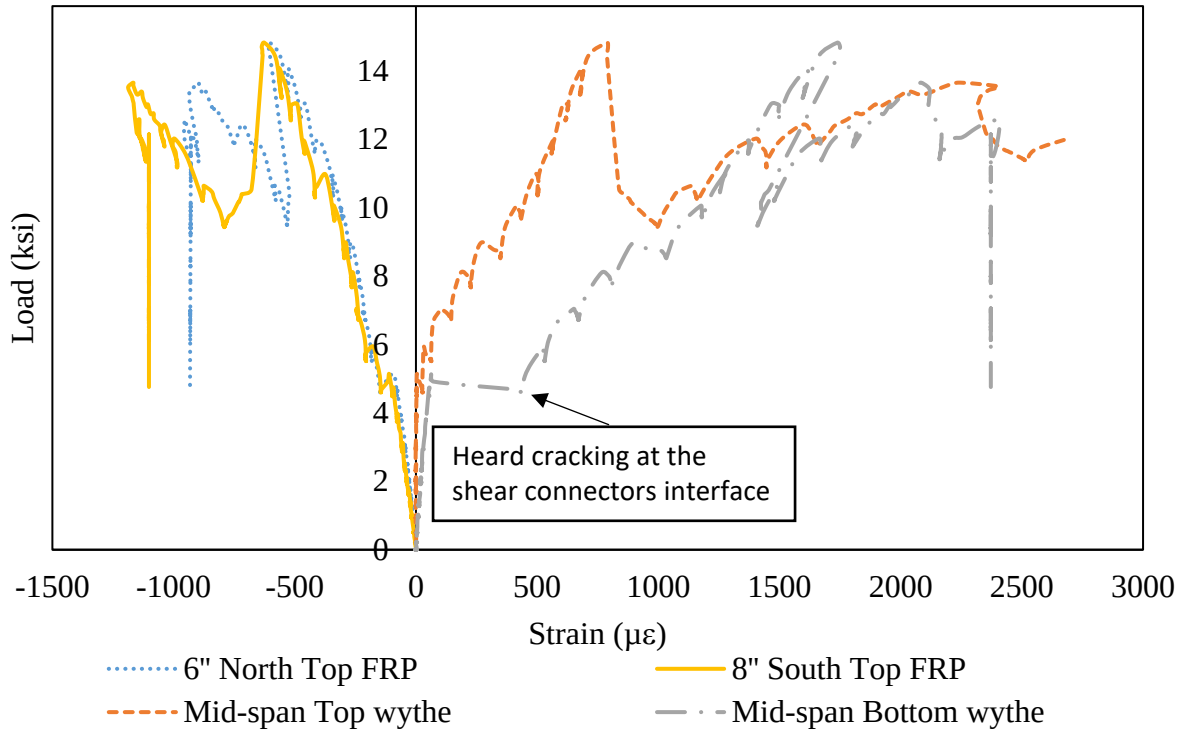

Figure 3.31 Strain at mid-width vs. load

Figure 3.31 shows the strain at the mid-width of the panel at different positions. The strain in the longitudinal rebar went through a sudden slip around 4.9 kips, this happened due to cracking of the concrete under tension close to the shear connectors, which resulted in loss of the bond between the FRP and concrete. The figure also shows that before this point, the strain in the top wythe rebar was around zero, which indicates that the panel was achieving high composite action. However, after the cracking point, the strain undergoes tension values which indicates that the panel was acting as noncomposite or as a low composite action panel.

3.4. Conclusions

An innovative multifunctional sandwich panel was developed which can act as both active and passive energy system. Throughout this study, several conclusions can be drawn as listed:

1. Solar cells worked properly under the service load.
2. The panel had enough strength and stiffness, with 82% DCA.
3. The concept of PVICS was proven based on the findings from (1) and (2).
4. Shear-lag was observed, which needs further investigation, as will be presented in Chapter 5.
5. Further study needs to be conducted on the strain effect on the performance of solar cells, since solar cells become a part of the structure. This topic will be further studied in Chapter 4.

To fully utilize the multifunctional purpose of the panel, several recommendations are advised:

1. Ensure good bond between FRP and concrete, which can be achieved through increasing the FRP embedded area inside the concrete from the sides.
2. To increase the strength of the shear connectors, more layer can be added or bidirectional FRP can be used at the sides.

3. As the top FRP and confinement effect can provide extra strength for the panel, it is advised to reduce the top steel reinforcement. This can also subject the solar cell placed at the top of the panel to extra strain which can assist in detecting cracks. More details will be discussed in chapter 4.

3.5. References

ABAQUS. (2013). "ABAQUS Documentation." Dassault Systèmes, Providence, RI, USA.

ACI. (2014). *Building Code Requirements for Structural Concrete (ACI 318-14) and Commentary (ACI 318R-14). ACI 318-14*.

Benayoune, A., Abdul Samad, A. A., Trikha, D. N., Abang Ali, A. A., and Ellinna, S. H. M. (2008). "Flexural behaviour of pre-cast concrete sandwich composite panel - Experimental and theoretical investigations." *Construction and Building Materials*, 22(4), 580–592.

Bush, T. D., and Wu, Z. (1998). "Flexural analysis of prestressed concrete sandwich panels with truss connectors." *PCI journal*, Precast/Prestressed Concrete Institute, 43(5), 76–86.

Chen, A., Norris, T. G., Hopkins, P. M., and Yossef, M. (2015). "Experimental investigation and finite element analysis of flexural behavior of insulated concrete sandwich panels with FRP plate shear connectors." *Engineering Structures*, 98, 95–108.

Cho, J.-R., Cho, K., Park, S. Y., Kim, S. T., and Kim, B.-S. (2010). "Bond characteristics of coarse sand coated interface between stay-in-place fibre-reinforced polymer formwork and concrete based on shear and tension tests." *Canadian Journal of Civil Engineering*, 37, 706–718.

Einea, A., Salmon, D. C., Fogarasi, G. J., Culp, T. D., and Tadros, M. K. (1991). "State-of-the-Art of Precast Concrete Sandwich Panels." *PCI Journal*, 36(6), 78–98.

Einea, A., Salmon, D. C., Tadros, M. K., and Culp, T. (1994). "A New Structurally and Thermally Efficient Precast Sandwich Panel System." *PCI Journal (Precast/Prestressed Concrete Institute)*, 39(4), 90–101.

Frankl, B. A., Lucier, G. W., Hassan, T. K., and Rizkalla, S. H. (2011). "Behavior of precast, prestressed concrete sandwich wall panels reinforced with CFRP shear grid." *PCI journal*, Precast/Prestressed Concrete Institute, 56(2), 42–54.

Henin, Eliya Morcous, George Tadros, M. K. (2011). "Precast concrete sandwich panels for floor and roof applications." *PCI/NBC*, Intergovernmental Panel on Climate Change, ed., Cambridge University Press, Cambridge, 1–30.

Norris, T. G., and Chen, A. (2016). "Development of insulated FRP-confined Precast Concrete Sandwich panel with side and top confining plates and dry bond." *Composite Structures*, Elsevier Ltd, 152, 444–454.

Sugar, J. G. (2007). "Photovoltaic Performance of Amorphous Silicon Flexible Solar Modules Under Mechanical Loading." UCLA.

CHAPTER 4. STRAIN EFFECT ON THE PERFORMANCE OF AMORPHOUS SILICON AND PEROVSKITE SOLAR CELLS

A paper to be submitted to Solar Energy Journal

An Chen[1], Mostafa Yossef[2], Kai Zhu[3], Chao Zhao[3]

Abstract

Clean, plentiful, and easy-to-harvest solar energy is the ultimate renewable energy. It is becoming more important as the world begins to take notice of the burgeoning carbon emission problems that come with burning fossil fuels. Thin-film solar cells have been increasingly used for energy harvesting. This paper studies the strain effect on the performances of amorphous silicon (a-Si) and perovskite solar cells. To this end, compression and tension tests were conducted on a-Si solar cells bonded to Fiber-Reinforced Polymer (FRP) plates and tension tests were carried out on perovskite solar cells attached to glass substrate. A projector was used to illuminate the cells during the tests to simulate 100% sun. J-V characteristic curves were measured at different strains until the samples failed. It can be concluded that there are strain thresholds for both compression and tension for a-Si solar cells, which worked properly below the thresholds but degraded rapidly once the thresholds were passed. Perovskite solar cells are more ductile, which can withstand a strain of 3%. No degradation of the performance was observed before the substrate failed.

[1] Major Professor
[2] Main Contributor
[3] Provided Perovskite samples and facilitated testing at NREL

4.1. Introduction

The solar power industry has gained global interest in the last few decades. Being one of the renewable sources of energy, it is becoming a primary source of energy considering limited resources for fossil fuel. As a result, solar cells have been increasingly used in different applications, including space stations, solar cars, military camps, buildings, and solar farms.

Nowadays, silicon-based solar cells are the most widely used solar cells that are commercially available. However, their relatively high cost is an obstacle for the solar industry to become a dominant source of energy. Current research is focused on reducing the cost by using relatively cheap materials such as organic and inorganic-organic (hybrid) solar cells, e.g., perovskite solar cells. Recently, perovskite solar cells have achieved an efficiency of about 22%, compared to around 14% for a-Si solar cells (NREL, 2017).

Ongoing research at Iowa State University is focused on attaching the solar cells directly to supporting structures, which can reduce the cost due to the elimination of the mounting structures and provide an aesthetic view. In order for the solar cells to work properly when attached to supporting structure, their performance under strain effect needs to be evaluated, since the supporting structures are subjected to different strain states from the loads they are taking, including dead, live, wind, seismic loads, etc.

The research on the performance of solar cells could date back when large-area electronics (LAE) were introduced. LAE can be solar cells, displays, X-ray sensors that are flexible and non-breakable. Early research studied the performance of LAE when subjected to bending strains. The objective was to develop LAE that were flexible enough to be mounted on roofs, tents, and wrapped around the fingertip [Gleskova and Wagner (1999); Suo et al. (1999); Theiss and Wagner

(1996); Utsunomiya and Yoshida (1989)]. It was concluded that amorphous silicon (a-Si) solar cells could achieve high flexibility and performed well under bending. Other solar cells were also developed to provide flexibility, such as Cadmium telluride (CdTe) and Copper indium gallium diselenide (CIGS). These solar cells are known as "thin-film solar cells" [Aberle (2009); Chopra et al. (2004)].

It was not until mid-2000's that a-Si solar cells could be manufactured for commercial use. Since then, several studies were focused on integrating solar cells as a part of the structural system. Among others, Keller et al. (2010) investigated the thermal and mechanical behavior of small-scale sandwich specimen with two types of silicon-based solar cells. They concluded that exposure to artificial sunlight increased the temperature of the solar cells to almost the glass transition temperature of the resin used for encapsulation. The results showed that polycrystalline solar cells encounter higher temperature than thin-film silicon solar cells. Bending test was performed to simulate walking loads. Polycrystalline silicon experienced an early brittle failure. Pascual et al. (2014) encapsulated a-Si solar cells into Glass Fiber Reinforced Polymer (GFRP) using hand lay-up and vacuum method. Light transmittance and solar radiation were measured, and they concluded that 83% of solar irradiance in the band of 300-800 nm reached the solar cell surface. Sugar et al. (2007) conducted tension tests on solar cells, measured their performances, and plotted the relationships between the Maximum Power Point (MPP), Fill Factor (FF) and the strain. Additional cyclic loading tests were performed on the same type of solar cells. It was concluded that the MPP and FF decreased with the increase of the applied load (Sugar 2007). Maung et al. (2010) attached solar cells to Carbon FRP (CFRP) and tested them under cyclic loading. They found that a slight degradation of solar cells was recorded after 0.3% strain and a significant

degradation was observed at 1% strain when subjected to a cyclic loading up to 100 cycles. Kim and Cheong (2014) performed a parametric study on the adhesive material used to bond monocrystalline silicon solar cells to composite plates, including ethylene vinyl acetate (EVA), resin, and elastic adhesion. They found that the elastic adhesion was suitable for maintaining the electrical performance of the solar module regardless of the loading. Fan et al. (2015) investigated the mechanical and electrical performances of organic photovoltaic (OPV) with two different substrates: Ethylene tetrafluoroethylene (ETFE) and Polyethylene terephthalate (PET). OPV is a multilayer photovoltaic composite which is known for fabrication easiness, low cost and flexibility to be integrated into structures. They found that adding Ag layer to the poly-3-hexyl thiophene (PEDOT) could maintain higher conductance than Ag layer. However, rapid drop in conductance was observed at a strain higher than 25%.

Although the aforementioned studies evaluated the performances of solar cells, they were focused either on tension or cyclic loadings for a-Si solar cells. Therefore, there is a need to investigate the performance of the solar cells, including both a-Si and perovskite solar cells, under other loading types, such as compression. In addition, solar cells were attached to CFRP in most of those studies due to their target applications. GFRP is more commonly used for building applications. Therefore, this research will evaluate the performances of a-Si solar cells attached to GFRP under both compression and tension. Tension tests were conducted on perovskite solar cells with glass substrate, since GFRP has chemical reaction with perovskite solar cells. The a-Si solar cells represent a commercially available thin-film solar cells, as the perovskite solar cell represents novel solar cells under development.

4.2. Experimental Program

4.2.1. Testing plan

The experimental program consisted of compression and tension tests of a-Si solar cells attached to GFRP plates and tension tests of perovskite solar cells on glass substrate, with five sample for each type of the test.

4.2.2. Materials

Chopped Stand Mat (CSM) and 404 isophthalic resin were used to manufacture FRP plates, with material properties listed in Table 4.1. Mechanical and electrical properties are only available for a-Si (SP3-12) as shown in Table 4.2 and Table 4.3 as its commercially available.

Table 4.1 Material properties

	Type	Tensile Strength (MPa)	Tensile Modulus (GPa)	Compressive Strength (MPa)	Density (gm/cm^3)
Resin	404 Isophthalic Resin	503.3	36.5	82.73	1.1
E-Glass Fiber	Chopped Strand Mat	2000	72.4	--	2.56

Table 4.2 Mechanical properties of solar module

Solar Module Type	Thickness (mm)	Length (mm)	Width (mm)	Aperture Size (mm)	Weight (g)
SP3-12	0.19	63.5	12.7	50.8 x 12.7	0.34

Table 4.3 Electrical properties of solar module

Solar Module Type	Wattage (W)	Voltage (V)	Open-Circuit Voltage (V)	Current (mA)	Short-Circuit Current (mA)
SP3-12	0.0255	3.0	4.5	8.5	10.7

4.2.3. Sample fabrication

4.2.3.1. A-Si Solar Cells Attached To FRP Plate

The samples were cast using vacuum bagging. First, a layer of polyethylene bag film was placed, followed by a breather cloth and a nylon release peel ply. A double-sided polyimide tape was used to bond the faces of the solar cells to the peel ply and protect the solar collector area from the epoxy. Next, layers of 101.7 kg/m^2 CSM were placed and the proper amount of resin was added.

The FRP plate manufactured was 304.8 x 304.8 mm^2 and placed on an aluminum plate. Isophthalic resin was added according to a fiber volume fraction (v_f) of 0.1877, similar to the FRP used in Chen and Davalos (2010) and Petersen et al. (2015). A 5% MEKP hardener was added to the resin. Resin and MEKP were carefully mixed to avoid any air bubbles formed inside the mix. The resin was spread over the FRP and divided evenly using an aluminum roller to eliminate air bubbles. The CSM was taped at the ends with perfect line tape (fibreglast), as shown in Figure 4.2, to act as a dam which prevented the resin from getting outside the CSM area and stopped the fibers from wrapping around the roller.

Next, the FRP layer was pressed down using an aluminum roller to eliminate the air trapped within the resin. A relatively large roller was used to prevent the fibers from wrapping around the roller during the manufacturing process. The process of adding the resin and CSM layer was repeated until the required thickness was achieved. Compression samples were 12 mm thick and tension samples were 6.35 mm thick. The breather cloth and the nylon peel ply were then folded around the FRP plate. Next, a polyethylene film was taped to both sides of the aluminum plate to seal the bag. The aluminum plate was 762 mm wide by 762 mm long and 63.5 mm thick with a hole in the middle, which was connected to a vacuum pump (fibreglast). The FRP was left to cure for 24

hours, and then the vacuum bag was opened and the FRP was removed. Figure 4.1 shows the manufacturing processes of the FRP plate with solar cells.

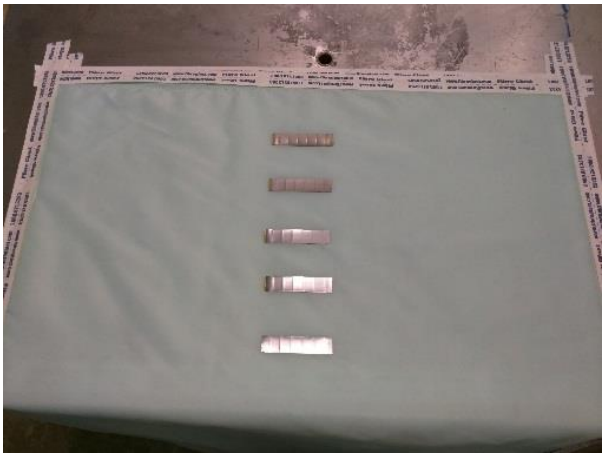

(a)

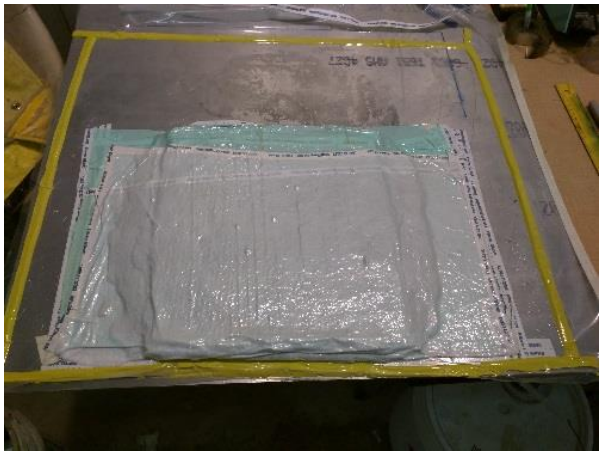

(b)

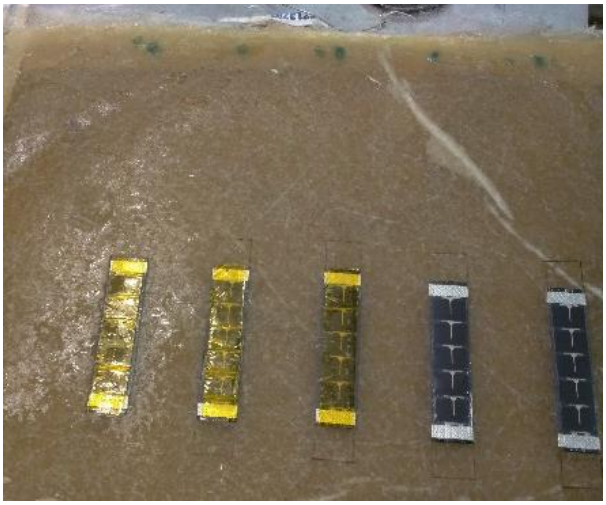

(c)

(d)

(e)

(f)

Figure 4.1 Sample preparation process (a) solar modules attached to peel ply, (b) sealed bag during curing process, (c) solar module attached to FRP plate, (d) Cutting compression samples, (e) Soldering wires to tension samples, (f) installing strain gages

4.2.3.2. Perovskite Solar Cells Attached To Glass Substrate

The other set of samples were fabricated to test perovskite solar cells which were provided by National Renewable Energy Laboratory (NREL). Perovskite solar cells were formed over rigid glass substrate instead of FRP because the chemical reaction can be formed between FRP surface and perovskite layer. Glass samples were chosen to be 100 mm long by 12.7 mm width so it could fit to the spinning machine. In order to connect wires to the perovskite solar cells, contact between perovskite and silver paint (Ted Pella, Inc.) was first examined which indicated no chemical reaction occurred, then the silver paint was used to bond wires for J-V measurements during loading, as shown in Figure 4.4.

Figure 4.2 Taped CSM

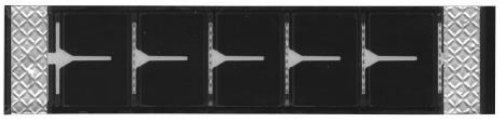

Figure 4.3 A-Si solar module SP3-12

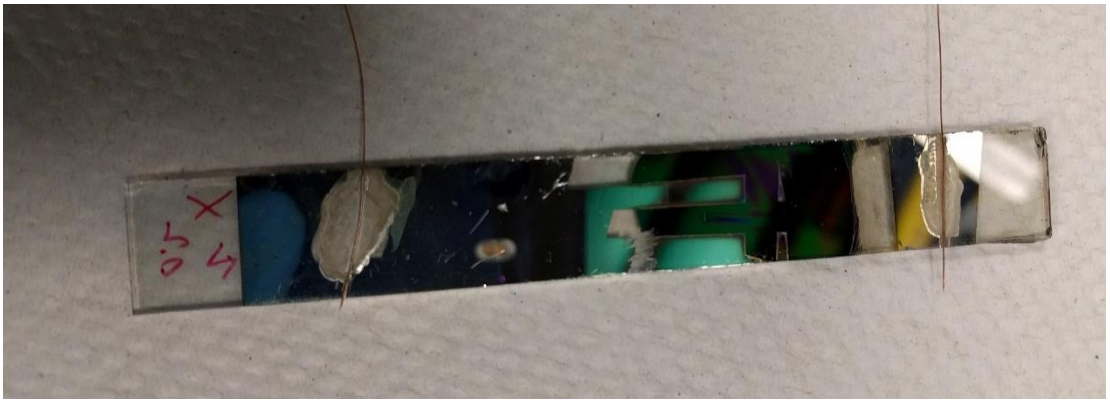

Figure 4.4 Perovskite solar connected to wires using fast drying silver paste

4.2.4. Sample details

For a-Si solar cells, compression samples were cut into 89 x 25.4 mm^2, as can be seen in Figure 4.5. Tension samples were 25.4 x 254 mm^2, where the middle 101.6 mm was narrowed down to 15.2 mm, as shown in Figure 4.6, according to ASTM D 638-12. SP3-12 solar modules were used to fit into compression and tension samples, as shown in Figure 4.5 and Figure 4.6, respectively. As for perovskite solar cells, samples were tested under tension without any modification as shown in Figure 4.4.

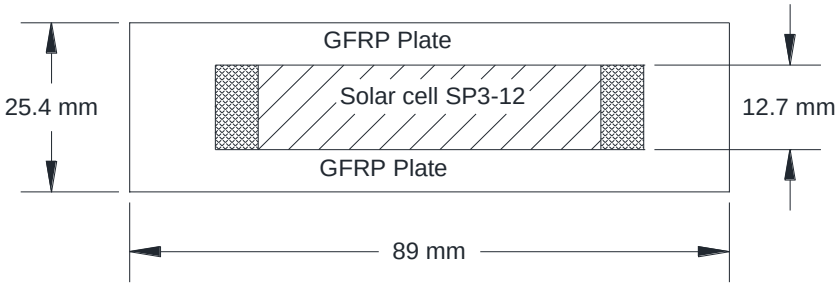

Figure 4.5 Compression sample dimensions

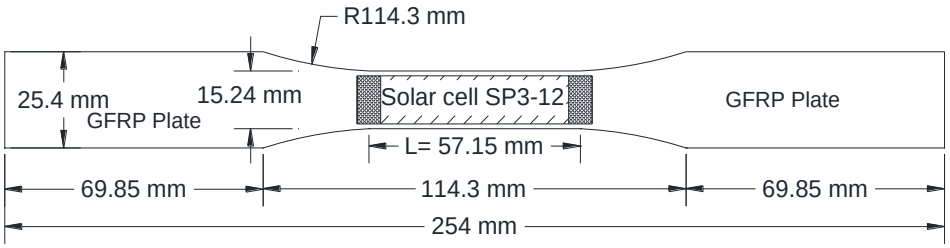

Figure 4.6 Tension sample dimensions

(a) (b) (c)

Figure 4.7 Keithley SourceMeter 2400 (a) connecting 4 test lead at the front, (b) GPIB-USB cable connected at the back, (c) connecting test lead to the sample wires

4.2.5. Testing setup

A-Si solar cell samples were tested using an MTS machine at ISU while perovskite solar cell samples were tested using an Instron machine at NREL. Loading rate was 5.08 mm/min for all the tests. The MTS machine was used to record the load and displacement and a Data Acquisition

System (DAS) was used to record the strain. The two sets of data were then synchronized and exported for data processing. Strain gages were installed on all the five samples for a-Si solar cell tests. For compression, a strain gage was placed at the middle. For tension, a strain gage was placed at the mid-span as shown in Figure 4.1(f). Instron machine provided load, displacement and strain. Therefore, no strain gage was needed for perovskite solar cell samples.

Keithley 2400 SourceMeter as shown in Figure 4.7 was connected to the solar module through a 4-wire connection to measure the solar cell's J-V characteristics and eliminate the lead resistance that could affect the measurement accuracy. A LabVIEW program created by Elshobaki (2015) was used to run and export J-V curves and other data, as shown in Figure 4.8.

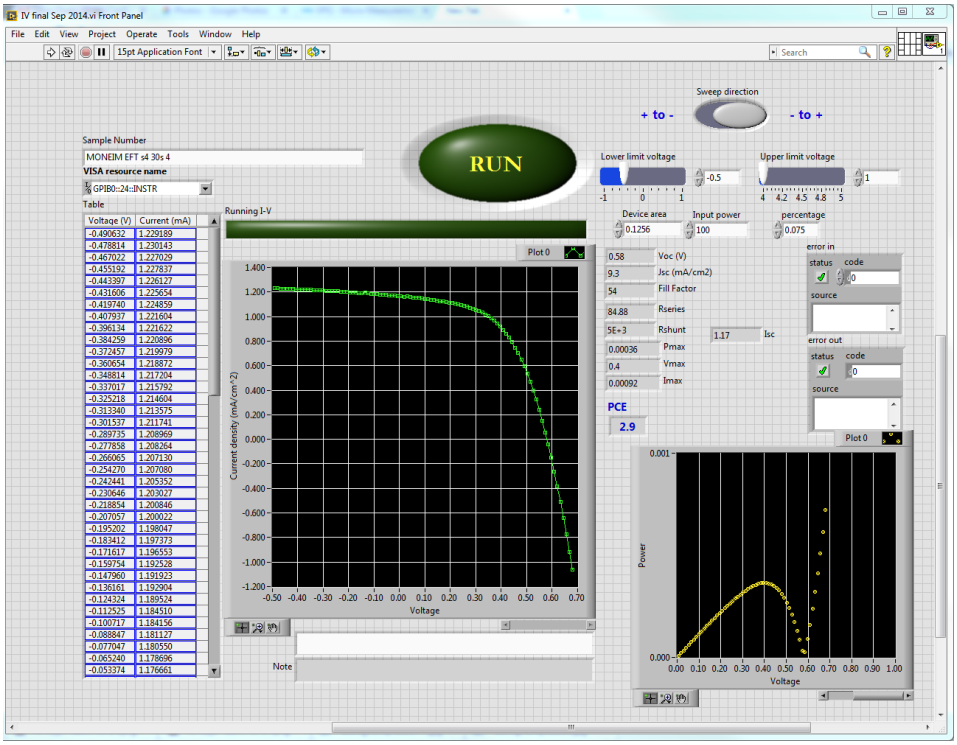

Figure 4.8 LabVIEW program screenshot

A Kodak Carsoul 750H with DEK 500W incandescent light bulb shown in Figure 4.9 was used to illuminate the cell surface during the tests where the distance between the projector and the

specimen was kept constant during the test. The same projector was used to provide consistent results for all samples. Sugar (2007) justified that since the quantum efficiency peaks of the solar cell - around 540 nm - are within the projector spectrum. Therefore, this projector can be used as a solar simulator for this study.

Figure 4.9 Compression test setup under Kodak carsoul projector illumination

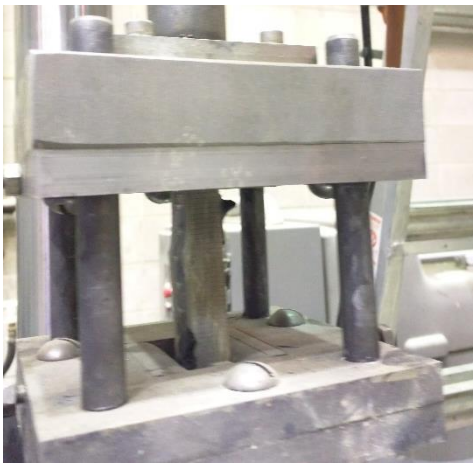
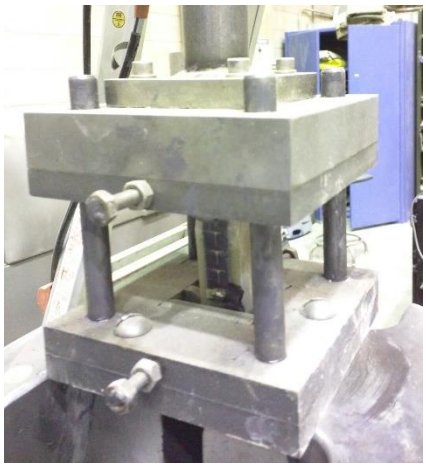

Figure 4.10 Close shots of the compression fixture

4.2.5.1. TESTING METHODS

4.2.5.1.1. COMPRESSION

To avoid buckling in the used fixture, the thickness of the compression sample was larger than that of tension specimens. A custom-made fixture developed by Makkapati (1994) was used to determine the compressive behavior of the solar cell attached to the FRP, as shown in Figure 4.10. The fixture consisted of an upper and bottom part where each part consisted of two square plates (127 x 127 mm^2). The inner plates had a cut-off in the center to fit the sample on it. Shims with side screws and tapered ends can be adjusted to provide constraint to the sample. The upper and lower part were connected using four guiding posts placed at each corner to provide perfect alignment during loading.

This fixture was chosen since, unlike ASTM D695 fixture, it allows the solar cell to be subjected to light during testing, as shown in Figure 4.10. The ASTM fixture has two sides that are attached to both sides of the compression sample to prevent buckling, which does not expose the compression sample to the light.

4.2.5.1.2. TENSION

MTS and Instron machine grips were used to hold the tension samples at both ends. The grip pressure was set to avoid damage and prevent slippage. The grip size was at least 25.4 mm for the perovskite samples.

Figure 4.11 Tension setup for perovskite solar cell samples

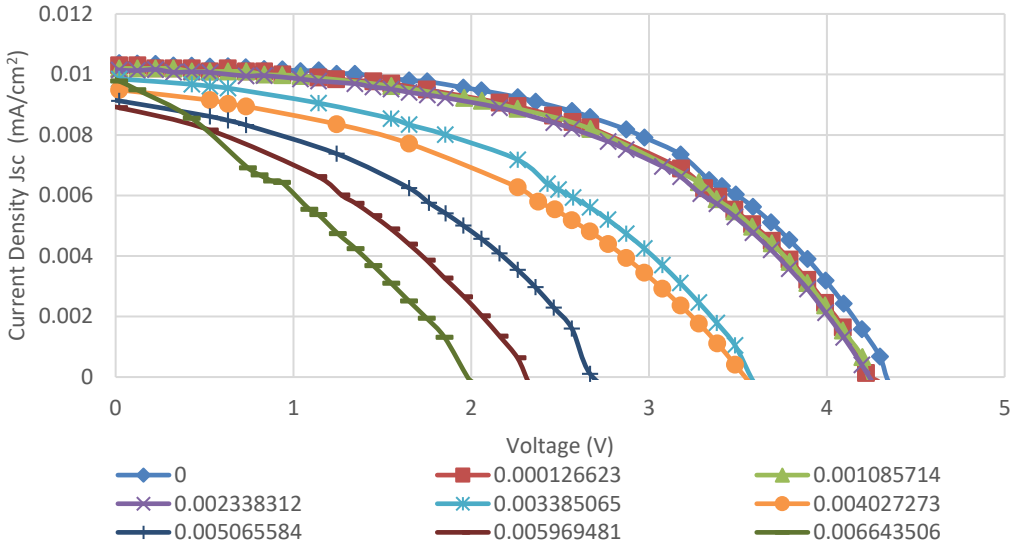

Figure 4.12 J-V curve of monotonic compression tests for different strain values

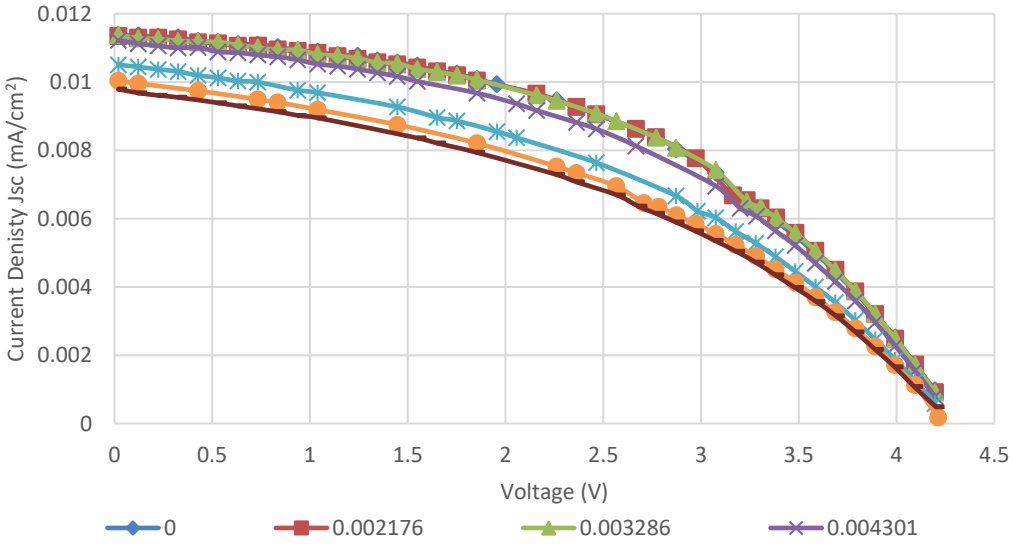

Figure 4.13 J-V curve of monotonic tension tests for different strain values

4.3. Testing Results

To evaluate the performances of the solar cells under loading, each sample was loaded under displacement control. The displacement was held constant for a limited time, so that the current from the solar cell could be measured as the voltage swept from 0 to 5 V using the LabVIEW

program, which was connected to the source meter. The current was recorded as the voltage changed, and the current density-voltage (J-V) curve was plotted. The displacement was then moved to the next level and J-V curve was recorded again. This process was repeated until the samples failed. J-V curves for both compression and tension obtained at different loading levels are shown in Figures 4 and 4.

The short circuit density (J_{sc}) and the open circuit voltage (V_{oc}) are where the J-V curve crosses the y-axis and x-axis, respectively. Sugar et al. (2007) presented Equation (35) shows the maximum power point (MPP), which is equal to the product of the maximum current density (J_{max}) and the maximum voltage (V_{max}). Figures 4 and 3 show J_{sc} and MPP vs. strain for compression and tension results, respectively.

$$MPP = (J_{max})(V_{max})(Area) \tag{35}$$

4.3.1. Temperature effect

An a-Si solar-FRP sample was subjected to illumination for 40 minutes where the MPP was measured through the illumination time to observe the effect of the temperature on the a-Si solar cell. Figure 4.14 shows that the temperature does not affect the performance of the a-Si solar cells attached to the FRP. As for the perovskite solar cell samples, no degradation was recorded during the loading duration. Therefore, it was concluded that the temperature did not affect the results of the perovskite solar cells.

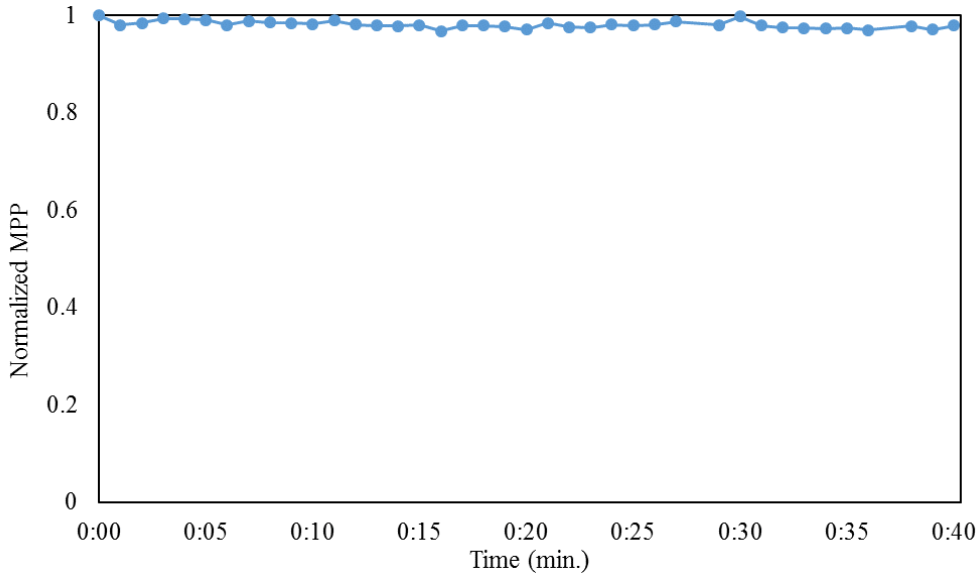

Figure 4.14 Normalized MPP through time

4.3.2. Loading effect

Figure 4.19 shows the stress-strain curve for a typical compression test for a-Si solar cells, where the samples failed around 1.6% strain. However, Figure 4.16 and Figure 4.15 show a drop in the solar performance starting from 0.5% to 1% strain for compression and 1% for tension, respectively. Therefore, it can be concluded that the degradation of the performance in case of compression loading is due to the solar module and not the GFRP. Figure 4.18 shows the results of perovskite solar cells under tension where the solar cell samples were able to hold up to 3% strain with a degradation of only 15% less than unloaded samples. This indicates that the perovskite shows a more ductile behavior than the a-Si solar cells.

The degradation range for solar cells under compression shown in Figure 4.16 varies from 0.5% to 1% due to the unpredictable nature of crushing. As the compression samples start to crush, the bond strength between the sample and the solar cell start to degrade at one or more spot. That yields to a different mode of buckling depending on the bond strength. If the buckling length becomes small, then, the solar cell is more likely to degrade at earlier strain as shown in Figure

4.17. Another researcher in our group is currently studying the effect of the buckling length on the degradation of the solar cells.

For further evaluation of the performance of the a-Si solar cell under compression loading, samples were subjected to loading and unloading until they failed. Readings were taken while loading or unloading without stopping as shown in Figure 4.20 to prevent load creep effect. The results indicate that 20% degradation was observed at 0.5% strain. However, further loading and unloading did not affect the performance of the solar cell. Degradation in compression loading happened mainly due to buckling of solar cell while it is still attached at several locations to the FRP as shown in Figure 4.17.

Figure 4.21 shows the tension loading and unloading results. The a-Si solar cells were attaching to FRP until it reached 1% strain, then when the sample was unloaded, the bond started to degrade due to fatigue loading. However, the solar cell was attached at several spots until FRP failure while the solar cell was delaminated from the FRP without cracking as Figure 4.23 show for tensile loading and loading failure modes.

A-Si compression and tension failure modes are shown in Figure 4.22 and Figure 4.23, respectively, where tension samples failed at the location of the solar taps in the middle, and compression samples failed in the middle due to crushing. Similar failure mode was noted for perovskite solar cells as shown in Figure 4.25.

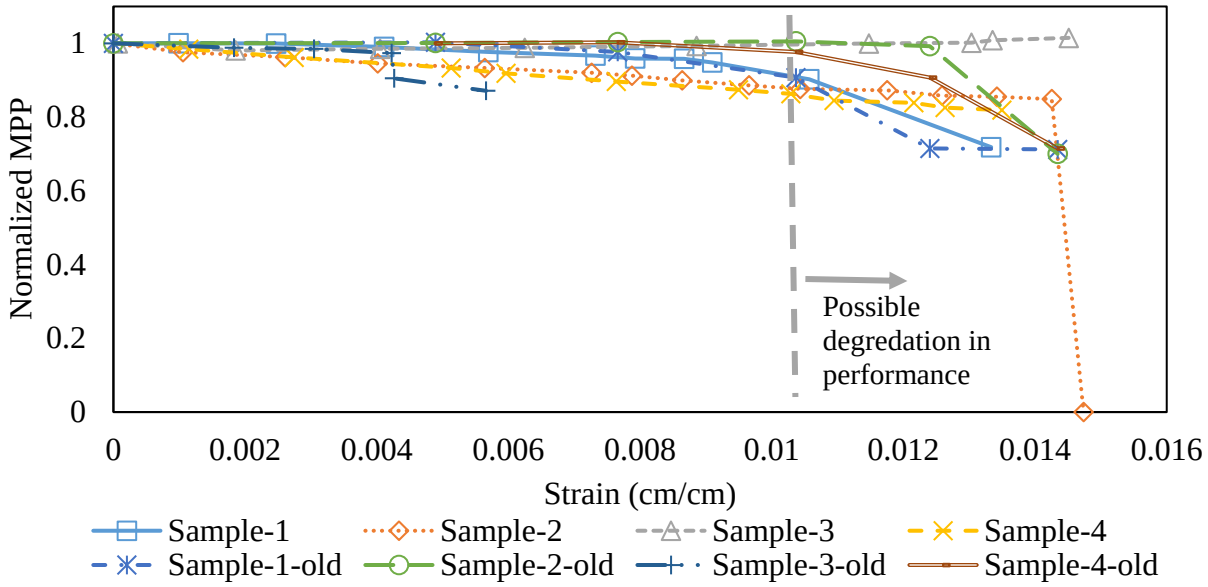

Figure 4.15 MPP vs. strain for a-Si solar cells subjected to tension monotonic loading

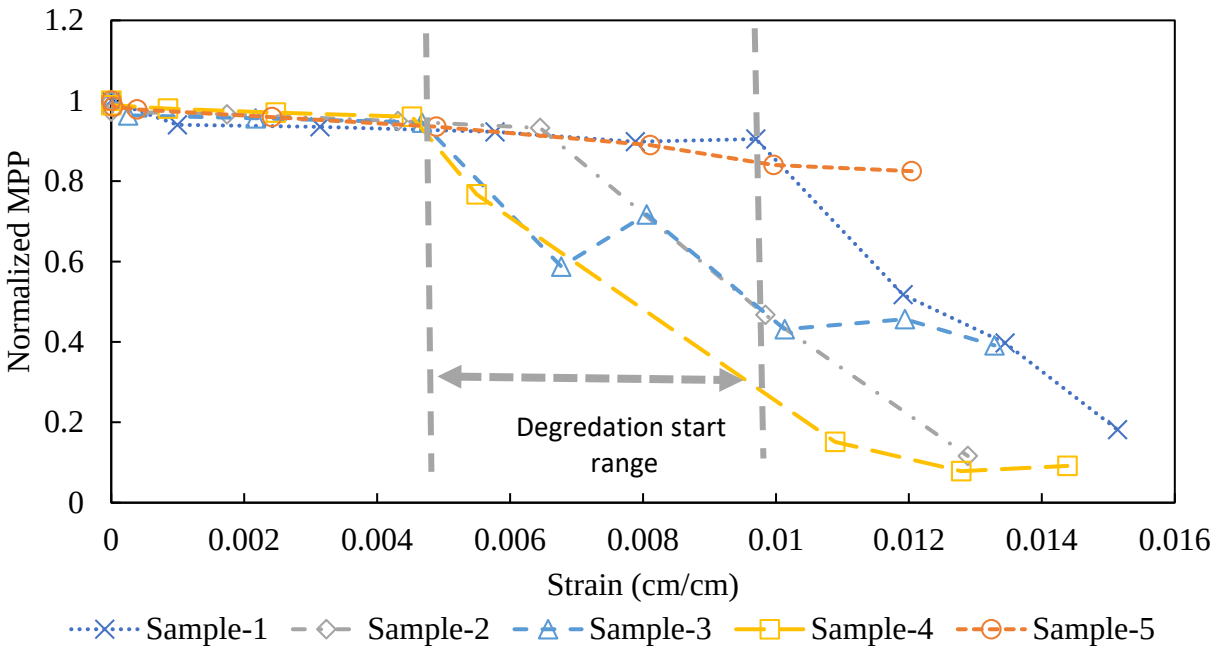

Figure 4.16 MPP vs. strain for amorphous silicon solar-FRP subjected to monotonic compression loading

Figure 4.17 Different modes of buckling of amorphous silicon solar subjected to compression loading

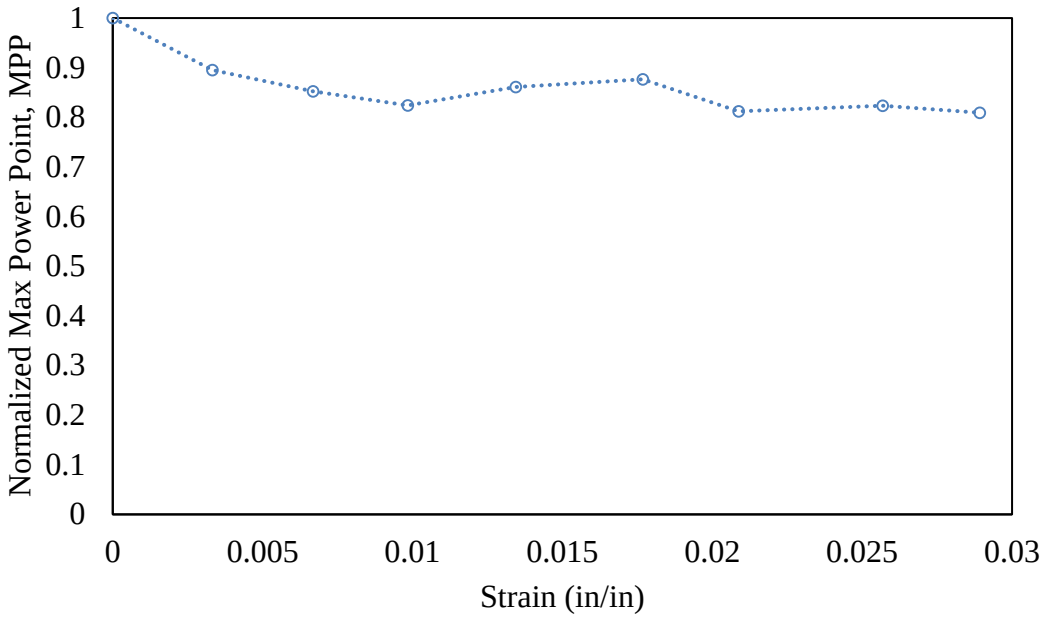

Figure 4.18 MPP vs. strain for perovskite solar on glass substrate

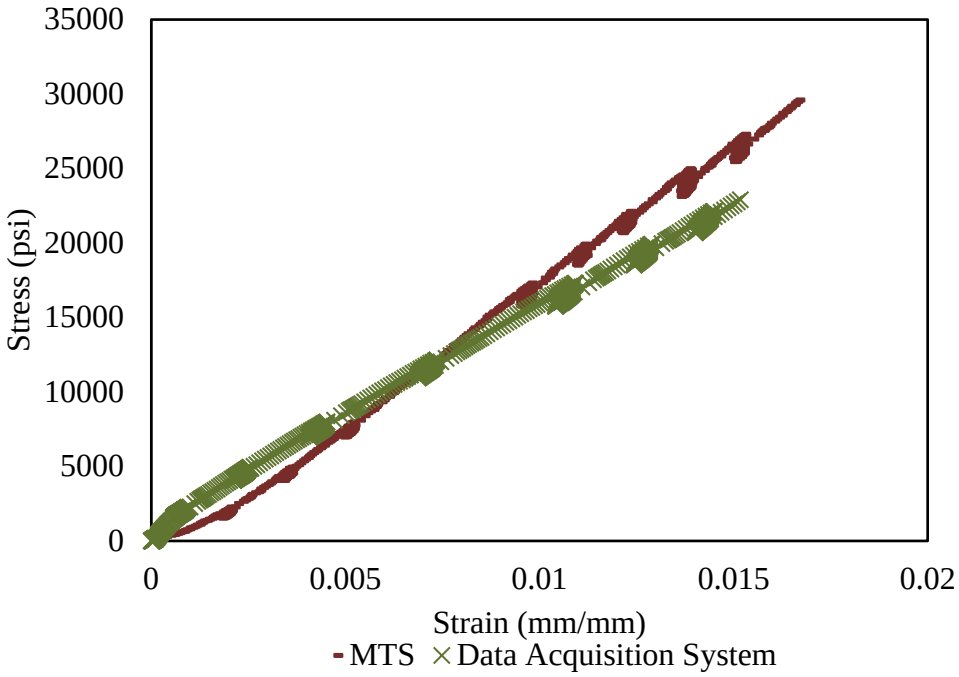

Figure 4.19 Compression stress-strain curve

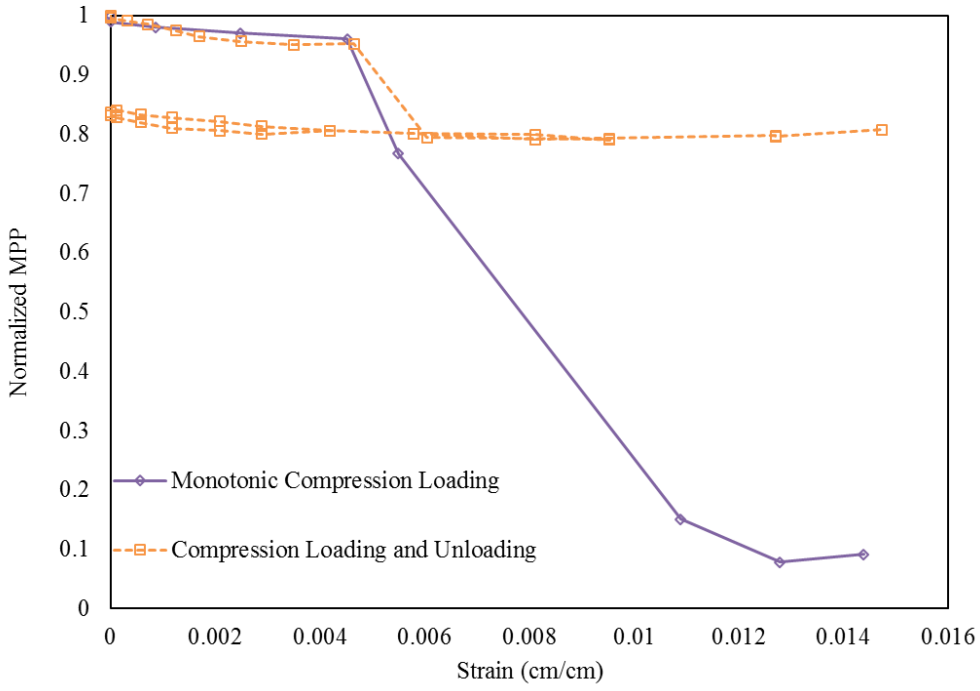

Figure 4.20 Normalized MPP vs. strain for compression loading and unloading

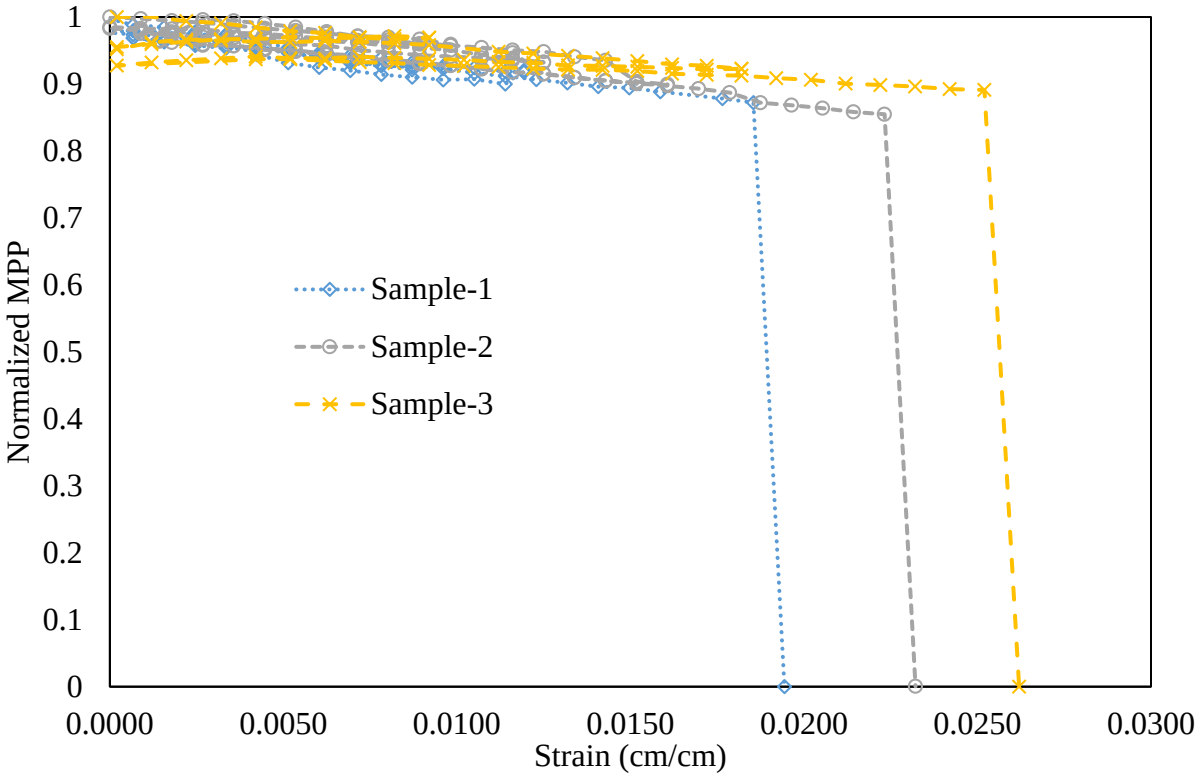

Figure 4.21 Normalized MPP vs. strain for tension loading and unloading

Figure 4.22 A-Si compression samples failure modes

Figure 4.23 Failure modes for a-Si tension samples subjected to tension loading and unloading

Figure 4.24 Failure modes for a-Si tension samples subjected to tension monotonic loading

Figure 4.25 Perovskite tension sample failure modes

4.4. Discussions And Conclusions

The performances of the solar cells attached to GFRP were investigated in this paper. Tension and compression samples were tested, J-V curves were measured and MPP and FF were calculated and plotted versus strain. From this study, it was observed that amorphous silicon solar cells started to degrade at about 0.5% to 1% strain under compression depending on buckling mode. Under tension, solar cells degrade at about 1%. It can be concluded that there are thresholds for the solar cells in both compression and tension, i.e., the solar cells work properly below the threshold but degrade rapidly once the threshold is passed for monotonic loading. For perovskite solar cells, a degradation of about 85% was observed when subjected to tension loading which can reach strain until 3%. It can be concluded that a-Si solar-FRP can be used as a strain indicator, while perovskite solar cell can be used in application where high strain deformation is more likely to occur.

4.5. References

Aberle, A. G. (2009). "Thin-film solar cells." *Thin Solid Films*, 517(17), 4706–4710.

Chen, A., and Davalos, J. F. (2010). "Strength evaluations of sinusoidal core for FRP sandwich bridge deck panels." *Composite Structures*, Elsevier Ltd, 92(7), 1561–1573.

Chopra, K. L., Paulson, P. D., and Dutta, V. (2004). "Thin-film solar cells: an overview." *Progress in Photovoltaics: Research and Applications*, John Wiley & Sons, Ltd., 12(23), 69–92.

Elshobaki, M. (2015). "Tailoring device-scale properties in organic electronics: Morphological, optical and electrode-interface related approaches." Iowa State University.

Fan, Z., Bastiani, M. De, Monticelli, C., Caironi, M., and Zanelli, A. (2015). "Performance investigation of organic photovoltaic layers on architectural membrane." *9th Energy forum*, 1255–1269.

Gleskova, H., and Wagner, S. (1999). "Amorphous silicon transistors on ultrathin steel foil substrates." *Applied Physics Letters*, 74(18), 2661.

Jason Maung, K., Hahn, H. T., and Ju, Y. S. (2010). "Multifunctional integration of thin-film silicon solar cells on carbon-fiber-reinforced epoxy composites." *Solar Energy*, 84(3), 450–458.

Keller, T., Vassilopoulus, A., and Manshadi, B. (2010). "Thermomechanical behavior of multifunctional GFRP sandwich structures with encapsulated photovoltaic cells." *Journal of composites for construction*, 14(4)(August), 470–478.

Kim, J. C., and Cheong, S. K. (2014). "I-V curve characteristics of solar cells on composite substrate under mechanical loading." *Journal of Mechanical Science and Technology*, 28(5), 1691–1696.

Makkapati, S. (1994). “Compressive strength of pultruded structural shapes.” West Virginia University.

NREL. (2017). “NREL Efficiency Chart.”

Pascual, C., de Castro, J., Schueler, A., Vassilopoulos, A. P., and Keller, T. (2014). “Total light transmittance of glass fiber-reinforced polymer laminates for multifunctional load-bearing structures.” *Journal of Composite Materials*, 48(29), 3591–3604.

Petersen, M. R., Chen, A., Roll, M., Jung, S. J., and Yossef, M. (2015). “Mechanical properties of fire-retardant glass fiber-reinforced polymer materials with alumina tri-hydrate filler.” *Composites Part B: Engineering*, 78.

Sugar, J. G. (2007). “Photovoltaic Performance of Amorphous Silicon Flexible Solar Modules Under Mechanical Loading.” UCLA.

Sugar, J. G., Scaffaro, R., Guo, Z., Maung, J. K., Ju, Y. S. Y. “Sungtaek,” Hahn, H. T., Maung, J. K., and Ju, Y. S.(2007). “Photovoltaic Performance of Amorphous Silicon Flexible Solar Modules Under Mechanical Loading.” *6th International Workshop on Structural Health Monitoring*, Stanford, CA, September 11–13., 61.

Suo, Z., Ma, E. Y., Gleskova, H., and Wagner, S. (1999). “Mechanics of rollable and foldable film-on-foil electronics.” *Applied Physics Letters*, 74(8), 1177–1179.

Theiss, S. D., and Wagner, S. (1996). “Amorphous Silicon Thin-Film Transistors on steel foil substrates.” *IEEE Electron Devis Letters*, 17(12), 521–531.

Utsunomiya, M., and Yoshida, A. (1989). “Effect of mechanical strain on electrical characteristics of hydrogenated amorphous silicon junctions.” *Journal of Applied Physics*, 66(1), 308–311.

CHAPTER 5. A SOLUTION CONSIDERING PARTIAL DEGREE OF COMPOSITE ACTION FOR INSULATED SANDWICH PANELS WITH GENERAL CONFIGURATION FLEXIBLE SHEAR CONNECTORS

A paper submitted to Engineering Structures Journal

Mostafa Yossef and An Chen

Abstract

Insulated sandwich panels consist of two wythes separated by a non-structural insulation layer. These two wythes are connected using shear connectors. In recent years, Fiber-Reinforced Polymer (FRP) shear connectors have been increasingly used due to their low thermal conductivity. However, they have lower stiffness compared to other rigid shear connectors, resulting in partial degree of composite action (DCA) for the sandwich panels. Until now, insulated sandwich panels are designed based on the assumption that the longitudinal stress is uniform across the wythe, which is not reasonable since the in-plane shear flexibility of the wythe causes non-uniform distributions of the stress, which is called shear lag effect. This paper presents an analytical solution to study the behavior of insulated sandwich panels with flexible shear connectors. To this end, a solution based on the shear lag model is firstly developed, where the partial DCA and boundary conditions from various configurations of the flexible shear connectors are considered. The effective width, an important parameter to describe the shear lag effect, is defined. The analytical model is then verified through close correlations between finite element and analytical results for an insulated concrete sandwich panel with FRP shear connectors. A parametric study is finally conducted using the analytical model to investigate the effects of deck

stiffness and aspect ratio on the effective width. The results from this study can be used for the design of insulated sandwich panels.

5.1. Introduction

5.1.1. Insulated sandwich panels

Insulated sandwich panels are typically composed of two wythes separated by a layer of insulation. They can be used in different structures, including residential and commercial buildings, schools, warehouses, etc., as walls, roofs, and floors due to their many advantages, such as energy efficiency, acoustic and vibration control, fire and blast resistance, etc. As shown in Figure 5.1, the insulated sandwich panels can be connected using various types of shear connectors, including steel ties, wire trusses, bent wires, truss-shaped connectors, and solid zones (Einea et al., 1991; Frankl et al., 2011; Salmon and Einea, 1995). Although these connectors can establish effective connections, they can cause thermal bridging between the wythes, which impairs the advantage of the sandwich panels as insulating elements. Recently, these connectors are being replaced by Fiber-Reinforced Polymer (FRP) shear connectors, since FRP has a thermal conductivity about 14% that of steel, which can significantly reduce the thermal bridging. In addition, the non-corrosive FRP can increase the durability and decrease the maintenance cost.

5.1.2. Shear lag effect

The importance of the sandwich panels demands the need for accurate description of their structural behavior. Until now, sandwich panels are designed as rectangular beams, where constant stress is assumed across the width of the cross-section. However, stress distribution for sandwich panels is non-uniform due to the in-plane shear flexibility of the wythe, which is called shear lag effect, as shown in Figure 5.2.

(a)

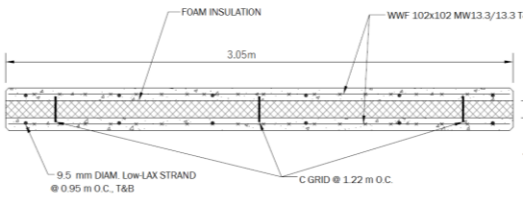

(b)

Figure 5.1 Sandwich panels with FRP connectors
(a)Tested panel with FRP shear grid (Frankl et al., 2011)
(b) Cross section of test panel (Hopkins et al., 2014)

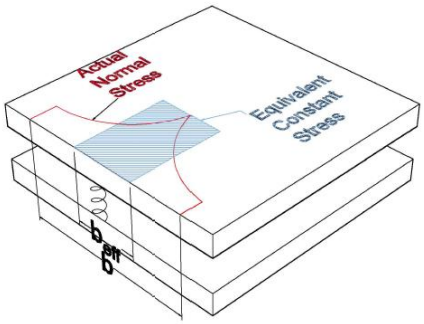

Figure 5.2 Effective width

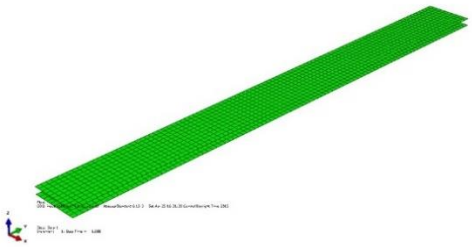

Figure 5.3 FE model

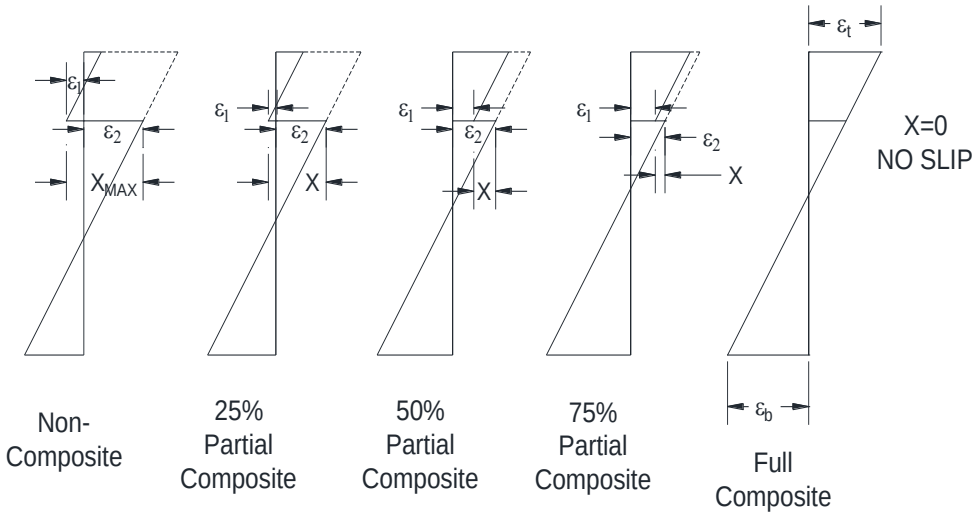

Figure 5.4 Partial composite action defined by AISC
(Lorenz and Stockwell, 1984)

Reissner (1941) introduced the concept of the shear lag effect for isotropic sections. Later, Reissner (1946) developed a shear lag model using the minimum potential energy for box beams. Kemmochi et al. (1980) followed Reissner's concept to obtain the shear lag for FRP sandwich panels with aluminum channel shear connectors. The authors were able to formulate the strain and deflection of the sandwich panel in terms of its flexural rigidity. However, the shear connectors were assumed to be rigid.

Evans and Taherian (1977a) proposed a bar method to predict the shear lag in box girders. In this method, the web and flanges of the box girder are converted into equivalent axial load carrying bars where the forces can be calculated at each bar. The bar simulation was then expanded to study multi-cell and continuous box girders (Evans and Taherian, 1977b). Upadyay and Kalyanaraman (2003) used the bar simulation method to study box girders undergoing distortion and buckling. Although this method is simplified, however, it still assumes perfect interaction between the webs and flanges of the box girders.

Evans and Shanmugam (1979) extended the bar method to grillage method to analyze the shear lag effect for multi-cellular structures. The grillage system is ideal for two-dimensional continuous bridge deck where it can be idealized into two perpendicular beam elements. Since then, the grillage method has been used for bridge design and analysis (Okeil and El-Tawil, 2004; Song et al., 2003; Ugale et al. 2006). However, this paper is focused on one-way sandwich panel.

Cheung and Chan (1978) used finite strip method to evaluate the effective width of a slab-on-multi-cellular box girders. The slab and girders were idealized into folded plates, which were divided into strips. However, this method was complicated and difficult to implement.

Kristek et al. (1990) proposed a shear lag model based on harmonic analysis. The method was applied to steel and steel-concrete composite box girders. This paper represents the keystone

for the shear lag analysis due to its simplicity and fairly accurate results. The shear lag model was then generalized to include multi-cellular structures (Evans et al., 1993). Kristek (2004) expanded the harmonic analysis model to account for the partial interaction between the concrete slab and steel box girder. However, the interaction was based on the friction between the overlapping area of concrete slab and steel flange and not the location of shear connectors, which limits this model to structures with one shear connector only.

Salim and Davalos (2005a) extended the harmonic method to model the shear lag for thin-walled composite beams. The model was based on the mechanics of laminated beams model proposed by Barbero et al. (1993). Explicit formulas were derived for single box, multi-box and wide-flange sections. Later, Zou et al. (2011) evaluated Salim's model for orthotropic FRP bridge decks, where good correlation was achieved between the analytical model and experimental results. However, these models did not consider partial Degree of Composite Action (DCA).

In all these studies, effective flange width was used to describe the shear lag effect, reducing the three-dimensional behavior of the structural system to the analysis of a two-dimensional section with a reduced width of flange. Figure 5.2 shows that a uniform stress can be assumed along the reduced width b_{eff}. The area of this stress block is equivalent to the area of the actual stress distributed along the width b. This reduced width b_{eff} is called effective flange width. This paper will extend the concept of effective flange width to insulated concrete sandwich panels based on the shear lag model. In particular, partial DCA will be considered, as described next.

5.1.3. Degree of Composite action (DCA)

Headed steel studs are typically used to connect the deck and girder for a deck-on-girder composite beam system. These connections are rigid and the slip between the deck and girder is

minimum. This slip is usually neglected in the calculation of effective flange width. Unlike rigid headed steel studs, FRP connectors are flexible. Therefore, the slip between the two wythes cannot be neglected for sandwich panels with FRP shear connectors. Degree of Composite Action (DCA) can be used to interpret this slip.

DCA depends on the shear force transferred through shear connectors between the two wythes. As shown in Figure 5.4, Lorenz and Stockwell (1984) pointed out that 100% and zero shear forces can be transferred for full-composite and non-composite cases, respectively. Partial DCA is from the limited amount of slip due to the inadequacy of the shear connectors to maintain strain compatibility.

Several studies have studied DCA for sandwich panels. Benayoune et al. (2008) calculated the DCA for sandwich panels based on the stress distribution as follows:

$$DCA = \frac{I_e}{I_g}, I_e = \frac{M \times h}{\sigma_b - \sigma_t} \tag{36}$$

where σ_b, σ_t are the stresses at the bottom and top faces of the panel, respectively, M is the applied bending moment, h is the depth of the panel, and I_g is the moment inertia of the sandwich panel and I_e is the effective moment of inertia, where the ratio of I_e and I_g provide the DCA.

The earliest investigation of GFRP as a shear connector for insulated sandwich panels was conducted at Iowa State University in 1988 (Wade et al., 1988), where the authors proposed a method to determine the DCA based on the percentage of the existing moment (M_{ext}) at the mid-span resisted by the internal non-composite moment of the top wythe (M_{tw}) and bottom wythe (M_{bw}):

$$DCA = \frac{M_{ext} - (M_{tw} + M_{bw})}{M_{ext}} \times 100, M_{ext} = \frac{wl^2}{8}, M_{tw} = S_{tw} \cdot E_c \cdot \varepsilon, M_{bw} = S_{bw} \cdot E_c \cdot \varepsilon \tag{37}$$

where S_{tw} and S_{bw} are the section modulus of the uncracked top and bottom wythe, respectively, E_c is the concrete modulus of elasticity and ε is the average strain difference at outer faces of wythe.

Frankl et al. (2011) conducted experimental study and proposed a displacement method to calculate DCA as:

$$DCA = \frac{\Delta_{noncomposite} - \Delta_{experimental}}{\Delta_{noncomposite} - \Delta_{composite}}(100\%) \tag{38}$$

where $\Delta_{composite}$, $\Delta_{noncomposite}$ are displacements measured at the selected load level corresponding to full- and non-composite action, respectively. Hopkins et al. Hopkins et al. (2014) adopted the displacement method and concluded that DCA has a significant effect on both stiffness and flexural strength of the panel.

Chen et al. (2015) performed experimental tests on sandwich panels with different shear connectors. DCA of the test panels was calculated based on:

$$DCA = \frac{\left(\frac{1}{EI}\right)_{0\%} - \left(\frac{1}{EI}\right)_{Actual}}{\left(\frac{1}{EI}\right)_{0\%} - \left(\frac{1}{EI}\right)_{100\%}}(100\%) \tag{39}$$

where $\left(\frac{1}{EI}\right)_{0\%}$, $\left(\frac{1}{EI}\right)_{Actual}$, and $\left(\frac{1}{EI}\right)_{100\%}$ represent the values for panels with non-composite; partial DCA; and full-composite actions, respectively.

However, limited studies are available for the shear lag model considering partial DCA. The authors (Chen and Yossef, 2015) have developed a shear lag model for deck-on-girder composite beam considering partial DCA. However, the model was only valid for interior girders. This paper will evaluate the applicability of the shear lag model for insulated concrete sandwich panels with general configuration shear connectors. To this end, a shear lag model is firstly derived,

where the partial DCA and different configurations of flexible shear connector are considered, based on which the effective width is defined. The analytical model is then verified through close correlations between Finite Element (FE) and analytical results for an insulated concrete sandwich panel with FRP shear connectors. Next, a parametric study is conducted using the analytical model to study the effects of deck stiffness and aspect ratio on effective width. The results from this study can be used for the design of insulated sandwich panels.

5.2. Analytical Model

The analytical model is built on the following assumptions:

1) Materials are linear elastic.
2) Cross-sections are symmetric, and therefore, torsion is not considered.
3) The shear deformation is predominately caused by the flexible shear connectors. Therefore, the shear deformation from the two wythes are neglected, i.e., the same curvature is assumed for the upper and lower wythes and thin plate theories can be applied.
4) The contribution from the insulation layer is neglected.
5) All shear connectors have the same properties.

The analytical model is based on orthotropic materials. A number of research studied composite sandwich panel (Dawood et al., 2010; Fam and Sharaf, 2010; Manalo et al., 2010; Reis and Rizkalla, 2008; Sharaf and Fam, 2011). Applying the Classical Lamination Theory (CLT), the constitutive relationship for an orthotropic wythe can be described as:

$$\begin{Bmatrix} \{N\} \\ \{M\} \end{Bmatrix} = \begin{bmatrix} [A] & 0 \\ 0 & [D] \end{bmatrix} \begin{Bmatrix} \{\varepsilon\} \\ \{\kappa\} \end{Bmatrix} \tag{40}$$

where $\{N\}$ and $\{M\}$ are in-plane load and moment vectors, respectively; $[A]$ and $[D]$ are extensional stiffness and bending stiffness matrices, respectively; and $\{\varepsilon\}$ and $\{\kappa\}$ are in-plane strain and curvature vectors, respectively. $[A]$ and $[D]$ can be calculated as:

$$[A] = t[Q] \tag{41}$$

$$[D] = \frac{t^3}{12}[Q] \tag{42}$$

where *t* is the thickness of the wythe. For an orthotropic material, we have

$$[Q] = \begin{bmatrix} \frac{E_x}{1-\nu_x\nu_y} & \frac{\nu_y E_x}{1-\nu_x\nu_y} & 0 \\ \frac{\nu_x E_y}{1-\nu_x\nu_y} & \frac{E_y}{1-\nu_x\nu_y} & 0 \\ 0 & 0 & G \end{bmatrix} \tag{43}$$

where E_x, ν_x, E_y, and ν_y are Young's modular and Poisson's ratios in x and y directions, respectively. Equation (40) can be re-written as follows by performing appropriate matrix inversions:

$$\begin{Bmatrix} \{\varepsilon\} \\ \{\kappa\} \end{Bmatrix} = \begin{bmatrix} [\alpha] & 0 \\ 0 & [\delta] \end{bmatrix} \begin{Bmatrix} \{N\} \\ \{M\} \end{Bmatrix} \tag{44}$$

where the compliance matrices are given by $[\alpha] = [A]^{-1}$ and $[\delta] = [D]^{-1}$.

Barbero et al. (1993) found out that when a plate is subjected to out-of-plane forces, the axial force N_y, moment M_y in y-direction and twisting moment M_{xy} can be assumed to be equal to zero. If a wythe is considered to be connected by two shear connectors at both edges, then only

edge shear transaction N_{xy} and axial force N_x exist as shown in Figure 5.5. Based on this assumption, Equation (44) can be reduced to:

$$\begin{Bmatrix} \varepsilon_x \\ \gamma_{xy} \\ \kappa_x \end{Bmatrix} = \begin{bmatrix} \alpha_{11} & 0 & 0 \\ 0 & \alpha_{66} & 0 \\ 0 & 0 & \delta_{11} \end{bmatrix} \begin{Bmatrix} N_x \\ N_{xy} \\ M_x \end{Bmatrix} \tag{45}$$

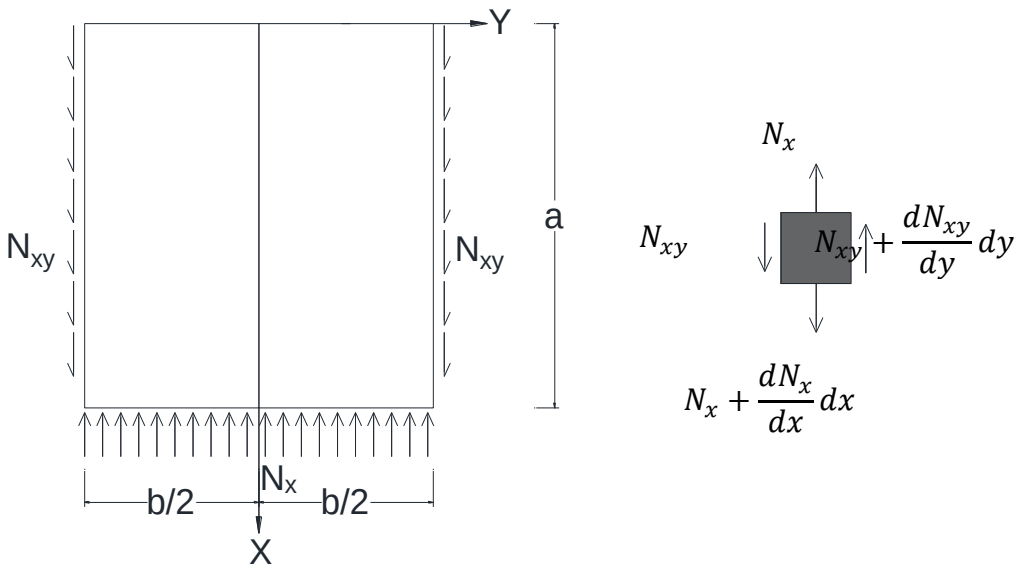

Figure 5.5 Forces in a wythe

Based on the equilibrium equation of an infinitesimal section of the plate, we have

$$\frac{\partial N_x}{\partial x} + \frac{\partial N_{xy}}{\partial y} = 0 \tag{46}$$

The compatibility equation for an orthotropic plate is given as:

$$\frac{\partial^2 \varepsilon_x}{\partial y^2} + \frac{\partial^2 \varepsilon_y}{\partial x^2} = \frac{\partial^2 \gamma_{xy}}{\partial x \partial y} \tag{47}$$

Since the deck is restrained in y direction by two shear connectors at two sides, ε_y is insignificant compared to ε_x, which can be neglected. Equation (47) becomes:

$$\frac{\partial^2 \varepsilon_x}{\partial y^2} = \frac{\partial^2 \gamma_{xy}}{\partial x \partial y} \tag{48}$$

Substituting Equation (45) into (48), and combining with Equation (46), we get:

$$\alpha_{11} \frac{\partial^2 N_x}{\partial y^2} + \alpha_{66} \frac{\partial^2 N_x}{\partial x^2} = 0 \tag{49}$$

Equation (49) can be reduced to an ordinary differential equation by a harmonic analysis. Assuming the wythe is simply supported at x=0 and a, the axial force can be obtained as:

$$N_x(x, y) = \sum_{j=1}^{\infty} N_j(y) \sin(\frac{j\pi x}{a}) \tag{50}$$

where $N_j(y)$ is an amplitude function. Substituting Equation (50) into (49), we get:

$$\frac{\partial^2 N_j}{\partial y^2} = \xi_j{}^2 N_j \tag{51}$$

where

$$\xi_j = \frac{j\pi}{a} \sqrt{\frac{\alpha_{66}}{\alpha_{11}}} \tag{52}$$

Salim and Davalos Salim and Davalos (2005b) obtained a general solution for Equation (51), which is:

$$N_j(y) = C_{1j} \cosh(\xi_j y) + C_{2j} \sinh(\xi_j y) \tag{53}$$

where C_{1j} and C_{2j} are constants that need to be determined.

5.2.1. Boundary conditions

Each cross-section has different boundary conditions. The boundary conditions can be defined through C_{1j} and C_{2j} values. In this paper, four cases are considered which cover most

configurations of the shear connectors: inner symmetric cross-section (equivalent to WF section), two shear connectors as a box-section, multiple shear connectors with equal spacing, and the cantilever section. A general case of single box section is presented first, and then different factors are identified for different cases.

5.2.2. Single box-section

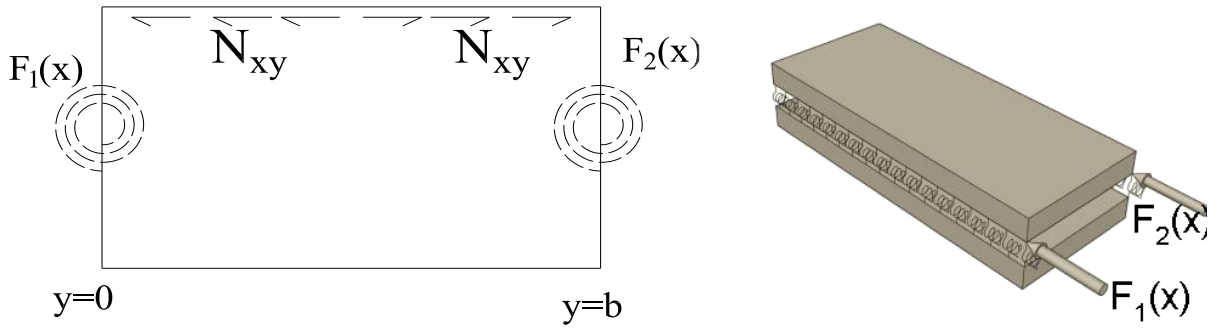

Figure 5.6 box cross-section with two shear connectors

Based on Equation (18), N_x can be expressed as

$$N_x(x,y)=\sum_{j=1}^{\infty}(C_{1j}\cosh(\xi_j y)+C_{2j}\sinh(\xi_j y))\sin(\frac{j\pi x}{a}) \tag{54}$$

Substituting Equation (54) into (46), we get

$$\frac{\partial N_{xy}(x,y)}{\partial y}=-\frac{\partial N_x(x,y)}{\partial x}=-\sum_{j=1}^{\infty}\frac{j\pi}{a}(C_{1j}\cosh(\xi_j y)+C_{2j}\sinh(\xi_j y))\cos(\frac{j\pi x}{a}) \tag{55}$$

Therefore,

$$N_{xy}(x,y)=-\sum_{j=1}^{\infty}\frac{j\pi}{a}\frac{1}{\xi_j}(C_{1j}\sinh(\xi_j y)+C_{2j}\cosh(\xi_j y))\cos(\frac{j\pi x}{a}) \tag{56}$$

Based on boundary conditions as shown in Figure 5.6, at $y=0$ and $y=b$, we have

$$\frac{dF_1(x)}{dx}=\frac{1}{\eta_l}N_{xy}(x,0)=-\frac{1}{\eta_l}\sum_{j=1}^{\infty}\frac{j\pi}{a}\frac{1}{\xi_j}(C_{1j}\sinh(\xi_j\cdot 0)+C_{2j}\cosh(\xi_j\cdot 0))\cos(\frac{j\pi x}{a}) \tag{57}$$

$$\frac{dF_2(x)}{dx} = -\frac{1}{\eta_r} N_{xy}(x,b) = \frac{1}{\eta_r} \sum_{j=1}^{\infty} \frac{j\pi}{a} \frac{1}{\xi_j} (C_{1j} \sinh(\xi_j b) + C_{2j} \cosh(\xi_j b)) \cos(\frac{j\pi x}{a}) \tag{58}$$

where *F(x)* is the force transferred through the shear connection, η is shear flow distribution factor depending on the shape of the cross-section, and *r* and *l* represent the right and left side of cell. For a single box, the shear flow initiates from the mid-point of the upper wythe, and goes through the shear connectors, until it reaches at the mid-point of the lower wythes. Therefore, the shear flow distribution factors for the single box sections are equal to one. Based on Equations (22) and (23), *F(x)* can be expressed as

$$F_1(x) = \frac{1}{\eta_l} \sum_{j=1}^{\infty} \frac{-1}{\xi_j} (C_{1j} \sinh(\xi_j \cdot 0) + C_{2j} \cosh(\xi_j \cdot 0)) \sin(\frac{j\pi x}{a}) \tag{59}$$

$$F_2(x) = \frac{1}{\eta_r} \sum_{j=1}^{\infty} \frac{1}{\xi_j} (C_{1j} \sinh(\xi_j b) + C_{2j} \cosh(\xi_j b)) \sin(\frac{j\pi x}{a}) \tag{60}$$

As pointed out by Newmark et al. Newmark et al. (1951) and Bradford Bradford (2011), the relative movement, or slip, between the slab and girder is given by

$$\gamma = \frac{q}{K} \tag{61}$$

where γ is the slip, *q* and *K* are the horizontal shear and stiffness at the interface of the two layers, respectively. *q* is equal to the change of force *F*, which can be expressed as

$$q = \frac{dF(x)}{dx} \tag{62}$$

Since the slip γ is the difference between the lower and upper wythes as shown in Figure 5.7, it can be expressed as

$$\gamma = u_2 - u_1 \tag{63}$$

Differentiating Equation (63), we get

$$\varepsilon_2 - \varepsilon_1 = \frac{d\gamma}{dx} \tag{64}$$

where ε_1 and ε_2 are strains calculated at neutral axis of the sandwich panel as shown in Figure 5.9.

Substituting Equations (61) and (62) into (64) results in

$$\varepsilon_2 - \varepsilon_1 = \frac{d^2F(x)}{K \cdot dx^2} \tag{65}$$

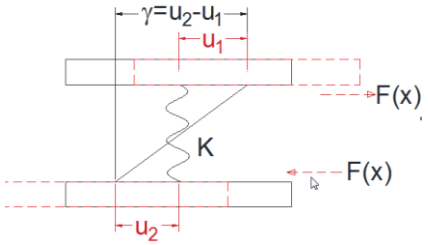

Figure 5.7 Shear Force Transformation

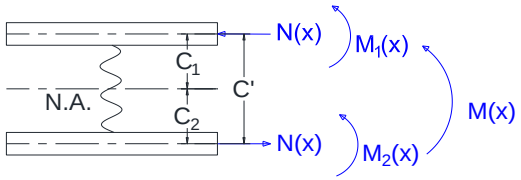

Figure 5.8 Axial and bending moment on sandwich panels

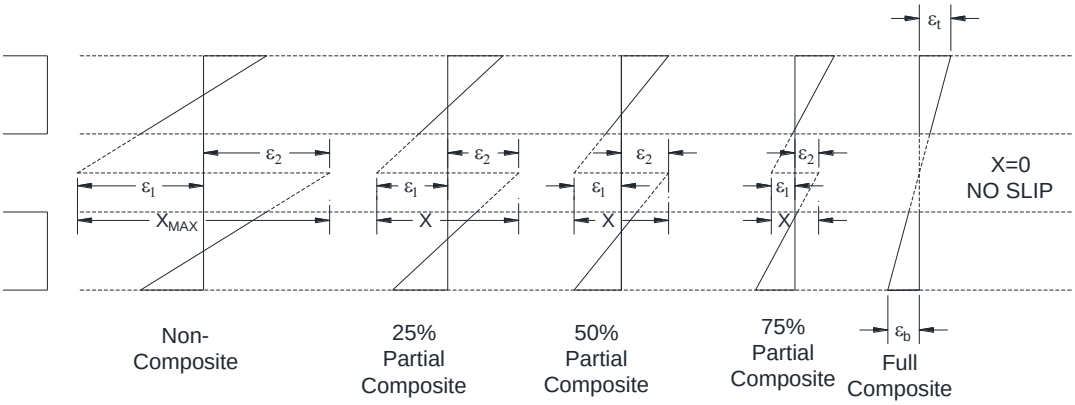

Figure 5.9 Partial Composite Action for Sandwich Panels

Based on the assumption that plane remains plane after deformation, the strain follows a linear distribution along the depth of both layers. Therefore, the strain can be calculated as a function of the axial force and moments on each layer shown in Figure 5.8, which leads to

$$\varepsilon_1 = -\alpha_{11}^{(1)} N_x(x, y_c) + \frac{M_1(x)\, C_1 / b}{D_{11}^{(1)}} \tag{66}$$

and

$$\varepsilon_2 = \alpha_{11}^{(2)} N_x(x, y_c) - \frac{M_2(x)\, C_2 / b}{D_{11}^{(2)}} \tag{67}$$

where $M_i(x)$, C_i, b , y_c and $D_{11}^{(i)}$ are moment, distance between mid-depth of the wythe to the neutral axis of sandwich panel, width of the sandwich panel, transverse coordinates where the shear connectors are located, i.e., y_c=0 and b, and flexural rigidity, respectively; and $i = 1$ and 2 represent the upper and lower wythes, respectively. The assumption that the upper and lower layer deflect equal amount of moment at all points along the length indicates that the angle changes along the length be equal, which can be expressed as:

$$\kappa(x) = \frac{M_1(x)}{bD_{11}^{(1)}} = \frac{M_2(x)}{bD_{11}^{(2)}} = \frac{M_1(x) + M_2(x)}{bD_{11}^{(1)} + bD_{11}^{(2)}} \tag{68}$$

Based on the equilibrium of the moment, we have

$$M_1(x) + M_2(x) + n \cdot F(x)(C') = M(x) \tag{69}$$

where C' is the distance between the neutral axis of the upper wythe and the neutral axis of the lower wythe as shown in Figure 5.8 and *n* is the number of shear connectors for the entire section which can be defined for single cell as

$$n = \eta_r + \eta_l \tag{70}$$

Substituting Equation (70) into (69), we get

$$M_1(x) + M_2(x) = \left(\frac{\eta_r + \eta_l}{n}\right) M(x) - \left(\eta_r + \eta_l\right) \cdot F(x)(C') \tag{71}$$

where η donates distribution factor, *r* and *l* represent the right and left side of cell, respectively. It should be noted that, due to symmetry in single box section, η_r and η_l are equal to 1 and n is equal to 2 which yield back to Equation (69).

Substituting Equation (71) into (68), we have

$$\kappa(x) = \frac{M_1(x)}{bD_{11}^{(1)}} = \frac{M_2(x)}{bD_{11}^{(2)}} = \frac{\left(\frac{\eta_r + \eta_l}{n}\right) M(x) - \left(\eta_r + \eta_l\right) \cdot F(x)(C')}{bD_{11}^{(1)} + bD_{11}^{(2)}} \tag{72}$$

Combining Equations (66), (67) and (72), we have

$$\varepsilon_2 - \varepsilon_1 = (\alpha_{11}^{(1)} + \alpha_{11}^{(2)}) N_x(x, y_c) - \frac{[\left(\frac{\eta_r + \eta_l}{n}\right) M(x) - ((\eta_r + \eta_l) \cdot F(x))(C')](C')}{b[D_{11}^{(1)} + D_{11}^{(2)}]} \tag{73}$$

Substituting Equation (65) into (73), we have

$$\frac{d^2F(x)}{K \cdot dx^2} = (\alpha_{11}^{(1)} + \alpha_{11}^{(2)}) N_x(x, y_c) - \frac{[\left(\frac{\eta_r + \eta_l}{n}\right) M(x) - ((\eta_r + \eta_l) \cdot F(x))(C')](C')}{b[D_{11}^{(1)} + D_{11}^{(2)}]} \tag{74}$$

In order to use Fourier series to solve Equation (74), the moment can be expressed as:

$$M(x) = \sum_{j=1}^{\infty} Q_j \sin(\frac{j\pi x}{a}) \tag{75}$$

where

$$Q_j = \frac{2}{a}\int_o^a M(x)\sin(\frac{j\pi x}{a})dx \tag{76}$$

Using Equations (54), (59), and (75) into (74) applied at y_c=0 *and* y_c=b, the solution of the partial differential Equation (74) can be obtained using Fourier series. Thus, through some simple mathematical transformations, we obtain

$$\begin{bmatrix} D11 \\ D11 \end{bmatrix} = \begin{bmatrix} C_{1j} \\ C_{2j} \end{bmatrix} \cdot \begin{bmatrix} B11\cdot\cosh(\xi_j\cdot 0) - \frac{1}{\eta_1}\cdot(A11+C11)\cdot\sinh(\xi_j\cdot 0) & B11\cdot\sinh(\xi_j\cdot 0) - \frac{1}{\eta_1}\cdot(A11+C11)\cdot\cosh(\xi_j\cdot 0) \\ B11\cdot\cosh(\xi_j b) + \frac{1}{\eta_2}\cdot(A11+C11)\cdot\sinh(\xi_j b) & B11\cdot\sinh(\xi_j b) + \frac{1}{\eta_2}\cdot(A11+C11)\cdot\cosh(\xi_j b) \end{bmatrix} \tag{77}$$

where

$$A_{11} = \frac{1}{K\xi_j}\left(\frac{j\pi}{a}\right)^2, C11 = \frac{(\eta_r+\eta_l)\cdot(C')^2}{b[D_{11}^{(1)}+D_{11}^{(2)}]\xi_j}, B11 = (\alpha_{11}^{(1)}+\alpha_{11}^{(2)}), M11 = \left(\frac{\eta_r+\eta_l}{n}\right)\frac{Q_j\cdot C'}{b[D_{11}^{(1)}+D_{11}^{(2)}]} \tag{78}$$

Solving for C_{1j} and C_{2j}, we get

$$\begin{bmatrix} C_{1j} \\ C_{2j} \end{bmatrix} = \begin{bmatrix} B11 & -\frac{1}{\eta_1}\cdot(A11+C11) \\ B11\cdot\cosh(\xi_j b) + \frac{1}{\eta_2}\cdot(A11+C11)\cdot\sinh(\xi_j b) & B11\cdot\sinh(\xi_j b) + \frac{1}{\eta_2}\cdot(A11+C11)\cdot\cosh(\xi_j b) \end{bmatrix}^{-1} \cdot \begin{bmatrix} M11 \\ M11 \end{bmatrix} \tag{79}$$

5.2.3. Multiple shear connectors (Multi-cell box section)

The solution for single box is still valid for multiple shear connector. However, the shear flow is not distributed equally between consecutive shear connectors. For the inner shear connectors, the shear flow distribution factor is divided into two distribution factors where the summation of the two factors is equal to 1. For the edge shear connector, the distribution factor is 1, as shown in Figure 5.10.

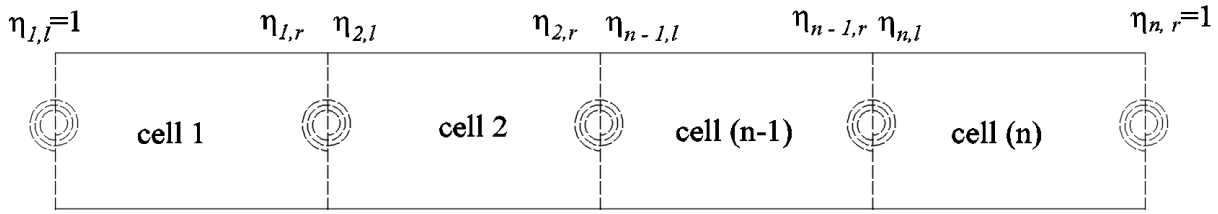

Figure 5.10 Distribution factors multiple shear connectors

The simplest case for multi-cell box is a double box where the two edge distribution factors are equal to 1, and the inner distribution factor is divided into two distribution factors where are equal to 0.5. For the case with more than two cell box section, two extra equations are needed to obtain the distribution factors at the shear connector positions. One equation can be obtained from the continuity of the stress over the cross-section as

$$\frac{N(x)_{(i-1),l}}{t_{(i-1)}} = \frac{N(x)_{(i),r}}{t_{(i)}} \tag{80}$$

where *i* donates the cell number, *t* is the thickness of the upper layer, *l* and *r* represent the left and right sections for a given cell *i*. If the thicknesses of the layers on both sides of the shear connector are the same, Equation (80) can be simplified into

$$N(x)_{(i-1),l} = N(x)_{(i),r} \tag{81}$$

The other equation is obtained from the summation of shear distribution factors at any shear connection, which can be described as

$$\eta_{(i-1),l} + \eta_{(i),r} = 1 \tag{82}$$

where $\eta_{(i-1),l}$ is the distribution factor of the cell (*i*-1) on the left side and $\eta_{(i),r}$ is the distribution factor of cell (*i*) on the right side, as shown in Figure 5.10. It should be noted that the values of the

distribution factors depend on the stiffness of the shear connector (K). Effective width b_{eff} can then be calculated for one cell as

$$b_{eff} = \frac{2 \cdot \int_{b/2}^{b} N_x(x,y)dy}{N_x(x,b)} \tag{83}$$

Equation (83) can be simplified further in terms of shear flow distribution factors as:

$$b_{eff} = \frac{\left(\frac{1}{\eta_{(i),r}} + \frac{1}{\eta_{(i-1),l}}\right)(\eta_{(i),l} + \eta_{(i),r}) \cdot F'(x)}{N_x(x,b)} \tag{84}$$

where $F'(x)$ can be expressed as:

$$F'(x) = \sum_{j=1}^{\infty} \frac{1}{\xi_j}(C_{1j}\sinh(\xi_j b) + C_{2j}\cosh(\xi_j b))\sin(\frac{j\pi x}{a}) \tag{85}$$

Combining Equations (82) and (84), we get

$$b_{eff} = \frac{\left(\frac{1}{\eta_{(i),r}(1-\eta_{(i-1),l})}\right)(\eta_{(i),l} + \eta_{(i),r}) \cdot F'(x)}{N_x(x,b)} \tag{86}$$

5.2.4. Cantilever cross-section

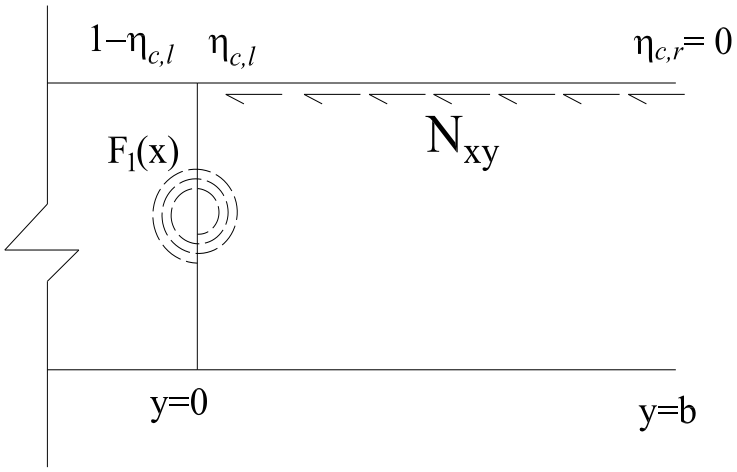

Figure 5.11 Cantilever cross-section

For cantilever cross-sections, we have $N_{xy}=0$ at $y=b$ where the shear flow transfers only at the shear connector at $y=0$. Therefore, Equation (56) can be reduced to

$$C_{1j}\sinh(\xi_j b)+C_{2j}\cosh(\xi_j b)=0 \tag{87}$$

and C_{1j} can be expressed as

$$C_{1j}=-C_{2j}\coth(\xi_j b) \tag{88}$$

Substituting Equation (88) into (56), we have

$$N_{xy}(x,y)=\sum_{j=1}^{\infty}\frac{j\pi}{a}\frac{1}{\xi_j}C_{2j}(\coth(\xi_j b)\cdot\sinh(\xi_j y)-\cosh(\xi_j y))\cos(\frac{j\pi x}{a}) \tag{89}$$

Based on the symmetric condition, at $y=0$, we have

$$N_{xy}(x,y)=\eta_c\frac{dF(x)}{dx} \tag{90}$$

where η_c is the shear flow distribution factor for cantilever section. Therefore, $F(x)$ can be expressed as

$$F(x)=\frac{-1}{\eta_c}\sum_{j=1}^{\infty}\frac{1}{\xi_j}C_{2j}[(\coth(\xi_j b)\cdot\sinh(\xi_j y)-\cosh(\xi_j y))]\sin(\frac{j\pi x}{a}) \tag{91}$$

Similar to Equation (74), we get

$$\frac{d^2F(x)}{K\cdot dx^2}=(\alpha_{11}^{(1)}+\alpha_{11}^{(2)})N_x(x,y)-\frac{[(\frac{\eta_{c,r}+\eta_{c,l}}{n})M(x)-(\eta_{c,r}+\eta_{c,l})F(x)(C^{'})](C^{'})}{b[D_{11}^{(1)}+D_{11}^{(2)}]} \tag{92}$$

Since there is no shear flow at the right side of the cantilever as shown in Figure 5.11, the distribution factor for the right section $\eta_{c,r}$ is equal to zero. Equation (92) can be reduced to:

$$\frac{d^2F(x)}{K\cdot dx^2}=(\alpha_{11}^{(1)}+\alpha_{11}^{(2)})N_x(x,y)-\frac{[(\frac{\eta_{c,l}}{n})M(x)-(\eta_{c,l})F(x)(C^{'})](C^{'})}{b[D_{11}^{(1)}+D_{11}^{(2)}]} \tag{93}$$

where $N_x(x,y)$ can be expressed as:

$$N_x(x,y)=\sum_{j=1}^{\infty}C_{2j}[(\sinh(\xi_j y)-\cosh(\xi_j y)\cdot\coth(\xi_j b))]\sin(\frac{j\pi x}{a}) \tag{94}$$

At shear connector location, $N_x(x,y)$ and F(x) are reduced to:

$$N_x(x,0)=-\sum_{j=1}^{\infty}C_{2j}\coth(\xi_j b)\sin(\frac{j\pi x}{a}) \tag{95}$$

$$F(x)=-\frac{1}{\eta_c}\sum_{j=1}^{\infty}\frac{1}{\xi_j}C_{2j}[(\coth(\xi_j b)]\sin(\frac{j\pi x}{a}) \tag{96}$$

Using Equations (91) and (75) into (92), the solution of the partial differential Equation (74) can be obtained using Fourier series. Thus, through some simple mathematical transformations, we obtain

$$\sum_{j=1}^{\infty}C_{2j}A_j\sin(\frac{j\pi x}{a})=\sum_{j=1}^{\infty}Q_j\frac{(C^{'})(\frac{\eta_{c,l}}{n})}{b[D_{11}^{(1)}+D_{11}^{(2)}]}\sin(\frac{j\pi x}{a}) \tag{97}$$

where

$$A_j = -\frac{1}{\eta_c}\frac{1}{K\xi_j}(\frac{j\pi}{a})^2 - \frac{1}{\xi_j}\frac{(C^{'})^2}{b[D_{11}^{(1)}+D_{11}^{(2)}]} - (\alpha_{11}^{(1)}+\alpha_{11}^{(2)})\cdot\coth(\xi_j b) \tag{98}$$

Solving for Equation (77), we have

$$C_{2j} = \frac{Q_j}{A_j}\frac{\eta_{c,l}}{n}\frac{(C^{'})}{b[D_{11}^{(1)}+D_{11}^{(2)}]} \tag{99}$$

here Q_j and A_j are defined in Equations (76) and (78), respectively. Effective width b_{eff} can then be calculated as

$$b_{eff} = \frac{\int_0^b N_x(x,y)dy}{N_x(x,0)} = \frac{F(x)}{N_x(x,0)} \tag{100}$$

For double cantilever section combined with a box section as shown in Figure 5.24, effective width can be calculated as

$$b_{eff} = \frac{\int_0^b N_x^{cant.}(x,y)dy + \int_0^{b/2} N_x^{box}(x,y)dy}{N_x(x,0)} = \frac{F_x^{cant.}(x)+F_x^{box}(x,0)}{N_x(x,0)} \tag{101}$$

5.2.5. WF section

WF section is a panel with one shear connector in the middle. It can also apply to the shear connector in the middle of even number of cells such as two or four-cell sections. Based on symmetric conditions about x-axis, we have $C_{2j}=0$. Therefore, Equation (53) can be reduced to:

$$N_j(y) = C_{1j}\cosh(\xi_j y) \tag{102}$$

Since there are two shear flows emerging at the same shear connector, the force F(x) can be expressed as:

$$F(x) = -2\int N_{xy}(x, \frac{b}{2})dx = 2\sum_{j=1}^{\infty} \frac{C_{1j}}{\xi_j} \sinh(\frac{\xi_j b}{2}) \sin(\frac{j\pi x}{a}) \tag{103}$$

Since there is only one shear connector, Equation (74) can yield to

$$\frac{d^2F(x)}{K \cdot dx^2} = (\alpha_{11}^{(1)} + \alpha_{11}^{(2)}) N_x(x, \frac{b}{2}) - \frac{[M(x) - F(x)(C')](C')}{b[D_{11}^{(1)} + D_{11}^{(2)}]} \tag{104}$$

Solving for C_{1j}, we get Equation (99) where

$$A_j = \frac{2}{K\xi_j} (\frac{j\pi}{a})^2 \sinh(\frac{\xi_j b}{2}) + \frac{2}{\xi_j} \frac{(C')^2}{b[D_{11}^{(1)} + D_{11}^{(2)}]} \sinh(\frac{\xi_j b}{2}) + (\alpha_{11}^{(1)} + \alpha_{11}^{(2)}) \cosh(\frac{\xi_j b}{2}) \tag{105}$$

Effective width b_{eff} can then be calculated as:

$$b_{eff} = \frac{\int_0^b N_x(x, y)dy}{N_x(x, \frac{b}{2})} = \frac{F(x)}{N_x(x, \frac{b}{2})} \tag{106}$$

5.3. Degree of Composite Action

The DCA defined by Lorenz and Stockwell Lorenz and Stockwell (1984) was used in the American Institute of Steel Construction (AISC) AISC (2010), as shown in Figure 5.4. As mentioned previously, 100% and zero shear transfer can describe full-composite and non-composite cases, respectively. Partial DCA can describe the limited amount of slip due to the inadequacy of the shear connectors to maintain strain compatibility. We can extend this concept to the sandwich panel, as shown in Figure 5.9. Thus, DCA can be expressed as:

$$DCA = 1 - \frac{x}{x_{MAX}} \tag{107}$$

where *x* indicates the amount of the horizontal slip. Based on strain distributions shown in Figure 5.9, Equation (107) can be re-written as:

$$DCA = 1 - \frac{\varepsilon_2 - \varepsilon_1}{\varepsilon_{\max}} \tag{108}$$

Substituting Equation (107) into Equation (73) we have

$$(1 - DCA) \times \varepsilon_{\max} = (\alpha_{11}^{(1)} + \alpha_{11}^{(2)}) N_x(x, \frac{b}{2}) - \frac{[\left(\frac{\eta_{i,r} + \eta_{i,l}}{n}\right) M(x) - \left(\eta_{i,r} + \eta_{i,l}\right) F(x)(C')](C')}{b[D_{11}^{(1)} + D_{11}^{(2)}]} \tag{109}$$

where ε_{max} can be calculated based on 0% DCA, as shown in Figure 5.9. It should be noted that the distribution factors can be replaced according to the cross section configuration as shown above in Equations (104) and (93) for WF and cantilever section, respectively. ε_{max} can be expressed as:

$$\varepsilon_{\max} = \frac{[\left(\frac{\eta_{i,r} + \eta_{i,l}}{n}\right) M(x)](C')}{b[D_{11}^{(1)} + D_{11}^{(2)}]} \tag{110}$$

Substituting Equation (110) into Equation , DCA can be expressed as:

$$DCA = \frac{(\alpha_{11}^{(1)} + \alpha_{11}^{(2)}) N_x(x, 0) - \left(\eta_{i,r} + \eta_{i,l}\right) \frac{F(x)(C')^2}{b[D_{11}^{(1)} + D_{11}^{(2)}]}}{\varepsilon_{\max}} \tag{111}$$

The stress and deflection can be calculated as:

$$\sigma(x, y) = \frac{N_x(x, y)}{t} \tag{112}$$

$$\Delta(x) = e_r \iint \kappa(x) dx^2 \tag{113}$$

where *t* is the thickness of the upper wythe at a given cross-section, e_r is a correction factor to account for the assumption of all cell have the same curvature, which can be assumed to be 2/3 for

box and cantilever sections, and $\kappa(x)$ is the curvature and depend on the boundary conditions discussed earlier.

5.4. Verification

For verification purpose, the derived closed-form solution and FE method were used to study an insulated concrete sandwich panel, which was tested by Hopkins et al. Hopkins et al. (2014), as shown in Figure 5.1(b). The wythes were 3,032 mm (119.375 in) wide, 7,049 mm (277.5 in) long, and 76.2 mm (3 in) thick. They were separated by a 102 mm (4 in) thick foam core. The two wythes were connected with three CFRP shear connectors where the spacing between the shear connectors was 1,219 mm (48 in). CFRP shear connectors were flexible enough to provide partial DCA, they consisted of truss elements rotated at 45^o to transfer shear from upper wythe to lower wythe. Linear elastic FE models using ABAQUS ABAQUS (2013) were created to validate different configurations. The FE model for WF section is shown in Figure 5.3. The Young's modulus and Poisson's ratio for concrete were 29,322 MPa (4,253 ksi) and 0.15, respectively. For all the configurations, 44,482 N (10,000 lb) point load was applied above the shear connector. Four-node shell element (S4R) was used to model the concrete wythes. The mesh size was set to 50.8 mm by 50.8 mm (2 in x 2 in) for multi-cell box sections, whereas for WF and single box, the mesh size was decreased to 12.19 mm by 7.05 mm (0.47 in x 0.27 in) to provide more accurate results. To simulate different DCAs, the concrete wythes were connected using CONN3D element, where all stiffnesses were set to be rigid except the stiffness in the y-direction. It should be noted that the stiffness of any shear connector can be calculated through material properties, or by measuring displacement induced from lateral force subjected to the upper wythe while fixing the

lower wythe. The boundary conditions were set to be pin on one side and roller at the other side. The other two sides of the sandwich panel were also restrained.

The stress and displacement results at mid-span from the FE and analytical model for different DCAs are shown in Figures 5-5, where good correlations can be observed. The shear connector stiffness (K) were chosen to generate 100%, 75%, 50%, 25% and 0% DCAs. It should be noted that the shear connector stiffness in the analytical model is assumed to be continuous. However, in the FE model, the shear connectors exist only at each node in the longitudinal direction as shown in Figure 5.24. Therefore, the analytical stiffness (K) needs to be converted to the FE stiffness (K_{FE}) as follows:

$$K_{FE} = K \cdot \frac{a}{mesh\ size} \tag{114}$$

where *a* is the sandwich panel span. Stiffness values are shown in Table 5.1. Figure 5.25 shows the relationship between Effective Width Ratio (EWR) and DCA for different configuration, where again good correlations can be observed between the analytical and FE results. EWR is defined as the ratio between the effective width and width of the panel. EWR for double cantilever with single box are the lowest among other configuration which reach 0.62 for 100% DCA based on analytical results.

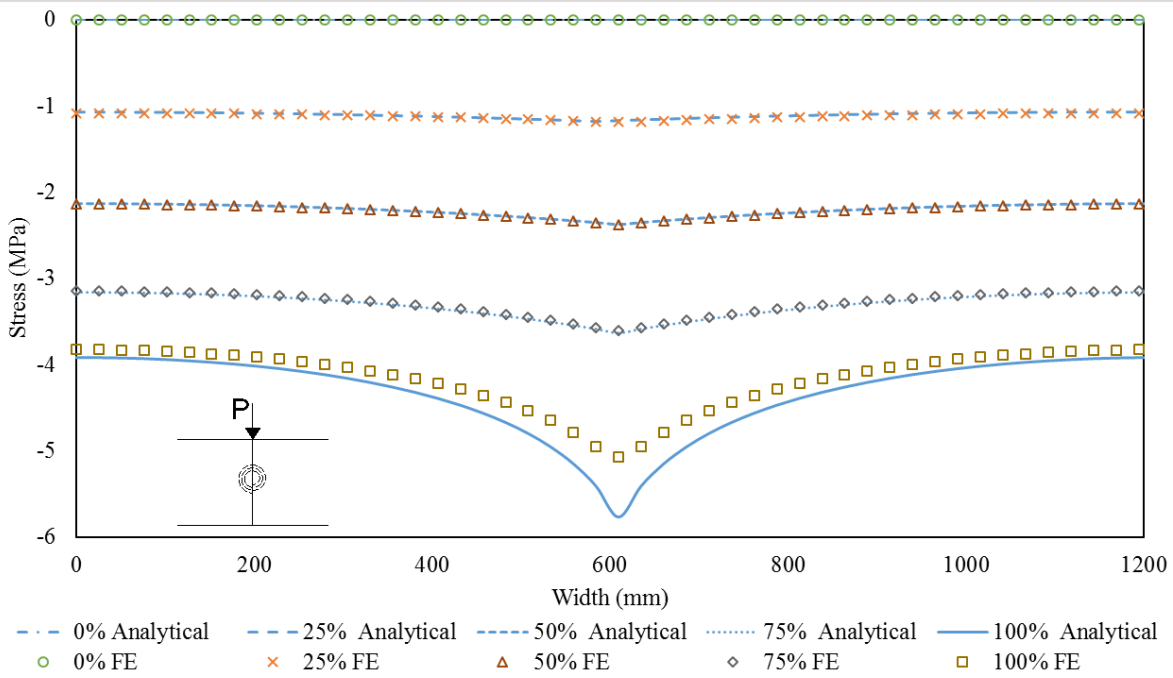

Figure 5.12 Stress distribution at mid-span for wide flange (WF) section

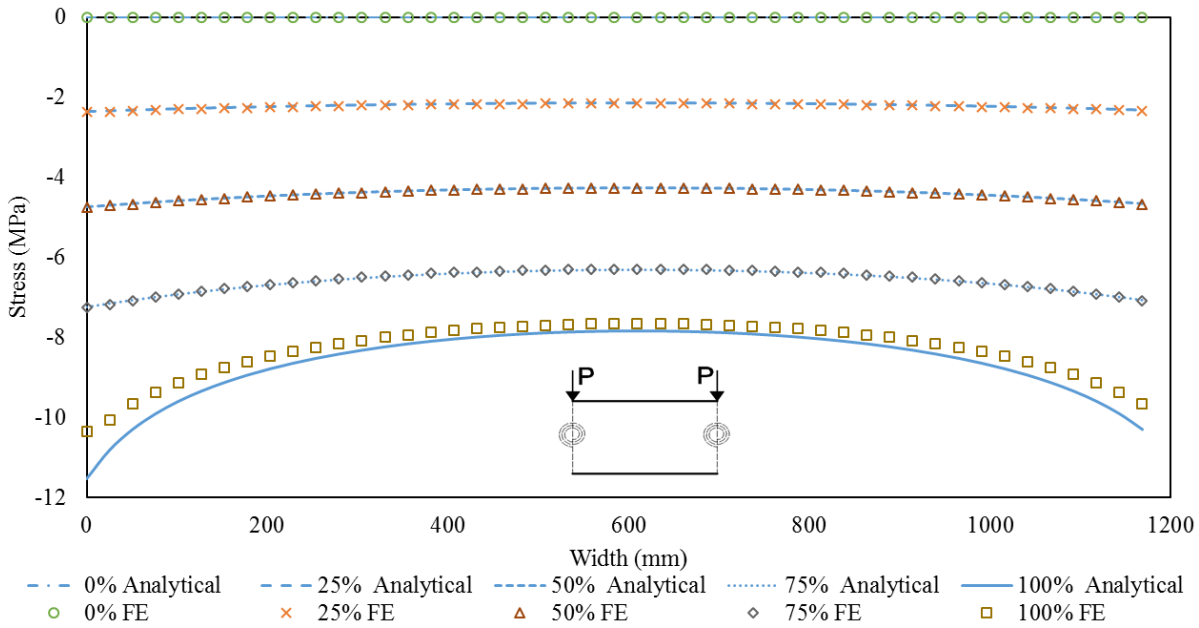

Figure 5.13 Stress distribution at mid-span for single box section

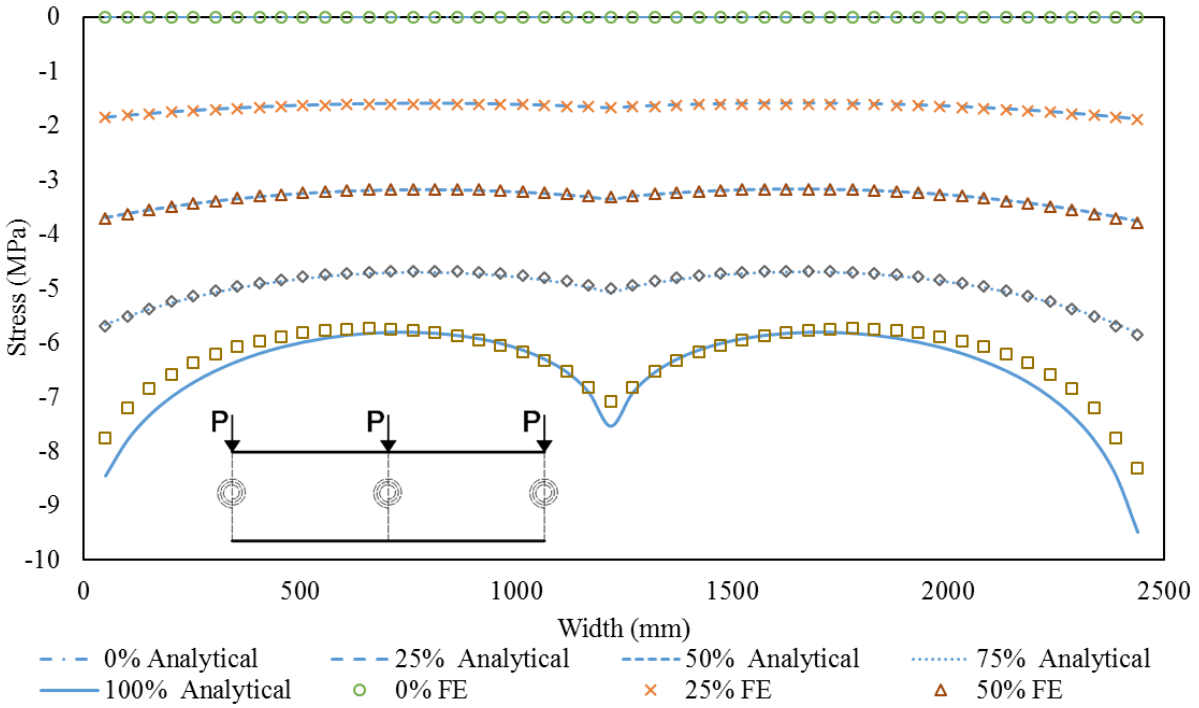

Figure 5.14 Stress distribution at mid-span for double box section

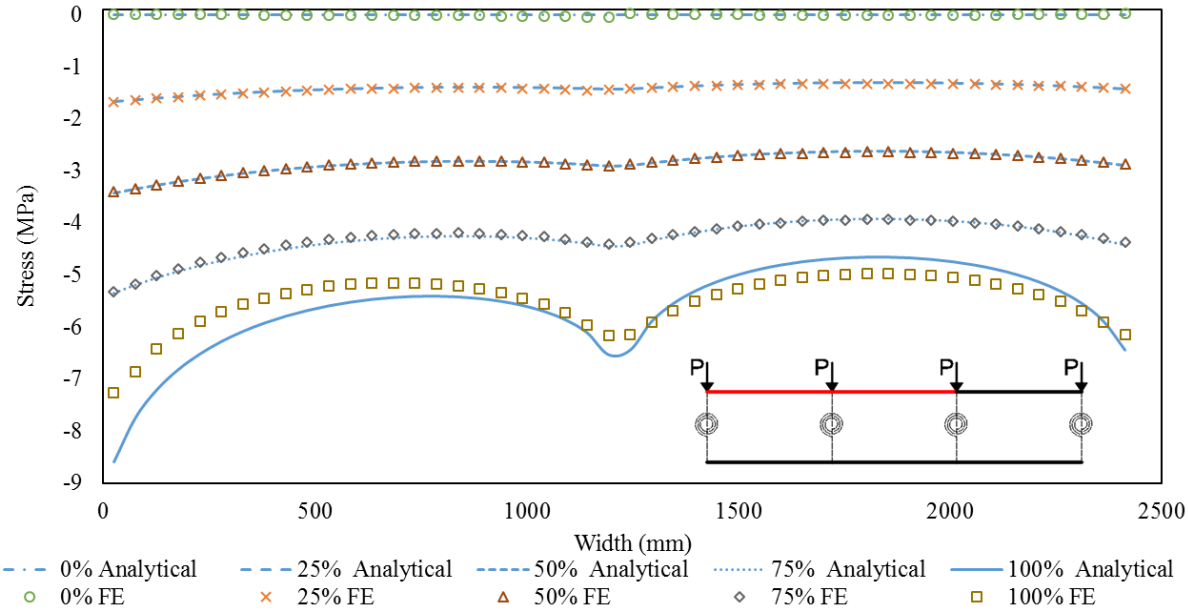

Figure 5.15 Stress distribution at mid-span for 3-cell box section

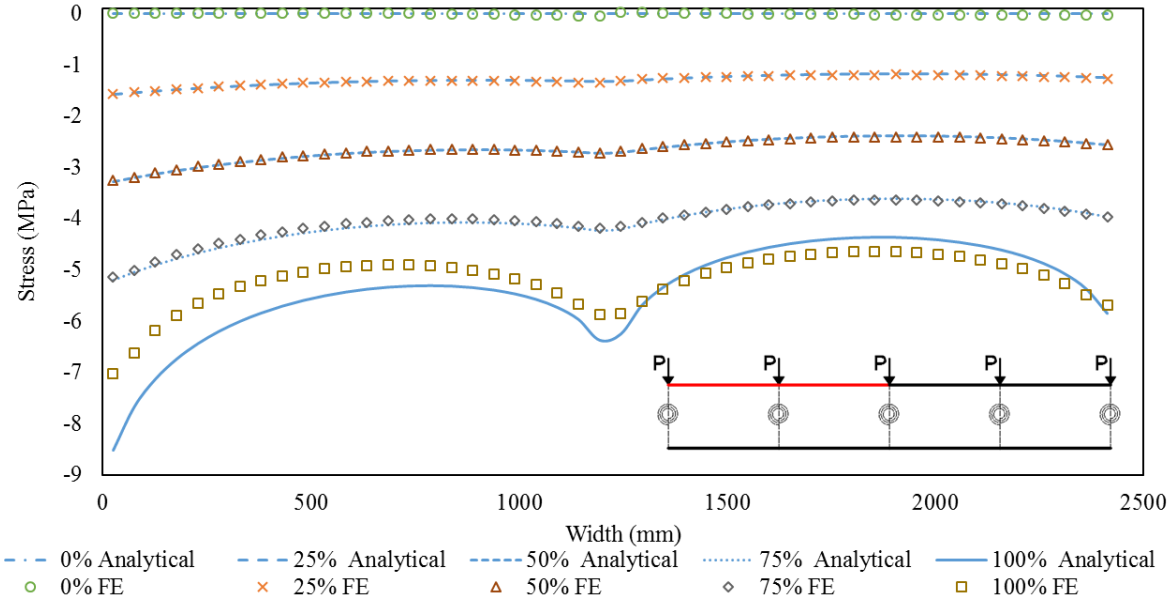

Figure 5.16 Stress distribution at mid-span for 4-cell box section

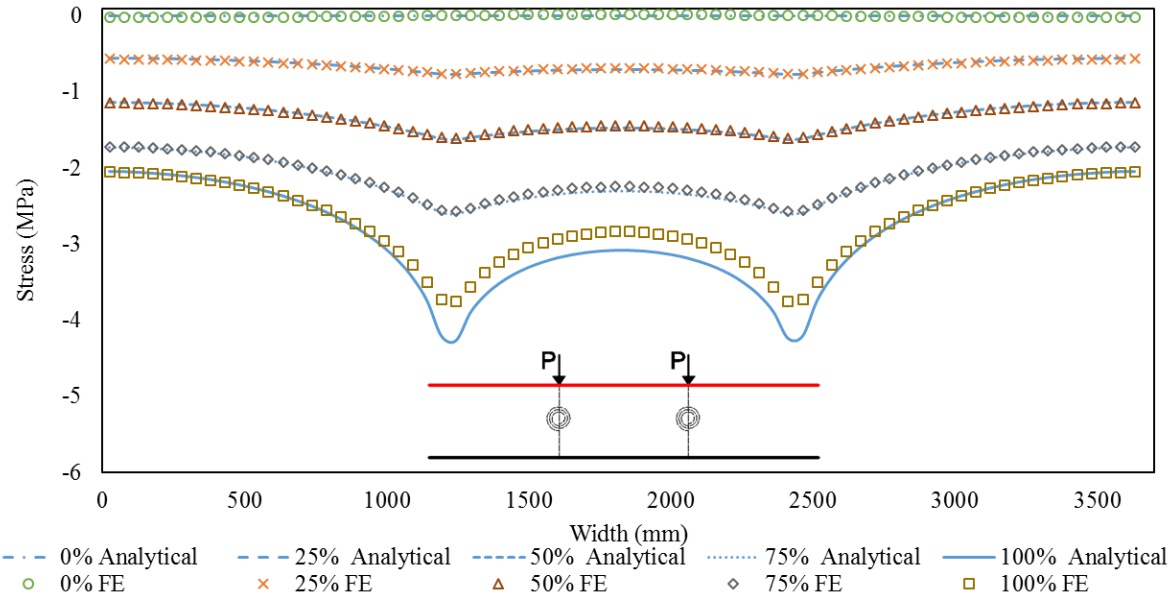

Figure 5.17 Stress distribution at mid-span for single box with double cantilever section

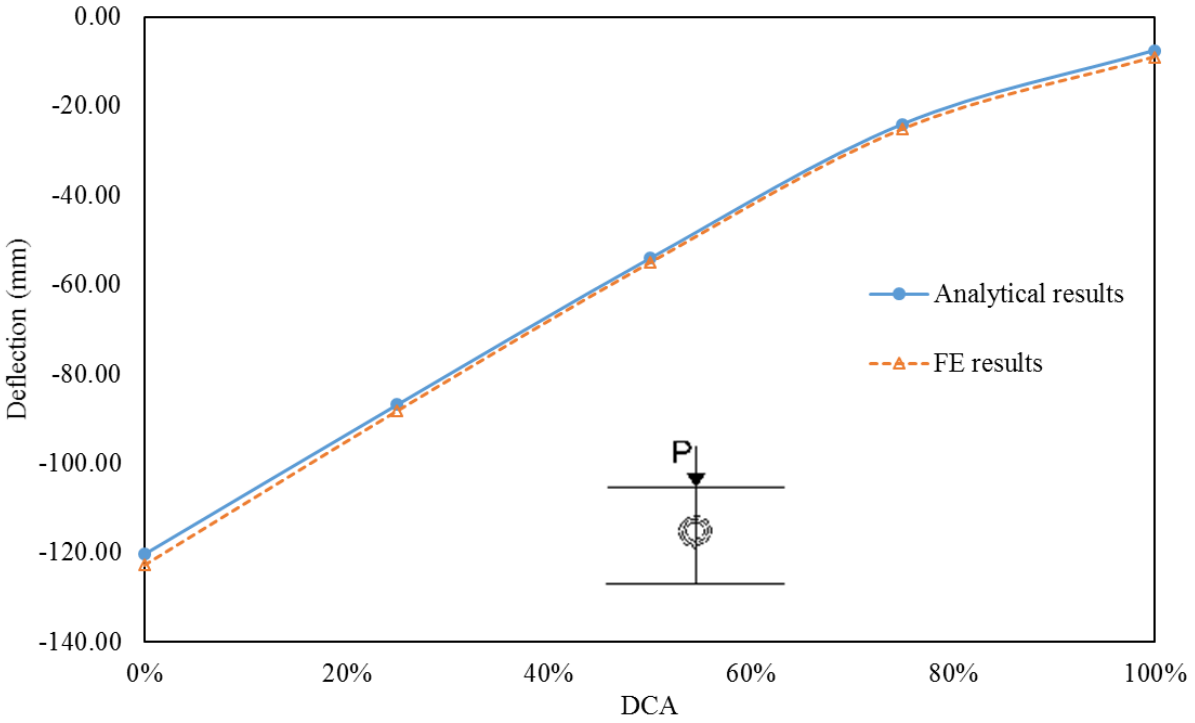

Figure 5.18 Deflection at mid-span for wide flange (WF) section

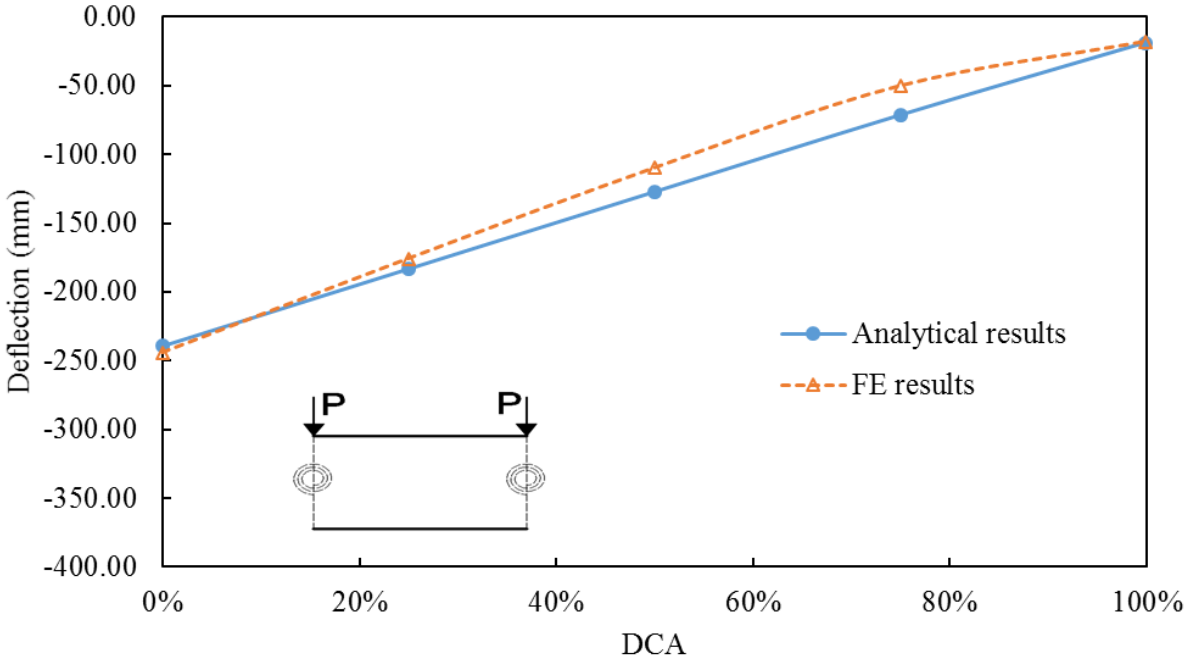

Figure 5.19 Deflection at mid-span for single box section

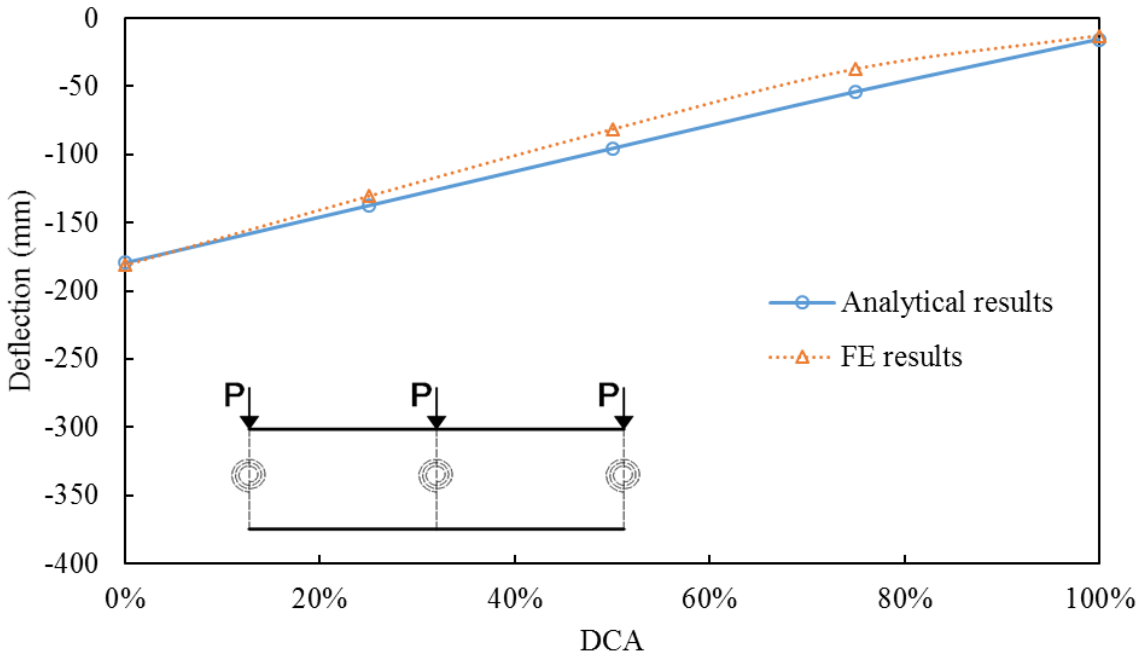

Figure 5.20 Deflection at mid-span for double box section

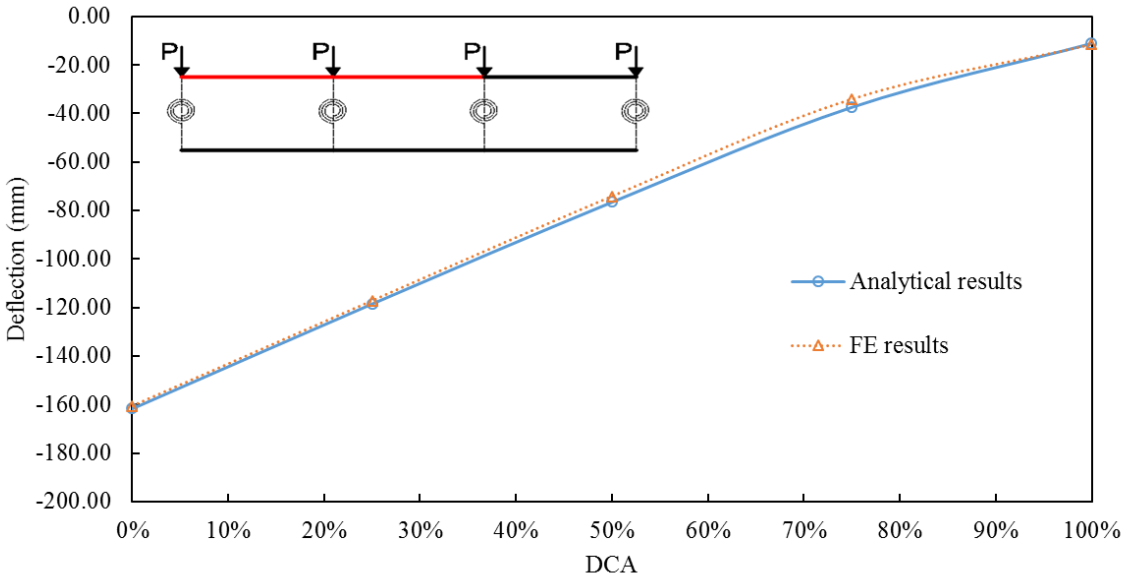

Figure 5.21 Deflection at mid-span for 3-cell box section

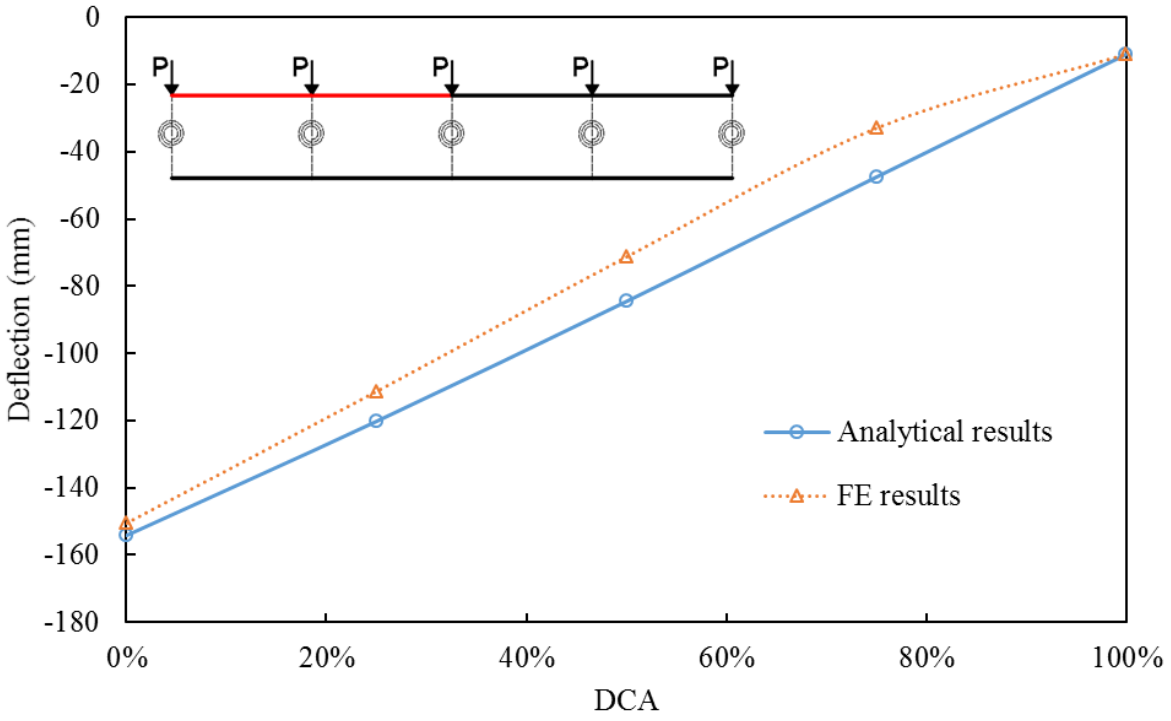

Figure 5.22 Deflection at mid-span for 4-cell box section

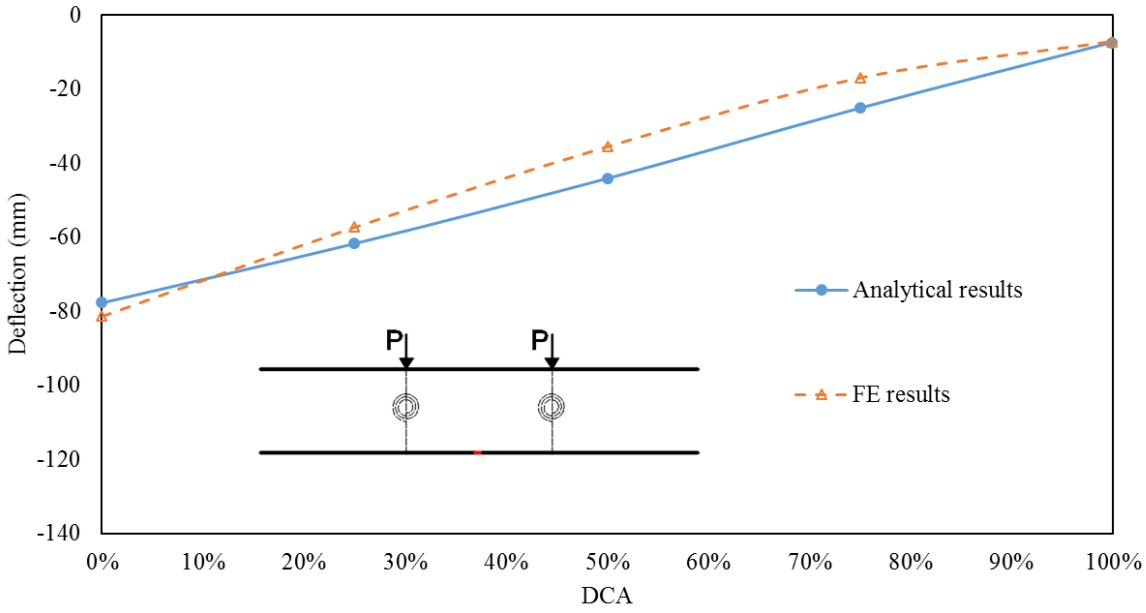

Figure 5.23 Deflection at mid-span for box section with double cantilever section

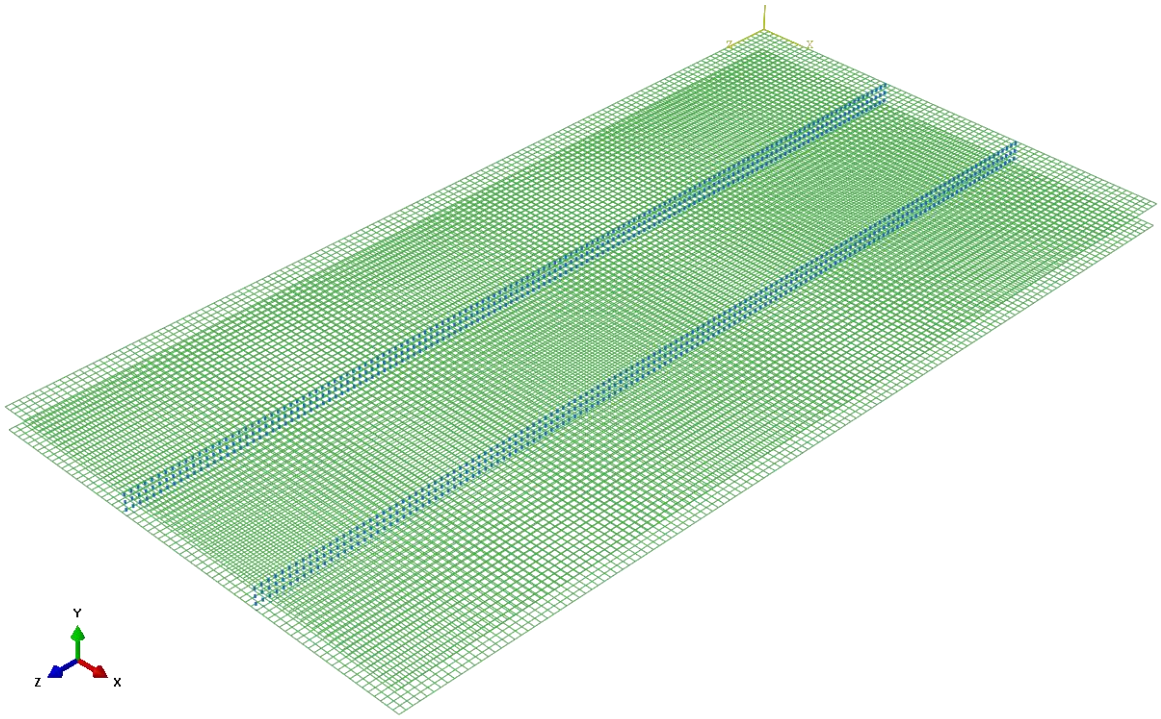

Figure 5.24 FE model for single box with double cantilever

Table 5.1 Shear connector stiffness (K) for different configurations

DCA	Cantilever		WF		Single-box	
	Analytical	FE	Analytical	FE	Analytical	FE
0%	0.00	0.00	0.00	0.00	0.00	0.00
25%	8.67	439.53	6.82	48.01	3.41	24.00
50%	29.50	1496.15	23.20	163.39	11.60	81.69
75%	124.65	6320.90	97.96	689.78	48.98	344.89
100%	3.20E+05	1.63E+07	2.47E+05	1.74E+06	1.24E+05	8.71E+05
DCA	Double box		3-cell		4-cell	
	Analytical	FE	Analytical	FE	Analytical	FE
0%	0.00	0.00	0.00	0.00	0.00	0.00
25%	4.56	32.13	4.87	246.96	4.95	251.03
50%	15.54	109.44	16.59	841.49	16.87	855.40
75%	65.93	464.22	70.47	3573.67	71.66	3633.95
100%	1.24E+05	8.71E+05	2.07E+05	1.05E+07	2.13E+05	1.08E+07

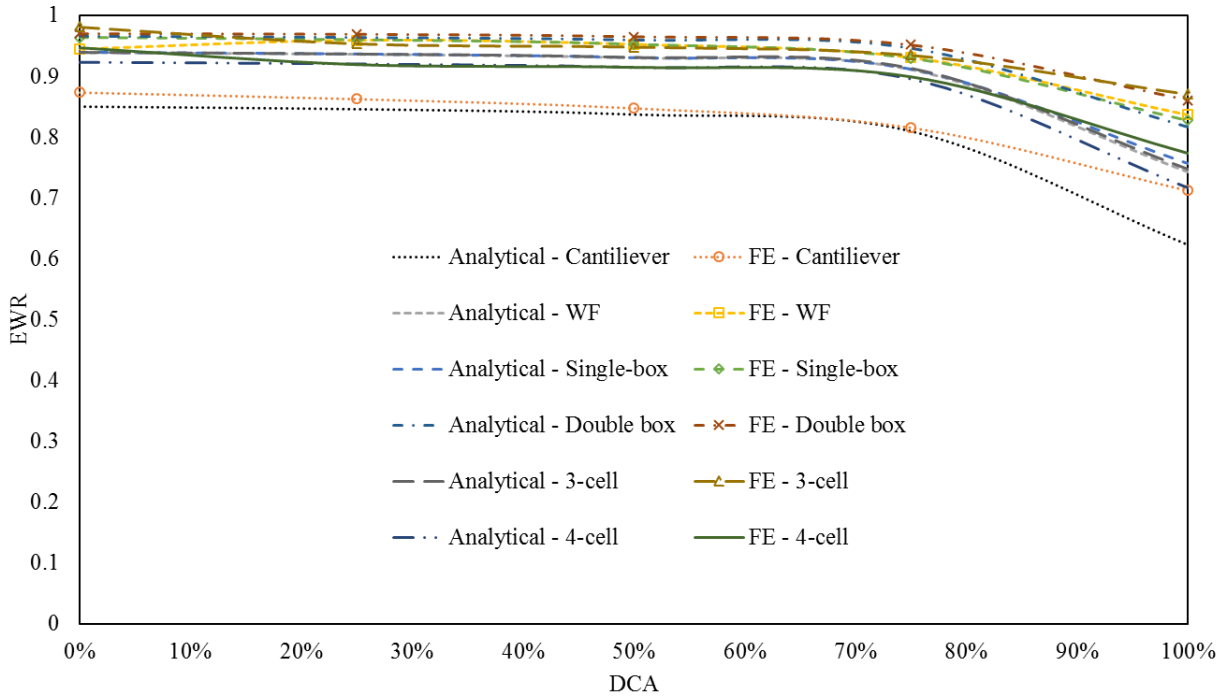

Figure 5.25 Effective width ratio (b_{eff}/b) vs. DCAs for different configuration

5.5. Applications

A parametric study was performed to study effective width of the double cantilever with single box model which was verified above. Figure 5.26 shows that the core thickness has negligible effect on EWR for DCAs up to 75%. For 100% DCA, the effective width is about 14% lower than that of 75% DCA with the same core and wythe thickness. EWR decreases until it reaches 30% difference between 100% and 75% DCA for the core-wythe thickness ratio of 5 or greater. Therefore, 100% DCA provides the smallest value for effective width, which can be used as a conservative value representing all DCAs. This finding will be used to derive simplified method, as will be discussed next.

The aspect ratio has a significant effect on EWR, as can be seen from Figure 5.27. The EWR with an aspect ratio of one is about 20% lower than that with an aspect ratio of 10. Therefore, it can be concluded that the derived equation is applicable to one-way panels.

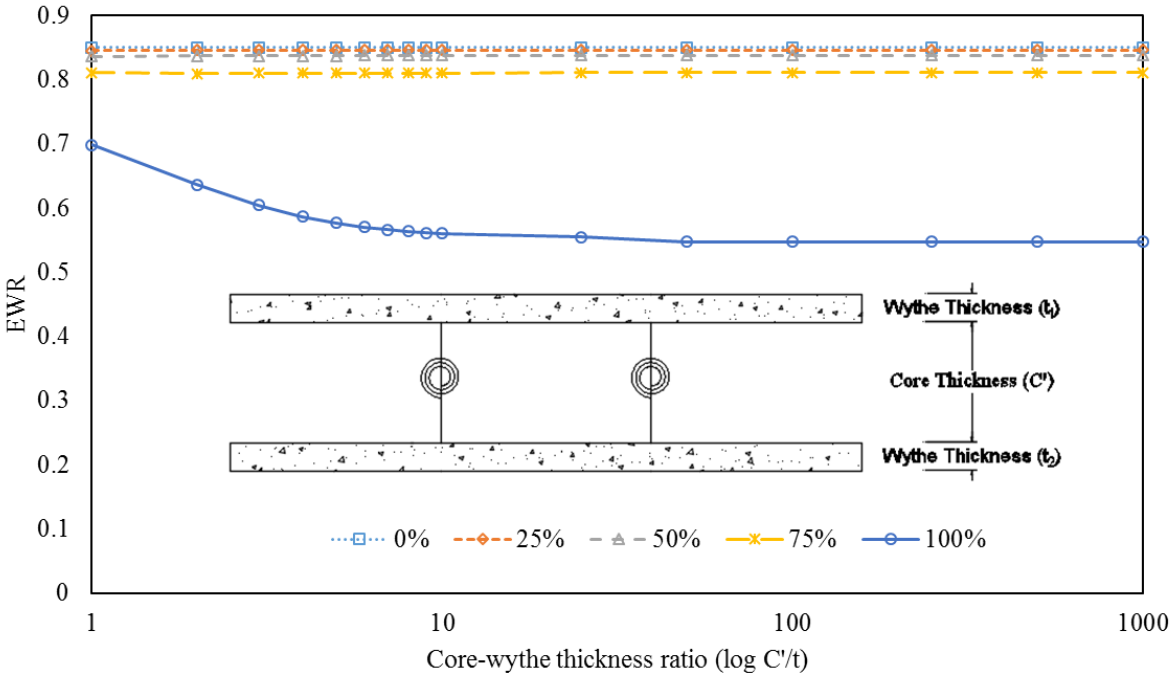

Figure 5.26 EWR vs. core/wythe thickness ratio for different DCAs

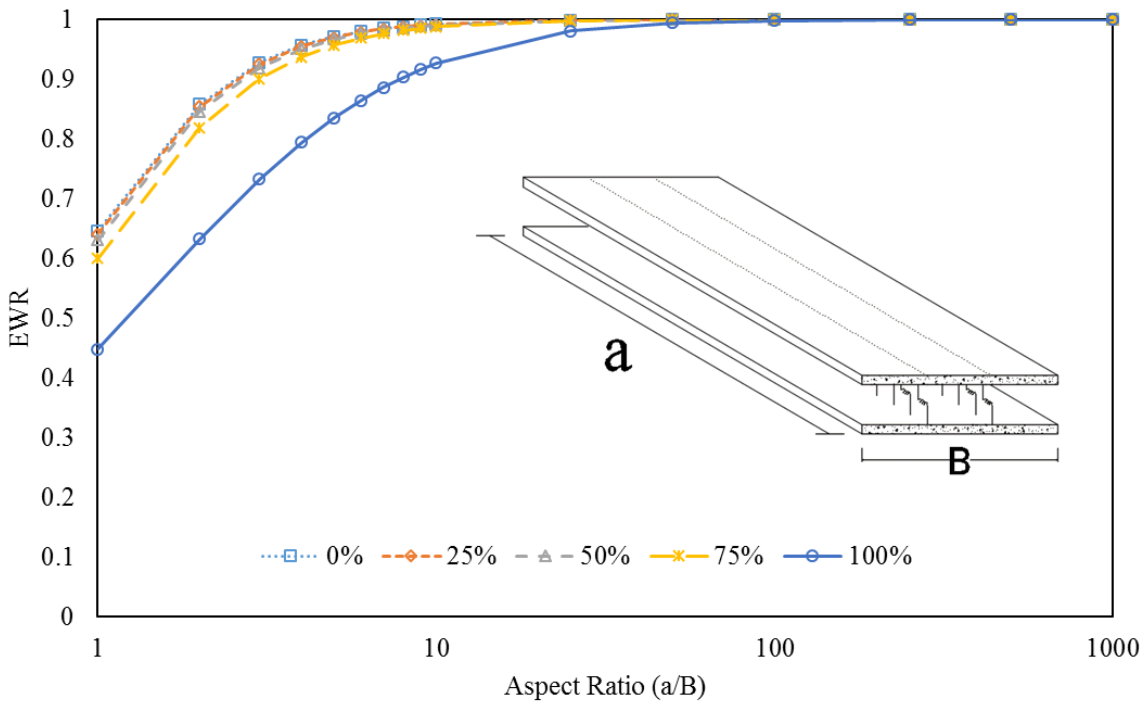

Figure 5.27 EWR vs. aspect ratio for different DCAs

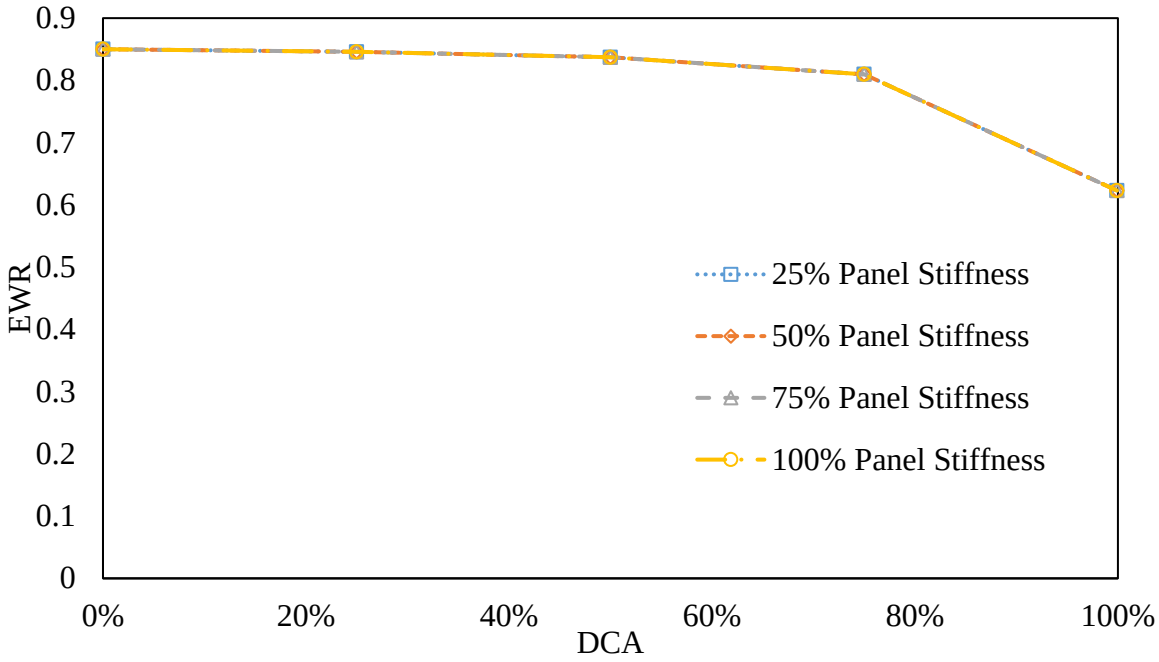

Figure 5.28 EWR vs. DCA for different panel stiffness

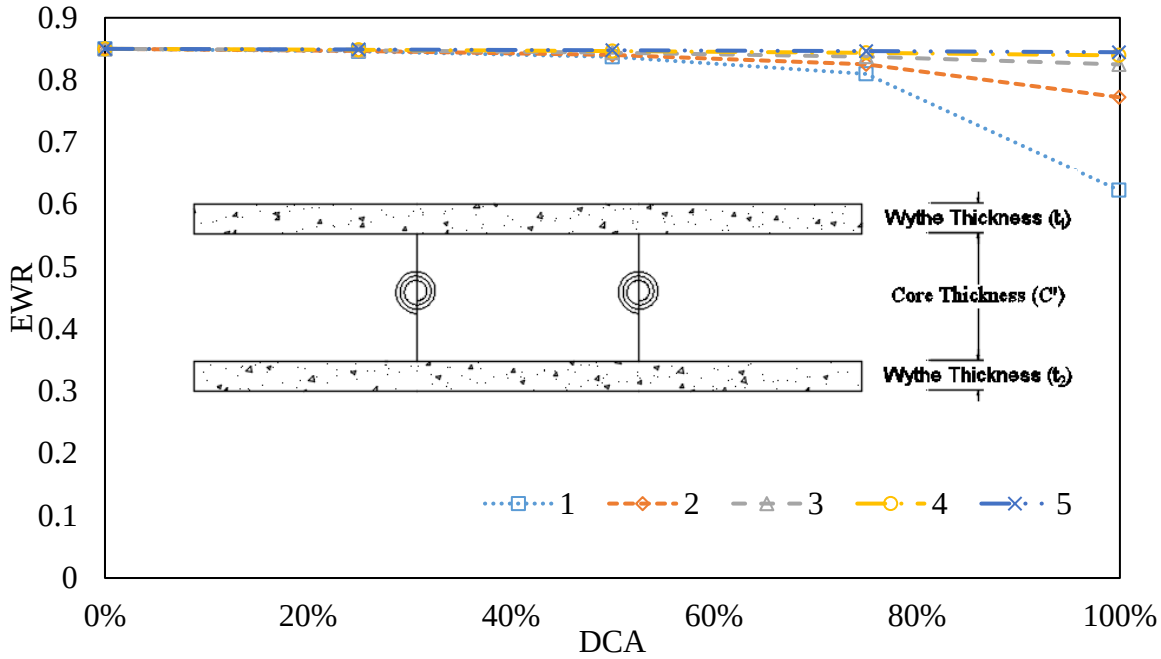

Figure 5.29 EWR vs. DCA for panel thickness ratio (t_1/t_2)

Figure 5.28 and Figure 5.29 show that stiffness and panel thickness ratio have negligible effects on EWR up to 75% DCA. When reaching 100% DCA, EWR drops about 17% for the same stiffness. EWR increases as the panel thickness ratio increases.

5.6. Simplified Method to Calculate the Deflection and Strain Distribution

In this section, a simplified method will be driven based on the parametric study results to calculate deflection and strain. The derivation is based on double cantilever with single box and is also valid for other configurations.

Based on Equations (46) and (90), Equation (80) can be approximated as:

$$\frac{1}{\eta_c} F_x^{cant.}(x) = \frac{1}{1-\eta_c} F_x^{box}(x,0) \tag{115}$$

Substituting Equation (115) into (101), $N(x,0)$ can be expressed as:

$$N(x,0) = \frac{F_x^{cant.}(x)}{\eta_c \cdot b_{eff}} \tag{116}$$

Based on the findings from the parametric study, b_{eff} for 100% DCA can be conservatively used to represent effective widths for other DCAs. Therefore, we can assume b_{eff} to be a constant. Substituting Equation (116) into (111), we have

$$DCA = \frac{F_x^{cant.}(x) \times [\frac{(\alpha_{11}^{(1)} + \alpha_{11}^{(2)})}{\eta_c \cdot b_{eff}} - (\eta_c) \frac{(C')^2}{b[D_{11}^{(1)} + D_{11}^{(2)}]}]}{\varepsilon_{\max}} \tag{117}$$

Therefore, DCA is in linear relationship to $F_x^{cant.}(x)$, i.e.

$$F_x^{cant.}(x) = DCA \times F_{100}(x) \tag{118}$$

where $F_{100}(x)$ is the maximum interfacial shear force transferred through the shear connection for a composite beam with 100% DCA. Based on this finding, the deflections and stresses of composite beams with partial DCA can be calculated from those with 100% and 0% DCAs as follows.

From Figure 5.8, we have

$$\kappa(x) = \frac{M(x)}{b \times D_{11}} = \frac{M_1(x)}{b \times D_{11}^{(1)}} = \frac{M_2(x)}{b \times D_{11}^{(2)}} = \frac{M_1(x) + M_2(x)}{b[D_{11}^{(1)} + D_{11}^{(2)}]} \tag{119}$$

where κ is curvature, D_{11} is the flexural rigidity, and $M(x)$, $M_1(x)$, and $M_2(x)$ are moments acting on the sandwich panel, upper layer, and lower layer, respectively. Applying 100% DCA to Equation (119), we have

$$\kappa_{100}(x)=\frac{M(x)}{b\times D_{11}}=\frac{M_{1-100}(x)}{b\times D_{11}^{(1)}}=\frac{M_{2-100}(x)}{b\times D_{11}^{(2)}}=\frac{M_{1-100}(x)+M_{2-100}(x)}{b[D_{11}^{(1)}+D_{11}^{(2)}]} \tag{120}$$

The subscript *100* denotes a 100% DCA composite action. For 0% DCA, we have

$$\kappa_{0}(x)=\frac{M(x)}{b\times D_{11}}=\frac{M_{1-0}(x)}{b\times D_{11}^{(1)}}=\frac{M_{2-0}(x)}{b\times D_{11}^{(2)}}=\frac{M_{1-0}(x)+M_{2-0}(x)}{b[D_{11}^{(1)}+D_{11}^{(2)}]} \tag{121}$$

where all symbols have the same meaning as those in Equation (120), but subscript *0* denotes a 0% DCA non-composite action.

Based on Equation (71) we have

$$F(x)(C')=M(x)-[M_1(x)+M_2(x)] \tag{122}$$

where *F(x)* is the interfacial shear force transferred through the shear connection. Combining Equations (118), (119) and (122), for any DCA, we have

$$\kappa(x)=\frac{M(x)-F^{cant}(x)(C')}{b[D_{11}^{(1)}+D_{11}^{(2)}]}=\frac{M(x)-DCA\times F_{100}(x)(C')}{b[D_{11}^{(1)}+D_{11}^{(2)}]} \tag{123}$$

Equation (123) can also be written as:

$$\kappa(x)=\frac{M(x)}{b[D_{11}^{(1)}+D_{11}^{(2)}]}-DCA\times\frac{F_{100}(x)(C')}{b[D_{11}^{(1)}+D_{11}^{(2)}]} \tag{124}$$

Based on Equation (122), we have

$$\kappa_0(x)-\kappa_{100}(x)=\frac{F_{100}(x)(C')}{b[D_{11}^{(1)}+D_{11}^{(2)}]}=\frac{M(x)}{b[D_{11}^{(1)}+D_{11}^{(2)}]}-\frac{M_1(x)+M_2(x)}{b[D_{11}^{(1)}+D_{11}^{(2)}]} \tag{125}$$

Using Equation (119) and (125) into (124), we have

$$\kappa(x)=\kappa_0(x)-DCA\times[\kappa_0(x)-\kappa_{100}(x)]=(1-DCA)\kappa_0(x)+DCA\times\kappa_{100}(x) \tag{126}$$

The deflection $\Delta(x)$ can be calculated by double integration of $\kappa(x)$ considering proper boundary conditions. For a simply supported sandwich panel considered in this study, we have

$$\Delta(x) = (1 - DCA)\Delta_0(x) + DCA \times \Delta_{100}(x) \tag{127}$$

The stress can be calculated based on $\kappa(x)$ for any layer as:

$$\sigma_z(x) = A_{11}[\kappa(x) \times z - \frac{\alpha_{11} \times DCA \times F_{100}(x)}{b_{eff}}] \tag{128}$$

Substituting Equation (126) into (128), we have

$$\sigma_z(x) = A_{11}\{[(1 - DCA)\kappa_0(x) + DCA \times \kappa_{100}(x)] \times z - \frac{\alpha_{11} \times DCA \times F_{100}(x)}{b_{eff}}\} \tag{129}$$

From Equation (128), we have

$$\sigma_{z0}(x) = A_{11}\kappa(x) \times z \tag{130}$$

$$\sigma_{z100}(x) = A_{11}[\kappa_{100}(x) \times z - \frac{\alpha_{11} \times F_{100}(x)}{b_{eff}}] \tag{131}$$

Comparing Equations (129) through (131), we can express Equation (128) in a similar expression to Equation (127) as

$$\sigma_z(x) = (1 - DCA)\sigma_{z0}(x) + DCA \times \sigma_{z100}(x) \tag{132}$$

where again the subscripts *0* and *100* denote composite beams with 0% and 100% DCAs, respectively.

To evaluate the accuracy of the proposed simplified method, Equations (127) and (132) are used to calculate the deflection and stresses at the mid-height and mid-span of either wythe, with the results shown in Figure 5.30 and Figure 5.31, respectively. It can be observed that simplified method and analytical results are close to each other except for the stress at 75% DCA, which has

a difference of 36%. Therefore, the simplified equations can be used to provide conservative results for deflections and stresses, which is applicable for practical design purposes.

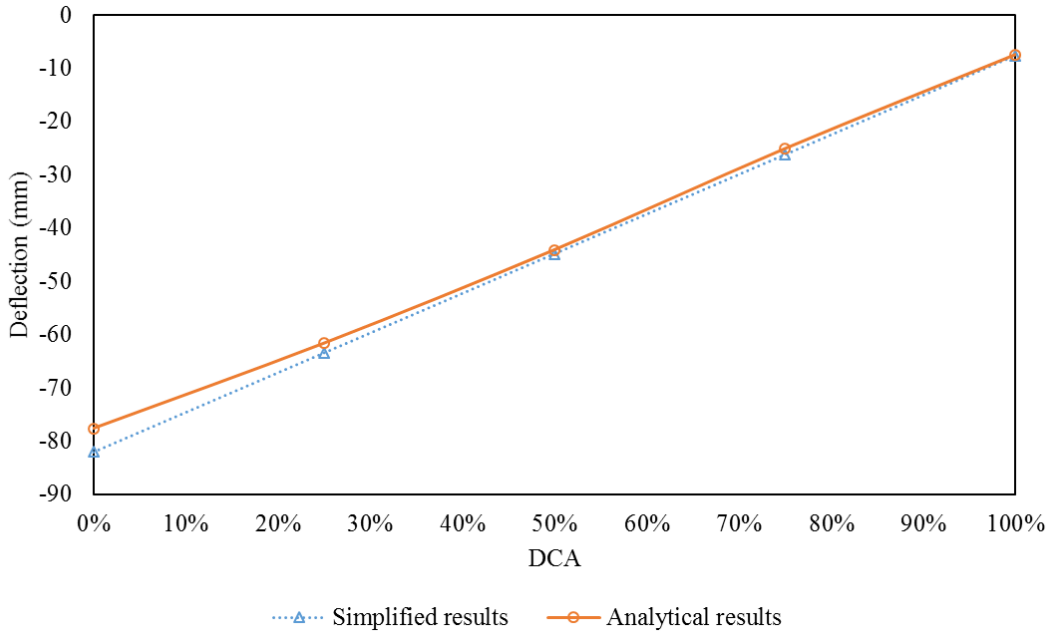

Figure 5.30 Mid-span deflection vs. DCA

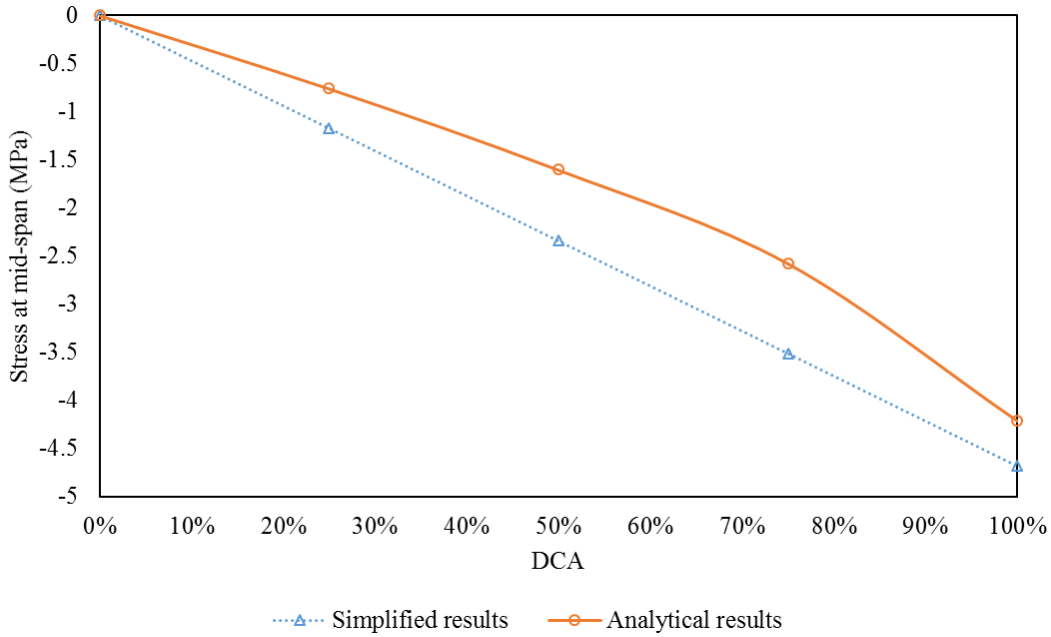

Figure 5.31 Mid-span stress vs. DCA

5.7. Conclusions

This study develops an analytical model for calculating effective width of sandwich panel based on shear lag model and considering partial DCA for single and multiple shear connectors. It can be concluded that:

1. The analytical model can accurately predict the behavior of the sandwich panels in terms of stress/strain and deflection, considering the partial DCA.
2. The analytical model can be used for single, multi-cell, wide flange, cantilever sections or a combination of any configuration.
3. DCA can significantly affect the stress and strain distributions.
4. The parametric study results show that the smallest value of effective width can be achieved with 100% DCA.
5. Aspect ratio is an important factor that affects the effective width. The derived closed-form equation is only valid for one-way panel.
6. Core thickness and panel stiffness have negligible effects on the effective width.

It is noted that this analytical model is based on elastic behavior. Further study is recommended to consider plastic behavior of sandwich panels.

5.8. References

ABAQUS. (2013). "ABAQUS Documentation." Dassault Systèmes, Providence, RI, USA.

AISC. (2010). *Specification for Structural Steel Buildings (ANSI/AISC 360-10). American Institute of Steel Construction*, Chicago-Illinois.

Barbero, E. J., Lopez-Anido, R., and Davalos, J. F. (1993). "On the mechanics of thin-walled laminated composite beams." *Journal of Composite Materials*, Sage Publications, 27(8), 806–829.

Benayoune, A., Abdul Samad, A. A., Trikha, D. N., Abang Ali, A. A., and Ellinna, S. H. M. (2008). "Flexural behaviour of pre-cast concrete sandwich composite panel - Experimental and theoretical investigations." *Construction and Building Materials*, 22(4), 580–592.

Bradford, M. A. (2011). "On the Interaction of Partial Interaction and Shrinkage in Composite Steel-Concrete T-Beams." *Procedia Engineering*, 14, 396–401.

Chen, A., Norris, T. G., Hopkins, P. M., and Yossef, M. (2015). "Experimental investigation and finite element analysis of flexural behavior of insulated concrete sandwich panels with FRP plate shear connectors." *Engineering Structures*, 98, 95–108.

Chen, A., and Yossef, M. (2015). "Analytical Model for Deck-On-Girder Composite Beam System with Partial Composite Action." *Journal of Engineering Mechanics*, 4015087.

Cheung, M. S., and Chan, M. Y. T. (1978). "Finite strip evaluation of effective flange width of bridge girders." *Canadian Journal of Civil Engineering*, NRC Research Press, 5(2), 174–185.

Dawood, M., Taylor, E., and Rizkalla, S. (2010). "Two-way bending behavior of 3-D GFRP sandwich panels with through-thickness fiber insertions." *Composite Structures*, 92(4), 950–963.

Einea, A., Salmon, D. C., Fogarasi, G. J., Culp, T. D., and Tadros, M. K. (1991). "State-of-the-Art of Precast Concrete Sandwich Panels." *PCI Journal*, 36(6), 78–98.

Einea, A., Salmon, D. C., Tadros, M. K., and Culp, T. (1994). "A New Structurally and Thermally Efficient Precast Sandwich Panel System." *PCI Journal (Precast/Prestressed Concrete Institute)*, 39(4), 90–101.

Evans, H. R., Ahmad, M. K. H., and Kristek, V. (1993). "Shear lag in composite box girders of complex cross-sections." *Journal of Constructional Steel Research*, 24(3), 183–204.

Evans, H. R., and Shanmugam, N. E. (1979). "An approximate grillage approach to the analysis of cellular structures." *Proc Inst Civ Eng (London)*, 67(pt 2), 133–154.

Evans, H., and Taherian, A. (1977a). "The prediction of the shear lag effect in box girders." *Proceedings of the Institution of Civil Engineers*, 63(1), 69–92.

Evans, H., and Taherian, A. (1977b). "The bar simulation method for the calculation of shear lag in multi-cell and continous box girders." *Proceedings of the Institution of Civil Engineers*, 63(4), 881–897.

Fam, A., and Sharaf, T. (2010). "Flexural performance of sandwich panels comprising polyurethane core and GFRP skins and ribs of various configurations." *Composite Structures*, 92(12), 2927–2935.

Frankl, B. A., Lucier, G. W., Hassan, T. K., and Rizkalla, S. H. (2011). "Behavior of precast, prestressed concrete sandwich wall panels reinforced with CFRP shear grid." *PCI journal*, Precast/Prestressed Concrete Institute, 56(2), 42–54.

Hopkins, P., Brown, K., Yossef, M., and Chen, A. (2014). "The effect of degree of composite action on flexural behavior of precast concrete sandwich panels." *7th International Conference on FRP Composites in Civil Engineering*, 1–6.

Kemmochi, K., Akasaka, T., Hayashi, R., and Ishiwata, K. (1980). "Shear-Lag Effect in Sandwich Panels With Stiffeners Under Three-Point Bending." *Journal of Applied Mechanics*, 47(2), 383.

Kristek, V. (2004). "A Shear Lag Analysis for Composite Box Girders with Deformable Connectors." *Acta Polytechnica - Journal of Advanced Engineering*, 44(5–6), 1–21.

Kristek, V., Evans, H. R., and Ahmad, M. K. M. (1990). "A shear lag analysis for composite box girders." *Journal of Constructional Steel Research*, 16(1), 1–21.

Lorenz, R. F., and Stockwell, F. W. (1984). "Concrete Slab Stresses in Partial Composite Beams and Girders." *Engineering Journal-American institute of steel construction*, 21(3), 185–188.

Manalo, A. C., Aravinthan, T., Karunasena, W., and Islam, M. M. (2010). "Flexural behaviour of structural fibre composite sandwich beams in flatwise and edgewise positions." *Composite Structures*, 92(4), 984–995.

Newmark, N. M., Siess, C. P., and Viest, I. M. (1951). "Tests and analysis of composite beams with incomplete interaction." *Proceedings of the Society of Experimental Stress Analysis*, 9(1), 75–92.

Okeil, A. M., and El-Tawil, S. (2004). "Warping Stresses in Curved Box Girder Bridges: Case Study." *Journal of Bridge Engineering*, 9(October), 487–496.

Reis, E. M., and Rizkalla, S. H. (2008). "Material characteristics of 3-D FRP sandwich panels." *Construction and Building Materials*, 22(6), 1009–1018.

Reissner, E. (1941). "Least Work Solutions of Shear Lag Problems." *Journal of the Aeronautical Sciences (Institute of the Aeronautical Sciences)*, American Institute of Aeronautics and Astronautics.

Reissner, E. (1946). "Analysis of shear lag in box beams by the principle of minimum potential energy." *Quarterly of applied mathematics*, 5(3), 268.

Salim, H. A., and Davalos, J. F. (2005a). "Shear Lag of Open and Closed Thin-walled Laminated Composite Beams." *Journal of Reinforced Plastics and Composites* , 24(7), 673–690.

Salim, H. A., and Davalos, J. F. (2005b). "Shear Lag of Open and Closed Thin-walled Laminated Composite Beams." *Journal of Reinforced Plastics and Composites* , 24(7), 673–690.

Salmon, D. C., and Einea, A. (1995). "Partially Composite Sandwich Panel Deflections." *Journal of Structural Engineering*, American Society of Civil Engineers, 121(4), 778–783.

Sharaf, T., and Fam, A. (2011). "Experimental Investigation of Large-Scale Cladding Sandwich Panels under Out-of-Plane Transverse Loading for Building Applications." *Journal of Composites for Construction*, American Society of Civil Engineers, 15(3), 422–430.

Song, S.-T., Chai, Y. H., and Hida, S. E. (2003). "Live-Load Distribution Factors for Concrete Box-Girder Bridges." *Journal of Bridge Engineering*, 8(5), 273–280.

Ugale, T. V, Patel, B. A., and Mojidra, H. V. (2006). "Analysis of Multicell Type Box Girder Bridges." *Advances in Bridge Engineering*, 207–216.

Upadyay, A., and Kalyanaraman, V. (2003). "Simplified analysis of FRP box-girders." *Composite Structures*, 59(2), 217–225.

Wade, T. G., Porter, M. L., and Jacobs, D. R. (1988). "Glass-fiber composite connectors for insulated concrete sandwich walls." *Engineering Research Institute, Iowa State University, Ames, Iowa*.

Zou, B., Chen, A., Davalos, J. F., and Salim, H. A. (2011). "Evaluation of effective flange width by shear lag model for orthotropic FRP bridge decks." *Composite Structures*, 93(2), 474–482.

CHAPTER 6. ANALYTICAL MODEL FOR DECK-ON-GIRDER COMPOSITE BEAM SYSTEM WITH PARTIAL COMPOSITE ACTION

A paper published at ASCE Engineering Mechanics Journal

An Chen and Mostafa Yossef

Abstract

In a deck-on-girder composite beam system, the deck and supporting girders work together to effectively provide loading capacity. This system has been widely used for bridges, buildings and other structures. Effective flange width is typically used to reduce a three-dimensional behavior of the composite beam system to the analysis of a T-beam section with a reduced width of deck. Current studies, including AASHTO Specifications, are mainly focused on concrete decks with full composite action. This paper presents a closed-form solution to study the composite beam system, which considers different degrees of composite action (DCAs) between the deck and supporting girders and can be applied to decks with orthotropic materials. The analytical model is verified through close correlations among test, finite element, and analytical results for two T-beams with concrete and Fiber-Reinforced Polymer (FRP) decks, in terms of both deflections and stress distributions. A parametric study is then conducted using the analytical model to study the effects of DCA, deck stiffness, and aspect ratio on effective flange width. Finally, a simplified method is proposed to analyze the composite beam system with different DCAs, which can be used for design purposes.

6.1. Introduction

As shown in Figure 6.1, composite beams are composed of decks and supporting girders. They are commonly used for large span applications for bridges, buildings, and other structures. Typically, the supporting girders are made of steel. The decks can be made of various materials,

including concrete, Fiber-Reinforced Polymer (FRP), timber, etc. Due to in-plane shear flexibility of the deck, the longitudinal normal stress over the deck section is non-uniform, as shown in Figure 6.1, which is known as shear lag effect. Effective flange width is typically used to describe this effect.

The behavior of the composite beam depends on the shear force transferred through the shear connections between the deck and supporting girders. For concrete–steel composite beams, the most commonly used shear connectors are headed shear studs, which can provide horizontal shear and prevent the slippage between the two components. Therefore, although there were limited studies reporting partial composite action for concrete slab-on-girder system (Newmark et al. 1951; Ranzi et al. 2004; Ranzi and Bradford 2006; Ranzi et al. 2006), majority of the studies treated the connection as full composite, including Heins and Fan (1976), Cheung and Chan (1978), etc. More recently, Chiesanichakorn et al. (2004) proposed a different method for defining the effective flange width for the composite section considering through-thickness variation of the stresses. Full composite case is also considered in AASHTO specifications (2014) to calculate effective flange width, primarily for concrete slab. They consider span length, girder spacing, slab thickness, and girder dimension as the most important parameters. The Canadian highway bridge design code CSA defines the effective flange width in a similar manner.

As pointed out by Lorenz and Stockwell (1984), if shear connectors are inadequate to maintain strain compatibility at the interface of the deck and the top of the steel, limited amount of slip will occur, resulting in a partial composite action. In recent years, FRP bridge decks have been increasingly used because of their advantages of fast construction, light-weight, and durability. Unlike shear connection for concrete slab-steel composite beams, there are two major types of connections for FRP deck-steel beams: (1) adhesive connection, which is formed by

applying adhesive glue at deck-girder interface (Keller and Gurtler 2005); and (2) mechanical connection, which is formed by connecting FRP decks to steel girders by using steel clamps, bolts, or shear studs (Moon et al. 2002; Keelor et al. 2004; Davalos et al. 2011). Various degrees of composite actions and effective flange widths were reported for different connections. Keelor et al. (2004) reported that under service load, the effective flange width corresponded to about 90% of the girder spacing for interior girders; and 75% of half girder spacing for exterior girders, respectively. Keller and Gurtler (2005) conducted lab tests on two large-scale T-sections. Their results showed that under service limit state, normal stress was almost uniform across the panel section. While under failure limit state, the normal stress decreased towards the panel edges, indicating a more pronounced effect of shear lag. Based on in-situ tests of Glass FRP (GFRP) decks, Moses (2006) reported that the composite behavior of GFRP decks degraded significantly in a few years. While composite behavior could be achieved at service limit state, they questioned that the composite behavior might not be appropriate at ultimate limit state. Based on comprehensive push-out tests at component level, and three-point bending tests on a T-section model at system level, Davalos et al. (2011) concluded that 25% composite action was achieved for the connection used in their study.

However, only limited studies and design equations are available to calculate the effective flange width for FRP deck-on-steel girder bridges with partial composite action, e.g., Davalos et al. (2012) proposed an equation to calculate effective flange for composite beams with partial composite action based on limited testing data. Until now, most of the design is still based on noncomposite action, i.e., the FRP deck is neglected in stiffness and strength calculations, which leads to excessively conservative design. Therefore, there is a need to systematically study the composite beam system with partial composite actions and define their effective flange widths,

which is the objective of this study. To this end, an analytical model, which can describe the performance of the composite beam system, including stiffness and stress distributions, needs to be developed.

Different methods have been used to study composite beams with partial composite action. Newmark et al. (1951) derived an analytical model for composite beam with incomplete interaction by solving a differential equation for the force transmitted through the shear connection. They provided expressions for the slip, shear between interacting elements, strains, and deflection. The analytical results were compared with those from the T-beam and push-out tests, and they were generally in good agreement. However, in their model, the slab was treated as a beam, and therefore, the shear lag effect could not be captured.

Ranzi et al. (2004) presented a direct stiffness method to derive stiffness matrices for two types of elements, with 6 and 8 degrees of freedom (DOF), for a composite beam with partial interaction to be implemented into finite element algorithms. The degrees of freedom considered in the 8-dof stiffness matrix were vertical displacement, rotation, slip, and axial displacement at the level of the reference axis; while those for the 6-dof stiffness matrix were vertical displacement, rotation, and slip. These elements could overcome the locking curvature problem which occurred due to the combination of inconsistent field equations. This method assembled the stiffness matrix from an initially unloaded element whose freedoms were constrained except one, for which a unit value was imposed. Ranzi and Bradford (2006) derived an exact analytical solution for the time-dependent analysis of composite steel–concrete beams with partial shear, based on three unknowns, i.e., the strain in the top fiber of the cross section, the curvature, and slip strain. Three equations were utilized to solve the problem: horizontal equilibrium at the cross section, rotational equilibrium at the cross section, and horizontal equilibrium of a free body diagram of the top

elements. Ranzi et al. (2006) further compared the above two methods with finite difference and finite element methods and concluded that the exact analytical solution and direct stiffness formulation provided identical results, as the stiffness coefficients of the latter formulation were derived based on the exact solution of the governing differential equations of the partial interaction problem. Although these methods can provide accurate results, they are complicated to implement. Furthermore, no calculation of effective flange width was provided in these studies.

On the other hand, Salim and Davalos (2005) used harmonic technique to conduct a shear lag analysis for thin-walled opened and closed composite beams. This method is easy to implement and has direct physical meaning. Zou et al. (2011) applied this method to study FRP deck-on-steel girder bridges with full composite action, i.e., there was no slip between the deck and supporting girders. This paper presents an important step to extend this theory for composite beams with partial composite action.

6.2. Research Significance

In this paper, a shear lag model is developed to study composite beams with partial composite action. This model is verified by close correlations among analytical, Finite Element (FE) and test results on two composite beams, one with concrete deck and the other with FRP deck. Parametric study is then conducted using the derived model and parameters that influence the effective flange width are identified, based on which a simplified method is proposed to calculate the deflections and stress/strain distributions of the composite beams considering different DCAs.

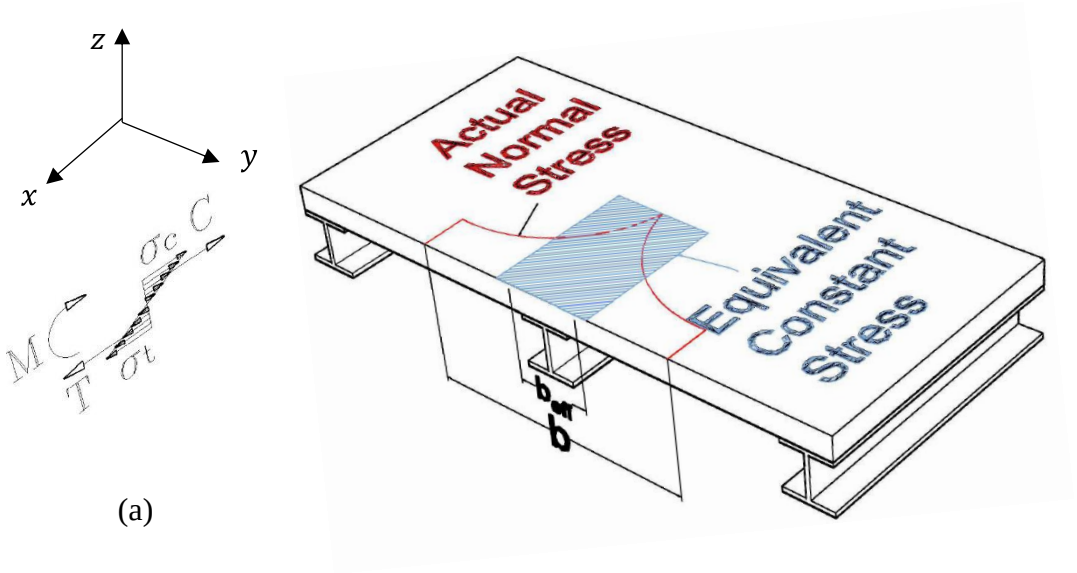

(a) (b)

Figure 6.1 Effective Flange Width (Zou et al. 2011), (a) Stress Distribution under out-of-plane Moment, (b) Shear Lag Effect

6.3. Analytical Model

Figure 6.1 displays a bridge consists of an orthotropic deck. The constitutive relationship for an orthotropic deck can be described as:

$$\begin{Bmatrix}\{N\}\\ \{M\}\end{Bmatrix} = \begin{bmatrix}[A] & 0\\ 0 & [D]\end{bmatrix}\begin{Bmatrix}\{\varepsilon\}\\ \{\kappa\}\end{Bmatrix} \tag{1}$$

where *{N}* and *{M}* are in-plane load and moment vectors, respectively; *[A]* and *[D]* are extensional stiffness and bending stiffness matrices, respectively; and *{ε}* and *{κ}* are in-plane strain and curvature vectors, respectively. *[A]* and *[D]* matrices can be calculated as:

$$[A] = h_1[Q]$$
$$[D] = \frac{h_1^3}{12}[Q] \tag{2}$$

where h_1 is the thickness of the deck. For an orthotropic material, we have

$$[Q] = \begin{bmatrix} \frac{E_x}{1-\nu_x\nu_y} & \frac{\nu_y E_x}{1-\nu_x\nu_y} & 0 \\ \frac{\nu_x E_y}{1-\nu_x\nu_y} & \frac{E_y}{1-\nu_x\nu_y} & 0 \\ 0 & 0 & G \end{bmatrix} \tag{3}$$

where ν_x and ν_y are Poisson's ratios in *x* and *y* directions, respectively; E_x and E_y are Young's moduli in *x* and *y* directions, respectively; and $\frac{\nu_y E_x}{1-\nu_x\nu_y} = \frac{\nu_x E_y}{1-\nu_x\nu_y}$

Eq. (1) can be re-written as follows by performing appropriate matrix inversions:

$$\begin{Bmatrix} \{\epsilon\} \\ \{\kappa\} \end{Bmatrix} = \begin{bmatrix} [\alpha] & 0 \\ 0 & [\delta] \end{bmatrix} \begin{Bmatrix} \{N\} \\ \{M\} \end{Bmatrix} \tag{4}$$

where the compliance matrices are given by $[\alpha] = [A]^{-1}$ and $[\delta] = [D]^{-1}$.

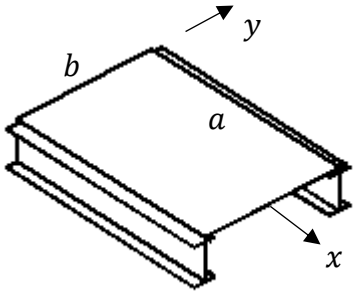

Figure 6.2 Bridge deck supported by two beams (Zou et al., 2011)

When the composite beam system is subjected to out-of-plane forces, the deck is under compression and the girder is under tension in *x*-direction, as shown in Figure 6.1(a). The compression force in the deck is transferred through shear connections at the interface between the deck and girder. Therefore, we can assume that the axial force N_y and moment M_y in the *y* direction, and the twisting moment M_{xy} are zero. If we consider a deck supported by two girders as shown in Figure 6.2 and Figure 6.3, only edge shear transaction N_{xy} and axial force N_x are present. Based on these assumptions, Eq. (4) can be reduced to:

$$\begin{Bmatrix} \varepsilon_x \\ \varepsilon_y \\ \gamma_{xy} \\ \kappa_x \end{Bmatrix} = \begin{bmatrix} \alpha_{11} & \alpha_{12} & 0 & 0 \\ \alpha_{21} & \alpha_{22} & 0 & 0 \\ 0 & 0 & \alpha_{66} & 0 \\ 0 & 0 & 0 & \delta_{11} \end{bmatrix} \begin{Bmatrix} N_x \\ N_y \\ N_{xy} \\ M_x \end{Bmatrix} \tag{5}$$

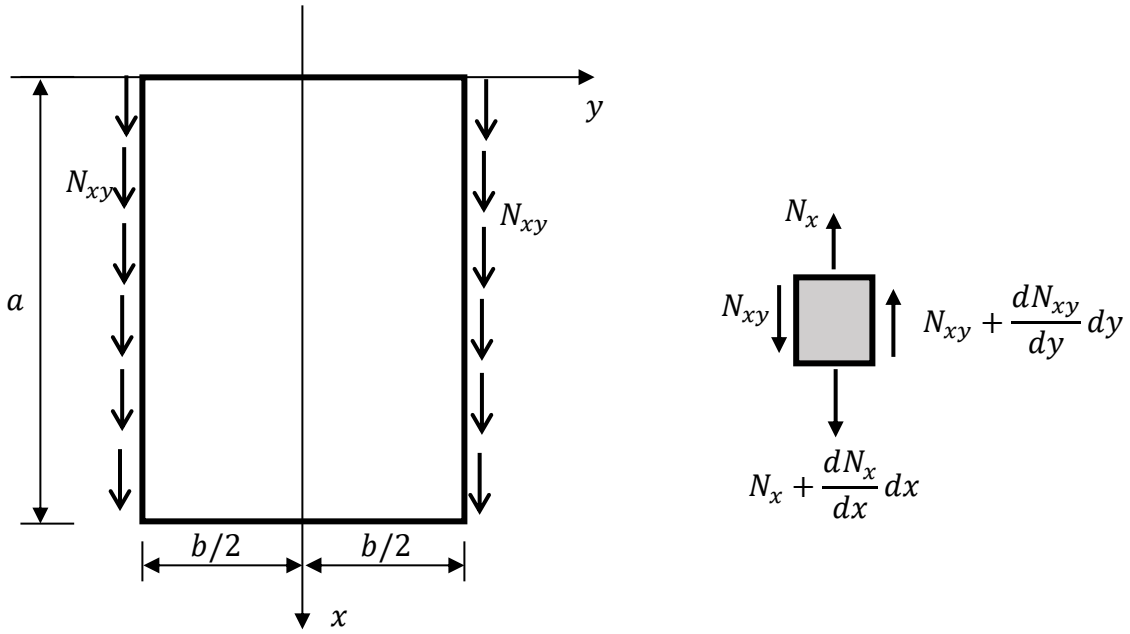

Figure 6.3 Forces in the deck

Based on the equilibrium equation of an infinitesimal section of the plate as shown Figure 6.3, we have

$$\frac{\partial N_x}{\partial x} + \frac{\partial N_{xy}}{\partial y} = 0 \tag{6}$$

The compatibility equation for an orthotropic plate is given as:

$$\frac{\partial^2 \varepsilon_x}{\partial y^2} + \frac{\partial^2 \varepsilon_y}{\partial x^2} = \frac{\partial^2 \gamma_{xy}}{\partial x \, \partial y} \tag{7}$$

Since the deck is restrained in y direction by two girders at two sides, ε_y is insignificant compared to ε_x, which can be neglected. Eq. (7) then becomes:

$$\frac{\partial^2 \varepsilon_x}{\partial y^2} = \frac{\partial^2 \gamma_{xy}}{\partial x \, \partial y} \tag{8}$$

Substituting Eq. (5) into (8), and combining with Eq. (6), we have

$$\alpha_{11} \frac{\partial^2 N_x}{\partial y^2} + \alpha_{66} \frac{\partial^2 N_x}{\partial x^2} = 0 \tag{9}$$

Eq. (9) can be reduced to an ordinary differential equation by a harmonic analysis. Since the deck is simply supported at *x=0* and *a*, the axial force can be obtained as:

$$N_x(x, y) = \sum_{j=1}^{\infty} N_j(y) \sin(\frac{j\pi x}{a}) \tag{10}$$

where $N_j(y)$ is an amplitude function. Substituting Eq. (10) into (9), we have

$$\frac{\partial^2 N_j}{\partial y^2} = {\xi_j}^2 N_j \tag{11}$$

where

$$\xi_j = \frac{j\pi}{a} \sqrt{\frac{\alpha_{66}}{\alpha_{11}}} \tag{12}$$

The general solution of Eq. (11) is

$$N_j(y) = C_{1j} \cosh\left(\xi_j y\right) + C_{2j} \sinh(\xi_j y) \tag{13}$$

where C_{1j} and C_{2j} are constants that need to be determined. Based on the normal stress distribution shown in Figure 6.1, $N_x(x, y)$ is symmetric about *y=0*. The two hyperbolic functions of *cosh* and *sinh* in Eq. (13) represent symmetric and antisymmetric conditions about *y=0*, respectively. Therefore, the coefficient C_{2j}, which is associated with *sinh* function, can be dropped. Eq. (13) can then be reduced to:

$$N_j(y) = C_{1j} \cosh\left(\xi_j y\right) \tag{14}$$

And N_x can be expressed as:

$$N_x(x,y) = \sum_{j=1}^{\infty} C_{1j} \cosh(\xi_j y) \sin(\frac{j\pi x}{a}) \tag{15}$$

Substituting Eq. (14) into Eq. (6), we have

$$\frac{\partial N_{xy}(x,y)}{\partial y} = -\frac{\partial N_x(x,y)}{\partial x} = -\sum_{j=1}^{\infty} \frac{j\pi}{a} C_{1j} \cosh\left(\xi_j y\right) \cos(\frac{j\pi x}{a}) \tag{16}$$

Integrating Eq. (16) in y and considering $N_{xy}(x, 0)=0$, we have

$$N_{xy}(x,y) = -\sum_{j=1}^{\infty} \frac{j\pi}{a} \frac{C_{1j}}{\xi_j} \sinh(\xi_j y) \cos(\frac{j\pi x}{a}) \tag{17}$$

As shown in Figure 3, based on symmetric condition, at $y = b/2$, we have

$$N_{xy}\left(x, \frac{b}{2}\right) = \frac{1}{2} \frac{dF(x)}{dx} \tag{18}$$

where $F(x)$ is the force transferred through the shear connection, as shown in Figure 6.5(b). Combining Eqs. (17) and (18), we have

$$\frac{dF(x)}{dx} = 2N_{xy}\left(x, \frac{b}{2}\right) = -2\sum_{j=1}^{\infty} \frac{j\pi}{a} \frac{C_{1j}}{\xi_j} \sinh(\frac{\xi_j b}{2}) \cos(\frac{j\pi x}{a}) \tag{19}$$

Integrating Eq. (19) in x and considering $F(0)=0$, we have

$$F(x) = -2\sum_{j=1}^{\infty} \frac{C_{1j}}{\xi_j} \sinh(\frac{\xi_j b}{2}) \sin(\frac{j\pi x}{a}) \tag{20}$$

As pointed out by Newmark et al. (1951), the relative movement, or slip, between the slab and girder is given by

$$\gamma = \frac{q}{K} \tag{21}$$

where γ is the slip, q and K are the horizontal shear and stiffness at the deck-girder junction, respectively. q is equal to the change of force F, which can be expressed as:

$$q = \frac{dF(x)}{dx} \tag{22}$$

The difference between the strain in the girder and deck is equal to the rate of change of slip, which can be expressed as:

$$\varepsilon_2 - \varepsilon_1 = \frac{d\gamma}{dx} \tag{23}$$

where ε_1 and ε_2 are strains at the interface for the deck and girder, as shown in Figure 6.5(c). Substituting Eqs. (21) and (22) into (23) results in

$$\frac{d^2F(x)}{Kdx^2} = \varepsilon_2 - \varepsilon_1 \tag{24}$$

Based on the assumption that plane remains plane after deformation, the strain follows a linear distribution along the depth of the beam, as shown in Figure 6.5(c). As shown in Figure 6.2 and Figure 6.3, the girders are at the locations of $y=\pm b/2$. Therefore, the strain at the deck-girder interface at $y=b/2$ can be described as

$$\varepsilon_1 = -\alpha_{11} N_x \left(x, \frac{b}{2}\right) + \frac{M_1(x) C_1 / b}{D_{11}} \tag{25}$$

and

$$\varepsilon_2 = \frac{F(x)}{E_2 A_2} - \frac{M_2(x) C_2}{E_2 I_2} \tag{26}$$

where $M_i(x)$, C_i, and b are moment, distance from the neutral axes to the deck-girder interface, and the width of the deck, respectively, as shown in Figure 6.4; E_i, A_i, I_i, and D_{11} are Young's modulus, area, moment of inertia, and flexural rigidity, respectively; and the subscript $i=1$ and 2 represent the deck and girder, respectively. The assumption that the deck and girder deflect equal amount at

all points along the length indicates that the angle changes along the length be equal, which can be expressed as (Newmark et al. 1951):

$$\frac{M_1(x)}{bD_{11}} = \frac{M_2(x)}{E_2 I_2} = \frac{M_1(x) + M_2(x)}{bD_{11} + E_2 I_2} \tag{27}$$

Based on equilibrium of the moment shown in Figure 4(b), we have

$$M_1(x) + M_2(x) + F(x)(C_1 + C_2) = M(x) \tag{28}$$

Substituting Eq. (28) into Eq. (27), we have

$$\frac{M_1(x)}{bD_{11}} = \frac{M_2(x)}{E_2 I_2} = \frac{M(x) - F(x)(C_1 + C_2)}{bD_{11} + E_2 I_2} \tag{29}$$

Combining Eqs. (25), (26), and (29), we have

$$\varepsilon_2 - \varepsilon_1 = \frac{F(x)}{E_2 A_2} + \alpha_{11} N_x \left(x, \frac{b}{2}\right) - \frac{[M(x) - F(x)(C_1 + C_2)](C_1 + C_2)}{E_2 I_2 + bD_{11}} \tag{30}$$

Substituting Eq. (24) into Eq. (30), we have

$$\frac{d^2 F(x)}{K dx^2} = \frac{F(x)}{E_2 A_2} + \alpha_{11} N_x \left(x, \frac{b}{2}\right) - \frac{[M(x) - F(x)(C_1 + C_2)](C_1 + C_2)}{E_2 I_2 + bD_{11}} \tag{31}$$

In order to use Fourier series to solve Eq. (31), the moment *M(x)* needs to be expressed in the series format as

$$M(x) = \sum_{j=1}^{\infty} Q_j \sin\left(\frac{j\pi x}{a}\right) \tag{32}$$

where

$$Q_j = \frac{2}{b} \int_0^b M(x) \sin\left(\frac{j\pi x}{a}\right) dx \tag{33}$$

Using Eqs. (15), (20) and (32) into Eq. (31), the solution of the partial differential Eq. (31) can be obtained using Fourier series. Thus, through some simple mathematical transformations, we obtain

$$\sum_{j=1}^{\infty} C_{1j} A_j \sin(\frac{j\pi x}{a}) = \sum_{j=1}^{\infty} Q_j \frac{(C_1 + C_2)}{E_2 I_2 + bD_{11}} \sin(\frac{j\pi x}{a}) \tag{34}$$

where

$$A_j = \frac{2}{K\xi_j}(\frac{j\pi}{a})^2 \sinh(\frac{\xi_j b}{2}) + \frac{2}{\xi_j}[\frac{1}{E_2 A_2} + \frac{(C_1 + C_2)^2}{E_2 I_2 + bD_{11}}] \sinh(\frac{\xi_j b}{2}) + \alpha_{11} \cosh(\frac{\xi_j b}{2}) \tag{35}$$

Solving for Eq. (34), we have

$$C_{1j} = \frac{Q_j}{A_j} \frac{(C_1 + C_2)}{E_2 I_2 + bD_{11}} \tag{36}$$

where Q_j and A_j are defined in Eqs. (33) and (35), respectively. Effective flange width b_{eff} can then be calculated as:

$$b_{eff} = \frac{\int_0^b N_x(x,y)dx}{N_x(x,b/2)} = \frac{F(x)}{N_x(x,b/2)} \tag{37}$$

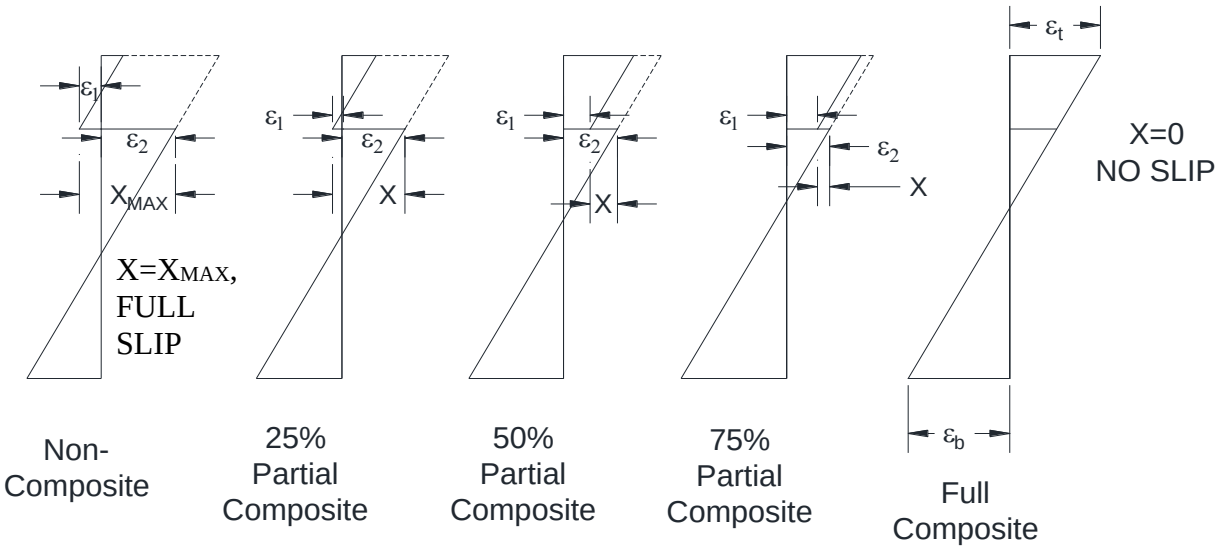

Figure 6.4 Partial Composite Action defined by AISC (Lorentz and Stockwell, 1984)

6.4. Degree of Composite Action

The definition of DCA used in this study is the same as that adopted by the American Institute of Steel Construction (AISC), as shown in Figure 6.4, where *x* indicates the amount of the horizontal slip (Lorenz and Stockwell, 1984). Based on Figure 6.4, DCA can be expressed as

$$DCA = 1 - \frac{x}{x_{max}} \tag{38}$$

According to Eq. (38), it is apparently that *DCA=0%* when $x=x_{max}$, and DCA=100% when *x=0*, which represents two extreme cases of non-composite and full-composite conditions. Based on strain distributions shown in Figure 6.5 and Figure 6.4, Eq. (38) can be re-written as

$$DCA = 1 - \frac{\varepsilon_2 - \varepsilon_1}{\varepsilon_{max}} \tag{39}$$

Substituting Eq. (39) into Eq. (30), we have

$$(1 - DCA) \times \varepsilon_{max} = \frac{F(x)}{E_2 A_2} + \alpha_{11} N_x(x, b/2) - \frac{[M(x) - F(x)(C_1 + C_2)](C_1 + C_2)}{E_2 I_2 + b D_{11}} \tag{40}$$

where

$$\varepsilon_{max} = \frac{M(x)(C_1 + C_2)}{E_2 I_2 + b D_{11}} \tag{41}$$

which is calculated based on 0% DCA at any section with a given *M(x)*, as shown in Figure 6.5. It will not change with the change of the stiffness at deck-girder interface. Substituting Eq. (41) into Eq. (40), DCA can be expressed as

$$DCA = \frac{\frac{F(x)}{E_2 A_2} + \alpha_{11} N_x(x, b/2) + \frac{F(x)(C_1 + C_2)^2}{E_2 I_2 + b D_{11}}}{\varepsilon_{max}} \tag{42}$$

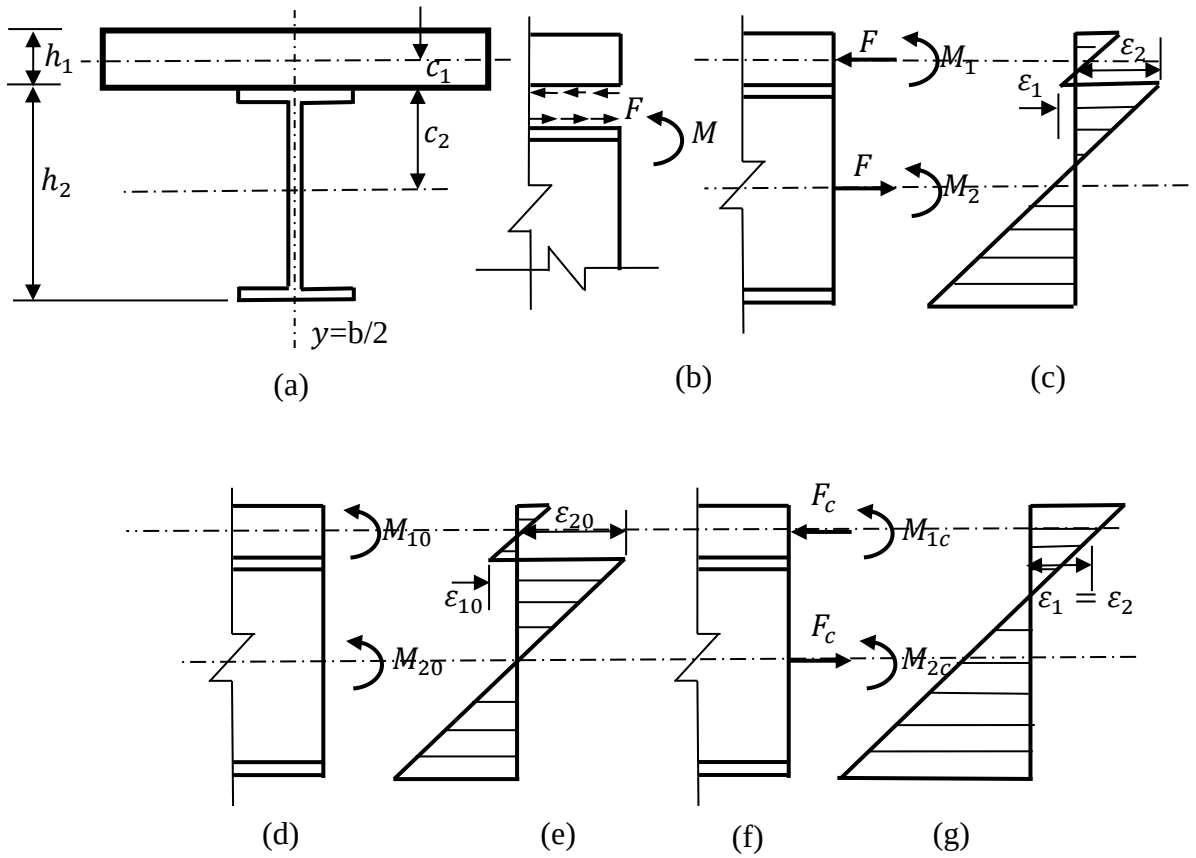

Figure 6.5 Composite beam with partial degree of composite action, (a) cross Section, (b) internal forces with partial DCA, (c) strain distribution with partial DCA, (d) internal forces with 0% DCA, (e) strain distribution with 0% DCA, (f) internal forces with 100% DCA, (g) strain distribution with 100% DCA

6.5. Verification

For verification purpose, the derived explicit closed-form solution and Finite Element (FE) method were used to study two T-beams, one with concrete deck and the other with FRP deck. The first one was a composite T-beam tested by Newmark et al. (1951). The T-beam consisted of a wide flange steel I-beam 24W76 and a 1.83 m (6 ft.) wide reinforced concrete slab, connected by channel shear connectors, as shown in Figure 6.6. Materials properties are shown in Table 6.2, which were taken from Newmark et al. (1951). Beam dimensions are shown Table 6.1. Load was

applied at mid-span. Displacement at the mid-span and bottom strains at 457 mm (18 inches) away from the mid-span were recorded during the test. The stiffness between slab and beam was 0.963×10^5 N/mm (5.5×10^6 lb./inch) based on a push-out test.

Table 6.1 Beam dimensions

Designation	Area (mm^2)	Depth d (mm)	Web Thickness t_w (mm)	Flange		Moment of Inertia I (mm^4)
				Width b_f (mm)	Thickness t_f (mm)	
24WF76	14451	607	11.2	228	17.3	8.724E+8
W40x199	37677	982	17	400	27	6.202E+9

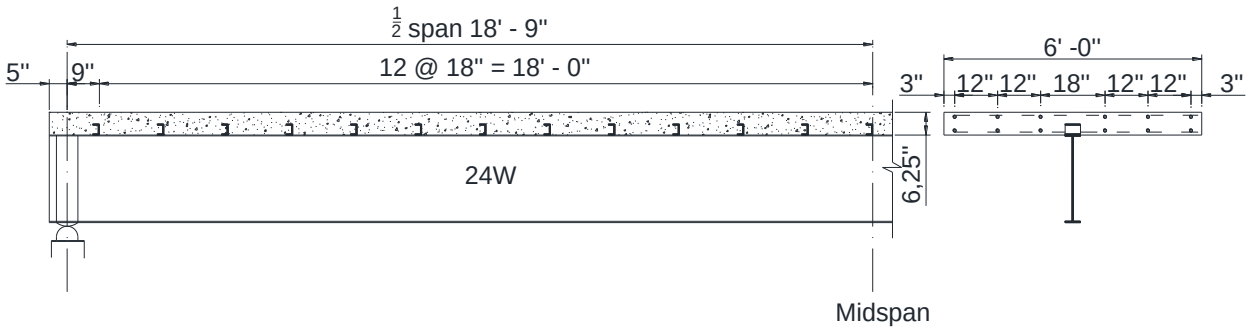

Figure 6.6 T-beam test (1 inch=25.4 mm; 1 ft.=304.8 mm) (Newmark et al. 1951)

Table 6.2 Material properties (Newmark et al. 1951)

Materials	Strength (MPa)	Modulus of Elasticity (GPa)
Concrete	37.9	28.7
Steel (flange)	246.8 (yield); 422.6 (ultimate)	214.4
Steel (web)	266.8 (yield); 443.3 (ultimate)	209.6

An FE model was created to simulate the T-beam section using ABAQUS (2014), as shown in Figure 6.7. The dimensions were the same as shown in Figure 6.6. Concrete and steel were treated as elastic materials in the model, with the material properties shown in Table 6.2. The elements

used in the model were general purpose shell element with reduced integration, defined as S4R in ABAQUS. The mesh size was 25.4 mm (1 inch). A point load was applied at the mid-span. Multi-point constraint connector elements (CONN3D2 in ABAQUS) were used to simulate the interaction between the slab and beam. All stiffnesses except the one in *y* direction were set to be rigid to couple the displacements in those directions. The stiffness in the *y* direction was set to be 0.963×10^5 N/mm (5.5×10^6 lb./inch), which was the value obtained from the test as described above. The boundary conditions were set to be pin on one side and roller on the other side of the bottom flange. Two sides of the slab were also restrained.

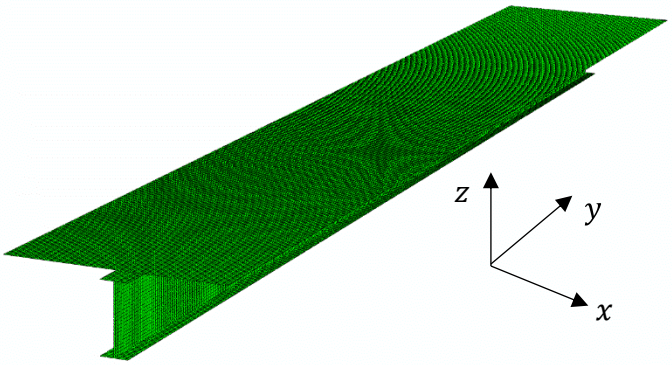

Figure 6.7 FE model

The results from the test, FE analysis, and analytical solution are shown in Figure 6.8 and Figure 6.9 for load vs. deflection at the mid-span and load vs. strain at 457 mm (18 inches) away from the mid-span, respectively, where close correlations can be observed, validating the accuracy of the derived analytical model.

Since the stress distributions along the *x* direction were not reported in the test, only the results from the FE model and analytical model are compared in Figure 6.10 for stress at the mid-depth of the deck with different DCAs. Although changing the number of connectors is more reasonable in practice to achieve different DCAs, fewer connector will result in more significant

local stress concentration. Therefore, we used as many connector elements as possible in the FE model and different DCAs were achieved by varying the stiffness between the deck and girder. The definition of DCA is the same as described above.

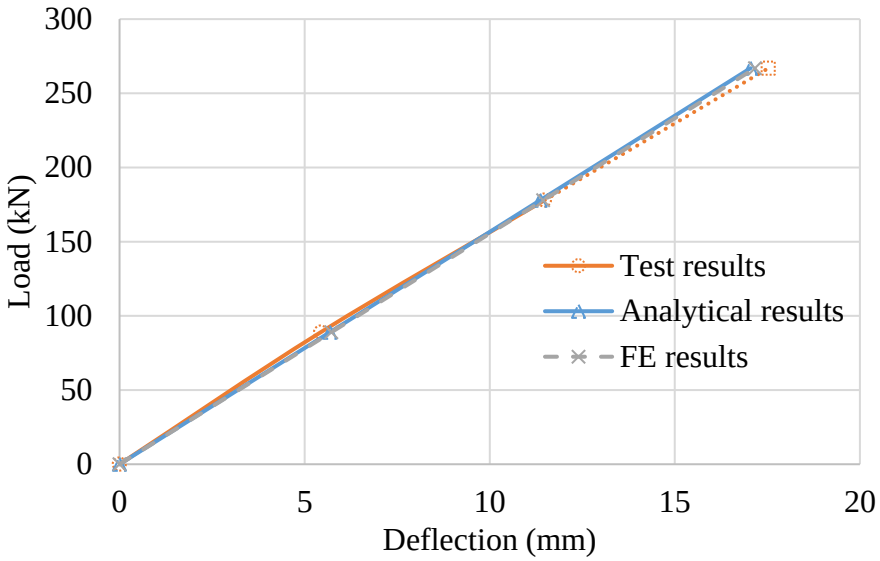

Figure 6.8 Load-deflection curves at mid-span

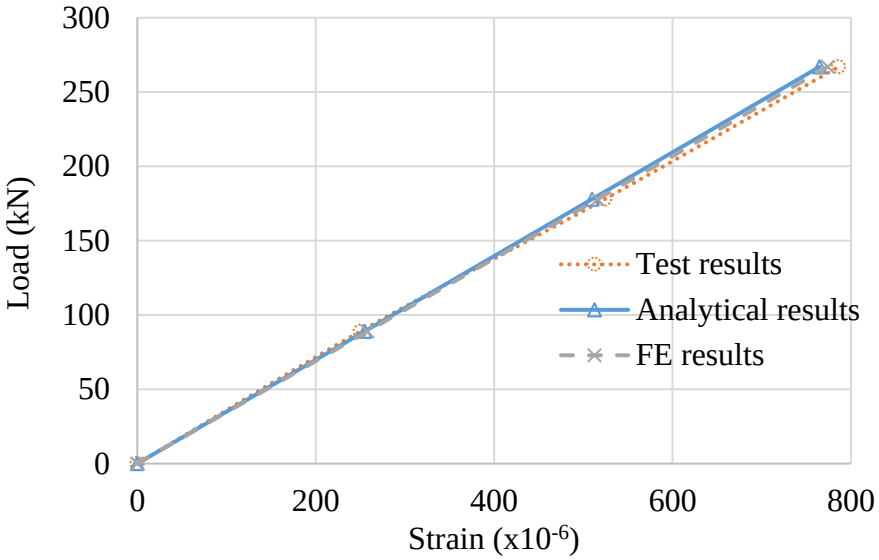

Figure 6.9 Load vs. strain at 457 mm away from mid-span

A point load of 267 kN (60 kips) was added at the mid-span. As shown in Figure 6.2 and Figure 6.3, the analytical solution is based on a plate with two edges simply supported by the two

girders at $y=\pm b/2$. The FE model is based on a T-beam, which spans from $y=0$ to $y=b$ according to the coordinate system in Figure 6.2 and Figure 6.3. Therefore, in the analytical model, interfacial stresses were calculated from *0* to *b/2*, which were then mirrored along $y=b/2$ to get stress distribution from *b/2* to *b*. Again, close correlation can be observed. It can also be seen from Figure 9 that the maximum stress increases as the DCA increase, and the shear lag effect becomes more prominent for higher DCA.

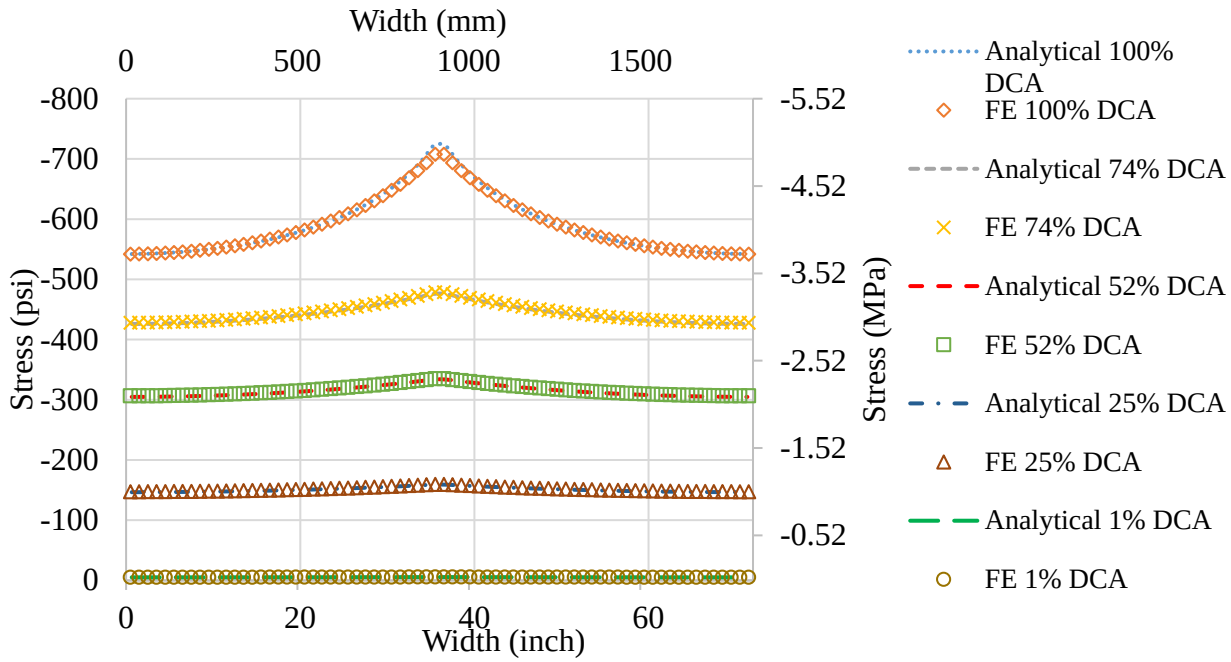

Figure 6.10 Stress distribution at mid-depth and mid-span of the deck

Another T-beam was an interior girder taken out from a bridge model from Chen and Davalos (2014), as shown in Figure 6.11. This model has the following configurations:

1. Simply supported 21.33 m span.
2. Five W40x199 Grade 50 rolled steel girders at 2.44 m on centers, with a yield strength f_y=345 MPa. The properties of W40x199 are provided in Table 6.1.
3. 254 mm thick FRP honeycomb sandwich deck panel connected to steel girders.

4. The deck configuration is shown in Figure 6.12. The equivalent properties of FRP panel are listed in Table 6.3 based on procedures to obtain the equivalent engineering properties in Davalos et al. (2001), as provide in Chen and Davalos (2014).

Table 6.3 Equivalent properties of FRP panel (Chen and Davalos 2014)

	$E_x(GPa)$	$E_y(GPa)$	ν_x	$G_{xy}(GPa)$
In-Plane	2.747	1.475	0.321	0.741
Bending	6.417	3.896	0.32	1.422

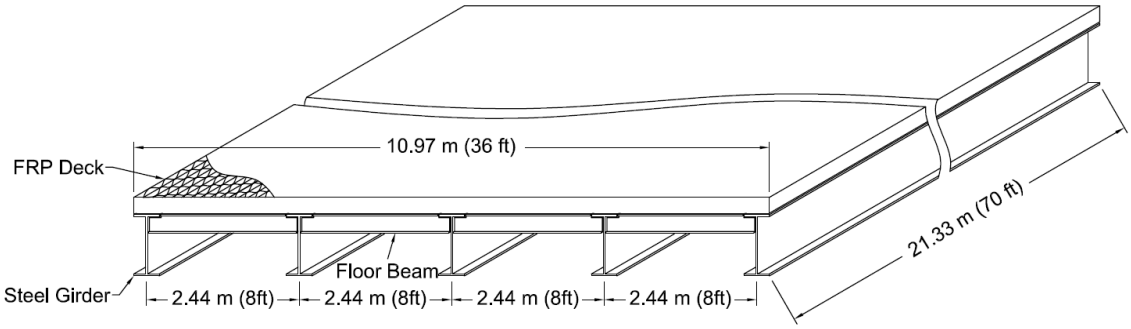

Figure 6.11 Bridge configuration (Chen and Davalos 2014)

An FE model similar to the one described above in Figure 6 was created with the mesh size of 40 mm. The stiffness between the deck and girder was varied to represent different DCAs. A point load of 170 kN was added at the mid-span. The results from FE model and analytical solution are shown in Figure 6.13 through Figure 6.15 for mid-span strain at the bottom flange of the girder, mid-span deflection, and effective flange width vs. DCA, respectively, where good correlations can be seen, proving the accuracy of the derived model. Similar to Figure 6.10, stress distribution at the mid-depth of the deck along *x* direction for different DCAs are plotted in Figure 6.16, where the analytical and FE results agree well with each other.

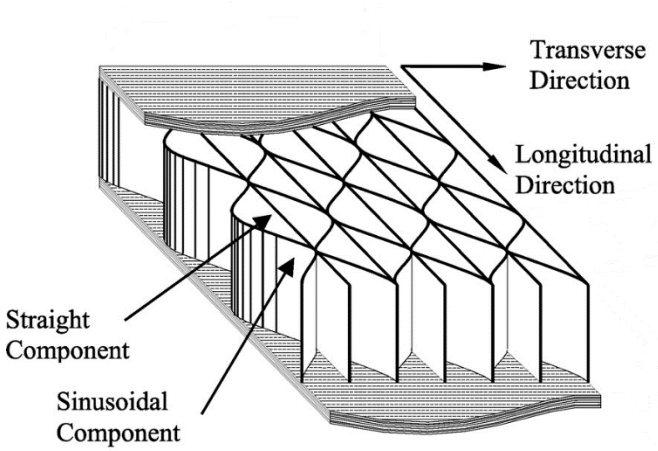

(a)

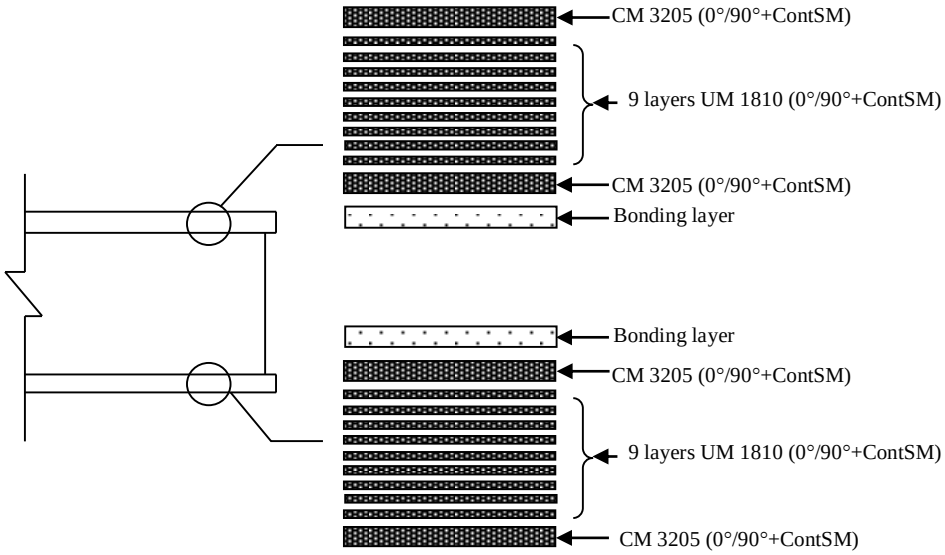

(b)

Figure 6.12 FRP deck configurations (reprinted from Chen and Davalos 2014), (a) 3D image of FRP deck, (b) facesheet configurations

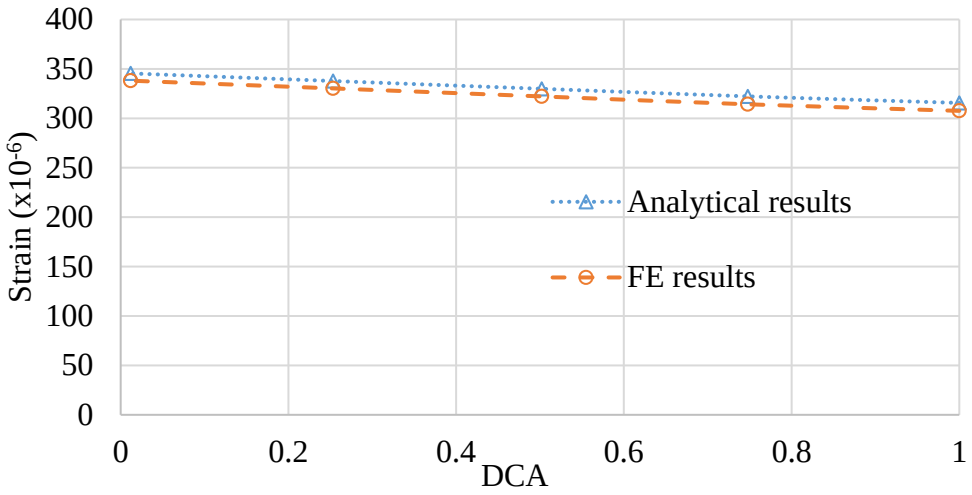

Figure 6.13 Strain at the bottom flange of the girder vs. DCA at mid-span

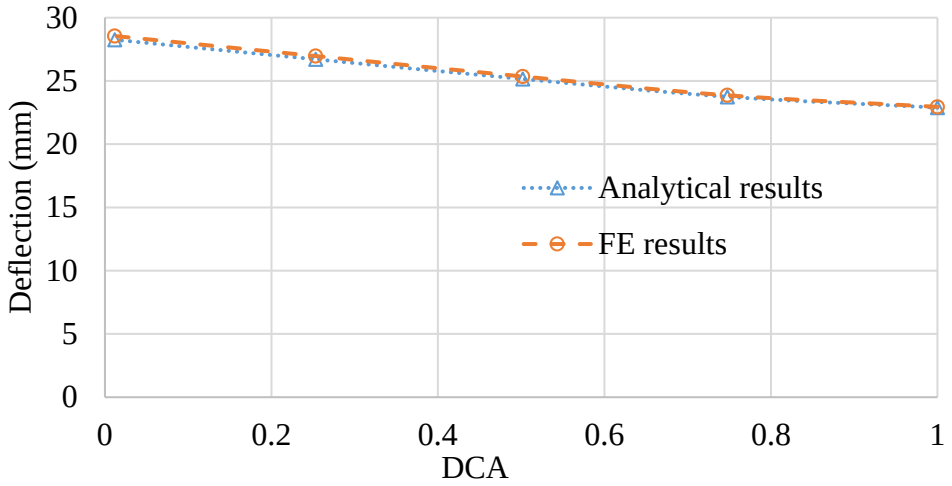

Figure 6.14 Mid-span deflection vs. DCA

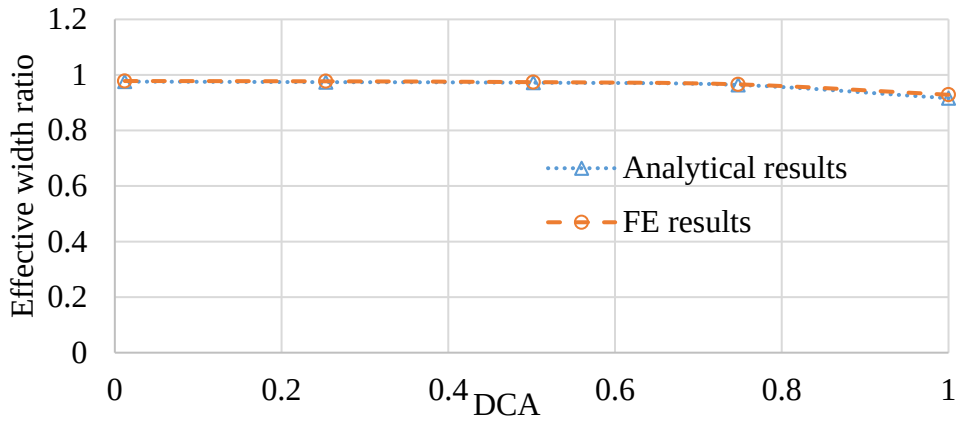

Figure 6.15 Effective width ratio (b_{eff}/b) vs. DCA

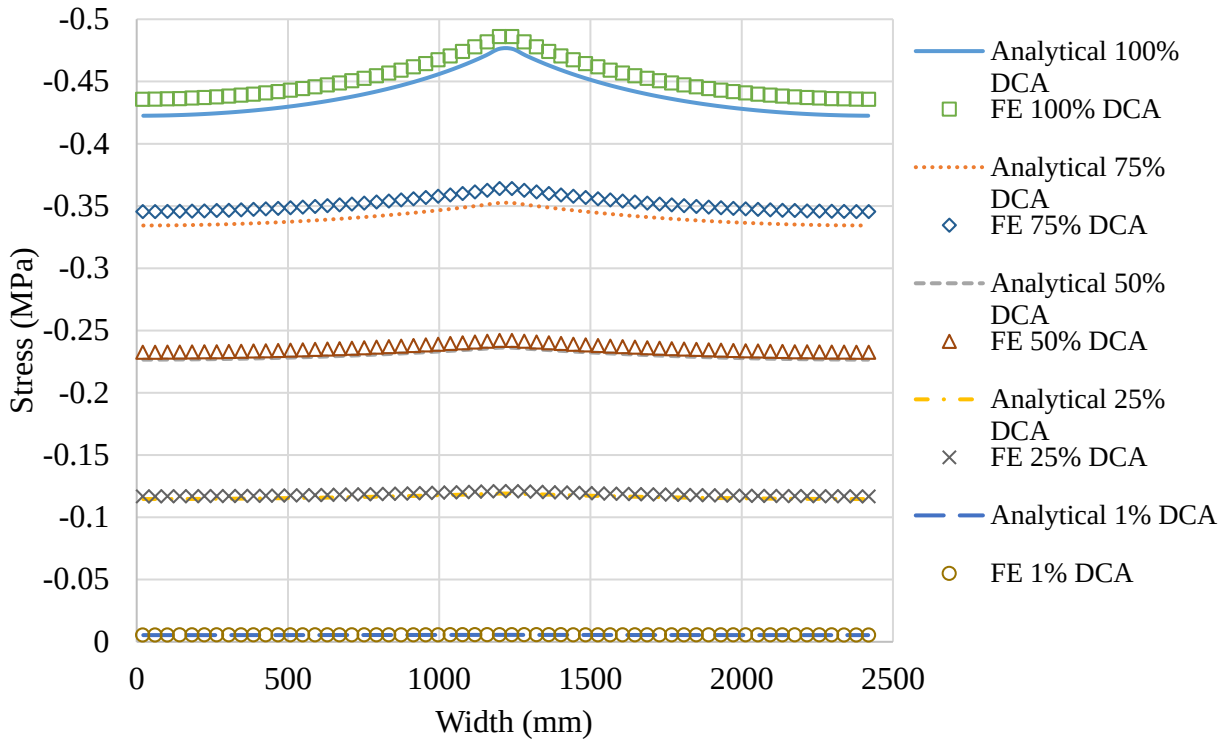

Figure 6.16 Stress distribution at mid-depth and mid-span of the deck

6.6. Application

A parametric study on effective flange width was conducted on the second T-beam with FRP deck studied above using the derived analytical model by varying the stiffness of the bridge deck from 25% to 100% of the stiffness of a concrete deck; and the stiffness at deck-girder interface from 0% to 100% DCA, respectively, as shown in Figure 6.17, which indicates that the stiffness of the deck has negligible effect on effective flange width. The interfacial stiffness also has insignificant effect on effective flange width for DCA up to 75%. For 100% DCA, the effective flange width drops about 10%. Therefore, the effective flange width for 100% DCA can be conservatively used to represent those of other DCAs.

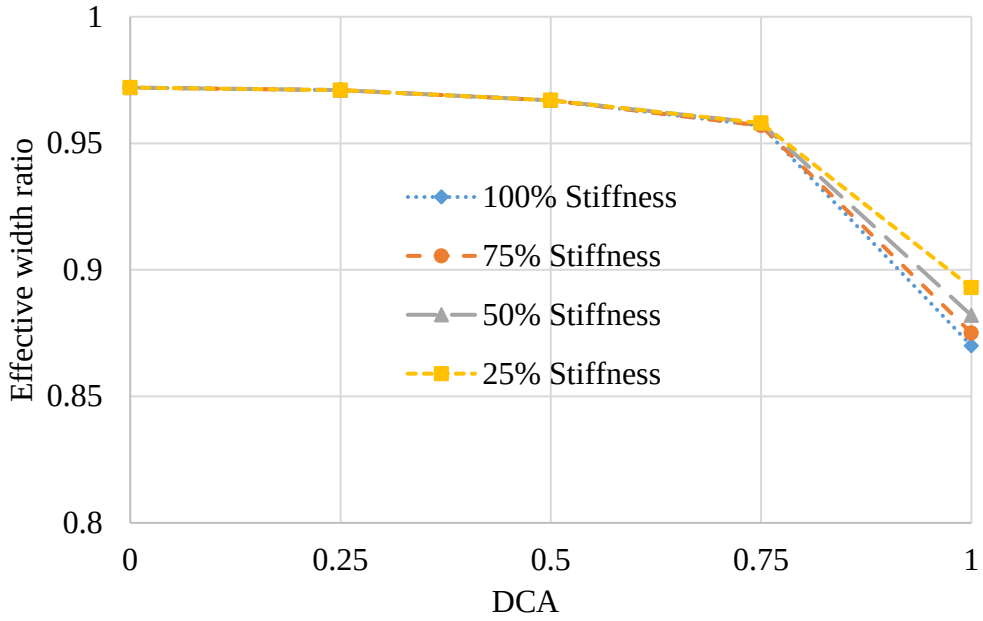

Figure 6.17 Effective width ratios (b_{eff}/b) for different deck stiffness

Furthermore, the span of beam *L* was varied to study the effect of the aspect ratio *L/b* on the effective flange width. Two stiffnesses for the deck were considered, i.e., 25% and 100% of the concrete deck stiffness. The DCAs were varied from 0% to 100%. The results are shown in Figure 6.18. It can be seen that the aspect ratio has a significant effect of on the effective flange width, where the effective flange width with an aspect ratio of 1 is about 60% lower than that with an aspect ratio of 8.7. Therefore, the equation of the effective flange width adopted in current studies, including the one in AASHTO Specifications (2014), is only applicable to slab within a certain limit of the aspect ratio.

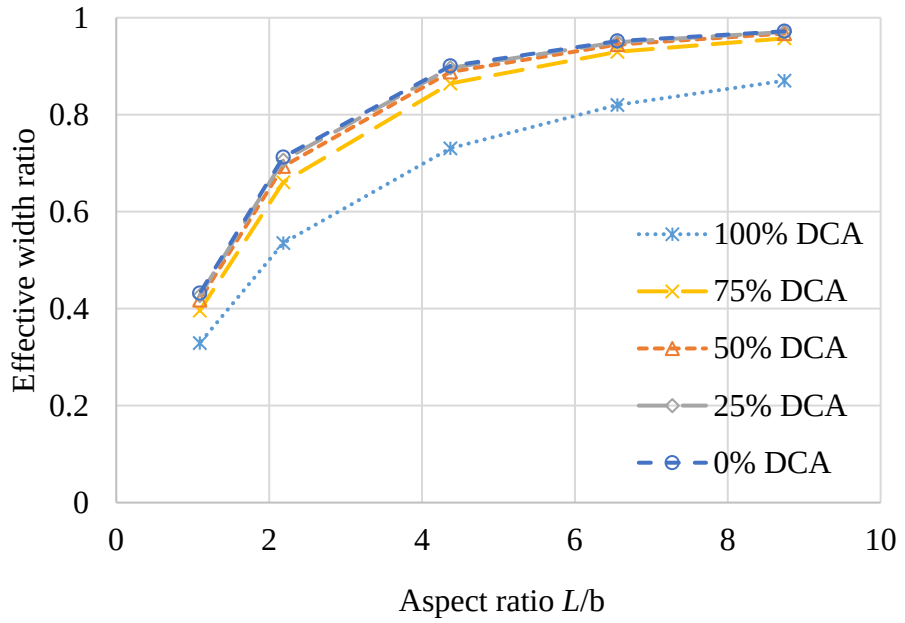

(a)

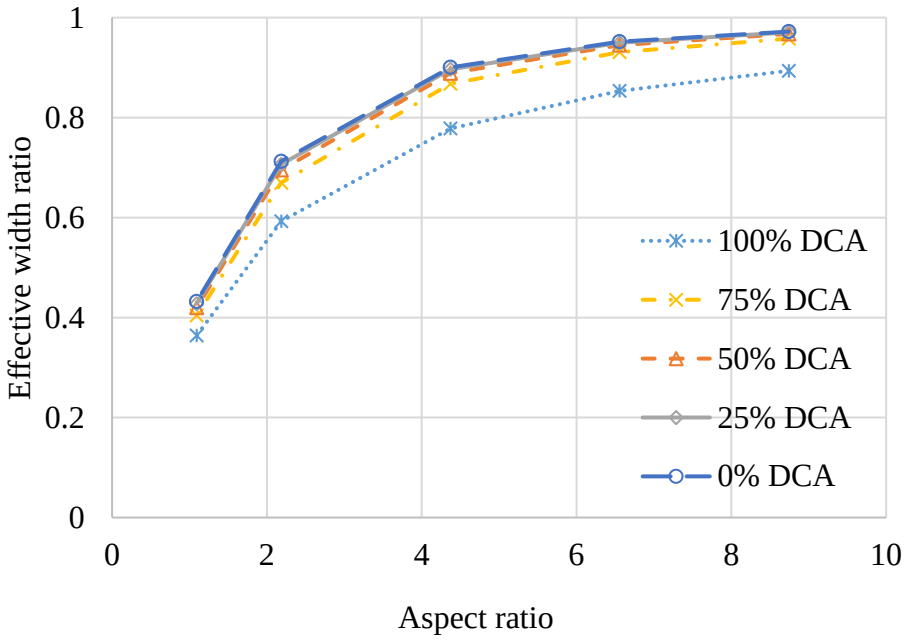

(b)

Figure 6.18 Effective width ratio (beff/b) vs. aspect ratio for different DCAs,

(a) 100% deck stiffness, (b) 25% deck stiffness

6.7. Simplified Method to Calculate the Deflection and Strain Distribution

Eq. (37) gives

$$N_x(x, b/2) = \frac{F(x)}{b_{eff}} \tag{43}$$

Based on the findings from the parametric study as shown in Figure 17, b_{eff} for 100% DCA is the lowest. Therefore, it can be conservatively used to represent effective flange widths for other DCAs. Therefore, we can assume b_{eff} to be a constant. Substituting Eq. (43) into (42), we have

$$DCA = \frac{F(x)\left[\frac{1}{E_2A_2} + \frac{(C_1 + C_2)^2}{E_2I_2 + bD_{11}} + \frac{\alpha_{11}}{b_{eff}}\right]}{\varepsilon_{max}} \tag{44}$$

Therefore, DCA is in linear relationship to $F(x)$, i.e.,

$$F(x) = DCA \times F_c(x) \tag{45}$$

where $F_c(x)$ is the maximum interfacial shear force transferred through the shear connection for a composite beam with 100% DCA. Based on this finding, the deflections and stresses of composite beams with partial DCA can be calculated from those with 100% and 0% DCAs as follows.

For 100% DCA (Figure 4f and g), we have

$$\kappa_c(x) = \frac{M(x)}{(EI)_c} = \frac{M_{2c}(x)}{E_2I_2} = \frac{M_{1c}(x)}{bD_{11}} = \frac{M_{1c}(x) + M_{2c}(x)}{bD_{11} + E_2I_2} \tag{46}$$

where κ is curvature, EI is the flexural rigidity, and $M(x)$, $M_1(x)$, and $M_2(x)$ are moments acting on the composite beam, deck, and girder, respectively. The subscript c denotes a 100% DCA composite beam.

For 0% DCA (Figure 4d and e), we have

$$\kappa_0(x) = \frac{M(x)}{bD_{11} + E_2I_2} = \frac{M_{10}(x)}{bD_{11}} = \frac{M_{20}(x)}{E_2I_2} = \frac{M_{10}(x) + M_{20}(x)}{bD_{11} + E_2I_2} \tag{47}$$

where all symbols have the same meaning as those in Eq. (46), but subscript *0* denotes a 0% DCA noncomposite beam.

Similarly, for beams with partial composite action (Figure 4b and c), we have

$$\kappa(x) = \frac{M_2(x)}{E_2 I_2} = \frac{M_1(x)}{bD_{11}} = \frac{M_1(x) + M_2(x)}{bD_{11} + E_2 I_2} \tag{48}$$

Based on Eq. (28), we have

$$F(x)(C_1 + C_2) = M(x) - [M_1(x) + M_2(x)] \tag{49}$$

where *F(x)* is the interfacial shear force transferred through the shear connection. Combining Eqs. (48) and (49), for any DCA, we have

$$\kappa(x) = \frac{M(x) - F(x)(C_1 + C_2)}{bD_{11} + E_2 I_2} = \frac{M(x) - DCA \times F_c(x)(C_1 + C_2)}{bD_{11} + E_2 I_2} \tag{50}$$

Eq. (50) can also be written as

$$\kappa(x) = \frac{M(x)}{bD_{11} + E_2 I_2} - DCA \times \frac{F_c(x)(C_1 + C_2)}{bD_{11} + E_2 I_2} \tag{51}$$

Based on Eq. (49), we have

$$\frac{F_c(x)(C_1 + C_2)}{bD_{11} + E_2 I_2} = \frac{M(x)}{bD_{11} + E_2 I_2} - \frac{M_{1c}(x) + M_{2c}(x)}{bD_{11} + E_2 I_2} = \kappa_0(x) - \kappa_c(x) \tag{52}$$

Using Eqs. (47) and (52) into Eq. (51), we have

$$\kappa(x) = \kappa_0(x) - DCA \times [\kappa_0(x) - \kappa_c(x)] = (1 - DCA)\kappa_0(x) + DCA \times \kappa_c(x) \tag{53}$$

The deflection can be calculated by double integration of $\kappa(x)$ considering proper boundary conditions. For a simply supported T-beam considered in this study, we have

$$\Delta(x) = (1 - DCA)\Delta_0(x) + DCA \times \Delta_c(x) \tag{54}$$

The stress can be calculated based on $\kappa(x)$ as:

$$\sigma_z(x) = A_{11}[\kappa(x)\times z - \frac{\alpha_{11}\times DCA\times F_c(x)}{b_{eff}}] \tag{55}$$

for the deck and

$$\sigma_z(x) = E_2[\kappa(x)\times z + \frac{DCA\times F_c(x)}{E_2A_2}] \tag{56}$$

for the girder. Substituting Eq. (53) into Eq. (56), we have

$$\sigma_z(x) = E_2\{[(1-DCA)\kappa_0(x) + DCA\times\kappa_c(x)]\times z + \frac{DCA\times F_c(x)}{E_2A_2}\} \tag{57}$$

From Eq. (56), we have

$$\sigma_{z0}(x) = E_2\kappa_0(x)\times z \tag{58}$$

$$\sigma_{zc}(x) = E_2[\kappa_c(x)\times z + \frac{F_c(x)}{E_2A_2}] \tag{59}$$

Comparing Eqs. (57) through (59), we can express Eq. (56) in a similar expression to Eq. (54) as

$$\sigma_z(x) = (1-DCA)\sigma_{z0}(x) + DCA\times\sigma_{zc}(x) \tag{60}$$

where again the subscripts *0* and *c* denote composite beams with 0% and 100% DCAs, respectively. Following a similar derivation, Eq. (55) can also be expressed in the form of Eq. (60).

6.8. Discussions

Other than the strain-based definition of DCA as shown in Figure 10, there is a displacement based definition of DCA which can be described as (Frankl et al. 2011):

$$DCA = \frac{\Delta_0(x) - \Delta(x)}{\Delta_0(x) - \Delta_c(x)} \tag{61}$$

This equation is essentially the same as Eq. (54). Therefore, the displacement-based expression of DCA is an approximate form of the strain-based expression, where b_{eff} is assumed to be a constant for the approximate method.

To better understand the accuracy of the proposed simplified method, Eqs. (54) and (60) are used to calculate the deflection and stresses at the mid-height of the deck at the mid-span of the beam, with the results shown in Figure 6.19 and Figure 6.20, respectively. It can be observed that the approximate and analytical results are close to each other, with a maximum difference of 11% and 8%, for the deflection and stress, respectively. Therefore, the simplified equations can be used to provide approximate and conservative results for deflections and stresses, which is accurate enough for practical design purposes.

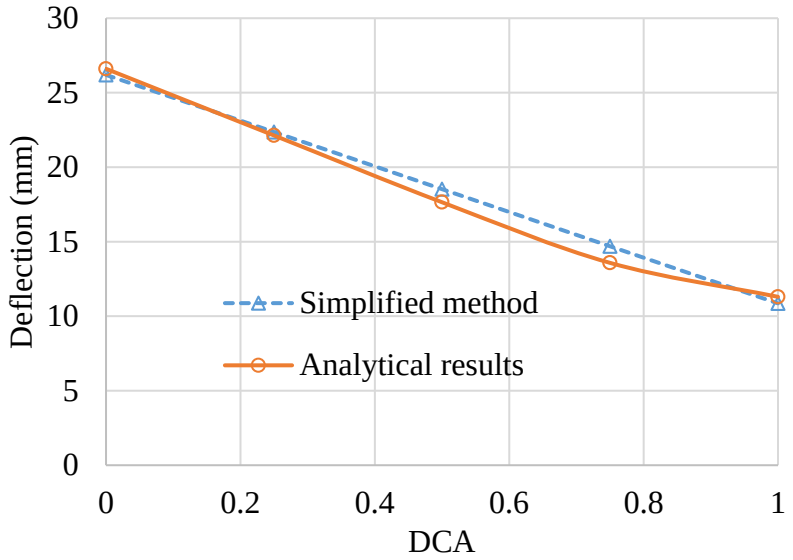

Figure 6.19 Mid-span deflection vs. DCA

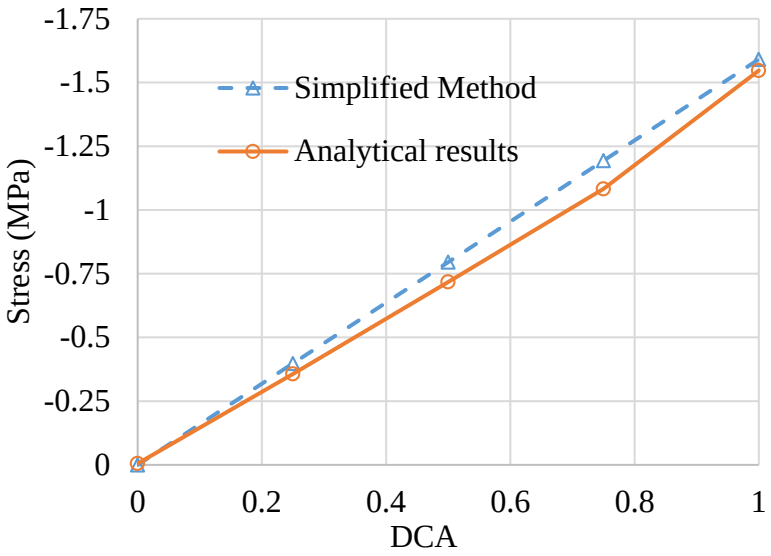

Figure 6.20 Mid-span stress vs. DCA

6.9. Conclusions

This study develops an analytical model for composite beams based on shear lag model and equilibrium equations, where the partial DCA due to the flexibility of the shear connector between the deck and girder is considered. This model permits the computation of stiffness as well as strain/stress distributions. From this study, the following conclusions can be drawn:

1. The analytical solution can accurately predict the behavior of composite beam in terms of both stiffness and stresses, accounting for the partial DCA from the shear connector, as verified by test and FE results.
2. DCA can significantly affect the stiffness and interfacial stress distributions.
3. A parametric study was conducted by varying the deck stiffness and DCA. It can be concluded that the bridge deck stiffness has negligible effect on the effective flange width. The interfacial stiffness also has insignificant effect on effective flange width for DCA up to 75%. For 100% DCA, the effective flange width drops about 10%. The

effective flange width for 100% DCA can be conservatively used to represent the effective flange width for other DCAs.

4. A simplified method is proposed to calculate the stiffness and strength distributions, which can be used for design purposes.

It is noted that connector elements are used in the FE model, which has non-ignorable error of local stress concentration. Although it has negligible effect on the global parameters, such as deflection and strain at the mid-span of the girders and effective flange width of the deck, more complicated model needs to be used to study local stress concentration at the connectors between the deck and girder. It is further noted that this study covers elastic materials and stiffness evaluations. Further study is recommended to consider the plastic behavior of composite beams and strength evaluations.

6.10. References

ABAQUS 6.12.2 (2014), Dassault Systems, Waltham, MA, USA.

American Association of State Highway and Transportation Officials (AASHTO). (2014). AASHTO LRFD bridge design specifications, 7th Ed., Washington, D.C.

Cheung, M. S., and Chan, M. Y. T. (1978). "Finite strip evaluation of effective flange width of bridge girders." Basin Res., 5, 174–185.

Chiewanichakorn, M., Aref, A. J., Chen, S. S., and Ahn, I. S. (2004). "Effective Flange Width Definition for Steel–Concrete Composite Bridge Girder." Journal of Structural Engineering, ASCE, 130(12), 2016-2031.

Chen, A., and Davalos, J. F. (2014). "Design Equations and Example for FRP Deck-Steel Girder Bridge Systems," Practice Periodical on Structural Design and Construction, ASCE, 19(2).

Davalos, J. F., Chen, A., and Zou, B. (2011). "Stiffness and Strength Evaluations of a Shear Connection System for FRP Bridge Decks to Steel Girders." J. Compos. Constr., 15(3), 441–450.

Davalos, J. F., Chen, A., and Zou, B. (2012). "Performance of a scaled FRP deck-on-steel girder bridge model with partial degree of composite action." Engineering Structures, 40, 51-63.

Davalos, J. F., Qiao, P., Xu, X. F., Robinson, J., and Barth, K. E. (2001). "Modeling and Characterization of Fiber-reinforced Plastic Honeycomb Sandwich Panels for Highway Bridge Applications." Composite Structures, 52, 441-452.

Heins, C. P., and Fan, H. M. (1976). "Effective composite beam width at ultimate load," J. Struct. Div. ASCE, 102(11), 2163–2179.

Keelor, D. C., Luo, Y., Earls, C. J., and Yulismana, W. (2004). "Service load effective compression flange width in fiber reinforced polymer deck systems acting compositely with steel stringers." J. Compos. Constr., 8(4), 289–297.

Keller, T., and Gurtler, H. (2005). "Composite action and adhesive bond between fiber-reinforced polymer bridge decks and main girders." J. Compos. Constr., 9(4), 360–368.

Lorentz, R. F. and Stockwell, F. W. (1984). "Concrete slab stresses in partial composite beams and girders." AISC Engineering Journal, 40, 51-63.

Moon, F. L., Eckel, D. A., and Gillespie, J. W. (2002). "Shear stud connections for the development of composite action between steel girders and fiber-reinforced polymer decks." J. Struct. Eng., 128(6), 762–770.

Moses, J. P., Harries, K. A., Earls, C. J., and Yulismana, W. (2006). "Evaluation of effective width and distribution factors for GFRP bridge decks supported on steel girders." J. Bridge Eng., 11(4), 401-409.

Newmark, N. M., Siess, C. P., and Viest, I. M., (1951). "Tests and analysis of composite beams with incomplete interaction." Proceedings of the Society of Experimental Stress Analysis, 9(1), 75-92.

Ranzi G, Bradford M. A. (2006). "Analytical solutions for the time-dependent behaviour of composite beams with partial interaction." Int. J. Solids Struct, 43, 3770-3793.

Ranzi G, Bradford M. A., Uy B. (2004) "A direct stiffness analysis of a composite beam with partial interaction." Int. J. Numer. Methods Eng., 61, 657–72.

Ranzi, G., Gara, F., Leoni, G., and Bradford, M. A. (2006). "Analysis of composite beams with partial shear interaction using available modelling techniques: A comparative study." Computers and Structures, 84, 930-941.

Salim, H. A. and Davalos J. F. (2005). "Shear lag of open and closed thin-walled laminated composite beams." Journal of Reinforced Plastics and Composites, 24(7), 673-690.

Zou, B., Chen, A., Davalos J. F., and Salim, H. A. (2011). "Evaluation of effective flange width by shear lag model for orthotropic FRP bridge decks." Composite Structures, 93, 474-482.

CHAPTER 7. CONCLUSIONS AND FUTURE WORK

In this dissertation, a multifunctional photovoltaic (PV) integrated insulated concrete sandwich (PVICS) panel is developed, which can act as a combined active and passive energy system to achieve a zero-carbonate building system. The active energy system is provided through energy harvesting using solar cells, and the passive energy system is provided through the insulation and FRP shear connectors, which can reduce the thermal conductivity and panel weight. The solar cells were attached to the concrete through innovative co-curing scheme, where FRP can act as an interface to enhance the bond between solar cells, FRP and concrete. The performance of solar cells under tension and compression loading was studied. An analytical model considering shear-lag effect was derived for single, multiple and edge shear connectors. The analytical model was further expanded to FRP deck-on-girder configuration. Specifically, the following conclusions can be drawn from this study:

7.1. Study on a Full-Scale Insulated Concrete Sandwich Panel

- FRP shear connectors could transfer shear between concrete wythes.
- The load-deflection curve and crack patterns obtained from the nonlinear FE model agrees well with those from the bending test.
- The FE model can be used to model sandwich panel with any shear connector given that the stiffness of the shear connector is provided.
- The test panel achieved 72%, 82% and 74% DCAs based on displacement, load and strain methods, respectively.
- Displacement and strain methods can be used in the linear region, while the load method can be used in the non-linear region.

- Shear lag effect is observed as a result of the stress concentration at the locations of the shear connectors.

7.2. Integrated Insulated Concrete Sandwich (PVICS) Panel

- The developed PVICS panel can act as both an active and passive energy system.
- Bonding aggregates to the FRP can increase the bond strength between FRP and concrete.
- The FRP shell can provide a confining effect to the concrete and act as shear connectors and reinforcement.
- Results from the derived analytical model correlated well with the test and FE results, which can be used for design purposes.
- The sandwich panel with GFRP shear connectors achieved nearly full composite action.

7.3. Performance of Solar Cells under Strain

- Amorphous silicon solar cells started to degrade from about 0.5% to 1% strain under compression depending on buckling mode.
- Under tension, solar cells degrade at about 1%.
- There are thresholds for the solar cells in both compression and tension, i.e., the solar cells work properly below the threshold but degrade rapidly once the threshold is passed for monotonic loading.
- For perovskite solar cell, a degradation of about 15% was observed when subjected to tension loading with a strain until 3%.

- A-Si solar-FRP can be used as a strain indicator, while perovskite solar cell can be used in application where high strain is more likely to occur.

7.4. Shear-Lag Analytical Model for Sandwich Panels

- The analytical model can accurately predict the behavior of the sandwich panels in terms of stress/strain and deflection, considering the partial DCA.
- The analytical model can be used for single, multi-cell, wide flange, cantilever sections or a combination of any configurations.
- DCA can significantly affect the stress and strain distributions.
- The parametric study results show that the smallest value of effective width can be achieved with 100% DCA.
- Aspect ratio is an important factor that affects the effective width. The derived closed-form equation is only valid for one-way panel.
- Core thickness and panel stiffness have negligible effects on the effective width.

7.5. Shear-Lag Analytical Model for Deck-On-Girder Composite Beam System

- The analytical solution can accurately predict the behavior of composite beam in terms of both stiffness and stresses, accounting for the partial DCA from the shear connector, as verified by test and FE results.
- Similar to the sandwich panel, DCA can significantly affect the stiffness and interfacial stress distributions.
- A parametric study was conducted by varying the deck stiffness and DCA. It can be concluded that:
    - The bridge deck stiffness has a negligible effect on the effective flange width.

- ♦ The interfacial stiffness also has insignificant effect on effective flange width for DCA up to 75%. For 100% DCA, the effective flange width drops about 10%.
- ♦ The effective flange width for 100% DCA can be conservatively used to represent the effective flange width for other DCAs.

- A simplified method is proposed to calculate the stiffness and strength distributions, which can be used for design purposes.

7.6. Future Work and Recommendations

The following items are recommended for future studies:

- Performance of PVICS under fire, humidity, UV rays and blast loading.
- Fracture energy modeling of the solar cell behavior to investigate the behavior of degradation to be used as a sensor.
- Expanding the analytical model to include the behavior of the sandwich panels under plastic behavior and nonsymmetrical shear connector configurations.
- Application of multiple and edge shear connector concepts to the deck-on-girder system.